Modeling, Design and Experimental Evaluation of an Agile Long-Reach Robotic Arm

By Jouke T. Hompes

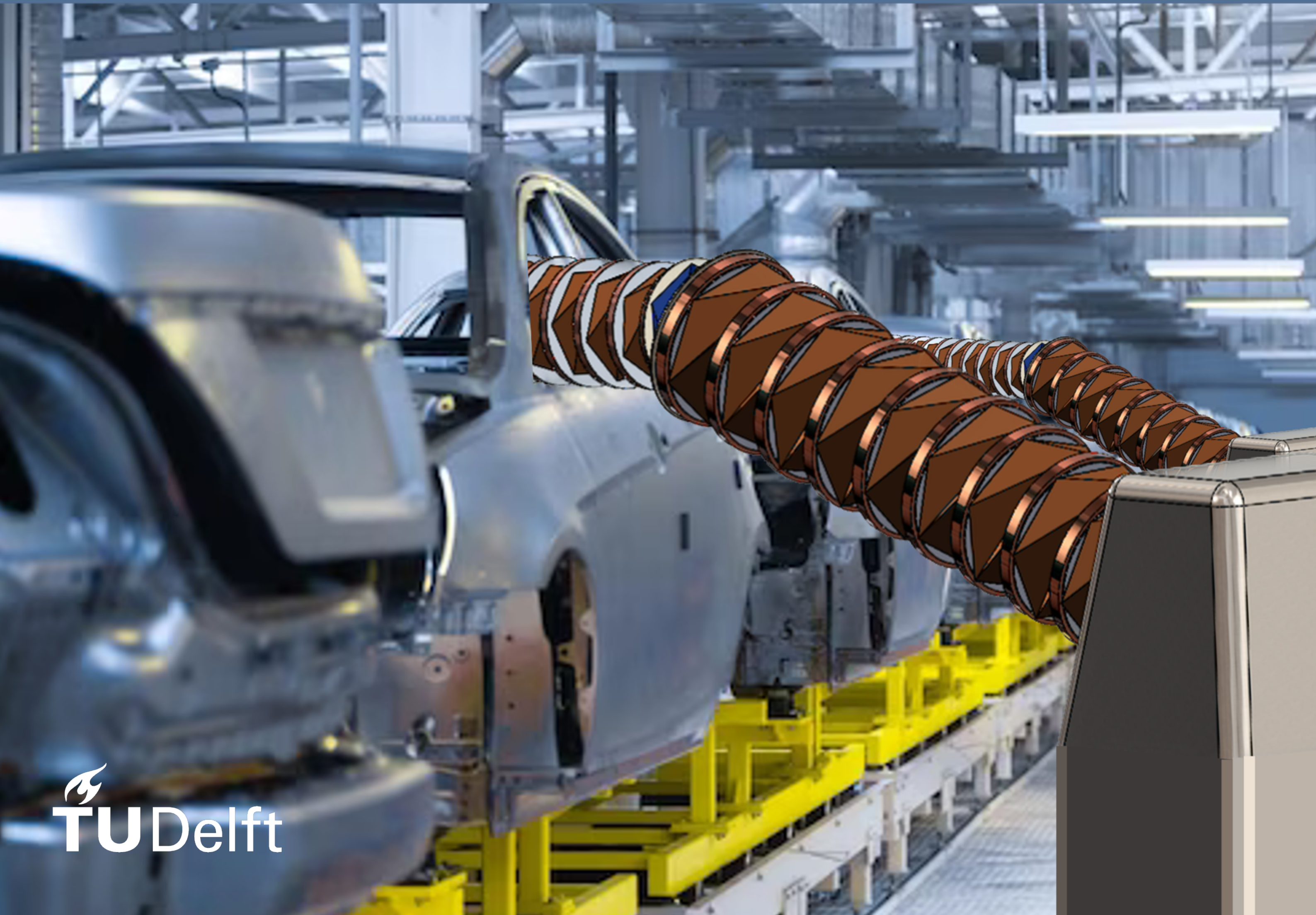

Modeling, Design and Experimental Evaluation of an Agile Long-Reach Robotic Arm

By

Jouke T. Hompes

Master Thesis

To obtain the degree of

Master Of Science
in Mechanical Engineering
at the Delft University of Technology

To be defended publicly on Thursday February 22, 2024, at 9:00h.

Student number:	4644867	
Report number:	2023.MME.8891	
Project duration:	June 2023 – February 2024	
Thesis committee:	Dr. J. Jovana	(TUD, Chair, MTT)
	Ir. V. Kortman	(TUD, Supervisor, BME)
	Ir. A. Napoleone	(TUD, MTT)
	Dr. Ir. A. Sakes	(TUD, BME)

This page is intentionally left blank.

Preface

"Talent is just a pursued interest." Even though this quote from painter Bob Ross is not in any way linked to engineering, flexible robotics, or any technical concept at all, it has been an important mainspring for my entire educational career, has driven me to finish this thesis, and has made me who I am today. Embarking on my educational journey, starting in primary school, I was never a 'talented' pupil when comparing myself to the children attending the advanced groups. At eleven years old, ready to set off to high school, my teachers told me that I was not even an average pupil and I was not allowed directly into my school of choice to pursue Dutch havo with my friends at the time. The main reason (ironically): "my arithmetic skills were certainly too weak." Only after proving my misplacement could I join them, which set my interest for the rest of school. After acquiring my havo diploma, my gut told me that high school had not challenged me enough, and in two additional years, I completed vwo (pre-university education). After developing a good basis in maths and physics, I was drawn to TU Delft to become an engineer. Strangely enough, it felt like primary school all over again, as brighter or 'talented' kids were everywhere. This thesis is a consequence of the same interest that drove me in high school and proves that talent is indeed merely a pursued interest and not necessarily something you are born with. You must only find the right interest, and the rest will automatically unfold. As with this thesis.

Chapter one will provide insights into the concepts that already existed before this thesis to reach into confined spaces. Chapter two entails the geometric modeling of a generic robotic arm to obtain clues into the kinematic requirements a full flexible robotic arm must adhere to, introducing a new approach to flexible robotic design. Chapter three dives into the process of designing and prototyping a new type of actuator which could finally enable flexible robotics to be introduced in an industrial setting by combining electromagnetism and deployable origami in a stand-alone system. The three chapters are intended to be readable and understandable individually, so feel free to skip to chapter 3 immediately to find out how creative one can get with block diagram drawing software as virtually all graphics are made with Microsoft Visio and Powerpoint, or appendix C to see all the worthy prototypes I created in the past months.

This work would never have been of the standard as it is now if it were not for Jovana. Starting from the Bachelor End Project (BEP), she has shown me how to properly work on a project, keep improving it, and make sure that you do not lose track of the essence. Therefore, I would like to show the greatest appreciation and thank her for all her help, effort, and belief in the past months. I would also like to thank Vera for her weekly, and sometimes even daily input in the prototyping process, and Ilse from DHL for her help in forming the project and providing great input on the practical side of the concept. Lastly, my thanks go to the guys in the RAS/JAM lab, Vittorio, Bart, and Andrea, to support and advise me to build my prototypes while not setting the faculty on fire, and for all the infamous coffee brainstorm sessions.

To end this preface, I want to thank my friends, my brothers, Jons and Jerome, and in particular my parents, Marcel and Caroline, for always believing in me and guiding me to achieve my full potential and being there to talk whenever the process was tough. I hope reading my thesis will bring some pleasure and potentially spark some interest.

Enjoy!

Jouke T. Hompes
Amsterdam, February 2024

Abstract

Flexible robotics offers promising solutions for navigating complex environments, and this study contributes to its advancement through innovative methodologies optimizing both flexible robotic arm kinematics and a novel flexible actuator. The first methodology focuses on optimizing kinematics using quadratic programming, enabling the determination of optimal segment configurations without prior knowledge of specific materials or working principles, thus introducing a novel systematic first step in flexible robotic design. Addressing computational intensity and solver compatibility limitations, valuable insights are provided into designing segmented flexible robotic arms, offering a systematic methodology for real-world challenges. Simultaneously, an electromagnetically actuated Kresling cylinder is introduced, leveraging tunability in axial stiffness and electromagnetic actuation. Through dimensional optimization using finite element analysis (FEA), critical design considerations such as coil dimensions and core configurations are systematically explored. Experimental validation extends the application to full-sized robotic arms for package unloading in confined spaces, underscoring the significance of magnetic force in overcoming gravitational resistance, especially in logistics environments. These methodologies represent significant contributions to the field of flexible robotics. The first provides a systematic framework for kinematic optimization, while the second introduces an innovative actuation mechanism tailored for flexible robotic arms in industrial settings requiring long-reach capabilities. Their integration opens new possibilities for designing adaptable robotic systems capable of complex tasks in diverse environments. By addressing computational challenges and practical constraints, this research advances the frontier of flexible robotics, facilitating real-world implementation across various industries.

Contents

List of Figures

List of Tables

Chapter 1

Innovations to Reach Confined Spaces

Abstract
This study investigates innovative solutions for reaching into confined spaces through a multidisciplinary lens. Three main categories of concepts are explored: deployable origami, continuum arms, and telescoping or weight-compensating devices. Deployable origami offers compact yet adaptable structures through versatile folding patterns. Continuum arms, drawing inspiration from flexible robotics, achieve complex motions using materials like silicone. Meanwhile, telescoping and weight-compensating devices provide unique capabilities for extending reach. A comparative analysis highlights the flexibility and reach of these devices, with weight-compensating mechanisms showing superiority in reaching long distances. The study envisions a future where robotics navigate constrained environments seamlessly, driven by flexible and adaptive characteristics gleaned from innovative small-scale studies, and revolutionizing larger-scale applications across industries like inspection, maintenance, and disaster response.

1.1. Introduction

Robotic arms, integral in diverse industries, find applications ranging from palletizing and material handling to welding, inspection, and pick-and-place operations [1–3]. The electric and electronics industry installed 137,000 units, while the automotive sector incorporated 119,000 units in 2021 [4]. The adaptability of robotic arms to various sizes and contextual needs emphasizes the importance of tailoring specifications to the working environment, influencing the selection of an optimal robot for specific tasks. Articulated robotic arms, characterized by straight sections and rotary joints, represent a prevalent choice for automating routine tasks. These manipulators typically offer a movement range of 6 to 7 Degrees Of Freedom (DOF) and excel in scenarios demanding stamina, lifting power, and robustness. Challenges arise when faced with obstacles, including encasements obstructing pick-up positions or scenarios demanding extended reach for enhanced robotic functionality. Conventional arms undergo a reduction in range of motion with each successive angle to pass when exposed to intricate corners [5, 6].

According to a data gathering conducted for this study from 3 of the largest manufacturers of articulated robotic arms, Fanuc, Yaskawa and Kawasaki, a trend is shown between reach and payload capabilities, meaning that longer reach arms are commonly capable of picking up heavier items. The trend between reach and payload is depicted in Figure 1.1. To substantiate the relationship between reach and payload, a Spearman rank correlation is computed and resulted in a value of 0.86 [7]. For this, it is assumed that the sample space of 187 arms is sufficient to represent the complete set of all articulated arms. High payloads are not always desired with long reach, for instance in the logistical sector where parcels are rarely heavier than 23 kg [8]. The mismatch of the widely deployed articulated robotic arm in more complex environments finds importance beyond only the logistical sector. Automation in operating in confined spaces finds applications for instance in vehicle manufacturing and inspection, cleaning and maintenance of confined spaces. In automated car assembly lines operations inside the frame of the car are often yet conducted by human hands and confined spaces often come with hazardous working conditions as 24% of confined space fatalities happen during maintenance, followed by 12% for cleaning and 11% for inspection [9, 10]. Many concepts have been developed to automate the entering of confined spaces, but most entail mobile concepts which do not suffice in automatic manufacturing or maintenance [11].

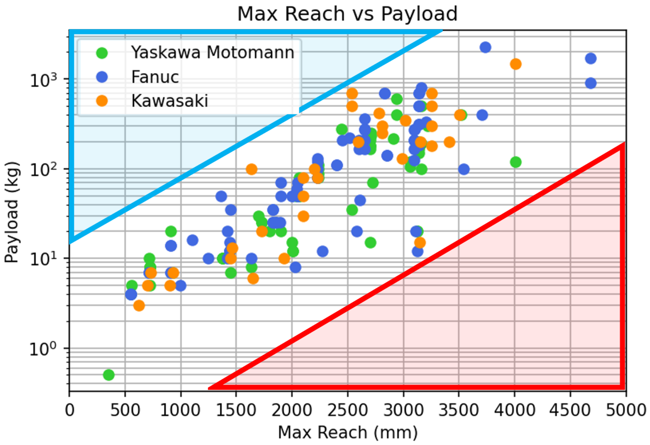

Figure 1.1: *Relation between reach and payload capabilities of articulated robotic arms from three major manufacturers, with indication of design freedom. (Red area) robotic arms with high reach/payload ratio, (blue area) robotic arms with high payload/reach ratio.*

Automatic operation in confined spaces can be characterized by an initial bridge or cantilever into the confined space, followed by a manipulation inside a confined volume. To specify, arms to be deployed in confined spaces must possess a high reach/payload ratio. According to Figure 1.1, articulated robotic arms are generally not designed for such applications as the area highlighted in red indicates the empty design space for arms with high reach/payload capabilities with regard to commercial articulated arms. For instance, if in logistics a parcel must be manipulated with a maximum mass of 23 kg from a distance of 5 meters, only a heavily over-engineered arm exists which is likely inconveniently large, which has payload capabilities of close to 1000 kg.

Due to the limitations presented by commercial articulated arms and the desire for automation in confined spaces, the primary objective of this literature study is to synthesize insights from structures that can either extend and retract, bend, or can do both using concepts deviant from traditional robotics where straight sections and rotary joints are central, for resolving complex reach issues in industrial settings and unveiling where science lacks in this area. A notable aspect of the sought after concepts is their ability to bridge gaps into confined spaces and bend accordingly. The study explores concepts from a range of dimensional orders, looking at elementary extending structures which are for instance found in origami [12–14], medium sized concepts in the form of continuum robots [15], and a state of the art of large-scale long-reach devices that surpass the flexibility and reach of the articulated robotic arm [16, 17]. Taking inspiration from all three mentioned categories, new insights can be created to tackle complex reach problems beyond the reach of traditional articulated robotic arms.

Figure 1.2: *Elementary motions central in this review to reach into confined spaces.*

This inquiry aligns with a departure from conventional approaches, notably witnessed in the realms of origami and kirigami. Originating from Japan, origami has evolved into a wellspring of inspiration for innovative solutions across diverse fields [12]. Furthermore, kirigami, an extension of origami that involves not only folding but also cutting materials, introduces additional possibilities for various applications [13]. The merger of principles from origami and kirigami leads to a more versatile concept: deployable structures, which can often perform efficient extension and contraction and sometimes accompanied by bending [14]. Additionally, flexible robotic concepts, often inspired by bio-phenomena by using flexible materials like silicone, are explored to expose which their role in complex reaching could be. The most popular flexible robotic structure is the continuum arm, which can often perform the motions described in Figure 1.2 by elongating, contracting and bending along various points on it's body [15]. Continuum robots are not solely found in silicone-like materials but all do pose potential for this review, and thus non-silicone continuum robots are also considered. To bridge the initial distance to a confined space, long-reach devices are essential. To cantilever over substantial distance, large deployable structures use various principles [16]. However, since most complex reach problems are situated on earth, to maintain stability while reaching far, weight compensation is required [17]. Taking inspiration from all three mentioned categories, new insights can be created to tackle complex reach problems beyond the reach of traditional articulated robotic arms.

1.2. Origami for reaching

For novel robotic arms to translate into confined spaces in an efficient way, folding devices bear great potential as they deploy with volumetric efficiency from their own footprint, highlighting potential for the extending and retracting motions from Figure 1.2. The pinnacle of folding structures lies in the Japanese art and now global science of paper folding. This chapter shall explain some of the most popular patterns that bear potential for reaching into confined spaces.

1.2.1. The basics of deployable origami

Origami, encompassing traditional origami, kirigami, and modular origami, has emerged as a versatile field with applications spanning various engineering sectors [38]. Origami involves folding a structure from a single sheet of paper, kirigami permits cutting, and modular origami combines both, often with intermediate attachment using glue. In aerospace, foldable structures inspired by origami play a crucial role, especially for large structures that need to be compacted during launch and later deployed in orbit [39]. For instance, space telescopes, larger than launch fairings, require innovative folding techniques [16]. Origami principles are also applied to the design of solar arrays for efficient deployment in space [40]. In this section, deployable origami is defined as origami structures that are designed to facilitate a shape change through folding, in contrast to stationary aesthetic origami.

Origami finds a highlight in Miura-ori, a folding pattern discovered by Japanese engineer Koryo Miura. Miura-ori enables the efficient packing of a 2D plate into a 3D volume, making it invaluable for space applications, such as folding solar arrays [41]. The Miura pattern's single-degree-of-freedom system ensures a flat middle plane during deployment, enhancing its value [42]. Miura origami prisms, with various cross-section shapes and base-unit patterns, find applications in sandwich structures, energy absorbers, origami robots, and metamaterials [43]. The versatility of Miura-ori extends beyond paper, proving useful for different materials interconnected by hinges. Yoshimura origami, characterized by the buckling of a thin-walled cylinder into a periodic pattern, offers stability and has applications in various studies [14, 44–46]. One application involves using Yoshimura origami to encapsulate flexible pneumatic actuators, providing flexibility and protection [47]. Another study explores Yoshimura origami as encapsulation for a one-motor peristaltic locomotion device [48]. In contrast, the Kresling pattern, arising from torsionally loaded thin-walled cylinders, is bi-stable and allows large displacements without strain. This feature makes Kresling origami an attractive option for deployable systems with versatile tuning options [49]. Further studies explore the development of a tri-stable Kresling origami, using multi-triangle cylindrical origami (MTCO), showcasing exceptional flexibility and strength [50]. The MTCO, with integrated ring-shaped magnets, achieves high stiffness in its unique third state, offering novel possibilities for deployable structures. A methodology was developed to create detailed requirements to actuate the Kresling cylinder [51]. The waterbomb pattern, another bi-stable origami pattern, is often employed symmetrically, leading to complex nonlinear dynamical behavior [52]. Studies highlight the asymmetric stable positions, nonlinear spring-like behavior, and tunable effective stiffness and natural frequency of the waterbomb pattern, and it is considered a desirable testbed for automating origami folding [53–55]. The waterbomb pattern can be configured in a cylindrical shape but does not linearly contract like the Yoshimura pattern and the Kresling pattern, but rather does so like an artificial muscle [56–58].

1.2.2. Origami-inspired innovations

Continuing the exploration of origami-inspired robotic arms, Zhang et al. proposed a continuum robot with three parallel origami modules based on the waterbomb crease pattern, enforced by a helical spring backbone for significant length variability. Actuated by three tendons, the arm exhibits bending and length variation through single and dual tendon actuation and contraction [32].

Table 1.1: *Studies of 4 of the most popular origami patterns as actuators.*

	Geometry	Direction	Actuation	Units	Lin. displ.	Ref.
Yoshimura	Cylindrical	Linear/bending	Pneumatic	2	NA	[18]
	Cylindrical	Linear/bending	Tendon	1	27 mm	[19]
	Cylindrical	Linear	Pneumatic	1	70 - 100 mm	[20]
	Cylindrical	Linear/bending	Tendon	1	40 mm	[21]
	Cylindrical	Linear/bending	Pneumatic	2	171 mm	[22]
Kresling	Cylindrical	Linear/bending	Magnetic	1	10 mm	[23]
	Cylindrical	Linear	Pneumatic	1	20 mm	[24]
	Cylindrical	Linear	Pneumatic	5	45 mm	[25]
	Cylindrical	Linear	Pneumatic	4	47 mm	[26]
	Cylindrical	Linear	SMA	1	15 mm	[27]
	Tri cylindrical	Linear/bending	Pneumatic	6	8 cm	[28]
Waterbomb	Sheet	In plane	Env. sensing	NA	NA	[29]
	Toroid	Radial	SMA	NA	NA	[30]
	Prismatic	Linear	SMA	1	5.1 cm	[31]
	Tube	Linear/bending	Tendon/spring	6	60 mm	[32]
Miura	Sheet	In plane	Magnetic	NA	NA	[33]
	Sheet	In plane	SMP	NA	NA	[34]
	Tube	Linear	Screw rods	6	140 mm	[35]
	Cylindrical	Linear/bending	Tendon	1	35.3 mm	[36]
	Cylindrical	Linear/bending	Pneumatic	3	27 mm	[37]

An anti-buckle medical support system for internal catheters, inspired by the bistable Kresling pattern, features a triangulated cylinder pattern with fixed and variable inner diameters. This design counteracts catheter buckling during insertion and is made from PET plastic [59].

Wu et al. present a multi-unit Kresling arm with integrated magnetic actuation, mimicking the tentacle of an octopus. The arm achieves omnidirectional bending and multimodal deformations, demonstrating complex bending, object grasping, and lifting weights. The arm is made from Tant origami paper or polypropylene film and utilizes specially designed magnetic plates [23].

A more articulated approach to origami robots is the two section extendable SRA origami arm connected by a 4-bellow pneumatic hinge [22] This design showcases the potential for deployment in space due to its 3D-printed nature and inherent airtightness. Each longitudinal section of the arm elongates based on the Yoshimura diamond origami pattern, providing length variation between 240 and 411 mm.

"Robogami" explores the automation of origami sheets, using bidirectional torsional actuators and piezoresistive angle sensors. The system, resembling thin sheets, can crawl and jump using electrical stimuli. "Mori," a modular origami robot, utilizes equilateral triangles as building blocks with active and passive units for reconfigurable and mobile systems. Both Robogami and Mori demonstrate the potential for automated origami structures [60–62].

Table 1.1 shows studies which assumed the four origami patterns and created actuators out of them. Evidently, the Yoshimura and Kresling patterns are mainly used in cylindrical form which makes them both attractive for linear elongating applications. Due to the 1D deployment of the Yoshimura pattern this structure can more easily also accommodate bends. The Kresling cylinder however presents a twisting motion upon linear elongation which also increases the moment of inertia in deployed state, making this structure more resistive to bending. One study also explores bending of the Kresling cylinder close to its folded state. Pneumatics are the most popular mode of actuation for both Yoshimura and Kresling cylindrical structures, with select studies deviating and introducing more innovative actuation principles. This shows that much space exists in this area to expand upon actuation principles in the art of cylindrical origami. The relation between these small scale origami concepts and reaching into confined space might not be easily recognised. However, the spacial efficiency which these concepts bear is maintained when these concepts are scaled, either dimensionally, or when presented in a modular build of many untis. This opens possibilities for origami-based long-reach devices. The Waterbomb and Miura patterns are more often used in a modular approach and in more creative form factors. Movement in many directions has been studied and innovative concepts have been combined to actuate the origami structures. However, inherently these patterns create sheet origami's which are not directly suitable for long-reaching. For these patterns, potential is hidden in a modular use. In general, research on origami structures only presents itself at a small scale, fabricated out of paper, with only 1 industry as an exception: aerospace. Here, the potential of origami has readily transpired.

1.3. Continuum robots in reach problems

This section shall present various continuum robotic design, of which many are influenced by flexible robotics, incorporating flexible materials like silicone. Flexible robotics, an emerging field in engineering, provides innovative solutions to challenges posed by conventional hard robots, such as limited collaboration capabilities and complexity [81]. The discussion introduces various continuum robotic designs interesting in the context of complex reaching, and categorizes them in mode of actuation in Table 1.2.

1.3.1. Pneumatic continuum robots

Pneumatic continuum arms often work according to the principle of interplay between pushing and pulling by inflating one of their often 3 parallel pneumatic chambers to create 3 degrees of freedom by elongation (1 DOF), and bending in two directions (2 DOF). When more of these parallel units are serially connected, a multi-section pneumatic continuum arm is created. Many examples exists in this field like the 3-section silicone PneuNets continuum arm [65]. PneuNets consist of pneumatic networks along a body which can be inflated to create extension to achieve bending and elongation, which in an arm form factor can achieve the grasping and manipulation of objects [63]. PneuNets structures can be actuated using any expanding gas like gas that expands upon exposure to near-infrared light [82]. Gong et al. enhance the PneuNets continuum arm by introducing radial rings of

Table 1.2: *Studies of flexible robotic continuum arms.*

	Backbone	Length	Ref.
Pneumatic/ hydraulic	silicone	165 - 291 mm	[63–66]
	fabric/pneumatic	1 mm	[67]
	muscular hydrostat	99 - 154 mm	[68–70]
	AM pneumatic	700 - 1100 mm	[71, 72]
	Tri-braided bellow	60 - 214 mm	[73]
	Anisotropic fabric	185 - 213 mm	[74]
	Anisotropic fabric	185 - 303 mm	[74]
Tendon	pneumatic	31 - 95 cm	[75]
	spring/mesh structure	110 mm	[76]
Smart material	silicon	320 mm	[77]
Hybrid	iron-infused elastomeric skin	300 μm	[78]
Variable stiffness	granular jamming	355 mm	[79]
	LMPA	600 mm	[80]

rubber, improving bending efficiency [66]. Another strong example is the OctArm, adopting a muscular hydrostat approach inspired by octopus arms, demonstrates superior flexibility and strength, using 3 parallel McKibben actuators per segment for pressurized muscles [68, 69]. Capable of two-axis bending and length variability, OctArm IV (4-section) and OctArm V (3-section) showcase remarkable grasping abilities and resilience in challenging conditions, operating effectively even when submerged in water [70]. With an appearance in the commercial field, Festo, a pioneering automation company, has translated its extensive research into the commercial domain with the development of the ’Bionic Handling Assistant’ (BHA) [71]. This pneumatic continuum arm is fabricated using Additive Manufacturing (AM) and has been the subject of various studies, investigating control and motion-related solutions to optimize its performance [83–88]. Similar to the OctArm V, Festo’s BHA comprises three sections, each actuated by three parallel channels of pneumatic components [71]. With the capability of bending over two axes and elongating, the BHA achieves over 9 degrees of freedom [72]. In contrast to the OctArm, the BHA incorporates rigid vertebrae along its entire length, ensuring structural integrity. These spine-like components provide radial support to the pneumatic sleeve, translating pressure changes into longitudinal movements [72]. The arm is equipped with a mechanical gripper as an end-effector and can extend from 70 cm to 1.10 m, translating to a contraction ratio of 0.36 [71]. Chen et al. present a nearly identical arm with a length range of 306 to 338 mm (contraction ratio of 0.095) [89]. Chen et al. propose an hydraulic flexible robotic manipulator which is capable of elongating and bending using three parallel modules using aramid and elastic fabrics [74]. Two proposed designs, AFA and EFA, show substantial force generation and significant elongating capabilities: from 185 mm to 213 mm and 185 mm to 303 mm respectively. Via a newly designed flexible actuator using a braided bellow (US^2A), the flexible arm of Wang et al. proposes a 3 section continuum arm in the fashion of OctArm, but with an contraction ratio of 0.72 by contracting from 214 mm to 60 mm [73].

1.3.2. Tendon driven continuum robots

Continuum robots can be actuated using simple tendon systems to create contraction and bending. Elongation is often realized using a relaxation of the tendons and an elastic response of an intermediate medium. Examples are the KSI tentacle manipulator and Air-Octor, snake-like robotic arms inspired by octopus tentacles, both utilizing a tendon-driven continuum design with a pneumatic backbone [75, 90]. Multi-sectioned for enhanced maneuverability, it employs a "hose-in-hose" concept with tendons in a star-like pattern for protection and pneumatic support. Despite limitations in load-carrying capacity compared to rigid-link arms, the Air-Octor excels in inspection tasks. A tendon driven continuum robot can also be enforced by springs [91–93].

1.3.3. Shape Memory Alloy continuum robots

Similar to tendon actuation, Shape Memory Alloy (SMA) wires, like NiTi can actuate a continuum arm. An example is presented by Yang et al [77]. This 4-section design, featuring a stiff inner core and integrated sensors, demonstrates lifting capabilities underwater and in the air.

1.3.4. Hybrid continuum robots

The Hybrid Continuum Robot (HCR) incorporates an outer flexible section, utilizing a serpentine flexible structure and metal-braided mesh for 1 DOF joint formation and enhanced torsional stiffness, while the 6-DOFs inner hybrid-structure section consists of a flexible section and a 2 DOFs rigid-joint wrist concentric with the outer section, allowing insertion/extraction motions and rotation for improved dexterity; the actuation system employs detachable backend transmission mechanisms for compact design, utilizing pulleys and capstans to drive cables and achieve translation, rotation, and insertion/extraction motions [76]. Therefore, this concept could also be placed under the tendon tab. A hybrid actuation between tendon and magnetic is also possible, as presented by Zhang et al. [78]. However, this concept was only developed on millimeter scale.

1.3.5. Variable stiffness continuum robots

Due to the frequent need to cantilever, many continuum robots lack stability to manipulate in a robust way. A way to counteract this is to integrate variable stiffness into the continuum arm. This can be achieved by integrating granular jamming in sections of the arm to create stiffness where and when needed [79]. The arm of Cheng et al. comprises of multiple sections and achieves bending through tendon drives and it’s stiffness is varied using pneumatics. Another way of creating variable stiffness is by integrating Low Melting Point Alloy springs along the length of the arm [80].

1.4. State of the art of long-reaching

Ranging from telescoping mechanisms designed for specific applications to weight compensating reach-devices engineered for nuclear plant inspections, each approach represents a unique stride in addressing the complexities of navigating and manipulating within tight spaces from a distance. To conclude the subsection, some concepts are compared

Table 1.3: *Long reach weight compensating and telescoping concepts with their backbone, actuation and reach specifications. The flexibility indicator shows the DOF of the tip segment: (- -) 0 DOF, (-) 1 DOF, (+) 2 DOF, (++) 3 DOF.*

		Backbone	**Actuation**	**Flex.**	**Reach [m]**	**Ref.**
Telescoping	Cubic arm	Interlock. blocks	Friction wheel	-	NA	[94]
	LMPA arm	LMPA links	Winding drum	- -*	NA	[95]
	Rod arm	Telescoping rods	Tendon	-	3.2	[96]
	Teles. arm	Interlock. rods	Push plates	-	3.5	[97]
	MERA	Scissor mech.	Belt drive	-	2	[98]
	TSERA	Tripple scissor	Lead screw	+	0.72	[99]
Weight comp.	PAC	Parallel. springs	Tendon	+	6	[100]
	AIA	Parallel. springs	Tendon	+	8.2	[101–103]
	3D CT-Arm	Tendon WC**	Tendon	+	14	[104, 105]
	Super Dragon	Tendon WC**	Tendon	+	10	[106]
	Giacometti	Helium gas	McKibben	+	20	[107, 108]
	Rotor arm	Prop. thrust.	Prop. thrust.	+	8.8	[109]
	OC	Exo and tendon	Tendon	++	2.2	[110]
	SLIM	Rigid links	Tendon	-	4.8	[111]
	Float arm	Parallel. springs	M-drive	+	7	[112, 113]

**The LMPA arm is indicated as 0 DOF since after deployment its position is fully frozen due to the solid low melting point alloy in the hinges.*
*** WC = Weight Compensation.*

to the current articulated robotic arms and an overview is made of the most promising concepts for adaptive reaching, stating their geometrical capabilities and actuation principle.

1.4.1. Mechanical extending/telescoping devices

Telescoping mechanisms provide an alternative perspective on deployable structures, allowing extensive linear deployment using limited actuators for applications such as camera elevation [114]. Jianfeng's telescoping arm uses cubic blocks connected serially with a hinge point, transforming into a stiff beam for deployment [94]. Seino et al. introduces an innovative chain-like approach with a Low Melting Point Alloy (LMPA) locking system for inspection at Fukushima Daiichi Nuclear Power Station [95]. Fujioka's compliant telescoping arm uses a nested approach, enabling distributed bending via an integrated tendon system in a fishing rod-like structure[96]. Ogawa explores a tendon-driven elastic telescopic arm with multiple extension stages, actuated by pushing plates and shafts for selective extension with obstacle avoidance capabilities due to bending [97]. The Mobile Extendable Robot Arm (MERA) employs a double scissor mechanism to reach high spots, addressing singularity through a belt drive system [98]. Shikari presents the Triple Scissor Extender Robot Arm (TSERA), featuring three segments with individual scissor mechanisms for agile movement and a fluid trajectory, adressing the 'last-one-foot' problem [99].

1.4.2. Weight compensating reach-devices

Long reaching, cantilevering devices create a high torque, and thus smart weight compensation must be accounted for in long-reach manipulators. In the previous chapters, relatively small scale concepts have been presented and their potential for deployable cantilevering capabilities has been discussed. When these concepts are scaled to be implemented in complex reach situations, appropriate weight compensation must be incorporated. This section delves into weight compensating concepts to reach into confined spaces.

In-arm weight compensation

A challenge with long reaching into confined spaces is the need for weight compensation. Sectional modules with integrated actuators prove effective, exemplified by PAC (porteur articule en cellulé), a 6-meter articulated inspection robot with a 1 kg payload capacity [100]. Although this design is seemingly similar to a traditional articulated robotic arm, this design consists of 5 sections, each 1.2 meters, boasts 11 degrees of freedom (DOF) and uses a parallelogram-spring gravity compensation system. This makes it stand out with respect to traditional articulated arms and would out-reach all arms found in Figure 1.1, while being designed for lifting almost the lightest payload as shown in Figure 1.3. A modified version, AIA (articulated inspection arm), extends up to 8.2 meters with a 10 kg payload, designed for tokamak inspection [101, 102]. AIA's plasma vessel operation in a high vacuum and 120°C demands robust design [103]. The 'Float arm' by Hibot, a snake-like manipulator in the commercial sector, is a long-reach, weight-compensating hyper-redundant robotic arm primarily used for inspection [112]. Like the PAC and AIA arms, Float arm also uses a parallelogram mechanism which accommodates vertical node displacement, and swivel joints at the nodes handle yaw movement. The arm's 2 DOF sections utilize the M-Drive actuation system, transmitting torque with a mid-tensioning force for both torque limiting and wire tensioning [113]. Initially designed with 4 sections, the Float arm has evolved to feature up to 9 sections in commercial applications, spanning 7 meters, weighing 35 kg, and supporting a 2 kg payload, as obtained from the website of Hibot (2023).

Base weight compensation

A multi-joint manipulator, '3D CT-Arm,' designed for nuclear reactor inspection, features 18 DOF and a 14-meter reach [104]. Its complex system of pulleys and tendons actuated and tensioned from its base enables precise control. A weight compensation system achieves efficient joint control and volumetric improvements [105]. The 'Super Dragon,' a 10-meter model of the 3D CT-Arm, successfully fulfills nuclear plant requirements [106].

Snake robots, such as the SAFIRE developed by OC Robotics, exhibit significant potential in applications such as aerospace, nuclear decommissioning, and bomb disposal [115]. In the context of nuclear power plant inspections, the limitations on human employability arise due to the risk of surpassing permissible radiation doses, particularly in areas like the control rod drive mechanism (CRDM) characterized by elevated radiation levels. The SAFIRE machine, remotely operated and equipped with a 2.2 m long, 12.5 mm wide robotic arm boasting 19 degrees of freedom, addresses this issue by relieving humans from the need for physical inspection [110]. The robotic arm, actuated and supported by wires and a modular rigid exoskeleton, achieves mobility in narrow pipes through snake-like undulatory movement, while maintaining stability using its large base as a counter weight [116]. It can also operate with algorithms for joint-specific or Cartesian actuation. Primarily designed for inspection, the arm exhibits compliance due to its large torque, limiting its strength capabilities. However, OC Robotics envisions designs with extended reach (up to 4 meters) and substantial payload capacity (±50 kg) [116]. Currently, the Series II - X125, with a 3.1-meter articulated reach, supports a payload of 10 kg, offering versatility for tasks such as inspection, gripper operation, high-pressure water-jet cleaning, or the use of fastening tools in commercial context as obtained from the website of OC Robotics (2023). The LaserPipe, a variation of the X125 designed for laser welding, features a 2.5-meter reach and a 5 kg payload capacity, boasting a welding tolerance of 0.2 mm as obtained from the website of OC Robotics (2023). A tendon-actuated snake-like robotic arm, named SLIM, exhibits long reach with 10 degrees of redundancy [111]. Comprising 12 connected modules, SLIM achieves a reach of 4.8 meters from the base with a payload of 1 kg. Module sizes vary to address stress considerations, with stronger modules near the base and lighter ones at the end-effector. Operated from a rigid base housing 12 linear actuators, SLIM features an actuation box that doubles as a storage location for parking. Despite its extended reach and 15 degrees of freedom, SLIM's agility is limited to reach in a single vertical plane.

Alternative weight compensation

The 'Giacometti' robot, a 20-meter deployable flexible robotic arm, innovatively uses helium-filled balloon sections for safety and compliance [107]. A 7-meter prototype with 7 DOF showcases the uniqueness of this compliant robot. The 20-meter model improves on drawbacks, demonstrating its capability to navigate through confined spaces for disaster cite inspection [108]. An articulated arm with an active weight compensation system based on electrically powered rotors achieves success in 6.6 and 8.8-meter prototypes [109]. The rod structure with propellers counters torsional disturbances, suitable for inspections at a safe distance. These diverse innovations cater to specific challenges in nuclear plant inspection and disaster site exploration.

1.4.3. Flexibility of telescoping and weight compensating devices

From Table 1.3 it is evident that substantial reach can be achieved with telescoping and weight compensating devices. Comparing telescoping and weight compensating devices, it is clear that weight compensating mechanisms surpass telescoping devices in both reach and flexibility of the last segment. The flexibility of the last segment is of importance since this will determine the applicability of the entire arm to a confined situation. Ultimately, 3 DOF is desired as this includes both tip retraction and the freedom to move in the two lateral directions. Judging from Table 1.3, only the snake-arm from OC Robotics possesses these capabilities. One substantial advantage of telescoping devices is that their volumetric use happens rather efficiently, as they mainly retract in their own footprint, whereas many of the weight compensating devices demand smart retraction in order to move out of the confined environment. A yet unexplored field is presented as telescoping behavior with longer reach and more flexibility. When comparing the articulated weight compensating devices with traditional articulated robots, it can be concluded that these designs offer unique capabilities, as is depicted in Figure 1.3. All arms but the OC Robotics arm show a reach/payload ratio that is higher than the traditional arms. However, the OC Robotics arm presents an additional degree of freedom in its tip with respect to articulated arms, showing superior performance in confined spaces.

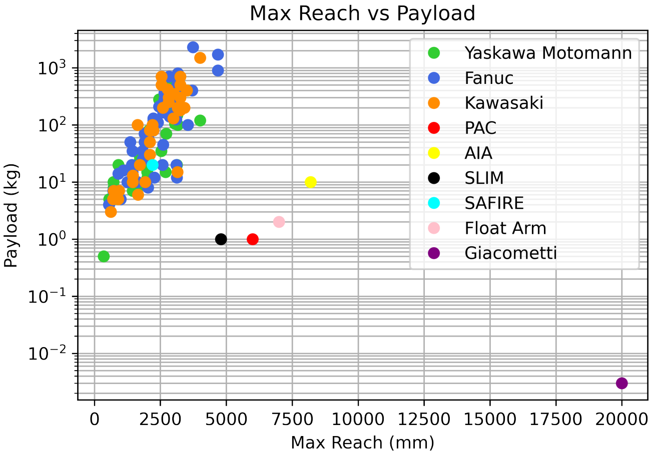

Figure 1.3: *Relation between reach and payload capabilities of articulated robotic arms from three major manufacturers and weight compensating long-reach manipulators.*

1.5. Concluding remarks

In this study, the challenge of reaching into confined spaces has been identified, and three groups of concepts are explored to highlight their potential for solving this challenge. In deployable origami, 4 base patterns are explained and the state of the art of actuation of these structures is presented. Moving up an order of magnitude, continuum arms are presented and a categorization is made in terms of actuation principles. Lastly, long-reaching devices are explored and are divided into telescoping devices and weight-compensating devices, the last being subdivided into three groups of weight compensation and are compared to the current state of articulated robotic arms. Figure 1.4 shows the three main categories from this review with their dimensional order of magnitude, with their main sub-groups and pros and cons.

By recognizing the limitations of current robotic designs and embracing the lessons learned from the presented innovations, the vision for the next generation of robotic arms is suggested. The future entails the development of robotic systems that seamlessly navigate through constrained spaces, adapt to various tasks, and interact with their surroundings with enhanced precision and control, consisting of (a combination of) deployable origami, continuum arms and/or telescoping or weight compensating devices. This evolution will not only redefine the capabilities of robotics in industries such as inspection, disaster response, and maintenance but also pave the way for a new era of versatile industrial robotic applications. The incorporation of flexible and adaptive characteristics from all diverse small-scale studies, combined with long-reach concepts sets the stage for revolutionizing larger applications, redefining the way we perceive robotics in the future.

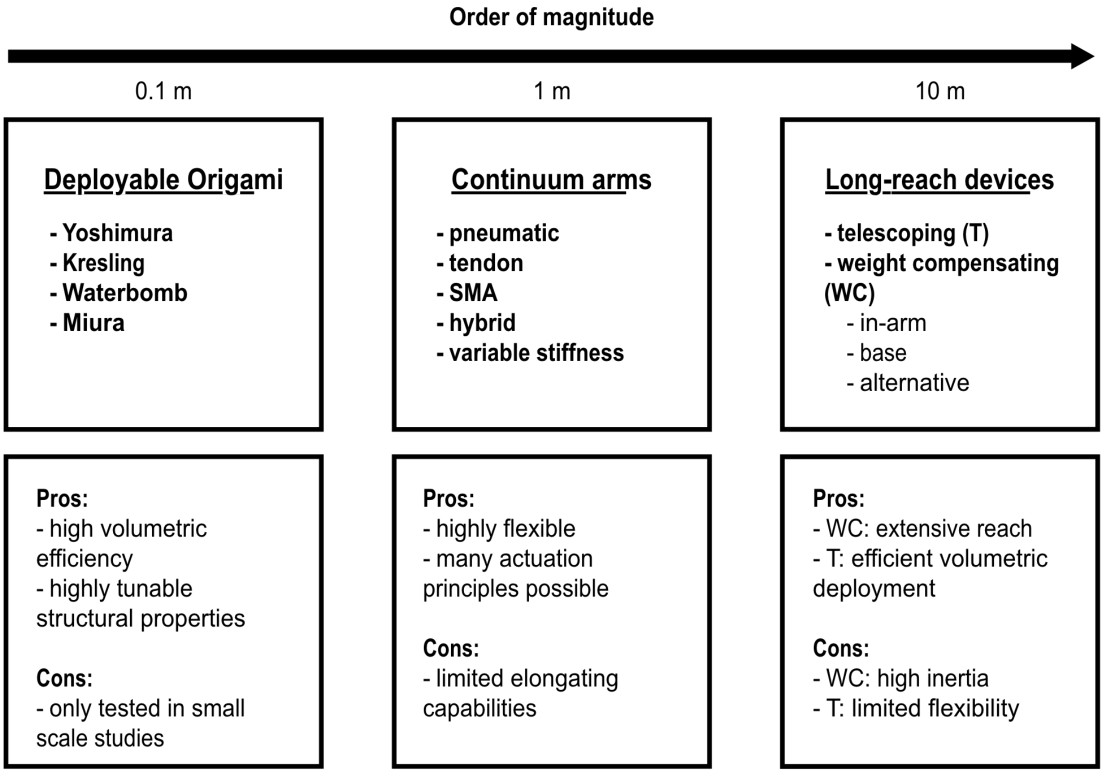

Figure 1.4: *Overview of principles for complex reaching.*

Chapter 2

Kinematic Optimization: A First Step in Flexible Robotic Arm Design

Abstract
Flexible robotics has emerged as a promising field for designing robots capable of navigating complex and geometrically constrained environments. This study presents a novel methodology for optimizing the kinematics of flexible robotic arms using quadratic programming optimization. The methodology is demonstrated through a generic scenario and a case study in logistics, showcasing its versatility and applicability across various robotic applications. By leveraging quadratic programming, the study enables the determination of the optimal number of segments, segment lengths, and deflection angles required for a given task without prior knowledge of specific working principles or materials, for a segmented arm. The study highlights the importance of addressing computational intensity and limitations in solver compatibility in kinematic optimization, offering recommendations for future research to address these challenges. Through comprehensive modeling and experimentation, the study provides valuable insights into the design process of segmented flexible robotic arms, introducing a new first step for designing flexible robotic arms to address real-world challenges. Overall, this study contributes to advancing the field of flexible robotics by providing a systematic methodology for designing flexible and adaptable robotic systems without having any prior knowledge on the working principles or materials of the system, to ultimately perform complex tasks in diverse environments.

2.1. Introduction

Robotic arms have seen a tremendous increase in interest in many industries [4]. Looking beyond traditional robotic arms, characterized by rigid straight sections connected by rotary joints, a new wave of robotics presents itself in academia in the form of soft and flexible robots [22, 23, 117–119]. For this new trend in robotics new design methods are needed. Currently, flexible robotic design heavily relies on instinct rather than rules, like in traditional robotic design [120]. In flexible robotic design, usually the working principles are introduced first, and afterwards the capabilities are assessed and linked to potential use cases, often limiting a concept's potential to be scaled into an application. As in traditional robotic design, flexible robotic design should be based on a sophisticated and structured design process, to optimally serve the application the robot shall be deployed in.

Optimization, or mathematical programming, involves finding the best solution to real-world challenges by formulating them into mathematical models, including objective functions to minimize or maximize and constraints, with methods ranging from linear to nonlinear programming, each increasing in complexity and computational requirements. Optimization in robotic design is found in many forms [121], however, design optimization most often entails finding the optimal topology for a certain shape. Optimizing the shape of a flexible robot to start the design process with a head start is scarcely found in literature. Connolly et al. [122] presented an optimization approach to determine the optimal lengths for each segment and fiber angle in a flexible robotic actuator to mimic a human finger. In this study, the number of segments is set as a parameter to mimic either the index finger or the thumb and is limited to the application of fiber-reinforced actuators. Park et al. [123] used a quadratic programming approach to position coupled arm robots to reach corners in a rectangular box, comprising exclusively rigid section arms. Ceccarelli and Lanni [124] used a multi-objective Sequential Quadratic Programming approach (SQP) to optimize the workspace volume and length of a 3 segment rigid manipulator arm. Paredis and Khosla [125] implemented an optimization approach to define the kinematic structure of a rigid robotic arm. The robotic arm consisted of multiple sections and a modular design method was proposed to optimize the arm for a specific task, depending on requirements such as workspace volume, reach and positional error. Despite presenting a valuable kinematic design optimization, the study is limited to a traditional robotic design using fixed length straight sections and rotary joints. Van Henten et al. [126] implemented an optimization approach to the kinematic design of a 3-actuator manipulator to autonomously harvest cucumbers. This approach makes use of various generalised actuators like rotary and prismatic, but the methodology is based on cucumber picking while applicability into other sectors remains unclear. Li et al. [127] proposes an optimization based methodology to design a tendon driven articulated mechanism. Albeit a promising study for the kinematic design optimization of robotic arms, merely rigid sections specifically actuated by tendons are researched. A quadratic programming optimization approach based on situational constraints for a modular elongating robotic arm is not present in literature. Most design optimizations regarding static kinematics include operational constraints as the main constraints. The explored studies entail kinematic design optimizations in rigid robotics, flexible robotic design optimizations with predefined working principles, or optimizations tailored to a specific sector. This study aims to propose a kinematic flexible robotic design optimization methodology which requires no prior knowledge on the working principles and is applicable to a vast range of situations.

This study proposes a design approach for a segmented flexible robotic arm of which the working principles are yet an abstraction. A segmented approach is used, considering elongating straight sections and intermediate elbows, as the purpose of this study is to propose a flexible robotic design methodology which can be used to design flexible robotic arms for operations of scale, which is supported by modularity. Using an optimization approach for the kinematic design of a flexible robotic arm, the global capabilities of the arm, like segment lengths, required contraction ratio of segments and number of segments can be assessed, to use as requirements in the selection and design of the working principle of the flexible robotic arm. Once the geometric requirements are set, Finite Element Analysis (FEA) can be used to further assess the desired performance of the arm. However, as FEA also considers material properties, which makes it less time efficient. Employing the kinematic optimization first ensures a well informed start in the time consuming process of the mechanical design of a flexible robotic arm.

After a general explanation of the methodology, a case from the logistical sector is explained to showcase the versatile applicability. In the core of this methodology lies an optimization approach, using quadratic programming to unveil positions a generic flexible robotic arm must be able to take. This type of design optimization is also referred to as size optimization [121]. In general, the goal of the quadratic program is to uncover how many sections the flexible robotic arm shall consist of, the length of the different segments and the elongation they should be designed for, by minimizing the distance from the tip of the arm to the end point as the primary objective and minimizing the length of the total arm as a secondary objective. This is done by solving the program for various coordinates in two or three dimensional Cartesian space to unveil the desired positions of the arm, their elongation ratios and the respective angles segments make.

This rest of this study is structured as follows. First, a generic situation is used to describe the basic kinematics of the model. Then, a case study is presented from the logistical sector to test the applicability of this modeling approach, starting with a 2D side view model of the situation. A 2D top view model is created in the same manner to gain more insights into the challenge. Lastly, two approaches for three dimensional results are explored and compared. The methodology for the modeling has been shown in Figure 2.1.

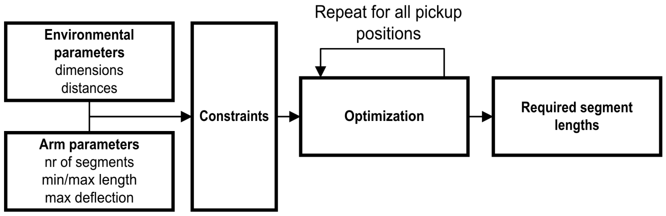

Figure 2.1: *Optimization methodology*

2.2. Kinematic model

In flexible robotic arm design, often a translation is desired reaching from a starting point to an end point, like in inspection of confined spaces, automatic manufacturing inside bare car bodies, or reaching into a cart to pick a parcel in logistics. A confined space can be characterized by an environment which poses limited space, obstacles and intricate corners. To navigate through a confined space from a starting point to an end point a flexible robotic arm must possess certain geometric capabilities, apart from the mechanical capabilities. Figure 2.2 shows a generic complex confined environment for a robot to navigate through. This methodology allows for the depicted situation to break down the intricate corners into a collection of obstacles to pass, like a wall. According to this, many situation can be simplified and approached using this methodology.

Prior to designing a flexible robotic arm based on a specific working principle, knowledge must be acquired on the kinematics that a flexible robotic arm must be capable of to make a well informed decision for the needed working principle. The methodology will unveil the kinematic requirements of the salmon dotted line in Figure 2.2. For instance, the optimization could reveal that the confined environment can be fully navigated by a 5-segment flexible arm, as described in Figure 2.3. After unveiling of the required number of segments, the bending angles between segments and segment lengths, literature can be consulted to select an appropriate working principle for the flexible robotic arm. If the required kinematic capabilies are not present in literature, a new principle according to the requirements can be developed. The optimization model in this study is made based on the Gurobi optimization package for Python using an academic license.

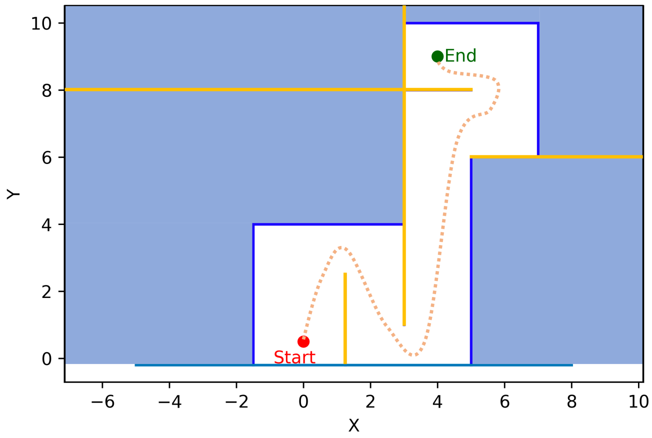

Figure 2.2: *Generic challenge of maneuvering through a complex confined environment like a cave or a disaster site. The salmon colored dotted line is a flexible robotic arm yet to be defined in terms of configuration. The yellow lines indicate the selection of obstacles that can define the simplified situation.*

2.2.1. Defining the arm

Translating from the complex cave as described by Figure 2.2, only the passing of a single obstacle is explained, since the passing of each obstacle is identical. The method explained in this section can be repeated as often as desired to mimic more obstacles and therefore more complex environments.

To create a path consisting of multiple sections, the coordinates of the tips of arm segments must be determined. Therefore, these coordinates are the first Decision Variables (DVs). Decision variables are the variables that will be determined by the optimization model which will ensure a minimum or maximum value of the objective function, while adhering to a set constraints.

Assuming that the arm consists of N segments, where the set of segments is J = [1,...,N] with j as index to indicate the segment, and each segment has a start (i=1) and an end (i=2), then each segment is described by an X and a Y coordinate for the staring point and an X and a Y coordinate for the end point. The structure of the X and Y coordinates is shown in Table 2.1 as they are determined by the optimization model. In this study, the number of segments is not defined as a decision variable, meaning that this is an input for user to

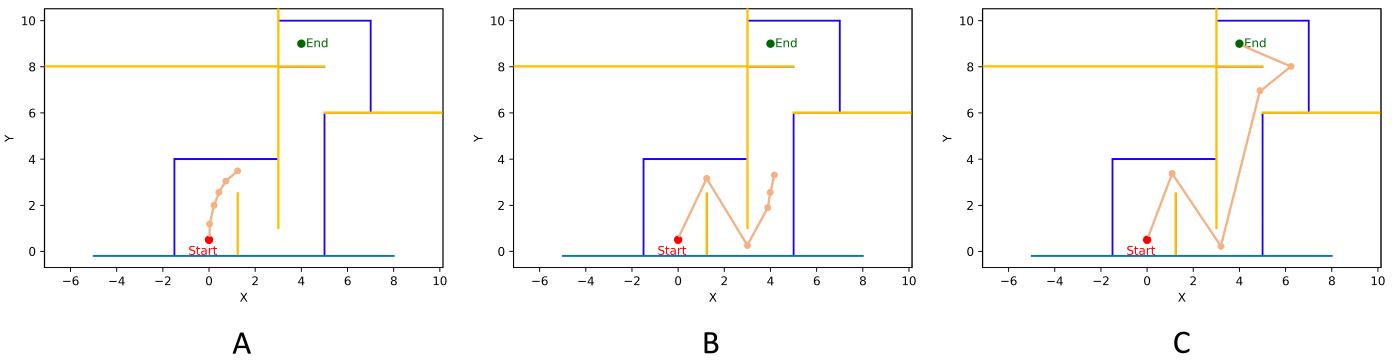

Figure 2.3: *Generic challenge of maneuvering through a complex confined environment like a cave or disaster site simplified into generic obstacles (yellow), which can be fully accessed by a 5-segment flexible arm (salmon line). The segments can either elongate, contract and initiate bends in between segments. (A) The arm starts in contracted position. (B) The arm extends piece-wise towards the end point. (C) The arm has reached the end point and is fully extended.*

choose. This is chosen to manage computational effort of the model, since with every additional segment, 4 continuous decision variables are added, which leads to higher optimization times.

	Segments (j)				
i	X_{ij}	**1**	**2**	**...**	**N**
Starting point	**1**	X_{11}	X_{12}	$X_{1...}$	X_{1N}
Ending point	**2**	X_{21}	X_{22}	$X_{2...}$	X_{2N}

	Segments (j)				
i	Y_{ij}	**1**	**2**	**...**	**N**
Starting point	**1**	Y_{11}	Y_{12}	$X_{1...}$	Y_{1N}
Ending point	**2**	Y_{21}	Y_{22}	$Y_{2...}$	Y_{2N}

Table 2.1: *Structure of the main decision variables.*

Parameters include the position of the obstacle in x-direction (WallPos), the height of the obstacle in y-direction (WallHeight), and the position of the end point (EP) which has the structure (x,y). The start of the robotic arm is conveniently placed at the origin (0,0). Regarding the segmented robotic arm, apart from the number of segments, some other parameters can be set according to the situation, like minimum segment length, maximum segment length and respective deflection of a segment with respect to its preceding segment.

Based on these initial decision variables and parameters, the objective function is formulated. This study focuses on creating a segmented arm which reaches the end point while adhering to efficient kinematics, i.e. the distance between the tip of the most outer segment and the end point is minimized and the length of the trajectory is minimized as a secondary objective. This is reasonable to assume since only minimizing the distance between the tip and the end point still yields a virtual infinite solution space and in reality the construction of flexible robotic arms can be challenging, so an efficient use of material is desired. To define the minimization of the distance to the end point as primary objective function and the length of the arm as a secondary objective, weighted factors (F1 and F2) are implemented to define importance. Factors are often chosen following $F1 + F2 = 1$ to express the importance in terms of a percentage. For example, the factors could be chosen as $F1 = \frac{999}{1000}$ and $F2 = \frac{1}{1000}$. The objective function is shown in Equation 2.1.

The Euclidean distance from the tip of the arm to the end point (D) is calculated using the Pythagorean theorem. The end point of the last segment is indicated by X_{2N} and Y_{2N} and the x and y coordinate of the end point as EP[0] and EP[1] respectively. Figure 2.5 shows a

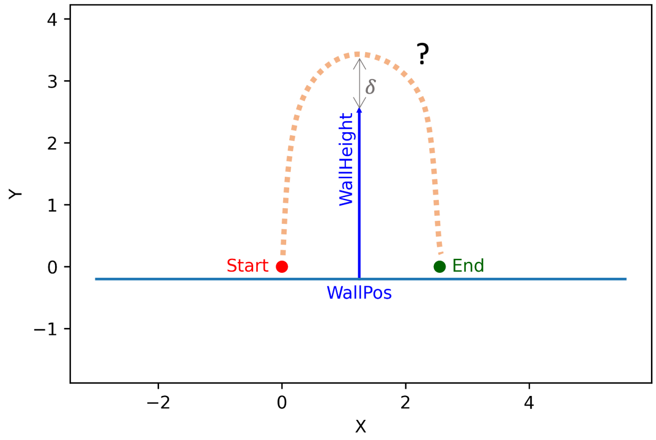

Figure 2.4: *Generic case to determine the kinematic requirements for a generic flexible robotic arm (salmon dotted line). The goal of the flexible robotic arm is to reach from the starting point (red) to the end point (green) while avoiding the obstacle (blue). δ is some clearance as it is assumed that the arm cannot touch the obstacle.*

Objective function:

$$Min\ F1((X_{2N} - EP[0])^2 + (Y_{2N} - EP[1])^2) + F2\sum_{j\in J}((X_{2j} - X_{1j})^2 + (Y_{2j} - Y_{1j})^2) \tag{2.1}$$

$$D^2 = (X_{2N} - EP[0])^2 + (Y_{2N} - EP[1])^2 \tag{2.2}$$

$$L = \sum_{j\in J} L_j = \sum_{j\in J}\sqrt{((X_{2j} - X_{1j})^2 + (Y_{2j} - Y_{1j})^2)} \tag{2.3}$$

$$L' = \sum_{j\in J}((X_{2j} - X_{1j})^2 + (Y_{2j} - Y_{1j})^2) \tag{2.4}$$

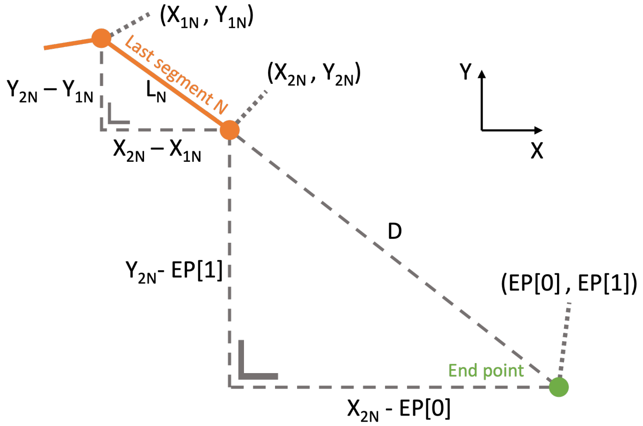

Figure 2.5: *Graphical description of the distance from the tip of the last segment to the end point and the length of a segment using the Pythagorean theorem. (orange) the last segment of the arm, (green) the end point.*

graphical description on how the distance to the end point and the length of a segment are determined. Equation 2.2 shows the distance to the end point and Equation 2.3 shows the formula used to calculate the total length of the arm based on Figure 2.5. Since square roots are not compatible with optimization models, these equations are to be used in a squared form according to [128]. This is allowed since squaring the Pythagorean theorem results in a monotonic function which minimizes similar to the original function.

To create a segmented arm out of the coordinates, the beginning and end point of each successive segment is connected by constraining the length between the end point of a segment and the staring point of the next segment to zero for their X and Y coordinates (constraint 1 in Table 2.4). Since the origin of the arm and the outer most tip are not connected to another segment, a subset is defined to only include the intermediate segment points: B = [1,...,N-1]. The starting point of the first segment must start at the origin (constraint 2 in Table 2.4). In reality, arm segments cannot retract until a length of zero and often extension is also bounded by physical implications. Therefore, constraints can be implemented to set bounds on the individual segment lengths (constraint 3 in Table 2.4).

2.2.2. Avoiding obstacles

The next section shall explain how obstructions between the starting point and the End Point can be avoided, like the obstacle in Figure 2.4. To maintain generality and simplicity, the avoidance of only a single obstacle shall be explained, but the same process can be repeated for as many obstructions as computationally possible.

As graphically shown in Figure 2.4, there is a single obstacle obstruction between Start and End. Naturally, the aim is to let the arm pass over the obstacle. To model this, the segment that passes the obstacle must be considered and the y-coordinate of the point that lies in the extension of the obstacle must be greater than the height of the obstacle with a margin if desired. The situation is graphically depicted in Figure 2.6, where Line1* indicates the obstacle and point1 and point2 the starting point and end point of the segment that passes the obstacle respectively. To ensure that the segment passes over Line1*, interpolation between point1 and point2 is used as shown in Equation 2.5.

Before this can be implemented into an optimization constraint, first an indicator is required to track which segment crosses the obstacle. For all segments, a binary variable is created: [C_1, C_2, ..., C_N], with N being the number of segments. To ensure that C_1 to C_N take correct values, the difference in x-coordinate between the two points of a segment and the x-coordinate of Line1 is utilized ($\Delta 1$ and $\Delta 2$ in Figure 2.6 A). If both points of a segment are in front of Line 1, $\Delta 1$ and $\Delta 2$ are both positive, and when both are behind, both are negative. In these cases the product of $\Delta 1$ and $\Delta 2$ is always a positive number. However, when one point of a segment lies in front of Line1 and the other behind, the product of the differences becomes negative. Generally, 0 is not an impossible outcome for the product of differences. To counteract this, a small margin θ is incorporated to transform the sole x-coordinate of Line1 into a small range to ensure that the product of differences is never 0. To mimic an 'if-statement', the Big-M method is used, to simulate 'if segment j passes WallPos, do ... for segment j.' The big-M method is a mathematical optimization technique used to handle mixed-integer linear/quadratic programming problems by introducing a large positive constant, denoted as "M," to penalize infeasible solutions, effectively ruling out unwanted solutions from the solution space [129, 130]. This combination ensures that the decision variable C becomes 0 when the product of differences is positive and thus the segment does not cross Line1, and becomes 1 when the product is negative, meaning that one point of the segment lies before Line1 and the other after. This is implemented as constraint 4 in Table 2.4.

However when considering Equation 2.5, as X and Y are decision variables, the second term presents a challenge for two reasons: the used optimizer cannot divide directly through a decision variable, and the term is not quadratic but cubic, which the solver is not capable of solving for either. To work around these challenges, two new decision variables are created: one to represent the division by δx, and one which fully represents the slope of the segment. The division by δx is shown as constraint 5 and the definition of the slope as indicated by constraint 7 in Table 2.4. The problem presents itself as the middle term in the summation of Equation 2.5. As the used solver cannot work with division, the middle term is written as $(y_{point2} - y_{point1}) \cdot \frac{1}{(x_{point2} - x_{point1})} \cdot x_{point1}$. The division of 1 by $x_{point2} - x_{point1}$ is replaced by a new decision variable dX. Using constraint number 6, dX is defined

$$y_{red} = \frac{y_{point2} - y_{point1}}{x_{point2} - x_{point1}} x_{Line1} - \frac{y_{point2} - y_{point1}}{x_{point2} - x_{point1}} x_{point1} + y_{point1} \geq y_{Line1} + \delta \tag{2.5}$$

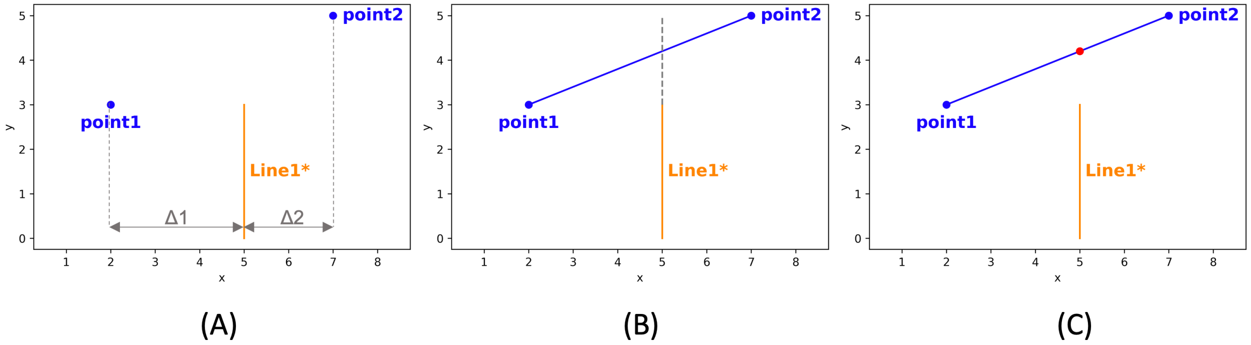

(A) (B) (C)

Figure 2.6: ***Analogy used to ensure that the point that crosses Line1 passes above line one using interpolation between the two relevant points.*** *(A) Initially two points exists of which one lies before Line1* and one after Line1* in x-direction. (B) The linear line connecting point 1 and point 2 has a coordinate which lies directly above Line1*. (C) Using interpolation the point is found and used in constraint 8.*

as $dX \cdot (x_{point2} - x_{point1}) = 1$ resulting in the term $(y_{point2} - y_{point1}) \cdot dX \cdot x_{point1}$. To work around the solver-related incompatibility of cubic terms, the slope is included as a new decision variable ($S1$) according to $S1 = \frac{(y_{point2} - y_{point1})}{(x_{point2} - x_{point1})} = (y_{point2} - y_{point1}) \cdot dX$ and is noted as constraint 6 in Table 2.4. Lastly, the binary decision variables C and u are constrained to 0 and 1 in constraint 7.

Looking at Figure 2.4, the possibility exists that a segment points in the negative X direction when reaching for the end point. If this happens, the manner in which the angle with the horizontal is defined in the model does not match the angle the model will return and thus a correction is needed. A binary decision variable u is created for each segment to indicate if the starting point of a segment lies further on the x-axis than the ending point, i.e. the segment reaches back in x-direction. Constraint 8 is created to define the behavior of the binary DV and is formulated such that u takes the value of 1 when the x-coordinate of the second point of a segment is smaller than that of the first point, and 0 when the x-coordinate of the first point of a segment is smaller, again using the Big-M method to mimic an 'if-statement,' here formulated as 'if segment j reaches back in x-direction, set $u_j = 1$, else set $u_j = 0$.' Corrections using this new decision variable are found in constraints 5 and 6, which are only affected once the specific segment reaches in negative x-direction (and $u_j = 1$) and the correction is needed. Constraint 9 in Table 2.4 shows the final constraint to ensure that the arm passes over the obstacle with some margin included as defined in Figure 2.4. Theoretically, the model would not violate any constraints if a segment point is set on WallPos, meaning that all binary decision variables 'C' remain 0 and the arm passes through the obstacle. Since at least one segment must pass over the obstacle, a constraint is included which forces at least one C variable to be 1. The constraint is included as number 10 in Table 2.4.

Constraints 1 to 10 fully define the kinematics of an abstract arm which must reach from a starting point to an end point while avoiding a obstacle. Figure 2.7 A shows results of computing with a maximum arm's length equal to the WallHeight and δ combined and a minimum arm's length of 2 for a 3 segment arm and Figure 2.7 B for a 4 segment arm with a minimum arm's length of 1. The specifications of the arms are noted in Table 2.2 and Table 2.3 respectively.

Theoretically, the arm can be set to comprise of as many segments as desired. In case the segment lengths are highly constrained in terms of maximum and minimum length and deflection angle and many segments are required, the generic situation could be solved using a 10 segment arm. A mock-up of this situation has been made to illustrate what such a solution could look like. However, optimizing for many segments is computationally heavy, and thus the illustration of 10 segments is presented as a graphical mock-up in Figure 2.7 C.

Table 2.2: *Results of model using constraints 1 to 10 for a 3 segment arm.*

Segment	**1**		**2**		**3**
Length	2.65		2.00		2.65
Deflection angle (deg.)		87.6		80.4	

Table 2.3: *Results of model using constraints 1 to 10 for a 4 segment arm.*

Segment	**1**		**2**		**3**		**4**
Length	1.19		1.76		1.51		1.44
Deflection angle (deg.)		12.1		133.7		0.4	

2.2.3. Constraining the deflection angle

With the current constraints the robot can make any turn possible. However, in contrast to conventional articulated robots, flexible robots are often made of flexible and bendable materials that are not capable of forming sharp corners. Deflection angles of flexible robotic actuators range between 35 and 100 degrees [37, 117, 131]. To exemplify the versatility of this approach, a maximum deflecting angle of 60 degrees is implemented.

To restrict the deflection of a segment with respect to its predecessor, the angle of each segment with respect to the horizontal must be determined. To increase efficiency in the optimization model, the segment angles are defined using a piece-wise linear (PWL) arctangent function, which creates a decision variable, A_j, for each segment according to its slope ($S1_j$) and is implemented as constraint 11 in Table 2.4. As the arctangent function is a highly non-linear function, this is computationally heavy. Simplifying this function into a linearized approximation relaxes the model while maintaining acceptable results. Since the arc tangent function only exists between $-\frac{1}{2}\pi$ and $\frac{1}{2}\pi$, the decision vari-

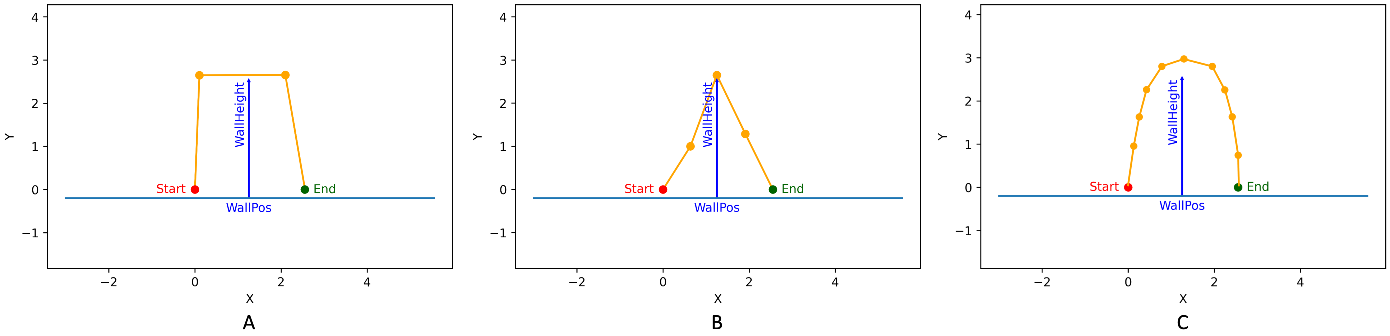

Figure 2.7: *(A) Results of generic situation using a maximum arm's length of WallHeight and* δ *(*$\delta = 0.06 \cdot WallHeight$*) and minimum arm's length of 2 combined for a 3 segment arm. Quantitative results in Table 2.2. (B) Results of generic situation using a maximum arm's length of WallHeight and* δ *(*$\delta = 0.06 \cdot WallHeight$*) combined and a minimum arm's lenght of 1 for a 4 segment arm. Quantitative results in Table 2.3. (C) 10 segment mock-up solution to generic segment to illustrate what a solution could look like when segment lengths and defection angles are highly constrained.*

able A_j that represents values from the arc tangent function must be constrained to these values (constraint 13 in Table 2.4). Figure 2.8 shows the relation between A_j and dX_j and the asymptotic bounds of A_j.

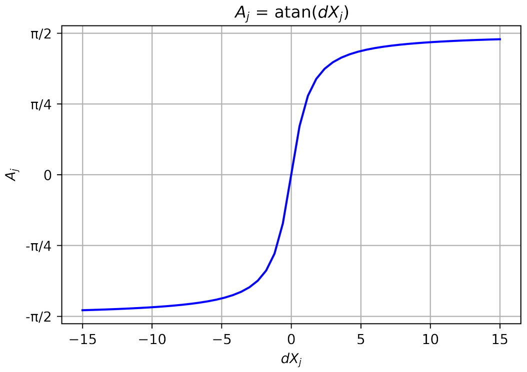

Figure 2.8: *Arc tangent relation between* A_j *and* dX_j*.*

This angle can be used to find the deflection angle of a segment with respect to its predecessor. By subtracting the angles w.r.t. the horizontal the deflection angle remains and can be restricted by parameters (maximum deflection (MaxD)). The correction for a backward pointing segment is required here too as shown in constraint 12 in Table 2.4.

A 4 segment arm and a deflection angle constraint of 100 degrees yields results as shown in Figure 2.10 and Table 2.5.

2.2.4. Extracting information

The described method can be used beyond the extraction of data from single runs. If multiple poses are explored for the same flexible robotic arm, required segment lengths between pick-up positions can be compared, and thus contraction ratios can be determined to use as criteria in selecting working principles for the physical design process of the arm. This section will showcase how to use the described methodology to extract information to initiate the design process for a flexible robotic arm according to a systematic approach.

Consider a 3-segment arm in the generalised setup from this section, while no constraints are set on the length of the individual segments, but with a maximum deflection angle of 100 degrees included.

Table 2.4: *Set of constraints to avoid an obstacle.*

	Constraints	
1.	$X_{2j} - X_{1j+1} = 0$	$\forall j \in B$
	$Y_{2j} - Y_{1j+1} = 0$	$\forall j \in B$
2.	$X_{11} = 0$	
	$Y_{11} = 0$	
3.	$(X_{2j} - X_{1j})^2 + (Y_{2j} - Y_{1j})^2 \leq MaxL^2$	$\forall j \in J$
	$(X_{2j} - X_{1j})^2 + (Y_{2j} - Y_{1j})^2 \geq MinL^2$	$\forall j \in J$
4.	$(WallPos - X_{1j}) \cdot (WallPos - X_{2j}) \leq -\theta + M \cdot (1 - C_j)$	$\forall j \in J$
	$(WallPos - X_{1j}) \cdot (WallPos - X_{2j}) \geq \theta - M \cdot C_j$	$\forall j \in J$
5.	$dX_j \cdot (X_{2j} - X_{1j}) = 1 - 2 \cdot u_j$	$\forall j \in J$
6.	$S1_j - 2 \cdot u_j \cdot S_j = (Y_{2j} - Y_{1j}) \cdot dX_j$	$\forall j \in J$
7.	$C_j, u_j \in 0, 1$	$\forall j \in J$
8.	$X_{2j} - X_{1j} \leq M \cdot (1 - u_j)$	$\forall j \in J$
	$X_{2j} - X_{1j} \geq -M \cdot u_j)$	$\forall j \in J$
9.	$S1_j \cdot WallPos - S1_j \cdot X_{1j} + Y_{1j} + M \cdot (1 - C_j) \geq WallHeight + \delta$	$\forall j \in J$
10.	$\sum_{j \in J}(C_j) \geq 1$	
11.	$A_j = PWL(arctan(S1_j))$	$\forall j \in J$
12.	$\frac{A_j - A_{j+1}}{\pi} \cdot 180 + 180 \cdot u_{j+1} \leq MaxD$	$\forall j \in B$
	$\frac{A_j - A_{j+1}}{\pi} \cdot 180 + 180 \cdot u_{j+1} \geq -MaxD$	$\forall j \in B$
13.	$-\frac{1}{2}\pi \leq A_j \leq \frac{1}{2}\pi$	$\forall j \in J$

Table 2.5: *Results of model using constraints 1 to 10 for a 4 segment arm.*

Segment	**1**	**2**	**3**	**4**
Length	0.70	2.52	1.15	2.33
Deflection angle (deg.)		-59.9	93.3	68.3

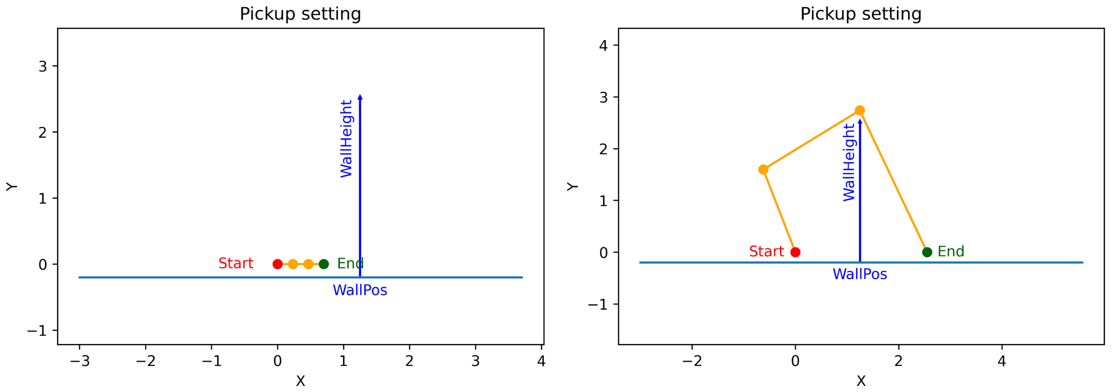

Pick-up point 1

Pick-up point 2

Figure 2.9: *First (left) and second (right) pick-up points to use for information extraction for a 3-segment arm without segment length constraints and with a segment deflection constraint of 100 degrees, minimizing the distance from the tip of the arm to the end point and the total length of the arm. To obtain kinematic requirements for the flexible robotic arm in this situation, the arm must move from pick-up point 1 to pick-up point 2. Table 2.6 shows the results for both pick-up points.*

Table 2.6: *Information extraction between two pick-up points in generic case results.*

Segment	**1**	**2**	**3**
Lengths point 1	0.23	0.23	0.23
Deflection angles 1 (deg.)	0	0	
Lengths point 2	1.71	2.19	3.03
Deflection angles 2 (deg.)	-100	95.9	
Contraction ratios	0.87	0.89	0.92

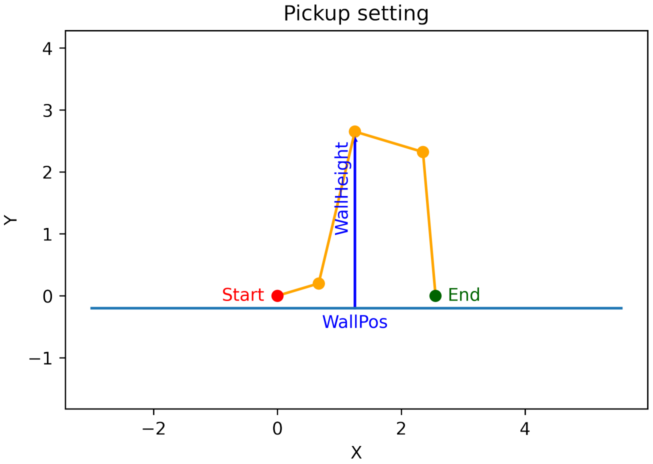

Figure 2.10: *Results of generic situation using a maximum arm's length of WallHeight and δ ($\delta = 0.06 \cdot WallHeight$) combined and a maximum deflection angle of 100 degrees for a 4 segment arm. Quantitative results in Table 2.5.*

The contraction ratio of each segment can be calculated according to Equation 3.7. Figure 2.9 show the first and second pick-up point to consider. The results of the data extraction are presented in Table 2.6.

$$\lambda_c = \frac{L_{max} - L_{min}}{L_{max}} \tag{2.6}$$

According to the results, the flexible robotic arm that is required to move to the end points shown in Figure 2.9 must comprise of a flexible robotic principle that can contract with a ratio up to 0.92, with a maximum length of 3.03 (this can be any length unit). It is evident that the set deflection constraint is of importance in this situation as the deflection angle between segment 1 and 2 is 100 degrees and the deflection angle between segments 2 and 3 closely approaches it. This information sets the first step in flexible robotic design to move from an abstraction in working principles to a well considered concept for a specific situation.

2.3. Situational sketch: a case study from logistics

In this section, the methodology as described in section 2.2 is leveraged to explain a case study found in logistics. Articulated robotic arms, known for their straight sections and rotary joints, are widely chosen for automating routine tasks due to their 6 to 7 Degrees Of Freedom (DOF) and prowess in stamina, lifting power, and robustness. However, challenges emerge in scenarios with obstacles or extended reach requirements, resulting in a reduced range of motion for conventional arms [5, 6]. In the logistical sector, these limitations are exemplified as articulated arms struggle to handle non-regular packages on confined

Unit Load Devices (ULDs) like roll containers or mail carts. Hypothetically, a flexible robotic arm could present solutions to these challenges. The examplary setup for this study considers a roll container, a belt conveyor and a base for the robotic arm. The belt conveyor is positioned in between the base of the robot and the roll container as shown in Figure 2.11. A photo of a roll container is shown in Figure 2.12. All used distances for this study are listed in section B.1 and section B.2.

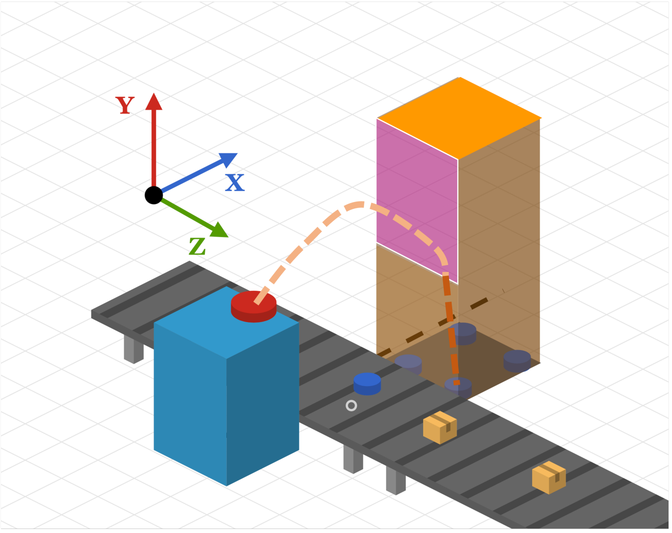

Figure 2.11: *The examplary setup as inspiration from logistics. (blue box) Base of the robot. (grey) Belt conveyor. (large orange boxes) Roll container which holds packages. (red disc) Starting point of robotic arm. (blue discs) Key spots to pick packages from and drop off. (salmon dotted line) Generic robotic arm reaching to one of the blue pick-up points. (magenta plane) access into the ULD.*

From Figure 2.11, the blue discs are considered the pick-up points for the flexible robotic arm as these are located in the bottom corners of the roll container. Reaching these spots requires most dexterity and are thus considered the hardest to reach spots. The blue disc on the belt conveyor represents the drop-off location for the packages, which is important to gain information on how the arm must behave to make this drop-off possible. The red disc in Figure 2.11 is assumed to be the starting point for the robotic arm. This point shall also be the origin of the Cartesian coordinate system. The situation is split up into a side view and a op view as depicted in Figure 2.13 and Figure 2.14.

2.4. 2D side view model

The used methodology is intended to progress in a constructive manner. Therefore, initially a way is sought after to simplify the first step to acquire a solution.

To do this, the 3-dimensional problem is divided into two 2-dimensional problems. In this case, a complex bend down into the cart is necessary as seen in Figure 2.13. Therefore, it was chosen to consider a view which captures this motion, the y-direction, first. Based on this side view, certain decisions can be made like how to narrow down on the potential number of segments, to relax further modeling in 3D. When considering which other dimension to include in the first model, the dimension with the largest solution space is chosen. X ranges between zero and two meters (Figure 2.13), whereas Z can only range between zero and one meters (Figure 2.14). Therefore, The XY-plane is considered first with X and Y as the initial decision variables. The graphical 2D

Figure 2.12: *Photo of a roll container as found in many logistical warehouses. The only access into the container is via the opening in the top half of one of the sides of the cart. The magenta plane shows the access point to unload the ULD through.*

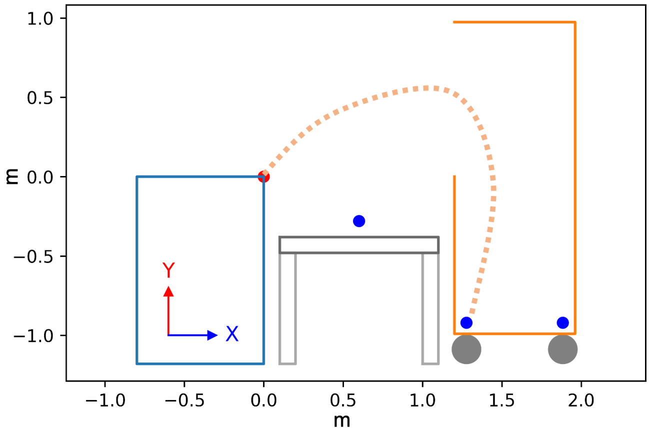

Figure 2.13: *Side model situation plot showing the base of the robot (blue), the belt (grey), the cart (orange), the origin of the model (red dot), the end points (blue dots), (orange dotted line) and the generic flexible robotic arm trajectory.*

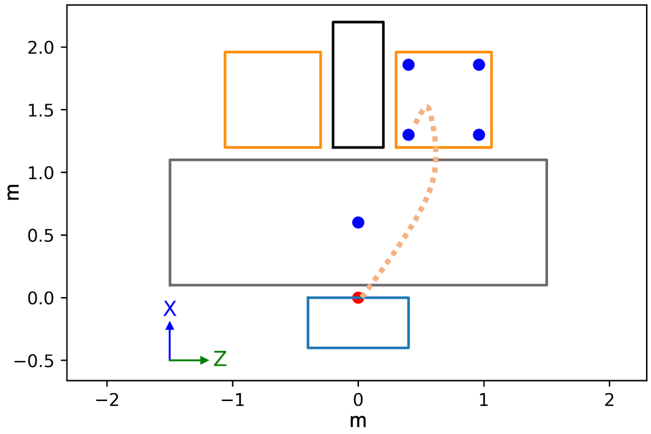

Figure 2.14: *Top view model situation plot with the base of the robot (blue), the belt (grey), the cart (orange), the origin (red dot), all end points (blue dots), (orange dotted line) and the generic flexible robotic arm trajectory.*

	Segments (j)				
i	X_{ij}	**1**	**2**	**...**	**N**
Starting point	**1**	X_{11}	X_{12}	$X_{1...}$	X_{1N}
Ending point	**2**	X_{21}	X_{22}	$X_{2...}$	X_{2N}

	Segments (j)				
i	Y_{ij}	**1**	**2**	**...**	**N**
Starting point	**1**	Y_{11}	Y_{12}	$X_{1...}$	Y_{1N}
Ending point	**2**	Y_{21}	Y_{22}	$Y_{2...}$	Y_{2N}

Table 2.7: *Structure of the main decision variables.*

solution space is depicted in Figure 2.13. A comprehensive explanation of the situation including all parameters is shown in section B.1.

2.4.1. Explanation of 2D side model

The structure of the decision variables is identical as in section 2.2 and is displayed in Table 2.7.

The objective function is adopted directly from section 2.2. Only the values of factors F1 and F2 are to be determined using trial and error. In this study, F1 = $\frac{999}{1000}$ and F2 = $\frac{1}{1000}$ yielded results of arms that reached the end point closely using an efficient trajectory. The end point is defined as EP which has the structure [X,Y].

The constraints needed to define the kinematic structure of the arm are adopted from subsection 2.2.1. The main obstacle to avoid in this situation is the front obstacle of the cart (Line1 in Figure B.1 found in section B.1). The binary variable to keep track of which segment crosses Line1 is referred to as C1. The approach used to avoid the obstacle in subsection 2.2.2 is adopted in this situation to reach into the roll container.

Since the working principles of the flexible robotic arm of this study are yet to be defined, an thus the maximum bending angle is not known, an average maximum angle is set of 60 degrees, well within the boundaries of 35 and 100 degrees as found in literature. The approach to constrain the deflection angle of the segments is adopted from subsection 2.2.3. The full model is found in section B.1.

Since this is an optimization model, there is no guarantee that the arm chooses the desired trajectory, which is through the opening of the cart. As of now, the model can set a route which ends right before the cart, close to the middle end point, but still just outside the cart. To ensure that the arm always enters the cart via its opening a constraint is added to force the tip of the most outer segment to be placed behind Line1 (Equation B.19 in section B.1).

	Segments (j)				
i	X_{ij}	**1**	**2**	**...**	**N**
Starting point	**1**	X_{11}	X_{12}	$X_{1...}$	X_{1N}
Ending point	**2**	X_{21}	X_{22}	$X_{2...}$	X_{2N}

	Segments (j)				
i	Z_{ij}	**1**	**2**	**...**	**N**
Starting point	**1**	Z_{11}	Z_{12}	$Z_{1...}$	Z_{1N}
Ending point	**2**	Z_{21}	Z_{22}	$Z_{2...}$	Z_{2N}

Table 2.8: *Structure of the main decision variables.*

2.4.2. Results of 2D side model

For the considered case study, important aspects of the robotic arm can be determined. To narrow number of segments that are relevant for this application down, several experiments have been conducted.

1. Using the example setup, variations on the number of segments have been performed for the two hardest to reach spots as explained in section 2.3.
2. Runs with blown up proportions have been executed to qualitatively assess the sensitivity of the required number of segments.
3. Runs with the belt drop-off have been performed to gain information on the elongating and contracting requirements of the flexible robotic arm.

After a qualitative assessment of the results from the experiments, a conclusion can be made on what number of segments is relevant to continue the case study with to maintain efficient time management.

For this 2D case it can be said that three, and at most four segments, would be sufficient to reach all the corners. It must be noted that in the 3D case, lengths and angles will change as this model only shows projections on this particular side-plane, but since deflection in the Z-direction is minimal, it can be assumed that the side view results are sufficient. When comparing the plotted trajectories, it becomes clear that, regardless of the distance of the cart, either 3 or 4 segments are adequate to reach the corners in an efficient manner. Judging from Figure 2.15 A and B, it can be determined that with more segments many unnecessary turns and non-deflecting elements exist which could be replaced by a single segment. In fact, such an assessment is made for all results found in section B.1. It was qualitatively determined that simulations with more than 5 segments did not present valuable results for this study, as many segments would present virtually no deflection and could thus be replaced by a single segment.

2.5. Top view model

The top view 2D model works identical to the side model but with some constraints removed and different parameters. In stead of the main decision variables being X and Y, now X and Z are optimized. The situation plot is shown in Figure 2.14.

2.5.1. Explanation of 2D top model

The structure of the decision variables is displayed in Table 2.8.

The objective function of the top view model is of identical form as presented in the generic case in Equation 2.1, but with Y changed for

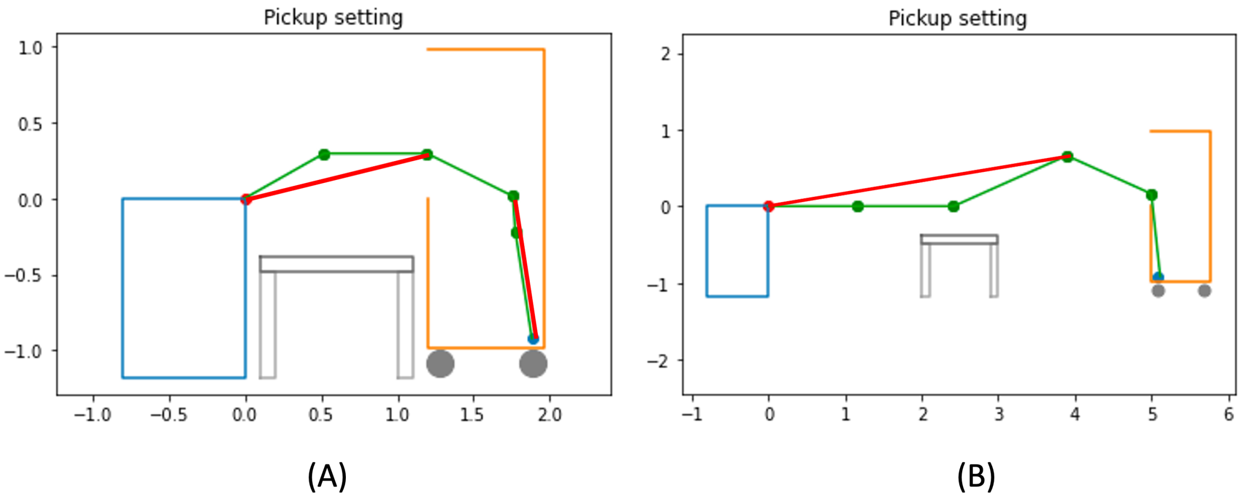

Figure 2.15: *(A) 2D 5-segment arm results which can be simplified into a similarly performing 3-segment arm. (B) 2D 5-segment arm at 5 meters distance result which can be simplified into similarly performing 3 segment arm.*

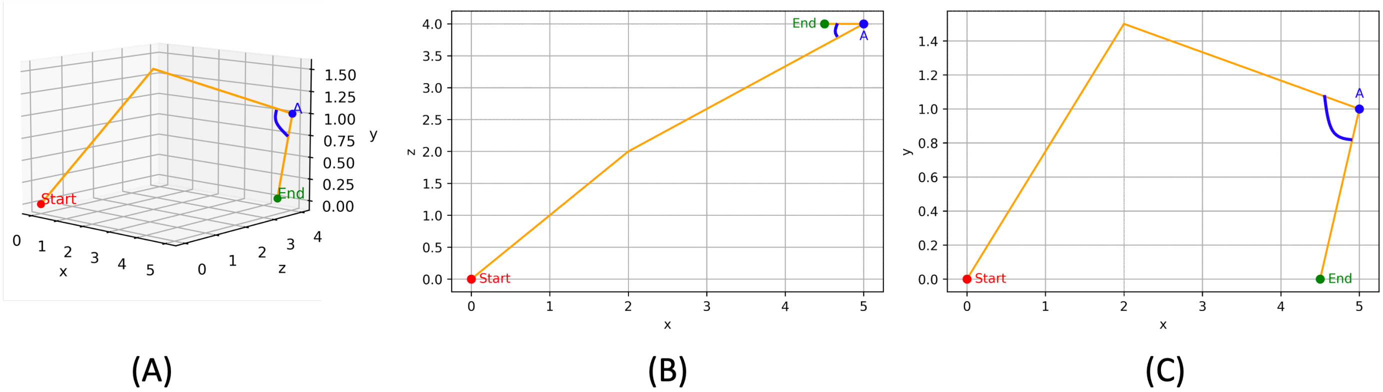

Figure 2.16: ***Visual explanation of distorted angles when looking at a 2D projection from a 3D segmented arm.*** *(orange) indicates the arm, (red) the starting point, (green) the end point, and (blue) the angle of interest. The arm is described by X = [0,2,5,4.5], Y = [0,1.5,1,0], and Z = [0,2,4,4]. The angle in blue is 78.8 degrees in the 3D scenario, 33.4 in the XZ projection, and 72.9 in the XY projection.(A) a 3D representation of the line segment. (B) The XZ projection of the 3D setup. (C) The XY projection of the setup.*

Z, and is depicted in its full form as Equation B.22 in section B.2. Similar to the side view model, this model uses a combination of minimizing the distance to the end point (here called TopEndPoint(TEP), defined as [Z,X]) and minimizing the arm's distance.

The constraints needed to define the kinematic structure of the arm are adopted from subsection 2.2.1. The main obstacle to avoid in this situation is Line2 in Figure B.29 found in section B.2). The approach used to avoid the obstacle in subsection 2.2.2 is adopted in this situation to reach into the roll container. The binary variable that keeps track of which segment passes Line2 is referred to as C2. The proposed method to realise the interpolation as described in section 2.2 has been adopted into the top view model.

The main difference between the side and the top model is the (absence of) use of a maximum angle constraint. Seen from the top plane the arm reaches a great deal 'into' the plane. Therefore the projected angle on this plane can present a very distorted seemingly sharp angle while the true angle in 3D might in fact be very shallow. Figure 2.16 shows a simplified situation to describe the nature of the distortion. In the figure, a similarly performing simplified arm is shown. The actual angle indicated in blue in 3D is 78.8 degrees, whilst the angle in the XZ projection indicates 33.4 degrees. The XY projection of the angle lies closer to the actual 3D angle with 72.9 degrees. Therefore, the angle constraint in the top view is left out, as in this specific scenario this angle presents highly distorted angles. This makes the need for a PWL arctangent function and a binary DV to map if a segment reverses in Z-direction obsolete, consecutively relaxing the model.

Similar to the side view model, the current model does not guarantee to take a route through the opening of the cart. To encourage, or rather force, the model to do so, a constraint is added to ensure that the tip of the arm ends inside the perimeter of the cart in Z-direction, denoted as constraint 9 and fully noted as Equation B.34 in section B.2.

	1D	2D	3D
Degree of non-convexity	1	2	3
Running time factor	1	4	9

Table 2.9: *Hypothetical running time of different non-convexity levels.*

2.5.2. Results 2D top model

The top view model does not yield vital information in contrast to the side view model. Therefore, no extensive experiments have been conducted with the 2D top view configuration. A correct top view model is however necessary to create a 3D model. To showcase the kinematics of the top view model, runs have been performed to show results for reaching all 4 corners of the cart as seen from the top view, with 3, 4, and 5 segments. The results are shown in subsection B.2.6. These results have shown that the top view model works accordingly.

2.6. 3D model

For the 3D model, 2 approaches have been considered.

1. A sequential optimization: first the side view optimization optimizing for X and Y as found in section 2.4, followed by the top view optimization optimizing only for Z as found in section 2.5 where the results for X are implemented as parameters in the top view optimization as depicted in Figure 2.17 A.
2. A single comprehensive 3D optimization optimizing for X, Y and Z as decision variables at the same time as depicted in Figure 2.17 B.

2.6.1. A comprehensive vs a sequential approach

In contrast to what is in this study referred to as a sequential optimization method, means in other studies the simplification of a complex non-linear problem into quadratic sub problems [132]. This study works around non-linearity's by intelligently introducing variables and refers to sequential optimization as a succession of two separate optimization models. From trial and error is was found that the sequential 3D model yielded more promising results than the comprehensive 3D model in reasonable time. Intuition might tell that the findings are contradictory, as both the comprehensive and the sequential model present at most quadratic terms and that since the side and top view models have some overlap, the comprehensive model would show better results in similar run times. However, theory suggests that the correlation between non-convexity and intractability, or solving complexity, is quite strong, i.e. the running time grows exponentially with the degree of non-convexity [133]. Also, since geometric problems are a type of classical non-convex problems, finding a global solution in a reasonable amount of time becomes difficult [134]. Considering that the comprehensive model uses three decision variables which show up in a quadratic form in the objective value twice in contrast to only two decision variables, it can be assumed that the model gains significantly in non-convexity compared to the sequential model. Assuming that hypothetically the non-convexity of the model grows linearly with the number of spatial decision variables (X, Y and Z) used in the optimization, the running time grows as seen in Table 2.9.

To quantify the difference in performance between the sequential and the comprehensive model, a comparison is made based on the level of non-convexity and the running time (expressed in a dimensionless time unit referred to as the 'running time factor'). Judging from Table 2.9, the running time from a sequential model, adding up 1D and 2D, results in 5 whereas a single 3D run shows a running time of 9. Since both models are inherently different, it cannot be assumed that the sequential model provides better results when solely looking at the optimal solution. The comprehensive 3D model could potentially yield better results, if computational time was not an issue. However, with only the single side view model (2D) demanding run times of 0.5 hours for an acceptable (not even an optimal) solution, validating, testing and experimenting with the comprehensive model is deemed to be too inefficient for this study.

Table 2.10: *Results sequential 3D optimization for lower right endpoint.*

Segments	3
Run times (side/top)	300.018/0.061 s
Deflection angles of side view proj.	[50.1, 60.0] deg
3D deflection angles	[47.02, 56.4] deg
3D segment lengths	[0.89, 0.59, 1.12] m
Total length	2.6 m

Table 2.11: *Results comprehensive 3D optimization for lower right endpoint.*

Segments	3
Run time	300.016 s
Deflection angles of side view proj.	[36.7, 60.0] deg
3D deflection angles	[71.79, 76.25] deg
3D segment lengths	[1.28, 0.27, 1.22] m
Total length	2.77 m

To substantiate this, runs have been performed with identical setups to compare the two approaches, of which the results are presented in Figure 2.18. Based on the results found in subsection 2.4.2, only a 3-segment arm has been considered. Both runs were limited to a computational time of 5 minutes and were solved for the same pick-up point inside the ULD. From tables 2.10 and 2.11, it can be observed that the sequential model presents an overall shorter length of the arm, more evenly distributed lengths and smaller deflections. This advantage of the sequential model was present across different setup runs and therefore the sequential model was chosen as the primary model to gain true spatial insights and generate requirements. The results of both approaches for comparison are found in Table 2.11, Table 2.10, and Figure 2.18

2.6.2. Adjustments for 3D

First, the side view model is solved exactly as presented in section 2.4. This yields values for the X and Y coordinates of the line segments. Consecutively, the top view model uses the values found for X in the side view model and uses these as parameters in the top view model to solve for the values of Z as depicted in Figure 2.17 A.

The objective function from section 2.5 contains a term in the Pythagorean theorem which assesses the difference between X-coordinates. Since these coordinates have become parameters in the top view optimization of the sequential model, it represents a constant and can therefore be left out and is therefore changed from D to D'. The objective function for minimizing the distance to the end point is shown as Equation 2.7. The objective function shall still be implemented in in a squared form since it would otherwise entail negative distances to the end point in the solution space. The same holds for the part of the objective function where the length of the arm is minimized. The objective function for minimizing the length of the arm is shown as Equation 2.8. The full sequential model can be found in section B.3.

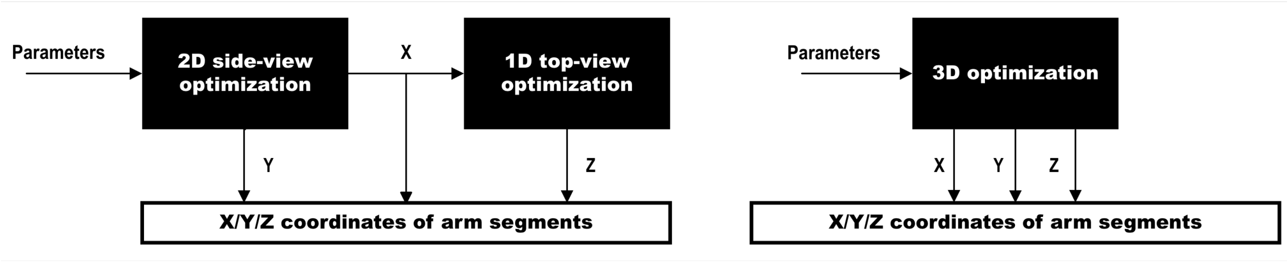

(A) (B)

Figure 2.17: *Graphical description of the (A) sequential and (B) comprehensive optimization approaches to gain 3D results.*

$$D'^2 = (Z_{2N} - TEP[0])^2 \tag{2.7}$$

$$L' = \sum_{j \in J}((Z_{2j} - Z_{1j})^2) \tag{2.8}$$

CartDist [m]	Segments	Max elongation ratio	Max deflection angle (deg.)
1.2	3	2.77	61.22
	4	2.92	58.4
	5	4.44	64.4
5	3	1.14	60.02
	4	0.74	58.14
	5	0.63	59.53
10	3	1.19	59.88
	4	0.59	59.66
	5	0.60	59.52

Table 2.12: *Maximum elongation ratios and deflection angles per setup. Some of the deflection angles are higher than 60 degrees despite the constraint of max 60 degrees. This is due to the fact that only the angle in the side view projection model was constrained, meaning that the angle in 3D can be higher or lower. Implementing this constraint would require an implementation of the dot product and was deemed outside the scope of the study as it was assumed that it would not lead to significant improvements with the required additional effort.*

Segment nr.	1		2		3	
	min	max	min	max	min	max
Lengths (m)	0.3	1.13	0.33	1.05	0.33	0.99
Elongation ratio	2.77		2.18		2.00	
Maximum angle (deg)		53.57		61.22		

Table 2.13: *Specifications of 3 segment arm configuration based on model.*

Segment nr.	1		2		3		4	
	min	max	min	max	min	max	min	max
Lengths (m)	0.22	0.74	0.24	0.87	0.24	0.82	0.24	0.94
Elongation ratio	2.36		2.63		2.41		2.92	
Maximum angle (deg)		58.40		54.39		40.01		

Table 2.14: *Specifications of 4 segment arm configuration based on model.*

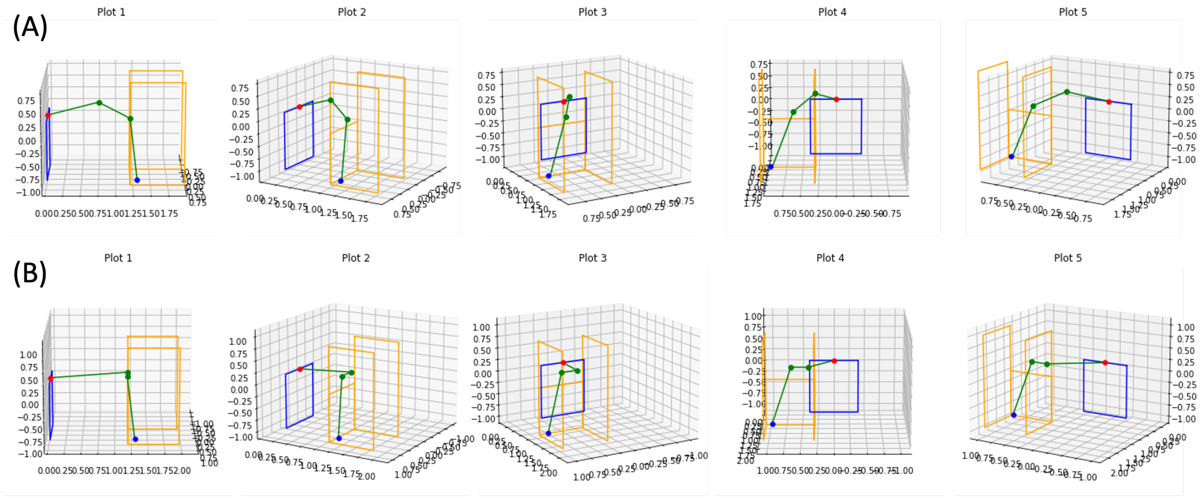

Figure 2.18: ***3D results for comparison of the sequential and comprehensive optimization approaches in an identical setup.*** *For a direct comparison of the performance of the sequential and the comprehensive 3D optimization approach, identical runs have been performed to compare both approaches. Based on the results found in subsection 2.4.2, only a 3-segment arm has been considered. The sequential model shows superior results in the form of overall shorter length of the arm, more evenly distributed lengths and smaller deflections as substantiated in tables 2.10 and 2.11. (A: sequential) 3D view plot results of one of exemplary pickup location solved using the sequential method for a 3-segment arm with a computational time of 5 minutes. (B: comprehensive) 3D view plot results of the same pickup location as used in the sequential approach solved using the comprehensive method for a 3-segment arm with a computational time of 5 minutes.*

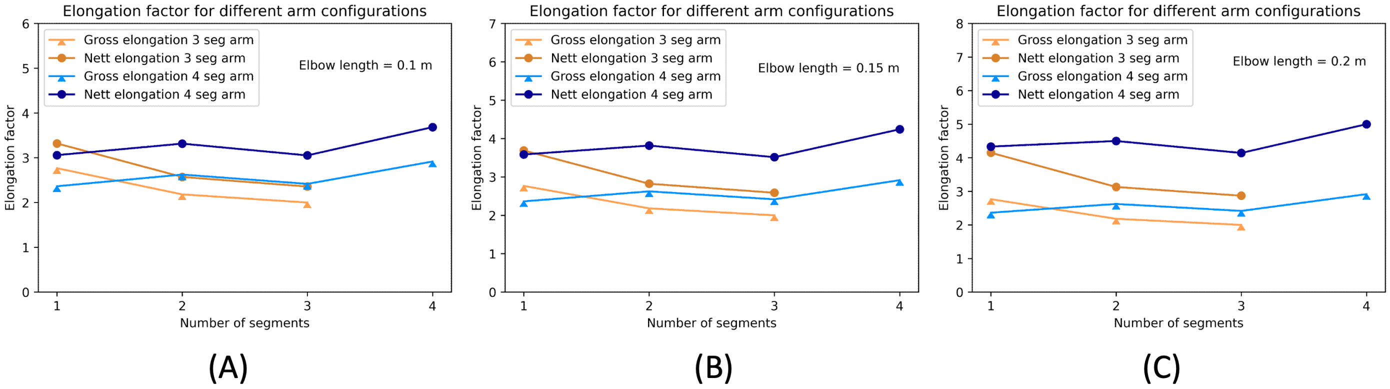

Figure 2.19: *Effect of integrated elbow section on required elongation ratio based on model results. Nett elongation and gross elongation is based on nett elbow length and gross elbow lengths as defined in Figure 2.21.*

2.6.3. Results of 3D model

With a correct model, various arm configurations can be obtained based on the different pickup points and number of segments. When enough data is gathered, conclusions can be drawn from the results, stating what the best number of segments is, which lengths the segments must be able to adhere to, and what angles the segments must be able to make. To gain knowledge of the sensitivity of the results, the distance between the arms base and the pickup locations was experimentally increased. These results were used to see if the conclusions would change based on different scenario setups.

Based on 3 experiments, the conclusive number of segments can be determined and information regarding the lengths of the segments including elongation and contraction ratios can be extracted. The experiments are listed below.

1. Runs for all 5 end points for 3, 4 and 5 segments with original distance between the base of the arm and the cart.
2. Runs for all 5 end points for 3, 4 and 5 segments with 5 meters distance between the base of the arm and the cart.
3. Runs for all 5 end points for 3, 4 and 5 segments with 10 meters distance between the base of the arm and the cart.

The results of the experiments are all gathered in Table 2.12. Data acquisition has been conducted according to the approach introduced in subsection 2.2.4, with 5 total pick-up points: 4 points in the bottom corners of the ULD, and one on the belt. The 3D deflection angles are acquired, which can vary from the angles from the 2D projections as explained in subsection 2.5.1, and the lengths of the segments for each pick-up point are used to define the maximum elongation ratio between all combinations of pick-up points. In the decision for the optimal number of segments, a trade-off is made between a limited maximum elongation and small deflection angles.

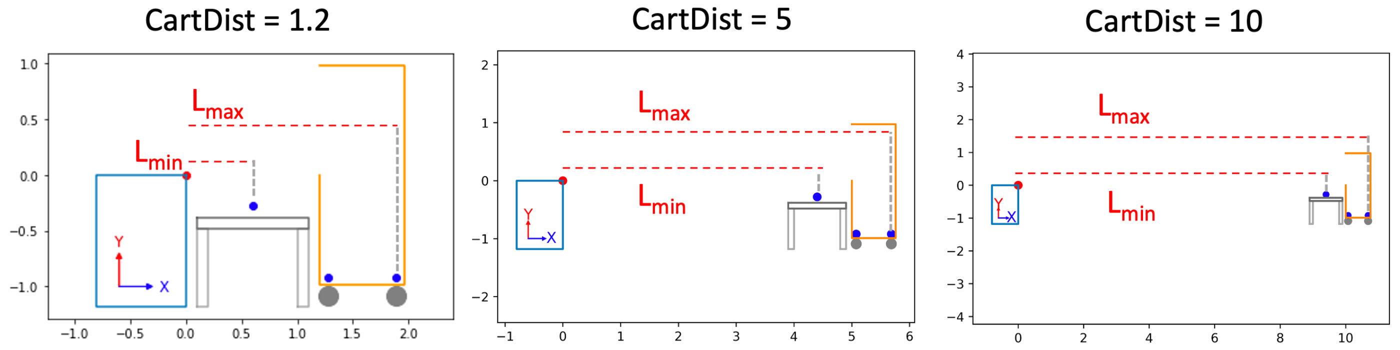

Figure 2.20: *Effect of CartDist on the maximum and minimum length to bridge. The difference between* L_{max} *and* L_{min} *becomes smaller relative to* L_{min}*, meaning that the elongation ratio becomes less significant with higher CartDist.*

Judging from the values from Table 2.12, 5 segments is in none of the cases significantly better than 4 segments. Elongation ratios in its distance class remain rather similar, defined as $\lambda_e = (L_{max} - L_{min})/L_{min}$. It is clear that with increased distance between the base of the arm and the cart, elongation ratios drop significantly. This might seem paradoxical but is is explained by the fact that in the simulations the distance between the base of the arm and the cart were increased and the location of the belt was unchanged with respect to the cart as depicted in Figure 2.20. Therefore the arm needs relatively less length to contract to place parcels on the belt, which translates into relaxed elongation ratios. Judging from tables 3.11 and 2.14, the maximum deflection angle remains relatively constant and does therefore indicate little to decide how many segments to choose. Since logistical warehouses are generally limited in space, the original CartDist should be taken in consideration (1.2 m). For this situation the elongation ratio is smallest with three segments. However, 4 segments shows a maximum elongation ratio not too deviant, but a maximum deflection angle of 3 degrees less. Considering that with an increased CartDist, the maximum elongation ratio between 3 and 4 segments decreases significantly, options could be explored to find ways to increase the CartDist and reduce the necessary elongation ratio by choosing a 4 segment configuration. Since 3 segments and 4 segments present such a close gap, both are summarized in Table 3.11 and Table 2.14.

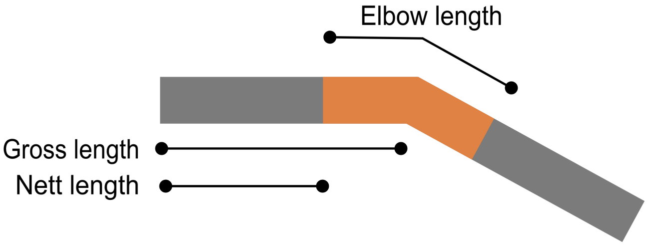

Figure 2.21: *Definition of an elbow section.*

One important note is that in practice the sections that bend will also take some space from the linear elongation sections. Elbow sections are defined as seen in Figure 2.21. Assuming that elbow sections do not support linear elongation but only facilitate bending, the effect the length of the elbow sections have on the required elongation ratios is presented in Figures 2.19 A, B and C. It becomes clear that with longer elbows the nett elongation ratio for the 4 segment configuration grows faster than for the 3 segment configuration. Since the true behavior of the elbow is not yet understood, and considering the possibility that it might not facilitate linear elongation at all, opting for a 3-segment configuration will guarantee the minimum upward correction required for achieving the necessary elongation ratio for the linear actuators.

2.7. Modelling discussion

This study has shown a methodology to initiate the design process of a segmented flexible robotic arm, before any decision has been made about working principles. An optimization model has been explained according to a generic situation where a flexible robotic arm must navigate around obstacles like a wall, and its applicability has been exemplified through a case study from the logistical sector. Generally, the presented methodology has shown a modeling approach which is applied before the conceptual design process starts, and presents a contribution to a highly desired structured design process for flexible robotics. This section shall discuss some limitations of the study, as well as some recommendations.

2.7.1. Limitations

Kinematic optimization often imposes complex spatial relations, which easily increase the non-convexity, and therefore the required effort to solve the model, as a result of quadratic, cubic or non-linear functions. Despite many techniques to linearize and relax optimization models, this type of optimization is limiting in finding truly optimal solutions as computational times increase rapidly, therefore posing limitations for situations where computing power is an issue. As touched upon in subsection 2.6.1, the sequential approach was chosen in this study to render kinematics in 3D, however, the comprehensive model bears a high potential to yield more inclusive results, which reflects the lack of computational effort as a limitation in this study.

This study has only considered lengths in its objective functions. Since flexible robotics are often made from flexible materials, bending is usually limited, and it would be therefore beneficial to be able to minimize the bending angle between all segments. However, this presents quite a challenge in quadratic programming. It is only possible to minimize a single angle, but not to minimize all angles individually at the same time, without prioritization in a 2D plane.

Lastly, for a more comprehensive decision on the best number of segments, it would be beneficial to include the number of segments in the optimization as a decision variable instead of a parameter. However, according to the used solver (Gurobi optimization with an academic license), this is not possible. This would require the size of the set of coordinate decision variables to be variable, which the solver does not allow. In this study, this limitation demanded a qualitative approach for the decision on how many segments was optimal. With the number of segments included in the optimization this would change into a more reliable quantitative approach.

2.7.2. Recommendations

For further expansion on the proposed methodology, adaption of the model to solve for multiple end points in a single run would result in an improved process. In this way, new variables could be included in the objective value like the elongation ratio. This circumvents the need to gather data from separate runs and assess performance afterwards, and opens the possibility to for instance minimize the elongation ratio of the arm between two pick-up points.

If ample computational power is available, it is recommended to reform the model into a non-linear model, which would allow the dot product to be included in the optimization. This would allow for the deflection angle to be constrained in a 3D setup, in contrast to only limiting the deflection angle in the 2D projection that most closely resembles the 3D kinematics of the arm. Therefore, an efficient non-linear optimization model would improve the accuracy of the results.

In the initial design stage of a flexible robotic arm, FEA cannot be used as usually the working principles, and thus mechanical properties, of the arm are unknown. The methodology explained in this chapter is recommended to be used prior to an FEA analysis to gain insights into the kinematics of the flexible arm design to ensure an informed start and time-efficient use of the flexible arm design process.

2.8. Concluding remarks

This study has presented a new methodology to optimize the kinematics of flexible and flexible robotic arms using a quadratic programming optimization approach. According to a generic situation and a use case in logistics to unload more complex unit load devices, a program has been showcased to exemplify the methodology to discover how many segments a new flexible robotic arm needs for a certain application, what the required minimum and maximum length per segment is, and what angles the respective segments must make with each other. The methodology has shown to be ultimately versatile and can be extended into many situations to design flexible robotic arms, like in inspection, automatic manufacturing and complex pick-and-place operations. This methodology contributes to a highly desired structured design approach in flexible robotics, by showcasing potentially the very first step in the process of designing a segmented robotic arm, as it does not require any prior knowledge about the working principles, materials or actuators in the arm. Limitations are mainly presented in quadratic solver compatibility and computational intensity and recommendations are given regarding expansion of the model and deviant computational methods.

Chapter 3

Long-Reach Unfold: Deployable Origami with a Twist of Electromagnetism

Abstract
This study presents a novel electromagnetically actuated Kresling cylinder designed for a versatile, highly contractible, long-reach robotic arm. The Kresling origami cylinder was chosen due to its remarkable tunability in axial stiffness while bearing stiffness in lateral direction, which is an ideal combination for electromagnetic actuation. Focusing on the developmental aspect, the paper systematically explores the dimensional optimization of circular copper coils and ferromagnetic cores using finite element analysis (FEA) software. Critical design considerations, including the number of polygon sides in the Kresling unit, effective height, and solenoid and core dimensions, are addressed. An experimental validation of the prototype verifies the proposed methodology, addressing key questions about core configurations, coil sizes, and the impact of a hole in the core on magnetic attraction. The results demonstrate that larger core holes minimally affect solenoid attraction, and the optimal coil size is determined through a balance between gravitational, energy dissipative, and magnetic forces. Scaling the concept, the study extends to the design of a full-sized robotic arm for efficient package unloading in confined spaces. Three arm segments are analyzed and designed, considering practical constraints from and example from the logistical sector. The study concludes with a graphical representation of force balances, emphasizing the significance of magnetic force in overcoming gravitational resistance for a long-reach flexible robotic arm. The proposed electromagnetic Kresling cylinder offers a promising avenue for applications in confined environments, such as logistics, showcasing advancements in flexible robotics with potential real-world impact.

3.1. Introduction

3.1.1. Challenges in traditional robotics

Robotic arms, integral in diverse industries, find applications ranging from palletizing and material handling to welding, inspection, and pick-and-place operations [1–3, 135]. The electric and electronics industry installed 137,000 units, while the automotive sector incorporated 119,000 units in 2021 [4]. Traditional robotics generally present rigid constructions with rotary joints and linear elongating beams with limited extension ratios (max 0.5 for a hydraulic beam as they can inherently only double in length) based on design analogies regarding strength as one of the prime performance factors [136, 137]. Enhancing automation is sought after, as the use of robotic automation enables increased scalability, enhances human capabilities, and generates a higher return on investment [138]. This return on investment is reinforced by the growing wages resulting from a shift away from unfulfilling or hazardous occupations, leading to labor gaps [139].

The rigid design analogy of the most popular robot in industrial settings, the articulated robotic arm, presents challenges when narrow spaces are imposed in situations like logistical pick-and-place-operations, vehicle manufacturing and inspection, cleaning and maintenance of confined spaces. Confined spaces often come with hazardous working conditions as 24% of confined space fatalities happen during maintenance and inspection, followed by 12% for cleaning and 11% for sole inspection [9, 10]. The limitations that articulated robotic arms bear in confined spaces exists due to their inherent design, consisting of straight sections and rotary joints, and is characterized by limitations when obstructions are present in their near surroundings [5, 6]. To summarize, articulated arms excel in heavy lifting, high precision and speedy tasks, but present challenges when their perimeter contains obstacles like walls or must reach into confined spaces.

3.1.2. Situational example

Currently, automatic depalletization of standardized pallets using articulated robotic arms (Figure 3.1 A) is common in logistical operations (Figure 3.1 B), but when more complex Unit Load Devices (ULDs) are introduced, like the one depicted in Figure 3.1 C and D, commercial robots lack versatility, as visualized in Figure 3.1 E and F. These incapability's are most often presented as blind spots in their kinematic reach. The articulated arm, is unfit for more complex situations as they generally comprise of 2 straight sections and 6 rotary joints, and can therefore not reach the corners on the bottom of the shown ULD. To reach into the ULD in Figure 3.1 C the straight sections should be long, but to remain mobile to move around inside the ULD, the sections must be short. Due to this contradiction, alternative robotic arms are desired in this sector to further increase the level of automation.

3.1.3. Benefits of flexible arms

Flexible arms pose benefits in accessing hard-to-reach places over traditional articulated arms as they are often capable of adapting to their environment due to their flexible nature. While the articulated robotic arm consists of two rigid straight sections with 6 rotary motors enabling bends at designated positions, flexible arms generally boast a flexible body capable of bending at multiple points along its length. Additionally, it possesses the remarkable ability to contract and elongate, offering superior potential in confined space access. In the case as described in subsection 3.1.2, ultimately a flexible arm is deployed that can vary its length and bend at various locations to flexibly navigate towards a hard-to-reach spot.

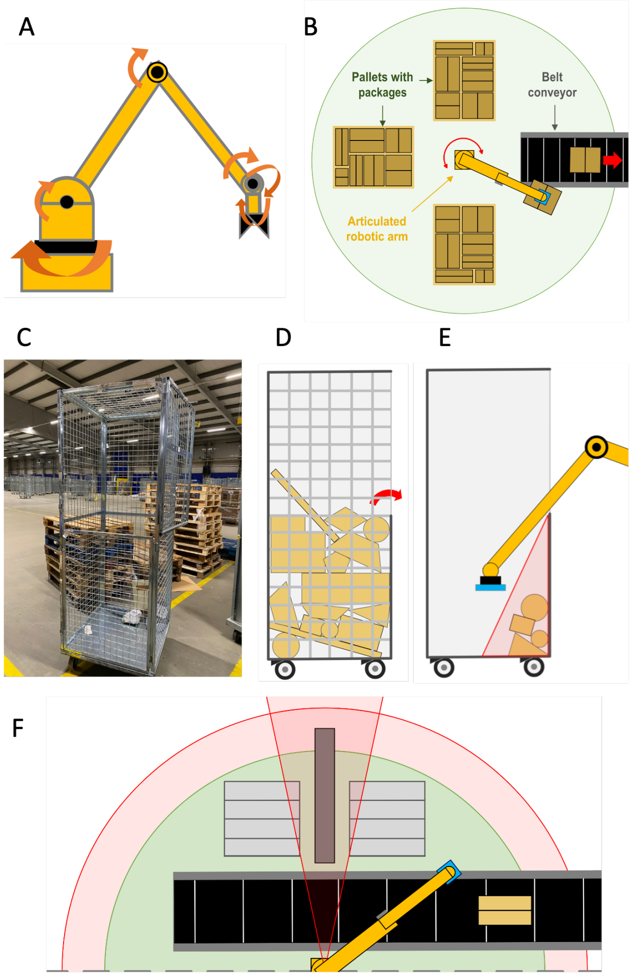

Figure 3.1: ***Examplary situation of challenges imposed by narrow spaces on articulated robotic arms.*** *(A) Sketch of an articulated robotic arm with 2 rigid straight sections and 6 rotary joints (orange arrows). (B) Ease of unloading of standardized pallets using articulated robotic arm schematic. (C) Common confined Unit Load Device (ULD) in logistical sorting centers. (D) Schematic of geometry and unloading access of confined ULD. (E) Blind spot visualisation (red section) of confined ULD using articulated robotic arm seen from side view. (F) Blind spot visualisation (red sections) of unloading of confined ULD onto a belt conveyor using an articulated robotic arm seen from top view. (G, H) Potential flexible robotic approach for confined space automation, example: unloading of confined ULD. To surpass the performance of a traditional articulated robotic arm to access confined spaces, ultimately a flexible modular arm is deployed which can locally vary its length and bend from a fully contracted position.*

3.1.4. State of the art of flexible arms

Bezha and Ito [140] took inspiration from the octopus' tentacles, crafting a flexible arm using silicone and tendons. With 71% contraction it excels in flexibility. However, due to the use of highly flexible silicone, the arm shows limitations in manipulation of objects at a horizontal distance. Sparrman et al. [118] demonstrated a 3D printed pneumatic bellow arm capable of flexible manipulation. It achieves flexible bending and a maximum shrinkage of 55%, showcasing potential for versatile applications. No force testing was executed and therefore performance regarding strength is yet unknown. Wang et al. [73] explored a pneumatic manipulator arm utilizing ultra-long stretchable fabric actuators. Despite a notable 61% contraction, its limitation lies in low stiffness, impacting precise control. Grissom et al. [69], devised the OctArm with McKibben actuators, offering a 38% contraction. OctArm can be altered between 3 and 4-segment configurations and shows remarkable grasping capabilities, but requires 3 thick parallel McKibben actuators to achieve this in each section. Chen et al. [117] achieved an impressive 80% contraction ratio with pneumatic bellows. However, this design sacrifices slimness, potentially limiting its maneuverability in tight spaces. Festo's Bionic Handling Assistant (BHA), as developed by Grzesiak et al. [71, 87], boasts nine degrees of freedom through three sections actuated by 3D printed pneumatic components presenting a modest contraction of 36%. Its flexible and adaptive nature shows potential in manipulation where versatility is needed. McMahan et al. [75] proposed a multi-segment, 'hose-in-hose' concept, continuum arm actuated using tendons and supported by a pneumatic backbone called Air-Octor. Although presenting a very flexible arm, the inside of the arm is fully occupied by the pneumatic backbone and payload capabilities are limited which allow a limited application to inspection. Gong et al. [66] developed a 2-section silicon flexible arm based on parallel pneumatic chambers for actuation. By implementation of radial rings the elongating performance of the arm is improved with respect to the similar PneuNets design arm by Martinez et al. [65] which does not include radial rings. The integration of the pneumatic chambers in the backbone of the manipulator improve volumetric efficiency, but the use of silicone limits the manipulating abilities in horizontal operation due to creation of a large torque resulting from the silicon body.

Santoso and Onal [141] developed an origami-inspired arm resistant to torsional bending, using tendons for actuation. While capable of a 20% contraction and the availability of usable space inside the actuator to place cables, the extending and bending motions rely on tendon pulling and bouncing back due to the elasticity of the folded shell, meaning that high force generation remains a challenge. Zhang et al. [37] explored flexible origami modules driven by gas, showcasing potential for intricate movements. However, the reliance on gas-based actuation poses challenges as found in pneumatic actuators, posing inefficiencies in terms of volume. Li et al. [22] presented a pneumatic two-section extendable origami arm with pneumatic hinges, demonstrating potential for space deployment as strength analysis remains absent.

Liang et al. [67] introduced a flexible fabric pneumatic arm featuring articulated movement through fabric pneumatic hinges. While this arm is ideal for close cooperation with humans due to its flexible nature, it is also actuated pneumatically and presents similar limitations as the articulated robotic arm as it consists of straight non-elongating sections.

Jiang et al. [142] integrated granular jamming with pneumatic McKibben muscles to achieve variable stiffness. While offering adaptability, it struggles with limited strain at maximum stiffness posing challenges in reaching into confined spaces. Jiang et al. [142] introduces a bio-inspired extensible continuum manipulator with variable stiffness. Experimental validation demonstrates a contraction ratio of 26% under an inflated air pressure of 2 bar. While the manipulator's variable bending stiffness performed satisfactorily in experimental tests, it was executed in vertical orientation only, which leaves application in horizontal operation to reach into confined spaces undefined.

Yang et al. [77] presented a silicon-based 4-segment flexible arm, actuated using shape memory alloy coils. The arm shows promising flexibility and manipulation capabilities. However, due to the massive silicon body of the arm, large torque becomes a challenge when manipulating at some distance, limiting the design to vertical manipulation.

3.1.5. Challenges with flexible arms

Many flexible arms, particularly those employing highly flexible materials like silicone or fabric, face limitations in manipulation range. Their flexibility often compromises their ability to exert force or manipulate objects at a distance effectively. Most studies entail designs of vertically operating flexible arms, presenting a gap in literature for flexible arms capable of operating horizontally.

Flexible arms may struggle with exerting sufficient force or bearing heavy loads, especially when compared to traditional rigid robotic arms. This limitation can affect their suitability for tasks requiring high force or precision which are often required in the industrial setting. Many flexible arms comprise of silicon bodies, which are often solid to maintain as much stability as possible. However, since silicon is not particularly lightweight, scaling these concepts becomes challenging, as the designs exponentially scale in weight.

Flexible arm designs, especially those employing pneumatic actuators, often suffer from volumetric inefficiencies. The bulky nature of pneumatic components can limit the compactness of the arm, affecting its maneuverability in confined spaces. This also results in limitations for implementation for additional equipment like usable space for electric wires or gas/fluid supply.

Flexible arms typically exhibit lower stiffness and stability compared to rigid counterparts. This limitation can impact their ability to maintain desired shapes or resist external disturbances during operation, limiting the precision of the devices.

Additionally, it's important to note that while many innovative flexible arm concepts show promise in research settings, most are not easily scalable to real-world applications due to these inherent limitations, presenting a void in literature.

3.1.6. Approach

As found in subsection 3.1.4, flexible robotic arms are often difficult to scale since they are mostly designed around a certain reference situation. To design a flexible robotic arm for confined space deployment, here a modular approach is assumed. Taking a modular approach enables the design process to focus on a single element, extending it seamlessly into a larger application and facilitating scalability to virtually any scale imaginable. The full robotic arm shall initially be modelled as a succession of coupled blocks with yet abstract capabilities and characteristics as depicted in Figure 3.2 A. The underlying principle of this approach is that if one element has a certain contraction ratio, a succession of these elements holds this contraction ratio. Figure 3.2 B shows a succession of 3 identical elements with each a contraction ratio of $\frac{Umax-Umin}{Umax} = \frac{2-1}{2} = 0.5$. The succession of the three elements also has a contraction ratio $\frac{Smax-Smin}{Smax} = \frac{6-3}{6} = 0.5$. An impression of the modular approach in confined space deployment is depicted in Figure 3.2 C. The different modules either elongate or bend in an orchestrated manner to reach the end point.

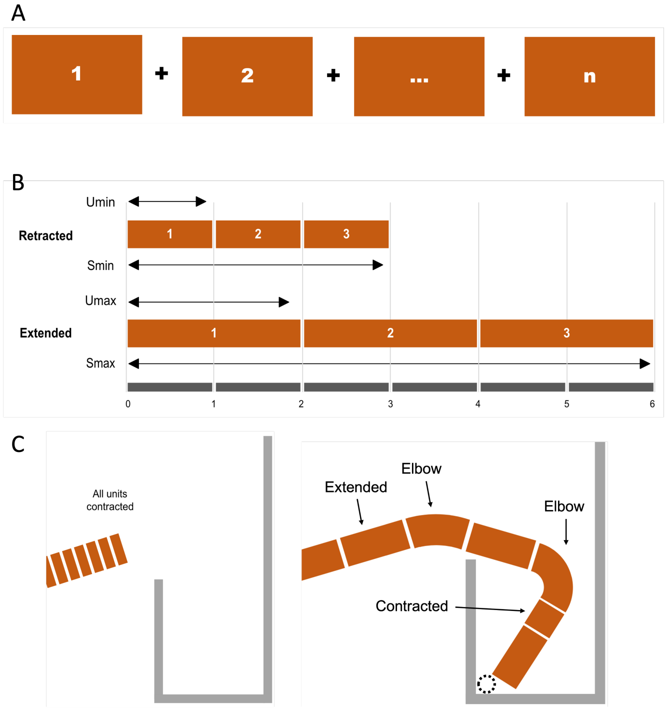

Figure 3.2: ***Schematic of modular principles of design.*** *(A) A depiction of a the modular succession of elements central in this study. (B) When a certain element has a contraction ratio, a succession of these elements holds this contraction ratio. Contraction ratio of the first element:* $\frac{Umax-Umin}{Umax} = 0.5$, *contraction ratio of all three identical elements in succession:* $\frac{Smax-Smin}{Smax} = 0.5$. *(C) An example of the modular approach in action for accessing a confined space. The modules either elongate or bend to reach the end point in the confined space.*

This signifies that by determining the required number of segments, their length ranges, and the corresponding contraction ratio for a full scale arm needed for the required flexibility in a specific confined space, a small-scale single unit can be designed and prototyped based on this contraction ratio. Subsequently, it can be scaled up and placed in succession to meet the demands of the given situation. This study mainly focuses on longitudinal displacement and forces of the arm.

3.1.7. The goal

The goal of this study is to design, model and experimentally test a novel linear actuator with a contraction ratio that outperforms traditional hydraulic actuators, that can be scaled up in a modular fashion into a full flexible robotic arm to be deployed for confined space operations, based on a case study found in logistics. This study is structured as follows. First, the approach is shown, then the modelling and design are explained, then the prototype is presented and experimentally validated, and lastly the validated model is used to design a full size arm. This arm will solve challenges that traditional robotic arms cope with when deployed in confined spaces.

3.2. Actuator design

Judging from the learning's in subsection 3.1.4, linear actuators made from silicone find challenges in large contraction ratios and are far from ideal for scaling up. Fabric based actuators have the potential to realize large deformations but pose significant challenges to possess stiffness. Folding thin walled cylinders, like origami cylinders, show characteristics that fit the requirements as they can fold into a relatively flat disc and show stiffness in lateral direction due to a large moment of inertia [14]. Due to the volume efficient manner in which origami cylinders deploy and collapse completely within their footprint, the moment of inertia is maintained along the deployment stroke, therefore maintaining bending stiffness at all times as inertia is gained through the placement of mass far from the axis of bending [143]. As origami cylinders are thin walled hollow structures, most mass is placed relatively far from the bending axis at all times during collapse or deployment. Two origami structures that can elongate in a volume efficient manner are the Kresling and Yoshimura origami cylinders, and therefore present attractive options for this study [144]. From the two, the Yoshimura cylinder poses more freedom for bending [145], meaning that the Kresling cylinder is stiffer and therefore desired for an actuator capable of horizontal operation [146].

3.2.1. The Kresling origami cylinder

The Kresling origami cylinder originates from the combined compression and transverse shear causing a buckling pattern in thin-walled tubular shells [147, 148]. The Kresling cylinder has been of interest in deployable structures due to its multi-stable, tunable and deformable properties, giving it a substantial potential for integration in to an actuator [49, 149–152].

Research has been conducted to investigate the mechanical properties, multi-stability, and tunable stiffness of the Kresling cylinder [153]. Kaufmann and Li [131, 146] exposed the variability and tunability of the bending stiffness of the Kresling cylinder for various folding pattern configurations by strategically switching between two stable states, and unveiled its potential to enable localized bending and stiffening in a stacked robotic arm configuration using tendons . Origami cylinders can also be manufactured out of materials other than paper, such as polymers. For example, Hu et al. [154] has uncovered hysteresis in polymer Kresling cylinders, has shown mechanical properties of the structure and characterized these properties. Moreover, the structure has proven to be an attractive option to function as a compliant building block and has shown to be able to bear high loads making it an interesting structure to integrate into a flexible yet configurable robotic arm [155, 156]. Wang et al. [50] has uncovered the stiffness profiles of Kresling cylinders with different geometries, which informs about the configuration of multistability and mode with minimal stiffness in axial direction, and showed applications for configurable metastructural building blocks and a versatile robotic arm configuration. Therefore, the Kresling origami cylinder poses as an attractive option to serve as the flexible structure in this study.

3.2.2. Kresling origami actuators

As unveiled in subsection 3.1.4 does pneumatic actuation not offer the right characteristics for this study, as volumetric efficiency is crucial in confined space deployment. The Kresling cylinder can be alternatively actuated using a tendon/winch system [157]. However, achieving specific localised actuation remains a challenge. Dielectric elastomeric actuators can theoretically be implemented in the hinges of the Kresling structure, but a practical realisation has not yet emerged [158]. Kresling structures have been actuated by electromagnetism [159]. Novelino et al. [160] introduces an electromagnetic origami system, coupling the bistable Kresling pattern with a magnetically responsive material for untethered and programmable multifunctionality, while Wu et al. [23] presents electromagnetically controlled origami robotic arms based on Kresling patterns, demonstrating precise magnetic actuation for complex bending and elongation motions. The advantage of electromagnetic actuation over for instance pneumatic actuation is that the structure does not have to be airtight and thus the inner volume of the structure can be used for other purposes (like running auxiliary wires). However, the actuation of these units is realized by placing them in a large magnetic field, meaning that even though actuation can happen locally, it does not present a standalone system since very large coils must be present around the structure for actuation, and therefore remains unfit for applications of scale. A concept utilizing the flexibility and tunable stiffness of the Kresling cylinder, while taking advantage of the spacial freedom electromagnetic actuation brings, integrated into a standalone system, holds a promising research gap. Therefore electromagnetic actuation is chosen as the driving principle for the Kresling cylinder actuator.

3.3. Prototype design

3.3.1. Requirements

Based on the kinematic modeling for this thesis, the highest required elongation ratio is 0.73. Therefore for a segment to possess this elongation ratio, a single actuator unit must possess a minimum contraction ratio of 0.73 to fulfill the situation when scaled up, as understood from subsection 3.1.6.

To repeat, the focus of this study is on the longitudinal operation of the flexible arm. Therefore, the actuator cells are required to generate enough force to actuate along its entire actuation stroke in every orientation. To show a proof-of-concept of an actuator cell, the actuator cell prototype is only required to actuate itself, disregarding the forces a full size robotic arm would pose to the cells.

Lastly, a single actuator cell is required to be stiff enough to show negligible deflection under its own weight. The requirements are summarized in Table 3.1.

Table 3.1: *Requirements for a single actuator cell prototype.*

	Requirements
1.	Contraction ratio of at least 0.73.
2.	Generate enough force to lift its own weight in any orientation.
3.	Be stiff enough to show negligible deflections under its own weight.

3.3.2. Overall design

The Kresling cylinder consists of two polygonal base plates, connected by a triangulated folding structure. The two base plates are free to move towards and away from each other whilst staying parallel as shown in Figure 3.3 A. To automate this deployment, external forces must be exerted on the base plates to attract and repulse them, indicated as F in Figure 3.3 B. If the external forces overcome the resistance that the Kresling cylinder imposes and the potential gravitational forces, the actuator can automatically deploy or collapse. The Kresling cylinder owes its resistance due to energy loss during the folding of the paper, since paper folds can be modeled as elastic rigid-facet hinges, which present elastic energy upon deformation (F_{dis} in Figure 3.3 B) [161]. Learning from Wu and Novelino [23, 160], to prepare the Kresling origami cylinder to be deployed in industrial settings, the magnetic actuation of the structure must be realised completely locally, without the need for large external magnetic field generation. Therefore a design with integrated copper coils is proposed. A Kresling origami cylinder is nestled in between a set of 2 copper coils, combined with each an individual steel core to enhance the magnetic response. Based on the direction of the current in the coils, the coils can be set to attract or repel each other, initiating a contraction or an extension of the Kresling cylinder. Figure 3.3 C shows the design in an extended and a contracted state. A list of all components is shown in Table 3.2. Technical drawings of the coil holder and PLA link plates are included as section C.4 and section C.5.

Table 3.2: *Design components*

Component	Material	Function
Kresling cylinder	Paper (80 g/m^2)	Facilitate connection between coils and ensure mechanical properties.
Copper coil	Copper wire (D0.3 mm)	Generation of magnetic field.
Coil holder	Aluminium	Keep coil in place and protected.
PLA link plates	3D printed PLA	Connect Kresling cylinder to coil holder and house the ferromagnetic core.
Ferromagnetic core	Steel	Enhance the magnetic response of the copper coils.

3.3.3. Design of the Kresling cylinder

The selection of the Kresling cylinder for this investigation is motivated by its exceptional tunability in the axial direction, coupled with its capacity to offer a spectrum of modes in terms of lateral properties, i.e. when the cylinder is fully deployed, it has a large moment of inertia and is

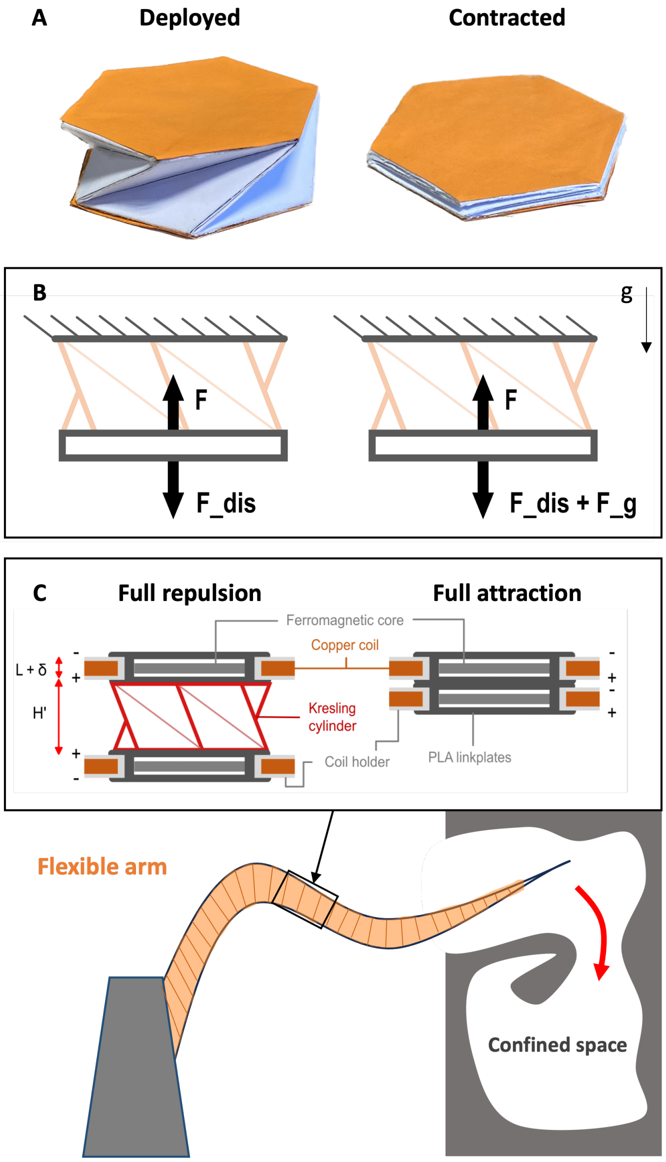

Figure 3.3: *(A) Kresling cylinder in its deployed and contracted states (here made from paper). For automatic actuation, the two base plates (orange) must be repulsed and attracted by an external force. (B) Forces acting on the free end of a Kresling origami cylinder to contract the structure when fixed on one of its base plates. When only contracting a paper cylinder, gravity can be neglected (left), but when contraptions with substantial mass are integrated to initiate the contraction, gravity must be included (right). F represents the external force to actuate the structure, F_{dis} is the dissipative force caused by the loss of elastic energy from the folding of the paper, F_g represent the gravitational force of an integrated contraption to exert the external force F. (C) Schematic of electromagnetically actuated Kresling cylinder prototype while the coils are fully repelling (left) and fully attracting (right) each other, and placement in an artist impression of a flexible robotic arm concept to reach into confined spaces.*

resistant to bending, but, when near the collapsed state the structure can facilitate bending motions when externally actuated [23, 131]. Given that the primary objective of this study is the development of an actuator for integration into a flexible robotic arm, a Kresling cylinder characterized by minimal resistance in the direction of movement is imperative. This requirement stems from the necessity for the electromagnetic solenoids' force to encounter as little obstruction as possible. To fulfill this criterion and design a structure with as little resistance during deployment and collapse, a Kresling configuration with $\alpha = 30\,\text{deg}$ and $\beta = 30\,\text{deg}$ was chosen (according to Figure 3.4) as it represents the lowest axial resistance configuration as elucidated by Wang et al. [50].

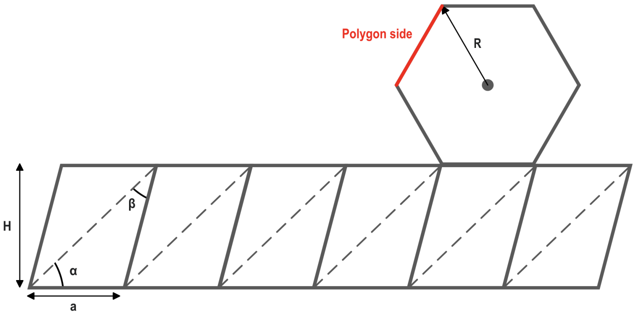

Figure 3.4: *Kresling pattern with a base with m=6 sides.*

Moshtaghzadeh et al. has found that with an increased number of polygon sides, the Kresling cylinder becomes more stable, and therefore a large number of sides is desired [162]. However, according to Equations 3.1 and 3.2 the maximum height of a Kresling cylinder is determined by the length of the polygon sides, meaning that with an increased number of sides the stability increases, but the actuation stroke (H) decreases when R is fixed. A full actuation stroke is depicted in Figure 3.3 A and C. Equation 3.1 describes the length of the sides of a regular polygon with radius R and number of sides m, and Equation 3.2 describes the maximum height of a Kresling cylinder with polygon side lengths a and construction angles α and β. With an actuation stroke that is relatively small, the actuator shall become too heavy, as after each Kresling unit a coil will be placed. To maximize the stroke length with respect to the polygon radius, a 6-sided polygon is chosen as the base, since it is assumed that Kresling units with less than 6 sides are too unstable [162]. The folding pattern as used for the prototype is included as section C.6.

$$a = 2Rsin(\frac{2\pi}{2m}) \tag{3.1}$$

$$H = a(sin(\alpha)cos(\alpha) + \frac{sin^2(\alpha)}{tan(\beta)}) \tag{3.2}$$

Experiment: the effective height of a Kresling cylinder

The chosen Kresling configuration is not low resisting along its entire deployment stroke H. From a full collapsed state (or 0) to the effective height (H'), or 'termination position', 0 → H', the deployment shows minimal resistance [50]. From the effective height (H') to 100% deployment (H), H' → H, the cylinder shows an energy bump to overcome to reach 'third stable state' [156]. In this study, only the deployment interval from full collapse to the effective height H', 0 → H', will be used to ensure minimal resistance for deployment using electromagnets. H' is not related to the polygon and cylinder configuration and must thus be experimentally determined [163]. In this experiment, a Kresling cylinders with regular hexagon base is considered with construction angles α and β both 30 degrees, in accordance to the rest of the study. The effective height H' of the cylinder is the dependent variable and depends on the length of a hexagon side (a) as from Figure 3.4, representing the independent variable. Here it is assumed that for Kresling cylinders with regular hexagon bases and similar construction angle configurations the ratio of H'/H is maintained regardless of the hexagon side-length a. Thus, the ratio is to be determined.

A Kresling cylinder with hexagon side lengths of 30 mm was constructed and deployed by hand until the energy bump, or excessive resistance, was felt. Then, the length (H') of the cylinder was measured using a measuring tape. According to Equation 3.2, H is calculated. The effective height ratio was determined using H'/H.

It was found that the effective 'low resisting' height (H') of a paper Kresling cylinder was about 77.0% of the maximum height as defined in Equation 3.2. The details are noted in Table 3.3.

Table 3.3: *Kresling cylinder specifications of prototype.*

Property	Value	Unit	Description
m	6	-	Number of polygon sides
a	30	mm	Length of sides of polygon
α	30	deg.	Configuration angle 1
β	30	deg.	Configuration angle 2
H	26	mm	Maximum height from Equation 3.2
H'	20	mm	Measured effective height
H'/H	77.0	%	Effective height ratio

3.3.4. Solenoid design

The challenge in designing solenoids to actuate the Kresling cylinder chosen for this study lies in the bridging of the relatively large gap between the two ends, since magnetic field strengths decreases rapidly when moving away from the source [164]. In this study, a Finite Element Analysis (FEA) approach has been used to determine the configuration of the actuator cells [165]. In designing the coils of the prototype, mainly requirement 1 and 2 must be met. Firstly, the length of the coil assembly, consisting of the coil length (L) and holder thickness (δ) in Figure 3.3, and the deployment length interval of the Kresling cylinder (H') determine the contraction ratio of the actuator. The coils must ensure that the total contraction ratio of 0.73 is adhered to. Additionally, the coils must generate enough force to actuate the cell in any orientation. Looking at a single cell, the hardest orientation to actuate is a vertical orientation, i.e. the coil combination must be strong enough to overcome the gravitational force of the bottom coil in its entire assembly combined with the resistance that the Kresling cylinder poses upon deployment/contraction.

To design the coils according to the requirements, a modeling approach has been implemented in the form of 2 identical circular coils and 2 identical circular cores as depicted in Figure 3.5. The model calculated two forces: F1 and F2. These forces correspond to the attracting forces between the two solenoids. The coils could be reshaped into the polygonal form of the base of the Kresling units but are assumed as circular for simplicity [166].

To design electromagnets that generate high forces with respect to their mass, the two parts that comprise the model must be considered: the coil and the core. Insights into a configuration of the cores is requisite. However, the exact behavior of the magnetic field inside the coils is unknown. Therefore it is unknown where the cores enhance the magnetic response most. To maintain a weight efficient design, the cores are optimized for low mass and high magnetic attraction. The cores are modelled as discs with a varying hole size to unveil the contribution of the magnetic field on the central axis of the solenoid, and whether it is more efficient to leave the center of the core empty. Assuming a fixed

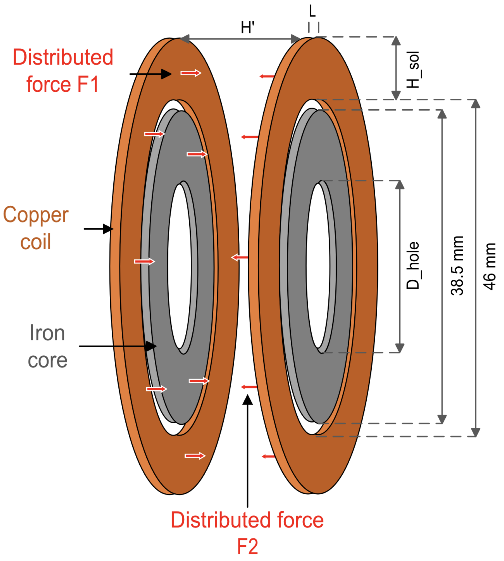

Figure 3.5: *FEA model setup.*

inner diameter of the coils, the length of the coils and the height of the coils is determined. The effect of the height and length of the coils is mapped, to unveil which configurations present high attracting forces with respect to the coil masses.

3.3.5. Performance evaluation

To evaluate the performance of the designs, a metric is created which is further referred to as the 'hanging test'. Ultimately, the electromagnetically actuated Kresling cylinder is intended to be implemented in a full size robotic arm. This infers that the actuator cells must be able to operate at any orientation. In a vertical orientation, the actuator prototype is designed to lift itself, presenting the most challenging scenario as it must overcome its entire weight with the generated magnetic force. To theoretically assess performance in this orientation, the hanging test determines if a specific configuration would fail. Figure 3.6 A shows the force diagram of the test. The final metric is evaluated as found in Equation 3.3. For a positive result the following should hold: $\eta > 0$, as this would result in a full contraction stroke in vertical orientation.

$$\eta = \frac{F_m - F_g - F_{dis}}{F_g + F_{dis}} \tag{3.3}$$

3.3.6. Results of core modeling

In Figure 3.7, it can be seen that larger core holes minimally impact solenoid attraction. Figure 3.6 B depicts the setup to determine the effect between hole diameter and magnetic and gravitational force. The line representing the attracting force hardly drops with an increased size of the hole in the cores, which leads to believe that the magnetic force concentrates closely around the wires of the coil and has only little presence in the central axis of the coils. The gravitational force of the cores, and there fore the gravitational force of the coil/core combination, drops significantly with an increased hole size in the cores. Considering the hanging test (excluding Kresling cylinder resistance), larger core holes enhance overall performance, i.e. according to Equation 3.3, with a larger hole in the core F_g decreases but F_m and F_{dis} remain relatively stable leading to an increasing η. To maintain a high η, the core holes are chosen as large as practically considered possible which is still possible to manufacture reliably with the CNC laser cutter: a hole diameter of about 90% of the core diameter. Considering that the largest relative difference between F_m and F_g result in the largest η, a 1 mm thick core (t) is chosen for the rest of this study.

3.3.7. Model validation

Here, the model of the prototype is validated by comparison of experimental results and modeling results.

A set up is created where a set of 2 coils and cores are placed at a distance of 20 mm in vertical orientation. The bottom coil has been fixed rigidly, with a load cell placed on a 3D printed PLA cap which also holds the core in place. On top of the load cell the second coil is placed on an identical cap. Due to the flat surface of the top and bottom of the load cell, the top coil can effectively balance on the load cell, circumventing any unknown reaction forces due to hypothetical structures. The setup is shown in Figure 3.8. When the coils are excited (I = 3A), the load cell will read a value which is a summation of the gravitational force of the top coil and the magnetic force. The magnetic force, the dependent variable, is related to the size of the coils and the dimensions of the ferromagnetic cores. The dimensions of the coils and cores are the independent variables, which combine into the gravitational force. In total 6 coil/core combinations were made to determine the magnetic attraction force. These 6 combinations were replicated in the FEA software and the theoretical attraction forces were evaluated.

The error between FEA results and prototype results from the 6 combinations was on average 71.8% as shown in Table 3.4. The difference between FEA results and real life fabrications can be explained due to imperfections in the experimental coils. The coils are hand wound, meaning that the packing density is not optimal and thus deviates from the ideal approximation of the FEA model [167]. To account for this difference, results obtained from the model must be adjusted according to this percentage in the physical design of coil sets to ensure correct force generation in the prototypes.

Experiment: the resistance of the Kresling cylinder

To integrate the Kresling cylinder into an electromagnetic actuator, the resistance of the Kresling cylinder must be known. In this experiment, this resistance is determined using a load cell in a setup which is depicted in Figure 3.9 A and B. This is of importance since to actuate the Kresling cylinder integrated with solenoids, the main forces to overcome are its own weight and the resistance of the intermediate structure.

The Kresling cylinder is placed horizontally to avoid the effects of gravity, with one end rigidly connected and the other end left free to move. To determine the resistance of the Kresling cylinder, the load cell is slowly but consistently pressed against the free end of the cylinder until about 50% displacement of the effective height to determine the resistive forces originating from the folding of the paper. 100% displacement is avoided since this would induce reaction forces from the frame, presenting biased results. For the magnetic actuation, the initial resistance of the Kresling cylinder is crucial, since the magnetic attraction is weakest here and it is most challenging to overcome the total actuation resistance here with magnetic force. When the coils are close to each other, their magnetic force has exponentially increased, which makes it acceptable to assume that the resistance of the Kresling cylinder becomes less of a challenge here. After 50% displacement is reached, the load cell is retracted and the Kresling cylinder is free to spring back into its resting position. This motion is repeated multiple times to average the recorded peak forces into the final Kresling cylinder resistance (F_{dis}). The details are recorded in Table 3.5.

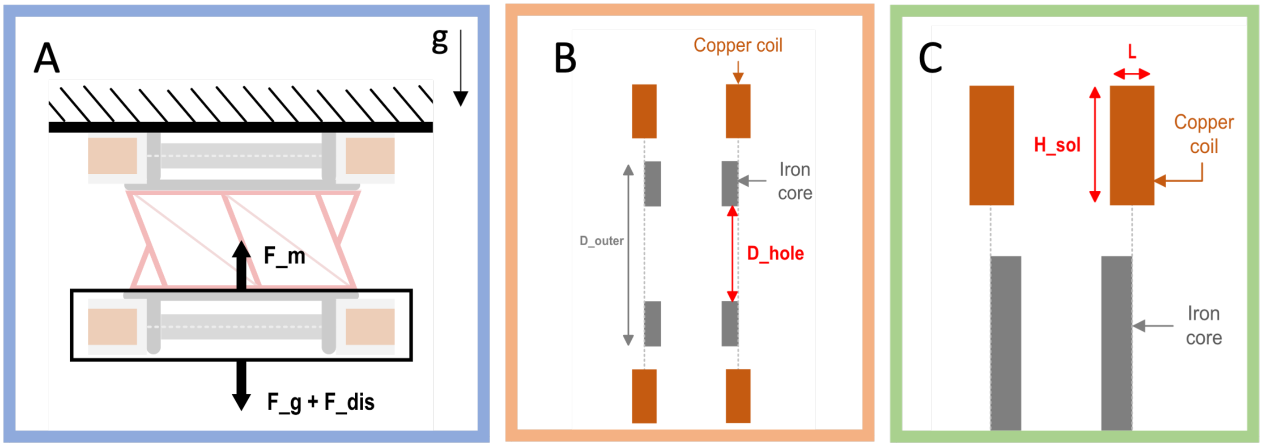

Figure 3.6: *(A) Force diagram of the 'hanging test'. F_m is the magnetic attracting force, F_g is the gravitational force of one of the coil assemblies, F_{dis} is the resisting force of the Kresling cylinder during deployment/contraction. (B) Setup for determination of effect of hollow core on relative performance. (C) Setup for determination of coil dimensions.*

Table 3.4: *Coil combinations for experimental validation of FEA model.*

N [-]	t [mm]	D hole [mm]	D outer	L [mm]	H sol [mm]	Fexp [N]	Fmodel [N]	Fexp/Fmodel
200	1	35	38.5	4.9	5.5	0.264	0.380	69.4%
200	2	20	38.5	4.9	5.5	0.292	0.401	72.9%
220	1	35	38.5	3.2	9.2	0.380	0.502	75.7%
220	2	20	38.5	3.2	9.2	0.403	0.531	75.9%
260	1	35	38.5	3.7	9.5	0.494	0.710	69.6%
260	2	20	38.5	3.7	9.5	0.527	0.780	67.5%
							Avg.:	**71.8%**
							SD:	**3.2%**

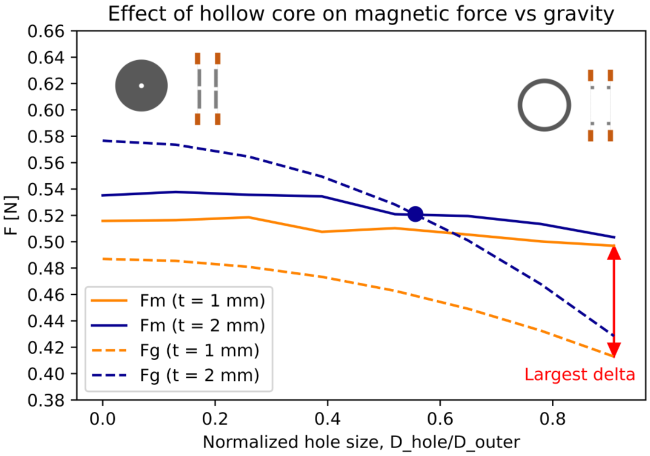

Figure 3.7: *Effect of hole in ferromagnetic core on magnetic attraction and gravitational force. F_m represents the theoretically generated magnetic force and F_z the gravitational force of the coil/core combination. t is the thickness of the cores.*

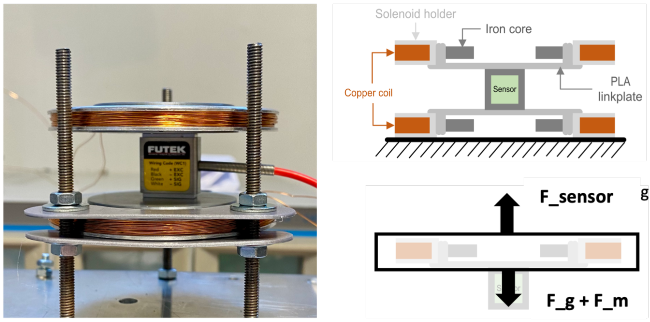

Figure 3.8: *Experimental setup for model validation. F_{sensor} represents the force as acquired through the load cell, F_g the gravitational force and F_m the generate magnetic force.*

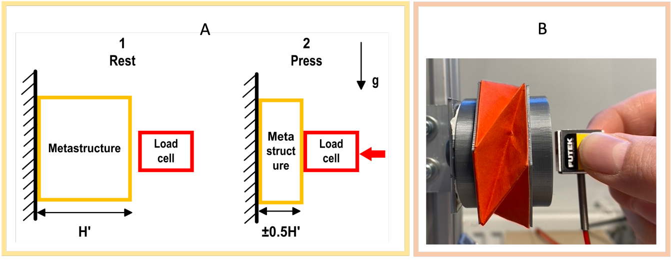

Figure 3.9: ***Setup to determine the resistance of the Kresling cylinder.****(A) Schematic representation of the experiment. The cylinder starts at rest (1), then the load cell is gently but consistently pushed against the free end of the cylinder to contract it until a displacement of about 0.5x the effective height H′ is reached (2). After this point is reached, the load cell is again retracted until it does not touch the cylinder anymore and the cylinder has sprung back to its resting length. This procedure is repeated 30 times to retrieve an average resisting value. (B) A photo of the setup.*

Table 3.5: *Details of experiment to determine Kresling cylinder resistance.*

Property	Value	Unit	Description
m	6	-	Number of polygon sides
a	30	mm	Length of sides of polygon
α	30	deg.	Configuration angle 1
β	30	deg.	Configuration angle 2
p	80	g/m^2	Paper type
n	30	-	Number of repetitions
F_{dis}	0.334	N	Average resistive force
σ	0.034	N	Standard deviation

Experiment: quantitatively validating the prototype

To quantitatively verify the prototype, an alternative prototype is evaluated (see Figure 3.12 D).

Table 3.6: *Description of the video frames from Figure 3.12 D.*

Instant T	Description of the frame
4.50 s	The prototype hangs free in rest.
6.50 s	The coils are excited and the bottom coil is lifted slowly by hand.
9.01 s	This frame indicates the last moment where the bottom coil makes contact with the experimenters finger
9.13 s	This frame shows the first instance where the bottom coil is lifted by the magnetic force at a distance of 11±1 mm.
9.50 s	In this frame the bottom coil is fully retracted by the magnetic force.

This prototype was built according to the coil dimensions L and H_{sol} 3.7 mm and 9.5 mm respectively, resulting in 260 turns. Similar cores as used in the final prototype are implemented. Following the analogy of the final prototype, this validation prototype should possess a performance in the hanging test $\eta = -0.49$, which means clear failure. Details of this prototype are found in Table 3.7. However, as magnetic attraction increases rapidly when closing the gap between two attracting items, presumably a tipping point exists where the magnetic attracting force does surpass the total of its gravity and the friction of the Kresling cylinder. To find this tipping point, the preliminary prototype is modelled in the FEA software and the attracting force is sampled at multiple distances between the two solenoids and is plotted in Figure 3.10. Then, the error found in Table 3.4 is included, and the results are compared to the total resisting force in the hanging test ($F_{g,total} + F_{dis}$). The total resistance to overcome resulted in being 0.974 N. Figure 3.10 shows the tipping point as the intersection between the blue magnetic force line and the dotted grey horizontal total resistance line.

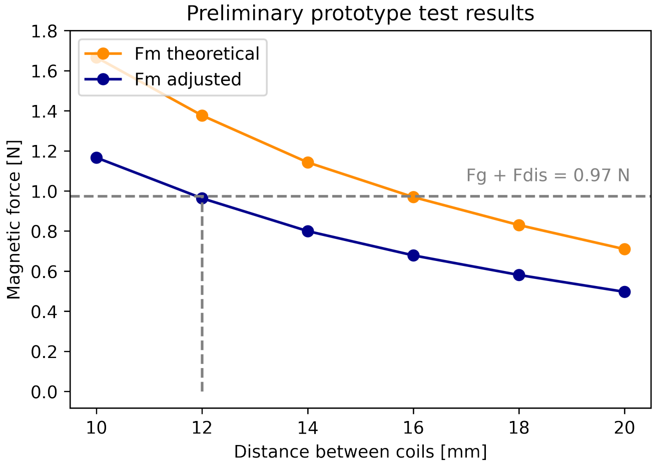

Figure 3.10: *Effect of distance between coils on magnetic attraction force from FEA model. With decreased distance between the coils, the magnetic force increases. To overcome the gravitational force of the preliminary prototype, the attracting force must be 0.97 N. This is the case with a distance between the coils of 12 mm. $F_m$theoretical represents the magnetic force as obtained from the FEA model and $F_m$adjusted indicates the magnetic attraction force after implementation of the correction between the FEA model and real life found in Table 3.4.*

The procedure is as follows. The coils of the prototype are excited and the bottom coil is lifted slowly by hand to see at what distance to the top coil the bottom coil is lifted by the magnetic force. As seen in Figure 3.12 D, the tipping point should be at a distance between the coils of 12 mm, at the intersection of the adjusted F_m and the total resisting force 0.974 N.

The video frames from Figure 3.12 D show the preliminary prototype in excited state, while the bottom coil is lifted until the tipping point is reached. An explanation per frame is given in Table 3.6.

Evidently from the frames, at instant T = 9.13 s the magnetic force overcomes the total resistance at a distance of 11±1 mm between top and bottom coil. This is in accordance with the expected tipping point found through the FEA analysis shown in the graph of Figure 3.12 D.

The configuration of the prototype

For the size of the copper coils, different values for the solenoid lenght (L) and solenoid height (H_{sol}) are considered to expose its performance in the hanging test. Figure 3.6 C shows the setup for the determination of the coil dimensions. Magnetic field strength in a coil is defined by the number of turns, the current in the wire and the length of the coil as seen in Equation 3.4 [168].

$$B = \frac{\mu_0 N I}{L} \tag{3.4}$$

$$\phi = A_{copper} / A_{total} = \frac{\pi (0.5 \cdot D_{wire})^2 N}{L \cdot H_{sol}} \tag{3.5}$$

To establish a connection between solenoid dimensions expressed as L and H_{sol} as defined in Figure 3.6 C and the generated magnetic

Table 3.7: *Details of preliminary prototype for quantitative validation.*

	Value	Unit	Description
L	3.7	mm	Length of solenoid
H_{sol}	9.5	mm	Height of copper coil
N	260	-	Number of turns
I	3.0	Ampère	Operational current
D_{wire}	0.3	mm	Diameter of wire
a	30	mm	Side length of hexagon
H′	20	mm	Effective height
$F_{g,coil}$	0.37	N	Gravity of copper coil
$F_{g,SH}$	0.12	N	Gravity of solenoid holder
$F_{g,MS}$	0.012	N	Gravity of Kresling cylinder
$F_{g,PLA}$	0.037	N	Gravity of PLA end cap
$F_{g,core}$	0.017	N	Gravity of ferromagnetic core
F_{dis}	0.42	N	Resistance of the Kresling cylinder
$F_{g,total}$	0.56	N	Total gravity for hanging test
$F_{m,theo}$	0.71	N	Theoretical magnetic attraction
$F_{m,adj}$	0.50	N	Magnetic attraction after adjustment
η	-0.49	-	Theoretical performance in hanging test

field, the average number of turns per cross-sectional area of coil is calculated based on physical measurements, considering the actual packing density of the coil prototypes. The packing density (ϕ) indicates the surface area of a cross section of the coils that is covered by copper wire turns as defined in Equation 3.5. A coil with dimensions L and H_{sol} measuring 3.1 mm and 9.5 mm respectively, with an inner radius of 23 mm, and a wire diameter of 0.3 mm was wound, resulting in 220 turns (N) with an average of $7.47E6\,\text{turns/m}^2$, equivalent to a packing density of ϕ = 52.8%. Simultaneously, the average density of the copper coils is employed to evaluate weight, yielding a value of $4771.3\,\text{kg/m}^3$. Subsequently, these determined values are used to calculate the number of turns and solenoid weight for various L and H_{sol} values. The overall mass of the solenoid system is then computed, taking into account the mass of the coils, solenoid holder, Kresling cylinder, PLA end cap, and core, which is then compared to the attracting force associated with the dimensions. Refer to Table 3.8 for a comprehensive breakdown of these components and Figure 3.13 for a schematic overview of the applied methodology. Figure 3.11 illustrates the performance of the solenoids in the hanging test in different combinations of L and H_{sol} based on modeling results.

From the data it is evident that the solenoid must comprise of a dimensional combination which lies right, or above, of the blue stair-step line as seen in the graph of Figure 3.11 for a design with positive η. A trend can be observed that with an increasing distance from this line the performance will only increase, and therefore a coil specification is chosen which lies well in this area. The final prototype and its details are found in Figure 3.12 A, B, and Table 3.8. A full actuation stroke to verify the hanging test is shown in Figure 3.12 C. From Figure 3.12 C, the contraction ratio can be verified. In fully extended and fully contracted position the distance that the Kresling cylinder and the thickness of the solenoid holder span are 30 mm and 10 mm in extended and contracted states respectively, which lead to a contraction ratio of 0.67.

3.4. Scaling the concept

In the preceding section, a model was validated for an electromagnetic Kresling cylinder cell to apply to a flexible arm suited to confined spaces. This section shall demonstrate the versatility of the modular approach by serving the example from the logistical sector as presented in subsection 3.1.2. The benefit of the modular approach is that it can be

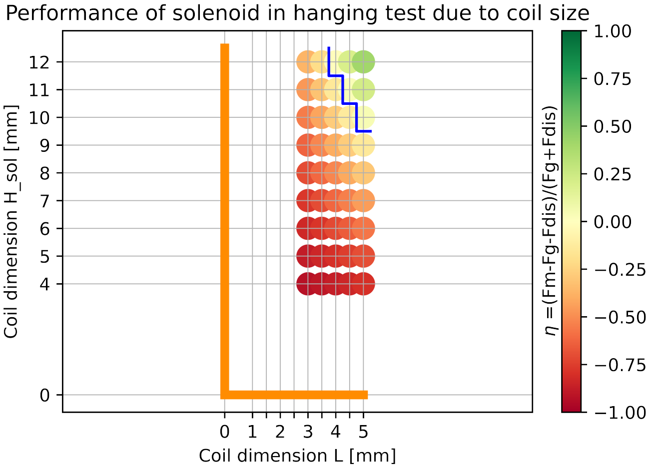

Figure 3.11: *Effect of coil dimensions L and H_{sol} on performance of solenoid based on the hanging test.*

Table 3.8: *Details of final prototype based on available material and requirements from predicted performance from modeling.*

	Value	Unit	Description
L	4.5	mm	Length of solenoid
H_{sol}	13.5	mm	Height of copper coil
N	450	-	Number of turns
I	3.0	Ampère	Operational current
D_{wire}	0.3	mm	Diameter of wire
a	30	mm	Side length of hexagon
H′	20	mm	Effective height
$F_{g,coil}$	0.53	N	Gravity of copper coil
$F_{g,SH}$	0.12	N	Gravity of solenoid holder
$F_{g,MS}$	0.012	N	Gravity of Kresling cylinder
$F_{g,PLA}$	0.037	N	Gravity of PLA end cap
$F_{g,core}$	0.017	N	Gravity of ferromagnetic core
F_{dis}	0.33	N	Resistance of the Kresling cylinder
$F_{g,total}$	0.72	N	Total gravity for hanging test
$F_{m,theo}$	2.72	N	Theoretical magnetic attraction
$F_{m,adj}$	1.95	N	Magnetic attraction after adjustment
η	0.73	-	Theoretical performance in hanging test

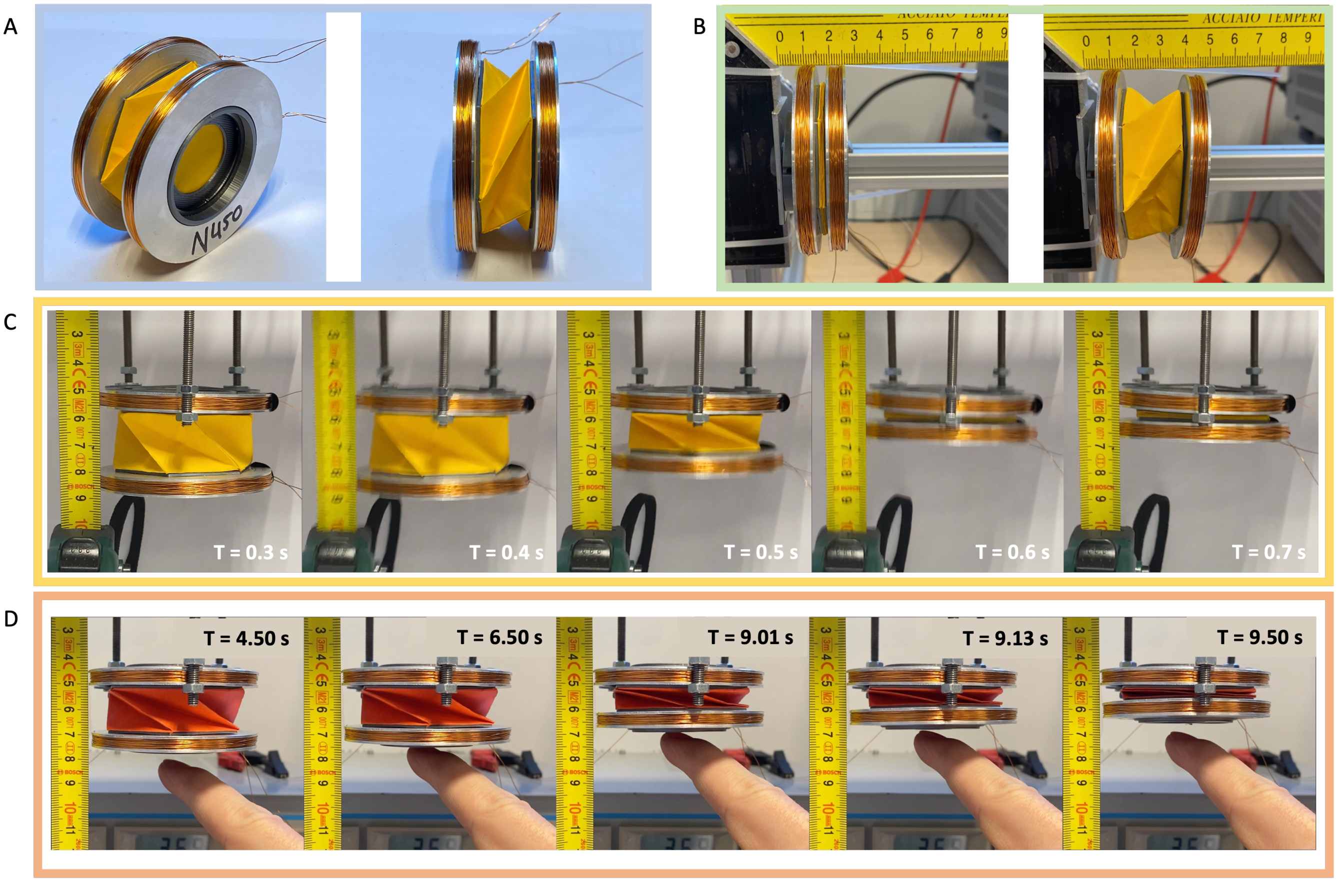

Figure 3.12: ***Electromagnetic Kresling cylinder prototypes and experimental validation.*** *(A) The final prototype. (B) Horizontal actuation, (left) full contraction, (right) full repulsion. (C) Hanging test contraction stroke due to magnetic force. (E) Validation of analogy using preliminary prototype in hanging test. According to Figure 3.10 the bottom coil should be lifted by the magnetic force when a distance of 12 mm is present between the two coils. The frames show that between 10 and 12 mm distance the bottom coil starts moving upward as a result of the magnetic force which is in accordance with the model. All details of the preliminary prototype are presented in Table 3.7.*

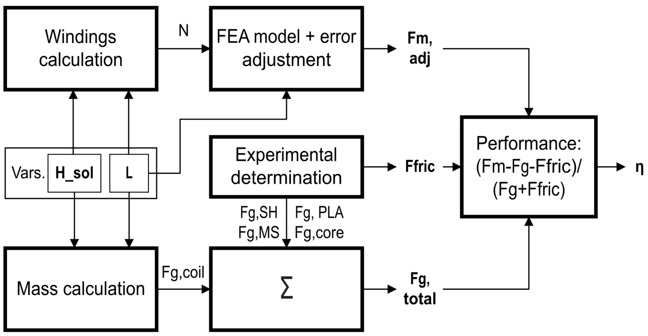

Figure 3.13: *Methodology for determining the performance (η) of different coil dimensions.*

extended into virtually any situation where automatic confined space access is desired.

The designed Kresling cylinder is not designed for hosting large lateral loads besides its own weight and therefore the lateral loads are assumed to lie outside the scope this section. From the modeling report it is evident that a flexible 3 segment arm is needed, following the concept as depicted in Figure 3.14 A. The results of the comprehensive modeling report in this thesis are used as requirements for the full scale arm. Three result graphs are depicted in Figure 3.14 B of unloading confined ULDs. For this case study, we present distinct arguments for each of the three arm segments to showcase the flexibility of the methodology, visually captured in Figure 3.15.

3.4.1. Scaling relations

When scaling the concept, not only the coils scale but also the core, solenoid holder and link disc become larger and thus heavier. For the scaling of these items, a simplified model is created as depicted in Figure 3.16. The inner radius of the coil (R_{min}) is defined to be the same as the radius of the inner scribed circle of the regular hexagonal base of the Kresling unit, which can be expressed in terms of R from Figure 3.4 as Equation 3.6. The outer radius of the core (R_{core}) should be close to

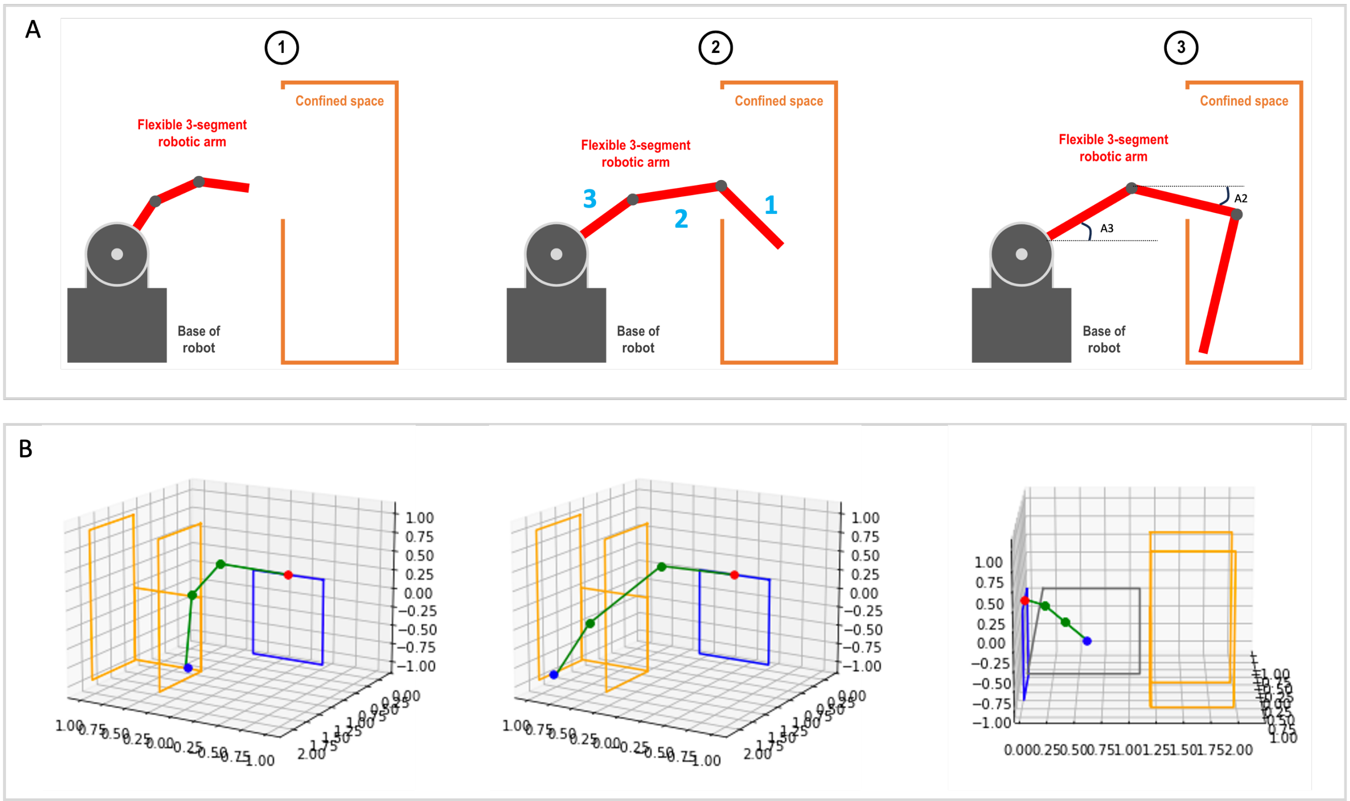

Figure 3.14: ***Visualisation of 3 segment arm concept and geometric requirements of flexible robotic arm for unloading of confined ULD.*** *(A) Concept of 3 segment flexible arm for confined space operation. The operating angles A2 and A3 are truly measured in 3D and thus show a mere projection in this figure. The blue numbers indicate segment 1, 2 and 3. (B) This graph shows the function of the individual segments. (orange) ULD, (blue) base of the robotic arm, (green) robotic arm, (red dot) origin of the robotic arm, (blue dot) pick-up position. The apex segment must presumably be able to operate at a complete vertical orientation, the second segment must only pull at a slight angle and the base segment must only push at a slight angle. (Left and middle) Challenging parcel pickup positions inside ULD. (Right) Drop off location on belt conveyor.*

but not similar to the inner radius of the coil as some space is needed for the solenoid holder and link disc and is therefore defined as 85% of R_{min}. The hole that the core features can be as large as practically possible for manufacturing, which is assumed as 90% of R_{core}. The cores are assumed to be made from average steel with a thickness per core of 1 mm for all segments as it was found that a thick core is not beneficial with respect to its F_m/F_g ratio. The PLA linkplate which connects the solenoid holder, the coil and the Kresling cylinder (see Figure 3.3) is modelled as a disc with the average radius of R and R_i and a thickness of 1, 2, and 3 mm for the respective segments as larger forces near the base are assumed to need more structural integrity. The solenoid holders are modelled as aluminium rings, similar in size as the coils but with thicknesses of 1, 2 and 3 mm per side for respective segments 1, 2 and 3, also assuming larger forces near the base. All scaling relations are summarized in Table 3.10. The mass of the Kresling cylinders could be assumed to be negligible since from the prototype it became evident that it only accounted for 1.7% of the total mass as calculated from Table 3.8. However, for completeness a small penalty for the mass of the Kresling cylinders is included as 0.25, 0.375, and 0.5 N for the units in segments 1, 2 and 3 respectively. The gravitational force of the prototype cylinder was 0.012 N. To ensure that the mass of the scaled cylinders are not under estimated, the mass of the cylinders in segment 1 are approximated to have a mass of about 20x the mass of the prototype's mass, which is assumed to be a safe guess knowing that in the scaled model the Kresling cylinder will likely not be made from paper but from a heavier material. Starting at the approximate mass of the Kresling cylinder in segment 1, the masses of the cylinders in segment 2 and 3 are approximated to be 1.5x and 2x the mass of that of segment 1. Similarly, the folding resistance of the Kresling cylinder is unknown due to this reason. In the prototype, the resistance of the Kresling cylinder yielded 0.33 N with respect to a total gravitational force of 0.72 N, showing that in the prototype the resistance of the Kresling cylinder was rather significant. However, in a full size arm the contribution of the cylinder to the resistance fades, since the gravitational pull to overcome per actuator cell grows significantly near the base of the robot since all must be added, while the resistance of the Kresling cylinder in a single actuator cell remains singular. For all segments a folding resistance of 0.33 N is included for completeness of the calculation, as taken from Table 3.8.

According to the geometric modelling conducted for this study, a 3-segment arm with the specifications found in Table 3.11 will suffice to reach all corners of the ULD.

$$R_i = \frac{\sqrt{3}}{2} R \tag{3.6}$$

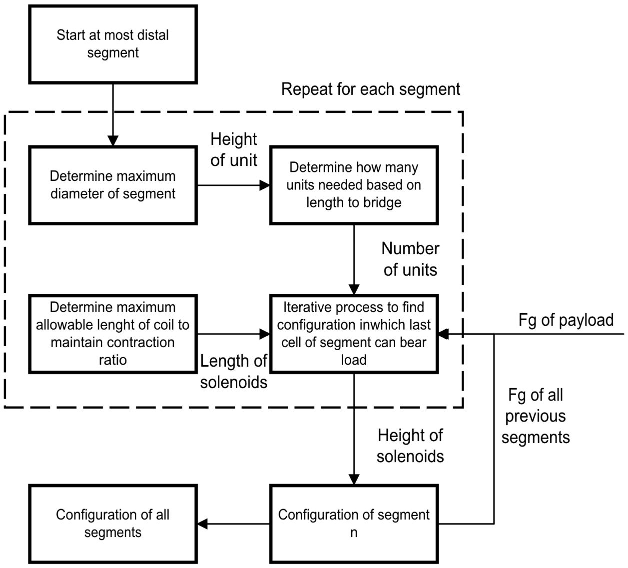

Figure 3.15: *Methodology of scaling of concept into large flexible arm.*

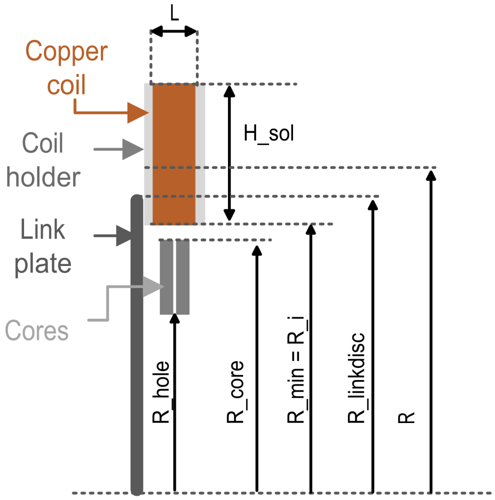

Figure 3.16: *Definitions for scaling of the concept.*

Table 3.9: *Specifications of 3 segment arm configuration based on model.*

Segment nr.	1		2		3	
	min	max	min	max	min	max
Lengths (m)	0.33	0.99	0.33	1.05	0.3	1.13
Contraction ratio	0.67		0.69		0.73	
Maximum angle (deg)		61.22		53.57		

Table 3.10: *Relations for scaling the concept*

	Relation	Remark
R_{min}	$R_i = \frac{1}{2}\sqrt{3}R$	Inner radius of the copper coil
R_{core}	$0.85R_{min}$	Outer radius of the core
R_{hole}	$0.9R_{core}$	Radius of the hole in the core
$R_{linkdisc}$	$\frac{1}{2}(R_{min}+R)$	Radius of the PLA linkdisc

3.4.2. Segment 1

Judging from the poses in Figure 3.14, segment 1 is the only segment that must have the capability to fully contract when in vertical orientation. To determine the maximum diameter of the units in segment 1, practical applications of the case are included. According to talks with employees at large parcel sorting centers, the minimum areal size of parcels allowed to be fed into a sorting machine is 100 mm x 150 mm. Picturing such a small parcel wedged into one of the corners of the ULD, segment 1 must be sufficiently slender to reach even these packages. Therefore, the size of the Kresling cylinder in segment 1 is based on this practical constraint, stating a maximum cylinder diameter of 100 mm, which sets the radii of the cylinder, core, core hole and link disc. Remembering from Equation 3.2 that the (effective) height of a Kresling unit (H') is directly linked to its radius (R), the effective height of the units of segment 1 shall amount to 0.033 m in extended position. As seen from Table 3.11, segment 1 must extend up to 0.99 m, which can be reached with s1 = 30 cells, s1 being the number of cells in segment 1, when the maximum Kresling cylinder diameter is set according to the minimum parcels size. A closeup of a CAD model of segment 1 is depicted in Figure 3.17.

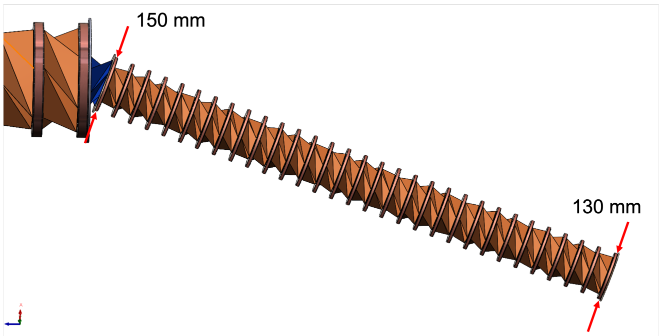

Figure 3.17: *Closeup of segment 1.*

$$\lambda_c = \frac{H'}{H' + (L + \delta)} \tag{3.7}$$

To maintain a contraction ratio (Equation 3.7) λ_c of 0.73 or higher, the coil should have a sufficiently short length. Considering the formula for the contraction ratio and the ratio goal as mentioned earlier, the constraint becomes $\lambda_c \leq 0.73$ where H' is the effective height, or actuation stroke of the Kresling cylinder, L the length of the coil and δ the thicknesses of the coil holders combined as displayed in Figure 3.3 A. To satisfy the constraint, $L + \delta$ should maximally be 11 mm. Assuming that the coil holders occupy 1 mm on each side of the coil and some extra space is desired to account for the folding of the Kresling cylinder, a coil length L of 6 mm is chosen for segment 1.

Naturally the size of the copper coils will add some diameter on top of the diameter of the Kresling cylinder, again influencing the

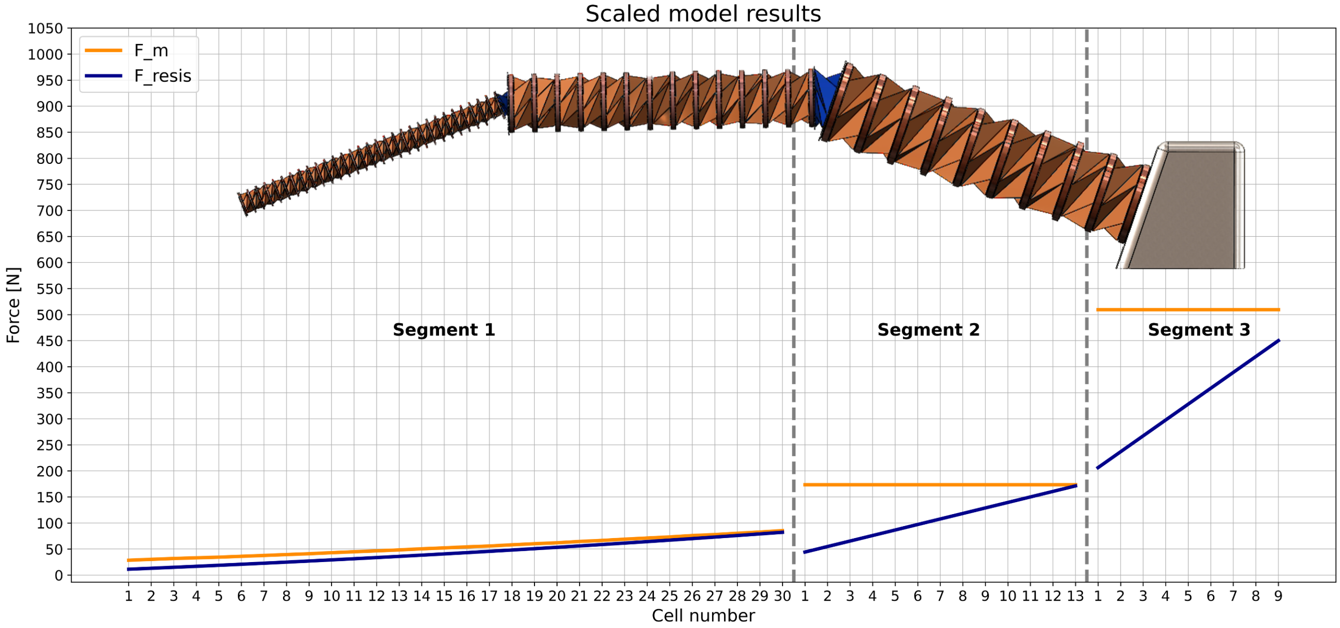

Figure 3.18: ***Visualisation of the inequalities as described in scaling section.*** *F_m represents the magnetic force generated by the coil pair at the designated cell in the segment. F_{resis} represents the force that the designated cell must overcome to actuate considering gravity, friction and the operating angle (see Figure 3.14 A). It is important to note that the magnetic force F_m lies above F_{resis} at every single cell, and that the operating angle heavily relaxes the need for high forces.*

Table 3.11: *Specifications of 3 segment arm configuration based on previous study. Segment 1 includes the tip of the arm and segment 3 includes the base. The definition of te operating angle is shown in Figure 3.14 A.*

Segment nr.	**1**		**2**		**3**	
	min	max	min	max	min	max
Lengths (m)	0.33	0.99	0.33	1.05	0.3	1.13
Operating angle (deg)	90		24.1		24.8	
Elongation ratio	2.00		2.18		2.77	

size of the segment. To ensure a relatively slender segment to pick all possible packages from the ULD, the diameter of the cylinder combined with the height of the solenoid cannot surpass 1.5x the smallest diameter of the smallest allowable package, which is 150 mm, since the diameter of the cylinder was already constrained to 1x the smallest dimension. This means that the height of the coils cannot surpass 25 mm, which fully defines the coils.

From the iterative process it was found that for segment 1 it was not possible to attain equilibrium in the force balance while maintaining a current of 3 A and the diameter of the wire similar to that of the prototype. To make this segment more weight efficient, a taper was introduced in the size of the coils towards the tip, with a constant Kresling cylinder size. The height of the coils was varied linearly between 15 mm and 25 mm and combined with a current of 8 A to achieve a positive force balance, or force inequality, in the entire segment as defined in Equation 3.8, where S1 = [1, 2, ... , s1-1, s1] is the set of all cells in the segment and s1 the number of cells in the segment. $F_{g1,i}$ denotes the gravitational force of actuator cell i, and $F_{m,j}$ the magnetic attraction force of actuator cell j. Due to the introduction of the taper in solenoid size, the force balance should be verified for all units in segment 1 since the mass of each unit due to different coil sizes in segment 1 is different.

$$F_{m,j} \geq F_{package} + F_{dis} + \sum_{i=1}^{j} F_{g1,i}, \ \forall j \in S1 \tag{3.8}$$

3.4.3. Segment 2

For segment 2, a different approach was used. From Figure 3.14 is was concluded that segment 2 its main purpose is to position itself above packages to pick. To ensure that the arm can position its tip above every single package that lies inside the perimeter of the ULD, the actuation stroke of a single unit must be smaller than the shortest side of the size of the smallest parcel, which again is 100 mm. A graphical explanation is shown in Figure 3.19.

Besides, it is desired to have Kresling cylinder cells that are as large as possible since this increases the lateral stiffness in the actuator which ensures that there is minimal 'sag' in horizontal position in the actuator itself. According to Equation 3.1 and 3.2, and the ratio for the effective height of 77.0% (H'), the largest R to ensure the right positioning resolution is 125 mm (when sampling R in increments of 25 mm), which is linked to an effective actuation stroke H' of 83 mm. In this size, the maximum length of segment 2 of 1.05 m is bridged with s2 = 13 cells, s2 being the number of cells in segment 2. According to the constraint $\lambda_c \geq 0.73$, $L + \delta$ should maximally be 28 mm. Considering the earlier mentioned thickness of the solenoid holders and some margin for the practical folding thickness the length of the coils is set to be 20 mm. Based on findings from the earlier study of which Figure 3.14 are based, the steepest angle at which segment 2 operates (A2) to pick all packages is 24.1 degrees. F_{g2} denotes the gravitational force of a single actuator cell which holds for all cells in segment 2. $F_{m,s2}$ denotes the magnetic force of the cell closest to segment 3, so number 13 counted from the tip. In contrast to segment 1, the force balance for segment 2 can only include the last unit of the segment. Since all units in the

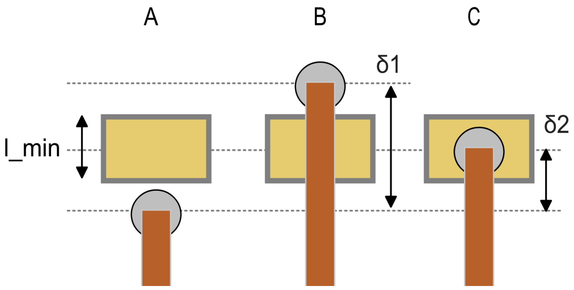

Figure 3.19: *The purpose of segment 2 is mainly to position segment 1 and a hypothetical gripper above the packages for pick-up. To ensure that segment 2 can position the tip above even the smallest packages, the minimum extension of the arm, or the actuation length of a single Kresling unit, must be smaller than the smallest dimension of the packages (l_{min}). (orange rectangle) arm, (grey circle) tip of arm, (yellow box) smallest package. (A) The tip of the arm is positioned just before a package. (B) If the minimum actuation length ($\delta 1$) is larger than l_{min}, the tip will overshoot. (C) If the minimum actuation length ($\delta 2$) is smaller than l_{min} the tip can be positioned above all packages.*

segment are identical, the force that all coils generate is identical and the force to overcome (mainly due to gravity) decreases with each unit towards the tip. Therefore it can be stated that if the force balance for the unit closest to the base shows equilibrium, all cells towards the tip are also in line with the force inequality. This balance is shown in Equation 3.9 and is satisfied with a solenoid height of 35 mm and a current of 3 A which is deemed possible due to the use in the prototype. A closeup of a CAD model of segment 2 is depicted in Figure 3.20.

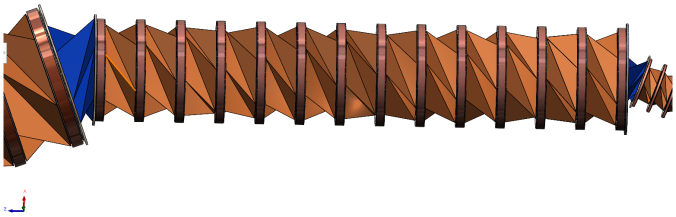

Figure 3.20: *Closeup of segment 2.*

$$F_{m,s2} \geq F_{dis} + sin(A2)(F_{package} + \sum_{i=1}^{s1} F_{g1,i} + s2 * F_{g2}) \tag{3.9}$$

3.4.4. Segment 3

For segment 3, again a different approach is used. From the results from the earlier study, it became clear that segment 3 will rarely reach into the ULD. However, it this does become necessary the arm should be prepared. Therefore, the maximum diameter of the Kresling cylinder in segment 3 is set as 0.5x width of the ULD opening, which is measured as 780 mm, to maintain ample design freedom to implement stiffness devices. It is assumed that this factor leaves enough space to maneuver in the ULD opening, even after the addition of the coils, which will increase the diameter of the segment on top of the diameter of the Kresling cylinder. This leads to a cylinder with an effective actuation stroke of 127 mm. From Table 3.11, segment 3 must extend up to 1.13 m, which can be reached with s3 = 9 units, s3 being the number of cells in segment 3. Obeying the contraction ratio of 0.73, the thickness of the solenoid holders and accounting for some practical margin the length of the solenoids is set to be 30 mm. From the findings depicted in Figure 3.14, segment 3 must mainly push in operation at an angle of A3 = 24.8 degrees. However, according to Equation 3.4, the magnetic field strength can alternate between direction due to a reverse of the direction of the current, while maintaining the magnitude of the field. Therefore, nothing changes in the methodology for segment 3 besides the plain fact that the movement differs in direction. Similarly to segment 2, only the force balance of the cell closest to the base should be considered. $Fg3$ denotes the gravitational force of a single cell in segment 3 and $Fm, s3$ the magnetic force the last cell of segment 3 generates. The balance is presented as Equation 3.10 and holds when a solenoid height of 35 mm is applied. A closeup of a CAD model of segment 3 is depicted in Figure 3.21.

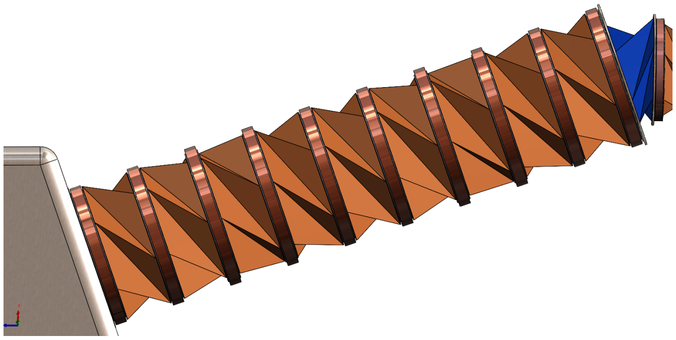

Figure 3.21: *Closeup of segment 3.*

$$F_{m,s3} \geq F_{dis} + sin(A3)(F_{package} + \sum_{i=1}^{s1} F_{g1,i} + s2 * F_{g2} + s3 * F_{g3}) \tag{3.10}$$

Figure 3.18 shows the inequalities graphically with a plot of the gravity profile of the arm to observed the effect of the operating angle on the required magnetic force. In segment 1 the gravity and resistance for actuation are relatively close due to the complete vertical orientation of the segment. For segment 2 and 3 the difference is more substantial since they work under relatively relaxed angles which makes use of the assumption that lateral loads are accounted for using another concept.

3.5. Discussion

This study has resulted in the design of a highly elongating flexible robotic arm for deployment in confined spaces, based on a novel electromagnetic Kresling cylinder actuator. The actuator has been modeled using FEA software and is experimentally tested to validate a proof-of-concept. The expansion of the single actuator cell to a full-scale arm has demonstrated the versatile design methodology which the actuator cell enables.

3.5.1. Performance

Considering requirement 1 from subsection 3.3.1, the final contraction ratio as measured from the final prototype was 0.67, which approaches but unfortunately does not surpass the goal of 0.73. In the contracted position a substantial gap between the solenoids is visible (Figure 3.12 C) due to the thickness of the paper Kresling cylinder, a practical implication as also noted by Liu et al. [169] as zero thickness in the folded state was assumed. If a practical solution is found to hide this thickness and a similar actuation stroke is assumed, the distances the Kresling cylinder and the thickness of the solenoid holder span would become 26 mm and 6 mm in extended and contracted state respectively, leading to a contraction ratio of 0.77. Also, the solenoids and solenoid holders could be made thinner in combination with a decreased length of the Kresling cylinder in folded position to fulfill the requirement of the contraction ratio. A last option would be to use a Kresling cylinder with a slightly larger value for a in Figure 3.4 to increase the actuation stroke of the actuator (H'), while using paper with the same thickness. This would effectively increase H' while the required space to store the cylinder in the folded state stays fixed as the number of folds is not affected, consecutively increasing the contraction ratio according to Equation 3.7.

Requirement 2 from subsection 3.3.1 has however fully been met. The final prototype has confirmed the proof-of-concept by completing an actuation stroke in vertical orientation. This validated the magnetic force generated by the prototype model.

Requirement 3 from subsection 3.3.1 has also been met in this study. Figure 3.12 B shows negligible deflection in horizontal orientation as a result of its own weight in fully extended position, proving stiffness in lateral direction.

3.5.2. Design limitations

This study has utilized a prototype as proof-of-concept for the novel electromagnetic actuator and is substantiated by a validated model. Since this prototype is made of paper, it is unclear how the actuator behaves using more durable materials for implementation in the industrial sector, as Hu et al. [154] already showcased hysteresis in Kresling cylinders made from polypropylene. In the logistical sector or in automatic manufacturing of automobiles, polypropylene might not be sufficiently strong. Yet undefined materials might present other characteristics in the Kresling configuration.

The full-scale arm designed in this study is completely adapted to the specific application as described by the case study. This includes that segments 2 and 3 are designed to only lift at the maximum angle they will encounter in the unloading of the ULD which, according to the model, can be achieved with a current in the wires (0.3 mm diameter) of 3A, which is identical as used in the tested prototype. Segment 1 however, is more constrained in its dimensions and is therefore required to run 8A through the same wires. A current of 8A in copper wires of 0.3 mm in diameter has not been tested and it is therefore unclear what implications this would bring, which limits the design.

The coils in this study are all hand-wound, resulting in an imperfect packing density and therefore limiting the generated force [167]. With a higher packing density, more turns are packed inside the same volume, opening the possibility to have more turns in the same volume or to make the solenoids thinner while maintaining the same number of turns.

Control remains the main challenge in flexible and soft robotics, since a general control architecture has not yet been defined [170]. Ultimately for autonomous deployment of flexible robotic arms, more research must be conducted before implementation can take place. Additionally, sensor implementation remains challenging, and therefore limits the applicability of flexible robots in the industrial sector.

3.5.3. Experiment limitations

The proof-of-concept of the final design was conducted using a qualitative approach. Despite the qualitative effort to validate the model based on a preliminary prototype, validation of the final prototype is limited, since it remains challenging to measure the pure magnetic force generated by a set of solenoids at precise distances with an integrated Kresling cylinder.

The experiment in Table 3.3.7 to define the resistance of the Kresling cylinder presumably approaches the resistance of the Kresling cylinder in the initial phase of collapse of the cylinder, but is limited in accuracy. More reliable results could be obtained with a linear stage, mapping force to distance to gain a better understanding of the specific resistance profile during collapse.

3.5.4. Design recommendations

The electromagnetic actuation of the Kresling cylinder has proven to be a forceful and fast mode of actuation. Upon excitation of the coils the cylinder collapses in a mere 0.4 seconds. It must be noted that excitation of the coils for testing was always executed when the coils were at room temperature. It was observed during unofficial tests, when the coils were still warm from a previous test, actuation happened less quick. Resistance in a wire changes upon shifts in temperature, which could cause the variability in performance. For implementation of the actuator in the industrial setting, a recommendation for future research is to find solutions to maintain a constant temperature in the coils for steady continuous performance over longer periods of time.

Under the concept of creating a 2 degrees of freedom elbow using opposing motions of pushing and pulling, and the existing knowledge that the Kresling cylinder has bending freedom [23], the magnetic Kresling actuator could potentially create the elbows needed in the full scale model. Figure 3.22 shows an initial idea to create a stand alone Kresling bending actuator. An impression of what this elbow would look like in the full arm is depicted in Figure 3.24. For future research it is recommended to explore ways to increase the maximum angle to increase the versatility of the arm even further.

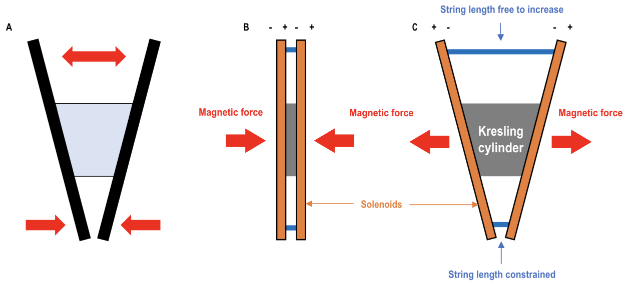

Figure 3.22: *Creating an elbow out of the Kresling cylinder idea. (A) Base concept of creating an elbow by an interplay of asymmetric pushing and pulling. (B) Electromagnetic actuator to create an elbow in contracted position. (C) Electromagnetic actuator to create elbow in bent position. The actuator coils (orange) create a repelling force (red arrows), while a string (blue) constrains one side of the actuator in extending while the other end is free to move.*

In this study, mainly coils consisting of coated copper wire with a diameter of 0.3 mm were used at a current of 3A. According to the magnetic field equation in a coil, Equation 3.4, the magnetic field increases with an increased current. From testing it was observed that the coils heated up significantly, affecting the magnetic forces the coils generated. For future research it is recommended to explore ways to increase the generated magnetic force with similar coil dimensions. This could be done by increasing the current in the coils, while avoiding overheating and maintaining performance. This would create opportunities to lift more weight, have a slimmer arm or increase the potential working speed due to a decreased mass inertia. It is expected that with an

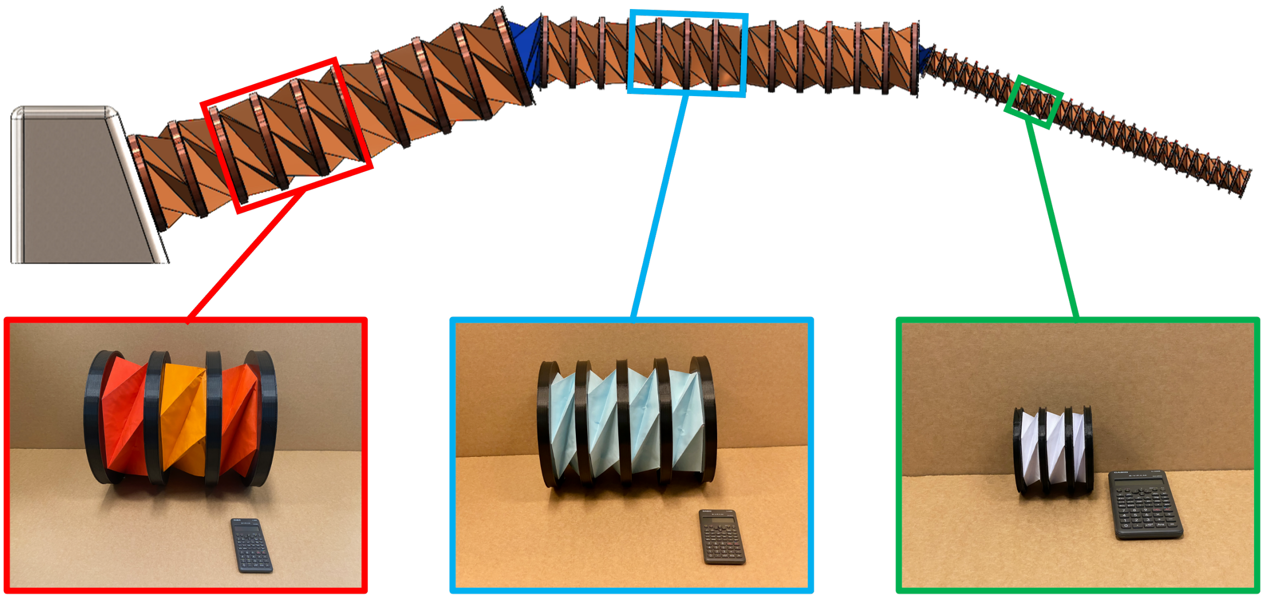

Figure 3.23: *Full arm assembly in fully extended position with 1:1 scale partial mock-ups of segments 1, 2 and 3. The calculator has a length of 15.5 cm for size reference. In the mock-ups the copper coils, solenoid holders, link plates and ferromagnetic cores are printed in one piece using a Builder Extreme 1500 Pro 3D printer using PLA filament.*

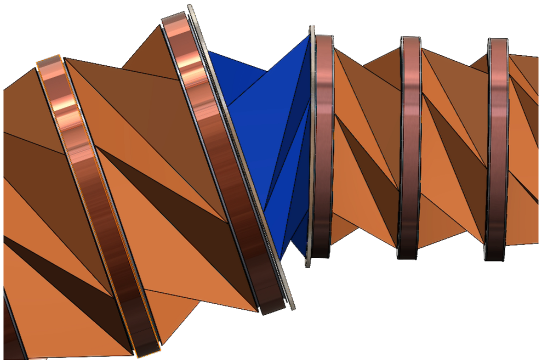

Figure 3.24: *Elbow concept in full-scale model*

innovative air or water cooled system the coils can be kept at acceptable temperatures while operating at a higher nominal current, since the utilization of aluminium solenoid holders already improved heat management with respect to solenoid holders made from 3D printed plastics as shown in section C.1. Another graspable way to increase the generated force with similar coil dimensions is by perfecting the packing density of the wires. In this study a packing density of $\phi = 52.8\%$ was achieved. Optimizing the packing density of circles with a fixed radius in a rectangular area has been studied before and packing densities of up to $\phi = 85\%$ are noted [171]. According to Equation 3.4 and Equation 3.5, this means that theoretically with a near optimal packing density and identical coil dimensions, the coils in this study would generate a magnetic field, and therefore force, which is 60% higher, which could be used for lifting more payload which is highly desired in the industrial sector. Also, coils with similar dimensions but higher force capabilities can be placed further apart in stead of lifting heavier loads. In size constrained situations, multiple Kresling cylinders can be stacked in between a set of two coils. This would reduce the required number of coils in a segment and therefore lowering the arm's mass. Additionally, opposite Kresling chirality can be used to cancel the net rotation angle of the segment upon deployment/collapse [153].

3.6. Concluding remarks

In this study an electromagnetic Kresling cylinder was modeled, designed and evaluated and scaled into a full size robotic arm for deployment in confined spaces. The prototype contained a specifically designed Kresling cylinder utilizing a low resistance configuration in axial direction. The actuator has reached a contraction ratio of 0.67, which is just short of the 0.73 from the requirements. However, a discussion has explained the graspable measures that can be taken to reach the requirement. Solenoids and ferromagnetic cores were designed using a validated FEA model which ensured that the Kresling cylinder actuator could lift its own weight while presenting minimal deflection in horizontal orientation. Lastly, after validation of the prototype, the methodology was extended and a full size 3-segment arm was designed to outperform a traditional articulated robotic arm in confined space reachability as shown in Figure 3.23. The used methodology can be used to design a flexible robotic arm to serve virtually every confined space scenario due to its modular nature. This design fills an important gap in research as it is the first design and prototype of an electromagnetically actuated Kresling cylinder with fully integrated actuation, opening the possibility to scale the concept into industrial settings.

Although the presented methodology for scaling the concept was applied to the logistical sector in this study, it can be extended into many sectors. Owing to its inherently adjustable force capabilities, prospective applications may be discerned in the realm of manufacturing. Additionally, given its notable contraction ratio, the exploration of its utility in confined spaces for tasks such as inspection, cleaning, or maintenance emerges as an appealing prospect.

Under the assumption that the arm will only operate under certain maximum angles, the design shows limitations in applications where all angles must be included in its working envelope. This would require much higher forces from the solenoids, posing uncertainties in terms of viability due to maximum currents possible in the wires, an aspect assumed out of the scope of this study. Further more, lateral load carrying was also mainly excluded from this study's scope, which might require much extra space around the arm, again limiting its applicability in certain confined spaces. This limitation leads to a proposition for further research: the design of a highly contractible variable stiffness device for lateral loads. Another proposition for future research is to expand the analogy of an electromagnetic Kresling cylinder bending actuator into a stand alone system, as opposed to the non-stand alone system of [23].

In conclusion, the developed electromagnetic Kresling cylinder presents a promising avenue for the creation of highly contractible, versatile robotic arms capable of operating in confined spaces, opening new possibilities for a wide range of applications.

Materials and methods

Construction of the prototype

The Kresling cylinders constructed in this paper are made from 80 g/m^2 paper (HEMA) and are supported by glue (Pattex). For folding the Kresling cylinders, the pattern shown in Figure C.20 is used. The PLA end caps are printed using a Prusa Mk3s 3D printer and were connected to the Kresling cylinder using strong glue (pattex). The cores were made from steel (not stainless) and were laser cut using a plate metal laser cutter. The solenoid holders are constructed using aluminium on a lathe. The coils are mainly hand-wound with D0.3 mm coated copper wire (Velleman). The coils were connected to two separate power supplies to ensure enough voltage for excitation with 3A (see Figure 3.25). The delivered voltage and power varied per set of coils since the current of 3A must be maintained for the required magnetic field strength and electric resistance in the coils is dependant on total wire length. It is important to note that to connect the power supply to the wires of the coils with, for instance, electrical clamps, the connection points must be prepared to expose the bare copper in the coil wires from the insulating layer. This can be done by filing the ends of the copper wires with an ordinary iron file.

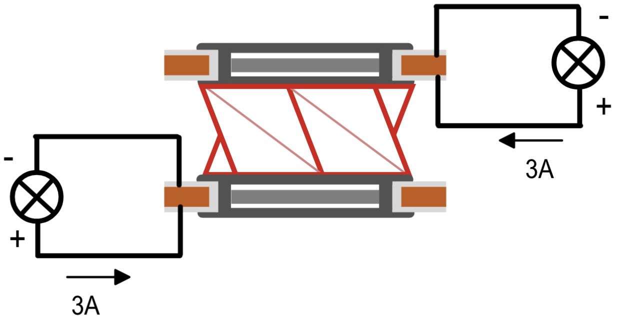

Figure 3.25: *Electric circuit to excite the prototypes. The power sources could be manually switched to switch the flow of current to create an attracting or repelling force between the coil sets.*

Conducting the experiments

For excitement of the coils two double VoltCraft PS-2403D laboratory power supplies were used, each capable of delivering up to 40 V and 3 A and for the force measurements a Futek load cell was utilized which was read using LabView. To ensure that 3 A was running through the coils, the double power supplies were placed in series to provide enough voltage. Data processing of the load cell was conducted using Python. Simulating the coils using FEA was conducted using COMSOL Multyphysics.

Bibliography

[1] M. Teulieres, J. Tilley, L. Bolz, P. Manuel Ludwig-Dehm, and S. Wägner, "Industrial robotics: Insights into the sector's future growth dynamics", McKinsey, Jul. 2019.

[2] H. A. F. Almurib, H. F. Al-Qrimli, and N. Kumar, "A review of application industrial robotic design", in *2011 Ninth International Conference on ICT and Knowledge Engineering*, Bangkok, Thailand: IEEE, Jan. 2012, pp. 105–112, ISBN: 978-1-4577-2162-5 978-1-4577-2161-8. DOI: 10.1109/ICTKE.2012.6152387.

[3] F. Ajewole, A. Kelkar, D. Moore, E. Shao, and M. Thirtha, "Unlocking the industrial potential of robotics and automation", McKinsey & Company, Jan. 2023.

[4] W. Kraus, C. Müller, M. Bill, and S. Bieller, "World robotics 2022", World Robotics 2022, Frankfurt Main, 2022.

[5] B. Curto, V. Moreno, and F. J. Blanco, "A general method for c-space evaluation and its application to articulated robots", *IEEE Transactions on Robotics and Automation*, vol. 18, no. 1, pp. 24–31, Feb. 2002, ISSN: 1042296X. DOI: 10.1109/70.988971.

[6] M. F. Aly and A. T. Abbas, "Simulation of obstacles' effect on industrial robots' working space using genetic algorithm", *Journal of King Saud University - Engineering Sciences*, vol. 26, no. 2, pp. 132–143, Jul. 2014, ISSN: 10183639. DOI: 10.1016/j.jksues.2012.12.005.

[7] P. Schober, C. Boer, and L. A. Schwarte, "Correlation coefficients: Appropriate use and interpretation", *Anesthesia & Analgesia*, vol. 126, no. 5, pp. 1763–1768, May 2018, ISSN: 0003-2999. DOI: 10.1213/ANE.0000000000002864.

[8] S. Hehir and R. Pikaar, "Safe design of a parcel sorting system", 2015.

[9] "Confined spaces - overview | occupational safety and health administration". (), [Online]. Available: https://www.osha.gov/confined-spaces (visited on 05/09/2023).

[10] M. P. Wilson, H. N. Madison, and S. B. Healy, "Confined space emergency response: Assessing employer and fire department practices", *Journal of Occupational and Environmental Hygiene*, vol. 9, no. 2, pp. 120–128, Feb. 2012, ISSN: 1545-9624, 1545-9632. DOI: 10.1080/15459624.2011.646644.

[11] L. Botti, E. Ferrari, and C. Mora, "Automated entry technologies for confined space work activities: A survey", *Journal of Occupational and Environmental Hygiene*, vol. 14, no. 4, pp. 271–284, Apr. 3, 2017, ISSN: 1545-9624, 1545-9632. DOI: 10.1080/15459624.2016.1250003.

[12] N. Turner, B. Goodwine, and M. Sen, "A review of origami applications in mechanical engineering", *Proceedings of the Institution of Mechanical Engineers, Part C: Journal of Mechanical Engineering Science*, vol. 230, no. 14, pp. 2345–2362, Aug. 2016, ISSN: 0954-4062, 2041-2983. DOI: 10.1177/0954406215597713.

[13] J. J. Park, P. Won, and S. H. Ko, "A review on hierarchical origami and kirigami structure for engineering applications", *International Journal of Precision Engineering and Manufacturing-Green Technology*, vol. 6, no. 1, pp. 147–161, Jan. 2019, ISSN: 2288-6206, 2198-0810. DOI: 10.1007/s40684-019-00027-2.

[14] S. D. Guest, "Deployable structures: Concepts and analysis", Ph.D. dissertation, University of Cambridge, May 1994.

[15] S. Kolachalama and S. Lakshmanan, "Continuum robots for manipulation applications: A survey", *Journal of Robotics*, vol. 2020, pp. 1–19, Jul. 18, 2020, ISSN: 1687-9600, 1687-9619. DOI: 10.1155/2020/4187048.

[16] L. Puig, A. Barton, and N. Rando, "A review on large deployable structures for astrophysics missions", *Acta Astronautica*, vol. 67, no. 1, pp. 12–26, Jul. 2010, ISSN: 00945765. DOI: 10.1016/j.actaastro.2010.02.021.

[17] V. Arakelian, "Gravity compensation in robotics", *Advanced Robotics*, vol. 30, no. 2, pp. 79–96, Jan. 17, 2016, ISSN: 0169-1864, 1568-5535. DOI: 10.1080/01691864.2015.1090334.

[18] S. Seo, W. Park, D. Lee, and J. Bae, "Origami-structured actuating modules for upper limb support", *IEEE Robotics and Automation Letters*, vol. 6, no. 3, pp. 5239–5246, Jul. 2021, ISSN: 2377-3766, 2377-3774. DOI: 10.1109/LRA.2021.3072810.

[19] S. Yoo, J. Kim, J. Park, and Y. Cha, "Design and analysis of origami-based multimodal actuator capable of linear and bending motion", *IEEE Robotics and Automation Letters*, vol. 9, no. 1, pp. 151–158, Nov. 2023, ISSN: 2377-3766, 2377-3774. DOI: 10.1109/LRA.2023.3331952.

[20] Q. Zhang, H. Fang, and J. Xu, "Tunable dynamics in yoshimura origami by harnessing pneumatic pressure", *Journal of Sound and Vibration*, vol. 544, p. 117 407, Feb. 2023, ISSN: 0022460X. DOI: 10.1016/j.jsv.2022.117407.

[21] Y. Dang, J. Chen, and J. Han, "Preliminary design and performance test of an origami actuator inspired by yoshimura pattern", in *2021 27th International Conference on Mechatronics and Machine Vision in Practice (M2VIP)*, Shanghai, China: IEEE, Nov. 26, 2021, pp. 435–439, ISBN: 978-1-66543-153-8. DOI: 10.1109/M2VIP49856.2021.9664993.

[22] H. Li, Y. Xu, C. Zhang, and H. Yang, "Kinematic modeling and control of a novel pneumatic soft robotic arm", *Chinese Journal of Aeronautics*, vol. 35, no. 7, pp. 310–319, Jul. 2022, ISSN: 10009361. DOI: 10.1016/j.cja.2021.07.015.

[23] S. Wu, Q. Ze, J. Dai, N. Udipi, G. H. Paulino, and R. Zhao, "Stretchable origami robotic arm with omnidirectional bending and twisting", *Proceedings of the National Academy of Sciences*, vol. 118, no. 36, e2110023118, Sep. 7, 2021, ISSN: 0027-8424, 1091-6490. DOI: 10.1073/pnas.2110023118.

[24] T. Jin *et al.*, "Origami-inspired soft actuators for stimulus perception and crawling robot applications", *IEEE Transactions on Robotics*, vol. 38, no. 2, pp. 748–764, Apr. 2022, ISSN: 1552-3098, 1941-0468. DOI: 10.1109/TRO.2021.3096644.

[25] K. Lee, P.-G. Jung, and Y. Cha, "Origami pump based on planetary gear system for pneumatic pressure", *IEEE/ASME Transactions on Mechatronics*, vol. 28, no. 3, pp. 1436–1445, Jun. 2023, ISSN: 1083-4435, 1941-014X. DOI: `10.1109/TMECH.2022.3223699`.

[26] Z. Zhang, W. Fan, G. Chen, J. Luo, Q. Lu, and H. Wang, "A 3d printable origami vacuum pneumatic artificial muscle with fast and powerful motion", in *2021 IEEE 4th International Conference on Soft Robotics (RoboSoft)*, New Haven, CT, USA: IEEE, Apr. 12, 2021, pp. 551–554, ISBN: 978-1-72817-713-7. DOI: `10.1109/RoboSoft51838.2021.9479194`.

[27] S. Liu, Q.-S. Yang, R. Tao, and X. Liu, "A highly-compressible, torsion-contraction coupling and self-transforming cylindrical bi-material metastructure", *Smart Materials and Structures*, vol. 29, no. 2, p. 025 016, Feb. 1, 2020, ISSN: 0964-1726, 1361-665X. DOI: `10.1088/1361-665X/ab6078`.

[28] X. Zou *et al.*, "Paper-based robotics with stackable pneumatic actuators", *Soft Robotics*, vol. 9, no. 3, pp. 542–551, Jun. 1, 2022, ISSN: 2169-5172, 2169-5180. DOI: `10.1089/soro.2021.0002`.

[29] B. Treml, A. Gillman, P. Buskohl, and R. Vaia, "Origami mechanologic", *Proceedings of the National Academy of Sciences*, vol. 115, no. 27, pp. 6916–6921, Jul. 3, 2018, ISSN: 0027-8424, 1091-6490. DOI: `10.1073/pnas.1805122115`.

[30] L. M. Fonseca, G. V. Rodrigues, M. A. Savi, and A. Paiva, "Nonlinear dynamics of an origami wheel with shape memory alloy actuators", *Chaos, Solitons & Fractals*, vol. 122, pp. 245–261, May 2019, ISSN: 09600779. DOI: `10.1016/j.chaos.2019.03.033`.

[31] L. J. Wood, J. Rendon, R. J. Malak, and D. Hartl, "An origami-inspired, SMA actuated lifting structure", in *Volume 5B: 40th Mechanisms and Robotics Conference*, Charlotte, North Carolina, USA: American Society of Mechanical Engineers, Aug. 21, 2016, V05BT07A024, ISBN: 978-0-7918-5016-9. DOI: `10.1115/DETC2016-60261`.

[32] K. Zhang, C. Qiu, and J. S. Dai, "An extensible continuum robot with integrated origami parallel modules", *Journal of Mechanisms and Robotics*, vol. 8, no. 3, p. 031 010, Jun. 1, 2016, ISSN: 1942-4302, 1942-4310. DOI: `10.1115/1.4031808`.

[33] B. Cowan and P. R. Von Lockette, "Fabrication, characterization, and heuristic trade space exploration of magnetically actuated miura-ori origami structures", *Smart Materials and Structures*, vol. 26, no. 4, p. 045 015, Apr. 1, 2017, ISSN: 0964-1726, 1361-665X. DOI: `10.1088/1361-665X/aa5a9e`.

[34] Y. Liu *et al.*, "Shape memory behavior and recovery force of 4d printed laminated miura-origami structures subjected to compressive loading", *Composites Part B: Engineering*, vol. 153, pp. 233–242, Nov. 2018, ISSN: 13598368. DOI: `10.1016/j.compositesb.2018.07.053`.

[35] H. Wu, H. Fang, L. Chen, and J. Xu, "Transient dynamics of a miura-origami tube during free deployment", *Physical Review Applied*, vol. 14, no. 3, p. 034 068, Sep. 29, 2020, ISSN: 2331-7019. DOI: `10.1103/PhysRevApplied.14.034068`.

[36] J. He, G. Wen, J. Liu, L. Xue, and Y. M. Xie, "A modular continuous robot constructed by miura-derived origami tubes", *International Journal of Mechanical Sciences*, p. 108 690, Aug. 2023, ISSN: 00207403. DOI: `10.1016/j.ijmecsci.2023.108690`.

[37] X. Zhang, M. Yu, W. Yang, Y. Yu, Y. Ding, and Z. Jiao, "A flexible mechanical arm based on miura-ori", in *Intelligent Robotics and Applications*, C. S. Chan *et al.*, Eds., Series Title: Lecture Notes in Computer Science, vol. 12595, Cham: Springer International Publishing, 2020, pp. 538–544, ISBN: 978-3-030-66644-6 978-3-030-66645-3. DOI: `10.1007/978-3-030-66645-3_45`.

[38] L. M. Fonseca, G. Rodrigues, and M. A. Savi, "An overview of the mechanical description of origami-inspired systems and structures", *International Journal of Mechanical Sciences*, vol. 223, p. 107 316, Jun. 2022, ISSN: 00207403. DOI: `10.1016/j.ijmecsci.2022.107316`.

[39] X. Zhang, R. Nie, Y. Chen, and B. He, "Deployable structures: Structural design and static/dynamic analysis", *Journal of Elasticity*, vol. 146, no. 2, pp. 199–235, Nov. 2021, ISSN: 0374-3535, 1573-2681. DOI: `10.1007/s10659-021-09860-6`.

[40] S. A. Zirbel, M. E. Wilson, S. P. Magleby, and L. L. Howell, "An origami-inspired self-deployable array", in *Volume 1: Development and Characterization of Multifunctional Materials; Modeling, Simulation and Control of Adaptive Systems; Integrated System Design and Implementation*, Snowbird, Utah, USA: American Society of Mechanical Engineers, Sep. 16, 2013, V001T01A026, ISBN: 978-0-7918-5603-1. DOI: `10.1115/SMASIS2013-3296`.

[41] Y. Chen, J. Yan, and J. Feng, "Geometric and kinematic analyses and novel characteristics of origami-inspired structures", *Symmetry*, vol. 11, no. 9, p. 1101, Sep. 2, 2019, ISSN: 2073-8994. DOI: `10.3390/sym11091101`.

[42] J. Cai, X. Deng, J. Feng, and Y. Zhou, "Geometric design and mechanical behavior of a deployable cylinder with miura origami", *Smart Materials and Structures*, vol. 24, no. 12, p. 125 031, Dec. 1, 2015, ISSN: 0964-1726, 1361-665X. DOI: `10.1088/0964-1726/24/12/125031`.

[43] Y. Du, T. Keller, C. Song, Z. Xiao, L. Wu, and J. Xiong, "Design and foldability of miura-based cylindrical origami structures", *Thin-Walled Structures*, vol. 159, p. 107 311, Feb. 2021, ISSN: 02638231. DOI: `10.1016/j.tws.2020.107311`.

[44] Y. Yoshimura, "On the mechanism of buckling of a circular cylindrical shell under axial compression", National Advisory Committy for Aeronautics, 19930093840, Jul. 1, 1955.

[45] J. Suh, T. Kim, and J. Han, "New approach to folding a thin-walled yoshimura patterned cylinder", *Journal of Spacecraft and Rockets*, vol. 58, no. 2, pp. 516–530, Mar. 2021, ISSN: 0022-4650, 1533-6794. DOI: `10.2514/1.A34784`.

[46] A. Micheletti, I. Giannetti, G. Mattei, and A. Tiero, "Kinematic and static design of rigid origami structures: Application to modular yoshimura patterns", *Journal of Architectural Engineering*, vol. 28, no. 2, p. 04 022 009, Jun. 2022, ISSN: 1076-0431, 1943-5568. DOI: `10.1061/(ASCE)AE.1943-5568.0000531`.

[47] L. Paez, G. Agarwal, and J. Paik, "Design and analysis of a soft pneumatic actuator with origami shell reinforcement", *Soft Robotics*, vol. 3, no. 3, pp. 109–119, Sep. 2016, ISSN: 2169-5172, 2169-5180. DOI: `10.1089/soro.2016.0023`.

[48] H. Banerjee, N. Pusalkar, and H. Ren, "Single-motor controlled tendon-driven peristaltic soft origami robot", *Journal of Mechanisms and Robotics*, vol. 10, no. 6, p. 064 501, Dec. 1, 2018, ISSN: 1942-4302, 1942-4310. DOI: `10.1115/1.4041200`.

[49] N. Kidambi and K. W. Wang, "Dynamics of kresling origami deployment", *Physical Review E*, vol. 101, no. 6, p. 063 003, Jun. 5, 2020, ISSN: 2470-0045, 2470-0053. DOI: `10.1103/PhysRevE.101.063003`.

[50] X. Wang, H. Qu, X. Li, Y. Kuang, H. Wang, and S. Guo, "Multi-triangles cylindrical origami and inspired metamaterials with tunable stiffness and stretchable robotic arm", *PNAS Nexus*, pgad098, Mar. 23, 2023, ISSN: 2752-6542. DOI: `10.1093/pnasnexus/pgad098`.

[51] K. Hu, T. Jeannin, J. Berre, M. Ouisse, and K. Rabenorosoa, "Toward actuation of kresling pattern-based origami robots", *Smart Materials and Structures*, vol. 31, no. 10, p. 105 025, Oct. 1, 2022, ISSN: 0964-1726, 1361-665X. DOI: 10.1088/1361-665X/ac9020.

[52] Y. Chen, H. Feng, J. Ma, R. Peng, and Z. You, "Symmetric waterbomb origami", *Proceedings of the Royal Society A: Mathematical, Physical and Engineering Sciences*, vol. 472, no. 2190, p. 20 150 846, Jun. 2016, ISSN: 1364-5021, 1471-2946. DOI: 10.1098/rspa.2015.0846.

[53] H. Han, L. Tang, D. Cao, and L. Liu, "Modeling and analysis of dynamic characteristics of multi-stable waterbomb origami base", *Nonlinear Dynamics*, vol. 102, no. 4, pp. 2339–2362, Dec. 2020, ISSN: 0924-090X, 1573-269X. DOI: 10.1007/s11071-020-06082-8.

[54] T. Mukhopadhyay *et al.*, "Programmable stiffness and shape modulation in origami materials: Emergence of a distant actuation feature", *Applied Materials Today*, vol. 19, p. 100 537, Jun. 2020, ISSN: 23529407. DOI: 10.1016/j.apmt.2019.100537.

[55] B. H. Hanna, J. M. Lund, R. J. Lang, S. P. Magleby, and L. L. Howell, "Waterbomb base: A symmetric single-vertex bistable origami mechanism", *Smart Materials and Structures*, vol. 23, no. 9, p. 094 009, Sep. 1, 2014, ISSN: 0964-1726, 1361-665X. DOI: 10.1088/0964-1726/23/9/094009.

[56] J. Ma, H. Feng, Y. Chen, D. Hou, and Z. You, "Folding of tubular waterbomb", *Research*, vol. 2020, pp. 2020/1735081, Jan. 2020, ISSN: 2639-5274. DOI: 10.34133/2020/1735081.

[57] F. Daerden and D. Lefeber, "Pneumatic artificial muscles: Actuators for robotics and automation", 2002.

[58] V. B. Piferrer, "The waterbomb actuator: A new origami-based pneumatic soft muscle.", University of California, Irvine, California, 2017.

[59] B. Sargent *et al.*, "An origami-based medical support system to mitigate flexible shaft buckling", *Journal of Mechanisms and Robotics*, vol. 12, no. 4, p. 041 005, Aug. 1, 2020, ISSN: 1942-4302, 1942-4310. DOI: 10.1115/1.4045846.

[60] A. Firouzeh and J. Paik, "Robogami: A fully integrated low-profile robotic origami", *Journal of Mechanisms and Robotics*, vol. 7, no. 2, p. 021 009, May 1, 2015, ISSN: 1942-4302, 1942-4310. DOI: 10.1115/1.4029491.

[61] Z. Zhakypov, M. Falahi, M. Shah, and J. Paik, "The design and control of the multi-modal locomotion origami robot, tribot", in *2015 IEEE/RSJ International Conference on Intelligent Robots and Systems (IROS)*, Hamburg: IEEE, Sep. 2015, pp. 4349–4355, ISBN: 978-1-4799-9994-1. DOI: 10.1109/IROS.2015.7353994.

[62] C. H. Belke and J. Paik, "Mori: A modular origami robot", *IEEE/ASME Transactions on Mechatronics*, vol. 22, no. 5, pp. 2153–2164, Oct. 2017, ISSN: 1083-4435, 1941-014X. DOI: 10.1109/TMECH.2017.2697310.

[63] F. Ilievski, A. D. Mazzeo, R. F. Shepherd, X. Chen, and G. M. Whitesides, "Soft robotics for chemists", *Angewandte Chemie International Edition*, vol. 50, no. 8, pp. 1890–1895, Feb. 18, 2011, ISSN: 14337851. DOI: 10.1002/anie.201006464.

[64] R. F. Shepherd *et al.*, "Multigait soft robot", *Proceedings of the National Academy of Sciences*, vol. 108, no. 51, pp. 20 400–20 403, Dec. 20, 2011, ISSN: 0027-8424, 1091-6490. DOI: 10.1073/pnas.1116564108.

[65] R. V. Martinez *et al.*, "Robotic tentacles with three-dimensional mobility based on flexible elastomers", *Advanced Materials*, vol. 25, no. 2, pp. 205–212, Jan. 11, 2013, ISSN: 09359648. DOI: 10.1002/adma.201203002.

[66] Z. Gong, Z. Xie, X. Yang, T. Wang, and L. Wen, "Design, fabrication and kinematic modeling of a 3d-motion soft robotic arm", in *2016 IEEE International Conference on Robotics and Biomimetics (ROBIO)*, Qingdao, China: IEEE, Dec. 2016, pp. 509–514, ISBN: 978-1-5090-4364-4. DOI: 10.1109/ROBIO.2016.7866373.

[67] X. Liang, H. Cheong, Y. Sun, J. Guo, C. K. Chui, and C. Yeow, "Design, characterization, and implementation of a two-DOF fabric-based soft robotic arm", *IEEE Robotics and Automation Letters*, vol. 3, no. 3, pp. 2702–2709, Jul. 2018, ISSN: 2377-3766, 2377-3774. DOI: 10.1109/LRA.2018.2831723.

[68] I. D. Walker *et al.*, "Continuum robot arms inspired by cephalopods", presented at the Defense and Security, G. R. Gerhart, C. M. Shoemaker, and D. W. Gage, Eds., Orlando, Florida, USA, May 27, 2005, p. 303. DOI: 10.1117/12.606201.

[69] M. D. Grissom *et al.*, "Design and experimental testing of the OctArm soft robot manipulator", presented at the Defense and Security Symposium, G. R. Gerhart, C. M. Shoemaker, and D. W. Gage, Eds., Orlando (Kissimmee), FL, May 5, 2006, 62301F. DOI: 10.1117/12.665321.

[70] W. McMahan *et al.*, "Field trials and testing of the OctArm continuum manipulator", in *Proceedings 2006 IEEE International Conference on Robotics and Automation, 2006. ICRA 2006.*, ISSN: 1050-4729, May 2006, pp. 2336–2341. DOI: 10.1109/ROBOT.2006.1642051.

[71] A. Grzesiak, R. Becker, and A. Verl, "The bionic handling assistant: A success story of additive manufacturing", *Assembly Automation*, vol. 31, no. 4, pp. 329–333, Sep. 27, 2011, ISSN: 0144-5154. DOI: 10.1108/01445151111172907.

[72] V. Falkenhahn, A. Hildebrandt, R. Neumann, and O. Sawodny, "Dynamic control of the bionic handling assistant", *IEEE/ASME Transactions on Mechatronics*, vol. 22, no. 1, pp. 6–17, Feb. 2017, ISSN: 1083-4435, 1941-014X. DOI: 10.1109/TMECH.2016.2605820.

[73] W. Wang, Y. Zhu, S. Cai, and G. Bao, "Ultralong stretchable soft actuator (US2a): Design, modeling and application", *Chinese Journal of Mechanical Engineering*, vol. 36, no. 1, p. 13, Feb. 1, 2023, ISSN: 2192-8258. DOI: 10.1186/s10033-023-00835-3.

[74] Y. Chen, J. Zhang, and Y. Gong, "Utilizing anisotropic fabrics composites for high-strength soft manipulator integrating soft gripper", *IEEE Access*, vol. 7, pp. 127 416–127 426, 2019, ISSN: 2169-3536. DOI: 10.1109/ACCESS.2019.2940499.

[75] W. McMahan, B. A. Jones, and I. D. Walker, "Design and implementation of a multi-section continuum robot: Air-octor", in *2005 IEEE/RSJ International Conference on Intelligent Robots and Systems*, ISSN: 2153-0866, Aug. 2005, pp. 2578–2585. DOI: 10.1109/IROS.2005.1545487.

[76] X. Ma, X. Wang, Z. Zhang, P. Zhu, S. S. Cheng, and K. W. Samuel Au, "Design and experimental validation of a novel hybrid continuum robot with enhanced dexterity and manipulability in confined space", *IEEE/ASME Transactions on Mechatronics*, vol. 28, no. 4, pp. 1826–1835, Aug. 2023, ISSN: 1083-4435, 1941-014X. DOI: 10.1109/TMECH.2023.3276076.

[77] H. Yang, M. Xu, W. Li, and S. Zhang, "Design and implementation of a soft robotic arm driven by SMA coils", *IEEE Transactions on Industrial Electronics*, vol. 66, no. 8, pp. 6108–6116, Aug. 2019, ISSN: 0278-0046, 1557-9948. DOI: 10.1109/TIE.2018.2872005.

[78] T. Zhang, L. Yang, X. Yang, R. Tan, H. Lu, and Y. Shen, "Millimeter-scale soft continuum robots for large-angle and high-precision manipulation by hybrid actuation", *Advanced Intelligent Systems*, vol. 3, no. 2, p. 2 000 189, Feb. 2021, ISSN: 2640-4567, 2640-4567. DOI: 10.1002/aisy.202000189.

[79] N. G. Cheng *et al.*, "Design and analysis of a robust, low-cost, highly articulated manipulator enabled by jamming of granular media", in *2012 IEEE International Conference on Robotics and Automation*, St Paul, MN, USA: IEEE, May 2012, pp. 4328–4333, ISBN: 978-1-4673-1405-3 978-1-4673-1403-9 978-1-4673-1578-4 978-1-4673-1404-6. DOI: `10.1109/ICRA.2012.6225373`.

[80] J. Zhang *et al.*, "Bioinspired continuum robots with programmable stiffness by harnessing phase change materials", *Advanced Materials Technologies*, vol. 8, no. 6, p. 2 201 616, Mar. 2023, ISSN: 2365-709X, 2365-709X. DOI: `10.1002/admt.202201616`.

[81] G. M. Whitesides, "Soft robotics", *Angewandte Chemie International Edition*, vol. 57, no. 16, pp. 4258–4273, Apr. 9, 2018, ISSN: 14337851. DOI: `10.1002/anie.201800907`.

[82] X. Fang, K. Wei, and R. Yang, "Untethered soft pneumatic actuators with embedded multiple sensing capabilities", *Soft Robotics*, soro.2023.0048, Nov. 10, 2023, ISSN: 2169-5172, 2169-5180. DOI: `10.1089/soro.2023.0048`.

[83] M. S. Malekzadeh, J. F. Queißer, and J. J. Steil, "Multi-level control architecture for bionic handling assistant robot augmented by learning from demonstration for apple-picking", *Advanced Robotics*, vol. 33, no. 9, pp. 469–485, May 3, 2019, ISSN: 0169-1864, 1568-5535. DOI: `10.1080/01691864.2019.1587313`.

[84] O. Lakhal, A. Melingui, and R. Merzouki, "Hybrid approach for modeling and solving of kinematics of a compact bionic handling assistant manipulator", *IEEE/ASME Transactions on Mechatronics*, vol. 21, no. 3, pp. 1326–1335, Jun. 2016, ISSN: 1083-4435, 1941-014X. DOI: `10.1109/TMECH.2015.2490180`.

[85] M. S. Malekzadeh, J. F. Queißer, and J. J. Steil, "Learning the end-effector pose from demonstration for bionic handling assistant robot", *. September*, 2016.

[86] A. Melingui, R. Merzouki, J. B. Mbede, C. Escande, and N. Benoudjit, "Neural networks based approach for inverse kinematic modeling of a compact bionic handling assistant trunk", in *2014 IEEE 23rd International Symposium on Industrial Electronics (ISIE)*, Istanbul, Turkey: IEEE, Jun. 2014, pp. 1239–1244, ISBN: 978-1-4799-2399-1. DOI: `10.1109/ISIE.2014.6864791`.

[87] I. Singh, O. Lakhal, Y. Amara, V. Coelen, P. M. Pathak, and R. Merzouki, "Performances evaluation of inverse kinematic models of a compact bionic handling assistant", in *2017 IEEE International Conference on Robotics and Biomimetics (ROBIO)*, Macau: IEEE, Dec. 2017, pp. 264–269, ISBN: 978-1-5386-3742-5. DOI: `10.1109/ROBIO.2017.8324428`.

[88] A. Melingui, R. Merzouki, J. B. Mbede, C. Escande, B. Daachi, and N. Benoudjit, "Qualitative approach for inverse kinematic modeling of a compact bionic handling assistant trunk", in *2014 International Joint Conference on Neural Networks (IJCNN)*, Beijing, China: IEEE, Jul. 2014, pp. 754–761, ISBN: 978-1-4799-1484-5 978-1-4799-6627-1. DOI: `10.1109/IJCNN.2014.6889947`.

[89] X. Chen, X. Zhang, H. Liu, and Y. Huang, "Design and development of a soft robotic manipulator", *International Journal of Mechanics and Materials in Design*, vol. 16, no. 2, pp. 309–321, Jun. 2020, ISSN: 1569-1713, 1573-8841. DOI: `10.1007/s10999-019-09471-z`.

[90] G. Immega and K. Antonelli, "The KSI tentacle manipulator", in *Proceedings of 1995 IEEE International Conference on Robotics and Automation*, vol. 3, Nagoya, Japan: IEEE, 1995, pp. 3149–3154, ISBN: 978-0-7803-1965-3. DOI: `10.1109/ROBOT.1995.525733`.

[91] R. Cieślak and A. Morecki, "Elephant trunk type elastic manipulator - a tool for bulk and liquid materials transportation", *Robotica*, vol. 17, no. 1, pp. 11–16, Jan. 1999, ISSN: 0263-5747, 1469-8668. DOI: `10.1017/S0263574799001009`.

[92] Q. Zhao and F. Gao, "Design and analysis of a kind of biomimetic continuum robot", in *2010 IEEE International Conference on Robotics and Biomimetics*, Tianjin, China: IEEE, Dec. 2010, pp. 1316–1320, ISBN: 978-1-4244-9319-7. DOI: `10.1109/ROBIO.2010.5723519`.

[93] M. W. Hannan and I. D. Walker, "Analysis and experiments with an elephant's trunk robot", *Advanced Robotics*, vol. 15, no. 8, pp. 847–858, Jan. 2001, ISSN: 0169-1864, 1568-5535. DOI: `10.1163/156855301317198160`.

[94] L. Jianfeng, L. Ruifeng, Z. Leiyu, Z. Shiping, and W. Haidong, "Configuration synthesis and design of a telescopic service robot", in *2018 International Conference on Virtual Reality and Intelligent Systems (ICVRIS)*, Changsha: IEEE, Aug. 2018, pp. 442–445, ISBN: 978-1-5386-8031-5. DOI: `10.1109/ICVRIS.2018.00114`.

[95] A. Seino, N. Seto, L. Canete, and T. Takahashi, "Long-reach compact robotic arm with LMPA joints for monitoring of reactor interior", in *2020 IEEE/RSJ International Conference on Intelligent Robots and Systems (IROS)*, Las Vegas, NV, USA: IEEE, Oct. 24, 2020, pp. 6384–6389, ISBN: 978-1-72816-212-6. DOI: `10.1109/IROS45743.2020.9341567`.

[96] T. Fujioka, G. Endo, K. Suzumori, and H. Nabae, "Proposal of tendon-driven elastic telescopic arm and initial bending experiment", in *2017 IEEE/SICE International Symposium on System Integration (SII)*, Taipei: IEEE, Dec. 2017, pp. 164–169, ISBN: 978-1-5386-2263-6. DOI: `10.1109/SII.2017.8279206`.

[97] A. Ogawa, T. Fujioka, H. Nabae, K. Suzumori, and G. Endo, "Tendon-driven elastic telescopic arm -integration of linear motion and bending motion-", in *2020 IEEE/SICE International Symposium on System Integration (SII)*, Honolulu, HI, USA: IEEE, Jan. 2020, pp. 1328–1334, ISBN: 978-1-72816-667-4. DOI: `10.1109/SII46433.2020.9026006`.

[98] S. Teshigawara and H. Harry Asada, "A mobile extendable robot arm: Singularity analysis and design", in *2019 IEEE/RSJ International Conference on Intelligent Robots and Systems (IROS)*, Macau, China: IEEE, Nov. 2019, pp. 5131–5138, ISBN: 978-1-72814-004-9. DOI: `10.1109/IROS40897.2019.8967768`.

[99] A. Shikari and H. Asada, "Triple scissor extender robot arm: A solution to the last one foot problem of manipulation", *IEEE Robotics and Automation Letters*, vol. 3, no. 4, pp. 3975–3982, Oct. 2018, ISSN: 2377-3766, 2377-3774. DOI: `10.1109/LRA.2018.2859022`.

[100] J. Chalfoun, C. Bidard, D. Keller, Y. Perrot, and G. Piolain, "Design and flexible modeling of a long reach articulated carrier for inspection", in *2007 IEEE/RSJ International Conference on Intelligent Robots and Systems*, San Diego, CA, USA: IEEE, Oct. 2007, pp. 4013–4019, ISBN: 978-1-4244-0911-2 978-1-4244-0912-9. DOI: `10.1109/IROS.2007.4399213`.

[101] L. Gargiulo *et al.*, "Operation of an ITER relevant inspection robot on tore supra tokamak", *Fusion Engineering and Design*, vol. 84, no. 2, pp. 220–223, Jun. 2009, ISSN: 09203796. DOI: `10.1016/j.fusengdes.2008.11.043`.

[102] Y. Perrot *et al.*, "Long-reach articulated robots for inspection and mini-invasive interventions in hazardous environments: Recent robotics research, qualification testing, and tool developments", *Journal of Field Robotics*, vol. 29, no. 1, pp. 175–185, Jan. 2012, ISSN: 15564959. DOI: `10.1002/rob.20422`.

[103] Y. Perrot *et al.*, "Long reach articulated robots for inspection in hazardous environments, recent developments on robotics and embedded diagnostics", in *2010 1st International Conference on Applied Robotics for the Power Industry (CARPI 2010)*, Montreal, QC, Canada: IEEE, Oct. 2010, pp. 1–5, ISBN: 978-1-4244-6633-7. DOI: `10.1109/CARPI.2010.5624425`.

[104] A. Horigome, H. Yamada, G. Endo, S. Sen, S. Hirose, and E. F. Fukushima, "Development of a coupled tendon-driven 3d multi-joint manipulator", in *2014 IEEE International Conference on Robotics and Automation (ICRA)*, Hong Kong, China: IEEE, May 2014, pp. 5915–5920, ISBN: 978-1-4799-3685-4. DOI: `10.1109/ICRA.2014.6907730`.

[105] A. Horigome, G. Endo, K. Suzumori, and H. Nabae, "Design of a weight-compensated and coupled tendon-driven articulated long-reach manipulator", in *2016 IEEE/SICE International Symposium on System Integration (SII)*, Sapporo, Japan: IEEE, Dec. 2016, pp. 598–603, ISBN: 978-1-5090-3329-4. DOI: `10.1109/SII.2016.7844064`.

[106] G. Endo, A. Horigome, and A. Takata, "Super dragon: A 10-m-long-coupled tendon-driven articulated manipulator", *IEEE Robotics and Automation Letters*, vol. 4, no. 2, pp. 934–941, Apr. 2019, ISSN: 2377-3766, 2377-3774. DOI: `10.1109/LRA.2019.2894855`.

[107] M. Takeichi, K. Suzumori, G. Endo, and H. Nabae, "Development of giacometti arm with balloon body", *IEEE Robotics and Automation Letters*, vol. 2, no. 2, pp. 951–957, Apr. 2017, ISSN: 2377-3766, 2377-3774. DOI: `10.1109/LRA.2017.2655111`.

[108] M. Takeichi, K. Suzumori, G. Endo, and H. Nabae, "Development of a 20-m-long giacometti arm with balloon body based on kinematic model with air resistance", in *2017 IEEE/RSJ International Conference on Intelligent Robots and Systems (IROS)*, Vancouver, BC: IEEE, Sep. 2017, pp. 2710–2716, ISBN: 978-1-5386-2682-5. DOI: `10.1109/IROS.2017.8206097`.

[109] Y. Ueno, T. Hagiwara, H. Nabae, K. Suzumori, and G. Endo, "Development of hiryu-II: A long-reach articulated modular manipulator driven by thrusters", *IEEE Robotics and Automation Letters*, vol. 5, no. 3, pp. 4963–4969, Jul. 2020, ISSN: 2377-3766, 2377-3774. DOI: `10.1109/LRA.2020.3004775`.

[110] R. O. Buckingham and A. C. Graham, "Dexterous manipulators for nuclear inspection and maintenance — case study", in *2010 1st International Conference on Applied Robotics for the Power Industry (CARPI 2010)*, Montreal, QC, Canada: IEEE, Oct. 2010, pp. 1–6, ISBN: 978-1-4244-6633-7. DOI: `10.1109/CARPI.2010.5624476`.

[111] C. Canali *et al.*, "Design of a novel long-reach cable-driven hyper-redundant snake-like manipulator for inspection and maintenance", *Applied Sciences*, vol. 12, no. 7, p. 3348, Mar. 25, 2022, ISSN: 2076-3417. DOI: `10.3390/app12073348`.

[112] S. Hirose, "Design of hyper-redundant arm", *Springer, London*, 1996. DOI: `https://doi.org/10.1007/978-1-4471-0765-1_61`.

[113] S. Hirose and R. Chu, "Development of a light weight torque limiting m-drive actuator for hyper-redundant manipulator float arm", in *Proceedings 1999 IEEE International Conference on Robotics and Automation (Cat. No.99CH36288C)*, vol. 4, Detroit, MI, USA: IEEE, 1999, pp. 2831–2836, ISBN: 978-0-7803-5180-6. DOI: `10.1109/ROBOT.1999.774026`.

[114] J. Yuan, W. Wan, K. Chen, Q. Fang, and W. Zhang, "Design and prototyping a cable-driven multi-stage telescopic arm for mobile surveillance robots", in *2014 IEEE International Conference on Robotics and Biomimetics (ROBIO 2014)*, Bali, Indonesia: IEEE, Dec. 2014, pp. 1845–1850, ISBN: 978-1-4799-7397-2. DOI: `10.1109/ROBIO.2014.7090604`.

[115] R. Buckingham, "Snake arm robots", *Industrial Robot: An International Journal*, vol. 29, no. 3, pp. 242–245, Jun. 1, 2002, ISSN: 0143-991X. DOI: `10.1108/01439910210425531`.

[116] R. Buckingham and A. Graham, "Snake-arm robots – a new tool for the aerospace industry", presented at the Automated Fastening Conference & Exposition, Sep. 8, 2003, pp. 2003–01–2952. DOI: `10.4271/2003-01-2952`.

[117] X. Chen, Y. Guo, D. Duanmu, J. Zhou, W. Zhang, and Z. Wang, "Design and modeling of an extensible soft robotic arm", *IEEE Robotics and Automation Letters*, vol. 4, no. 4, pp. 4208–4215, Oct. 2019, ISSN: 2377-3766, 2377-3774. DOI: `10.1109/LRA.2019.2929994`.

[118] B. Sparrman *et al.*, "Printed silicone pneumatic actuators for soft robotics", *Additive Manufacturing*, vol. 40, p. 101 860, Apr. 2021, ISSN: 22148604. DOI: `10.1016/j.addma.2021.101860`.

[119] K. Lee, Y. Wang, and C. Zheng, "TWISTER hand: Underactuated robotic gripper inspired by origami twisted tower", *IEEE Transactions on Robotics*, vol. 36, no. 2, pp. 488–500, Apr. 2020, ISSN: 1552-3098, 1941-0468. DOI: `10.1109/TRO.2019.2956870`.

[120] H. Jiang *et al.*, "Design, control, and applications of a soft robotic arm", Jul. 8, 2020. arXiv: `2007.04047[cs]`.

[121] F. Chen and M. Y. Wang, "Design optimization of soft robots: A review of the state of the art", *IEEE Robotics & Automation Magazine*, vol. 27, no. 4, pp. 27–43, Dec. 2020, ISSN: 1070-9932, 1558-223X. DOI: `10.1109/MRA.2020.3024280`.

[122] F. Connolly, C. J. Walsh, and K. Bertoldi, "Automatic design of fiber-reinforced soft actuators for trajectory matching", *Proceedings of the National Academy of Sciences*, vol. 114, no. 1, pp. 51–56, Jan. 3, 2017, ISSN: 0027-8424, 1091-6490. DOI: `10.1073/pnas.1615140114`.

[123] F. C. Park and J. E. Bobrow, "Geometric optimization algorithims for robot kinematic design", *Journal of Robotic Systems*, vol. 12, no. 6, pp. 453–463, Jun. 1995, ISSN: 0741-2223, 1097-4563. DOI: `10.1002/rob.4620120609`.

[124] M. Ceccarelli and C. Lanni, "A multi-objective optimum design of general 3r manipulators for prescribed workspace limits", *Mechanism and Machine Theory*, vol. 39, no. 2, pp. 119–132, Feb. 2004, ISSN: 0094114X. DOI: `10.1016/S0094-114X(03)00109-5`.

[125] C. Paredis and P. Khosla, "An approach for mapping kinematic task specifications into a manipulator design", in *Fifth International Conference on Advanced Robotics 'Robots in Unstructured Environments*, Pisa, Italy: IEEE, 1991, 556–561 vol.1, ISBN: 978-0-7803-0078-1. DOI: `10.1109/ICAR.1991.240594`.

[126] E. Van Henten, D. Van't Slot, C. Hol, and L. Van Willigenburg, "Optimal manipulator design for a cucumber harvesting robot", *Computers and Electronics in Agriculture*, vol. 65, no. 2, pp. 247–257, Mar. 2009, ISSN: 01681699. DOI: `10.1016/j.compag.2008.11.004`.

[127] J. Li, S. Andrews, K. G. Birkas, and P. G. Kry, "Task-based design of cable-driven articulated mechanisms", in *Proceedings of the 1st Annual ACM Symposium on Computational Fabrication*, Cambridge Massachusetts: ACM, Jun. 12, 2017, pp. 1–12, ISBN: 978-1-4503-4999-4. DOI: `10.1145/3083157.3083161`.

[128] S. P. Boyd and L. Vandenberghe, *Convex optimization*, Version 29. Cambridge New York Melbourne New Delhi Singapore: Cambridge University Press, 2023, 716 pp., ISBN: 978-0-521-83378-3.

[129] P. T. Boggs, P. D. Domich, and J. E. Rogers, "An interior point method for general large-scale quadratic programming problems", *Annals of Operations Research*, vol. 62, no. 1, pp. 419–437, Dec. 1996, ISSN: 0254-5330, 1572-9338. DOI: `10.1007/BF02206825`.

[130] M. Cococcioni and L. Fiaschi, "The big-m method with the numerical infinite m", *Optimization Letters*, vol. 15, no. 7, pp. 2455–2468, Oct. 2021, ISSN: 1862-4472, 1862-4480. DOI: `10.1007/s11590-020-01644-6`.

[131] J. Kaufmann and S. Li, *Harnessing the multi-stability of kresling origami for reconfigurable articulation in soft robotic arms*, Aug. 17, 2020. arXiv: `2008.07421[physics]`.

[132] B. A. Turlach and S. J. Wright, "Quadratic programming", *WIREs Computational Statistics*, vol. 7, no. 2, pp. 153–159, Mar. 2015, ISSN: 1939-5108, 1939-0068. DOI: `10.1002/wics.1344`.

[133] S. A. Vavasis, "Complexity issues in global optimization: A survey", in *Handbook of Global Optimization*, R. Horst and P. M. Pardalos, Eds., red. by P. Pardalos and R. Horst, vol. 2, Series Title: Nonconvex Optimization and Its Applications, Boston, MA: Springer US, 1995, pp. 27–41, ISBN: 978-1-4613-5838-1 978-1-4615-2025-2. DOI: `10.1007/978-1-4615-2025-2_2`.

[134] M. Danilova *et al.*, "Recent theoretical advances in non-convex optimization", in *High-Dimensional Optimization and Probability*, A. Nikeghbali, P. M. Pardalos, A. M. Raigorodskii, and M. T. Rassias, Eds., vol. 191, Series Title: Springer Optimization and Its Applications, Cham: Springer International Publishing, 2022, pp. 79–163, ISBN: 978-3-031-00831-3 978-3-031-00832-0. DOI: `10.1007/978-3-031-00832-0_3`.

[135] A. B. Humbe, P. A. Deshmukh, and M. S. Kadam, "THE REVIEW OF ARTICULATED r12 ROBOT AND ITS INDUSTRIAL APPLICATIONS",

[136] R. Jain, M. Nayab Zafar, and J. C. Mohanta, "Modeling and analysis of articulated robotic arm for material handling applications", *IOP Conference Series: Materials Science and Engineering*, vol. 691, no. 1, p. 012 010, Nov. 1, 2019, ISSN: 1757-8981, 1757-899X. DOI: `10.1088/1757-899X/691/1/012010`.

[137] E. Eliot, B. Deepak, D. Parhi, and J. Srinivas, "DESIGN & KINEMATIC ANALYSIS OF AN ARTICULATED ROBOTIC MANIPULATOR", *International Journal of Mechanical and Industrial Engineering*, pp. 12–15, Jul. 2014, ISSN: 2231-6477. DOI: `10.47893/IJMIE.2014.1177`.

[138] R. Sathia. "How robotic process automation drives innovation", CIO. (May 10, 2021), [Online]. Available: `https://www.cio.com/article/189362/how-robotic-process-automation-drives-innovation.html` (visited on 03/07/2023).

[139] G. Drenik. "Why robots are taking over the world - and that's a good thing", Forbes. Section: Leadership Strategy. (Sep. 12, 2022), [Online]. Available: `https://www.forbes.com/sites/garydrenik/2022/12/09/why-robots-are-taking-over-the-worldand-thats-a-good-thing/` (visited on 03/07/2023).

[140] K. Bezha and K. Ito, "Soft manipulator inspired by octopi: Object grasping in all anatomical planes using a tendon-driven continuum arm", *Artificial Life and Robotics*, vol. 28, no. 1, pp. 96–105, Feb. 2023, ISSN: 1433-5298, 1614-7456. DOI: `10.1007/s10015-022-00844-w`.

[141] J. Santoso and C. D. Onal, "An origami continuum robot capable of precise motion through torsionally stiff body and smooth inverse kinematics", *Soft Robotics*, vol. 8, no. 4, pp. 371–386, Aug. 1, 2021, ISSN: 2169-5172, 2169-5180. DOI: `10.1089/soro.2020.0026`.

[142] A. Jiang, G. Xynogalas, P. Dasgupta, K. Althoefer, and T. Nanayakkara, "Design of a variable stiffness flexible manipulator with composite granular jamming and membrane coupling", in *2012 IEEE/RSJ International Conference on Intelligent Robots and Systems*, Vilamoura-Algarve, Portugal: IEEE, Oct. 2012, pp. 2922–2927, ISBN: 978-1-4673-1736-8 978-1-4673-1737-5 978-1-4673-1735-1. DOI: `10.1109/IROS.2012.6385696`.

[143] R. C. Hibbeler, *Mechanics of Materials*, 8th ed. Pearson, 2010, ISBN: 0-13-602230-8.

[144] L. Lu, S. Leanza, and R. R. Zhao, "Origami with rotational symmetry: A review on their mechanics and design", *Applied Mechanics Reviews*, vol. 75, no. 5, p. 050 801, Sep. 1, 2023, ISSN: 0003-6900, 2379-0407. DOI: `10.1115/1.4056637`.

[145] Y. Dang, J. Chen, and J. Han, "Preliminary design and performance test of an origami actuator inspired by yoshimura pattern", in *2021 27th International Conference on Mechatronics and Machine Vision in Practice (M2VIP)*, Shanghai, China: IEEE, Nov. 26, 2021, pp. 435–439, ISBN: 978-1-66543-153-8. DOI: `10.1109/M2VIP49856.2021.9664993`.

[146] J. Kaufmann and S. Li, "Examine the bending stiffness of generalized kresling modules for robotic manipulation", 2020.

[147] B. Kresling, "The fifth fold: Complex symmetries in kresling-origami patterns", *Symmetry: Culture and Science*, vol. 31, no. 4, pp. 403–416, 2020, ISSN: 08654824, 22261877. DOI: `10.26830/symmetry_2020_4_403`.

[148] B. Kresling, "Natural twist buckling in shells: From the hawkmoth's bellows to the deployable kresling-pattern and cylindrical miura-ori", 2019.

[149] C. Jianguo, L. Yangqing, M. Ruijun, F. Jian, and Z. Ya, "Nonrigidly foldability analysis of kresling cylindrical origami", *Journal of Mechanisms and Robotics*, vol. 9, no. 4, p. 041 018, Aug. 1, 2017, ISSN: 1942-4302, 1942-4310. DOI: `10.1115/1.4036738`.

[150] C. Jianguo, D. Xiaowei, Z. Ya, F. Jian, and T. Yongming, "Bistable behavior of the cylindrical origami structure with kresling pattern", *Journal of Mechanical Design*, vol. 137, no. 6, p. 061 406, Jun. 1, 2015, ISSN: 1050-0472, 1528-9001. DOI: `10.1115/1.4030158`.

[151] M. Moshtaghzadeh and P. Mardanpour, "Design, mechanical characteristics evaluation, and energy absorption of multi-story kresling origami-inspired structures", *Mechanics Research Communications*, vol. 130, p. 104 125, Jul. 2023, ISSN: 00936413. DOI: `10.1016/j.mechrescom.2023.104125`.

[152] L. Lu, X. Dang, F. Feng, P. Lv, and H. Duan, "Conical kresling origami and its applications to curvature and energy programming", *Proceedings of the Royal Society A: Mathematical, Physical and Engineering Sciences*, vol. 478, no. 2257, p. 20 210 712, Jan. 2022, ISSN: 1364-5021, 1471-2946. DOI: `10.1098/rspa.2021.0712`.

[153] Z. Li, N. Kidambi, L. Wang, and K.-W. Wang, "Uncovering rotational multifunctionalities of coupled kresling modular structures", *Extreme Mechanics Letters*, vol. 39, p. 100 795, Sep. 2020, ISSN: 23524316. DOI: `10.1016/j.eml.2020.100795`.

[154] K. Hu, T. Jeannin, J. Berre, M. Ouisse, and K. Rabenorosoa, "Toward actuation of kresling pattern-based origami robots", *Smart Materials and Structures*, vol. 31, no. 10, p. 105 025, Oct. 1, 2022, ISSN: 0964-1726, 1361-665X. DOI: `10.1088/1361-665X/ac9020`.

[155] J. Berre, F. Geiskopf, L. Rubbert, and P. Renaud, "Toward the design of kresling tower origami as a compliant building block", *Journal of Mechanisms and Robotics*, vol. 14, no. 4, p. 045 002, Aug. 1, 2022, ISSN: 1942-4302, 1942-4310. DOI: `10.1115/1.4053378`.

[156] X. Wang, H. Qu, and S. Guo, "Tristable property and the high stiffness analysis of kresling pattern origami", *International Journal of Mechanical Sciences*, vol. 256, p. 108 515, Oct. 2023, ISSN: 00207403. DOI: `10.1016/j.ijmecsci.2023.108515`.

[157] P. Bhovad, J. Kaufmann, and S. Li, "Peristaltic locomotion without digital controllers: Exploiting multi-stability in origami to coordinate robotic motion", *Extreme Mechanics Letters*, vol. 32, p. 100 552, Oct. 2019, ISSN: 23524316. DOI: `10.1016/j.eml.2019.100552`.

[158] D. Kim, J. H. Park, S. Sikulskyi, E. Divo, and R. Martinez, "Numerical studies on origami dielectric elastomer actuator using kresling pattern", in *Electroactive Polymer Actuators and Devices (EAPAD) XXI*, Y. Bar-Cohen and I. A. Anderson, Eds., Denver, United States: SPIE, Mar. 13, 2019, p. 17, ISBN: 978-1-5106-2587-7 978-1-5106-2588-4. DOI: `10.1117/12.2514374`.

[159] X. Yang and S. Keten, "Multi-stability property of magneto-kresling truss structures", *Journal of Applied Mechanics*, vol. 88, no. 9, p. 091 009, Sep. 1, 2021, ISSN: 0021-8936, 1528-9036. DOI: `10.1115/1.4051705`.

[160] L. S. Novelino, Q. Ze, S. Wu, G. H. Paulino, and R. Zhao, "Untethered control of functional origami microrobots with distributed actuation", *Proceedings of the National Academy of Sciences*, vol. 117, no. 39, pp. 24 096–24 101, Sep. 29, 2020, ISSN: 0027-8424, 1091-6490. DOI: `10.1073/pnas.2013292117`.

[161] S. Li, H. Fang, S. Sadeghi, P. Bhovad, and K.-W. Wang, "Architected origami materials: How folding creates sophisticated mechanical properties", *Advanced Materials*, vol. 31, no. 5, p. 1 805 282, Feb. 2019, ISSN: 0935-9648, 1521-4095. DOI: `10.1002/adma.201805282`.

[162] M. Moshtaghzadeh, E. Izadpanahi, and P. Mardanpour, "Stability analysis of an origami helical antenna using geometrically exact fully intrinsic nonlinear composite beam theory", *Engineering Structures*, vol. 234, p. 111 894, May 2021, ISSN: 01410296. DOI: `10.1016/j.engstruct.2021.111894`.

[163] S. M. Alipour and J. Arghavani, "On the starting point in designing kresling origami", *Aerospace Science and Technology*, vol. 138, p. 108 301, Jul. 2023, ISSN: 12709638. DOI: `10.1016/j.ast.2023.108301`.

[164] G. Xiao-fan, Y. Yong, and Z. Xiao-jing, "Analytic expression of magnetic field distribution of rectangular permanent magnets", *Applied Mathematics and Mechanics*, vol. 25, no. 3, pp. 297–306, Mar. 2004, ISSN: 0253-4827, 1573-2754. DOI: `10.1007/BF02437333`.

[165] S. Babic and C. Akyel, "Magnetic force calculation between thin coaxial circular coils in air", *IEEE Transactions on Magnetics*, vol. 44, no. 4, pp. 445–452, Apr. 2008, ISSN: 0018-9464. DOI: `10.1109/TMAG.2007.915292`.

[166] I. Ciric, "Formulas for the magnetic field of polygonal cross section current coils", *IEEE Transactions on Magnetics*, vol. 28, no. 2, pp. 1064–1067, Mar. 1992, ISSN: 00189464. DOI: `10.1109/20.123865`.

[167] P. H. Schimpf, "A detailed explanation of solenoid force", *Int. J. on Recent Trends in Engineering and Technology*, vol. 8, no. 2, 2013.

[168] É. d. Trémolet de Lacheisserie, Ed., *Magnetism*, Norwell, Mass.: Kluwer Acad. Publ, 2002, ISBN: 978-1-4020-7224-6.

[169] F. Liu, T. Terakawa, S. Long, and M. Komori, "Rigid-foldable cylindrical origami with tunable mechanical behaviors", *Scientific Reports*, vol. 14, no. 1, p. 145, Jan. 2, 2024, ISSN: 2045-2322. DOI: `10.1038/s41598-023-50353-4`.

[170] C. Lee *et al.*, "Soft robot review", *International Journal of Control, Automation and Systems*, vol. 15, no. 1, pp. 3–15, Feb. 2017, ISSN: 1598-6446, 2005-4092. DOI: `10.1007/s12555-016-0462-3`.

[171] E. Specht, "High density packings of equal circles in rectangles with variable aspect ratio", *Computers & Operations Research*, vol. 40, no. 1, pp. 58–69, Jan. 2013, ISSN: 03050548. DOI: `10.1016/j.cor.2012.05.011`.

Appendix A

Scientific paper

[Separate document]

Appendix B

Kinematic optimization

B.1. Side view mathematical model

The first model encompasses a simple 2D side view of the situation. In this model, a maximum deflection of the segments with respect to each other of 60 degrees was detained, as described in subsection 2.4.1.

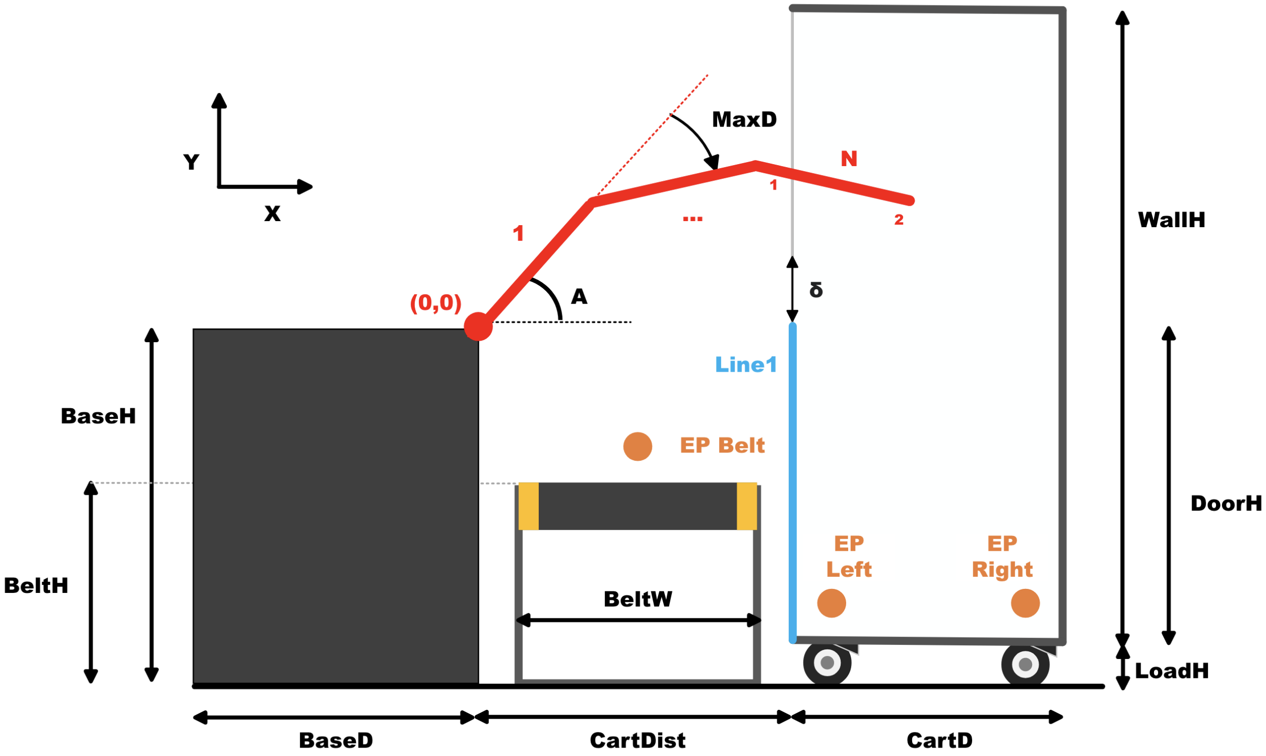

Figure B.1: *Side view model situational parameters explanation.*

Index	Description	
i	Point index of line segment	$i \in I$
j	Segment index	$j \in J$

Table B.1: *Indices*

Sets	Description	
I	Segment points	[1, 2]
J	Segments	[1, ..., N]

Table B.2: *Sets*

Subset	Description		
B	Segments subset	[1, ..., N-1]	$B \in J$

Table B.3: *Subsets*

B.1.1. Parameters

The parameters consist of fixed parameters, changeable parameters and 3 different end points, i.e. potential pick-up locations. The fixed parameters were assumed to be physical constraints which must be obeyed, and the changeable parameters with the different end points were varied during verification and validation of the model.

Table B.4: *Fixed parameters*

Parameter	Description	Value
BaseH	Height of the base of the robot	1.18
Base D	Depth of the base of the robot	0.8
Door H	Height of the lower door of the cart	0.99
Load H	Loading height of the cart	0.185
CartD	Depth of cart	0.760
WallH	Height of cart walls excluding loading height	1.965
BeltH	Height of belt conveyor	0.8
BeltW	Width of belt	1
δ	Clearance the robot needs to pass the door	0.15
θ	Range parameter for defining of C1	0.0001
M	Big M	1000
lbz	PWL arctan lower bound	-15
ubz	PWL arctan upper bound	15

Table B.5: *Changeable parameters*

Parameter		
CartDist	Perpendicular distance between robot base and cart.	1.2
N	Number of robot segments.	2, 3, ..., N
MaxL	Maximum length of each module.	1.4
MinL	Minimum length of each module.	0.2
MaxD	Max deflection of each segment.	60
Line1 ([x1, y1, x2, y2])	[CartDist, 0, CartDist, -DoorH]	

Table B.6: *End points for arm model*

EndPoint (EP)	[X,Y]
Left	[CartDist+0.1, -BaseH+1.4]
Right	[CartDist+0.9$\cdot CartD, -BaseH + 1.4 \cdot LoadH$]
Belt	[0.5,-BaseH+BeltH+0.1]

B.1.2. Decision variables

Table B.7: *Decision variables*

DV	Description
X_{ij}	X-coordinate of point i of segment j. i takes value 1 for the starting point of segment j and 2 for the end point of segment j.
Y_{ij}	Y-coordinate of point i of segment j. i takes value 1 for the starting point of segment j and 2 for the end point of segment j.
$C1_j$	Binary decision variable indicating if segment j crosses line 1. Takes value 0 when it does not cross line 1 and value 1 when it does.
dX_j	Inverse of difference between X_{1j} and X_{2j}. Auxiliary variable to achieve division.
$S1_j$	Slope of segment j.
A_j	Angle of segment j with respect to horizontal in radians.
u_j	Binary decision variable to indicate if segment j goes back in x-direction.

B.1.3. Objective

To achieve beneficial arm orientations, naturally the distance of the tip of the arm to the active end point must be minimized. However, it is expected that many orientations will result in the same optimal objective function so another optimization criteria is favourable. For industrial applications, efficiency is of significant importance. Therefore also the length of the arm is minimized to extract orientations which make optimal use of the geometry of the arm. Reaching the end point will stay the main objective so appropriate weights are implemented to scale both functions properly and give advantage to reaching the end point.

$$Min\ \frac{999}{1000}((X_{2N} - EP[0])^2 + (Y_{2N} - EP[1])^2) + \frac{1}{1000}\sum_{j\in J}((X_{2j} - X_{1j})^2 + (Y_{2j} - Y_{1j})^2) \tag{B.1}$$

B.1.4. Constraints

1. Connect consecutive coordinates.

$$X_{2j} - X_{1j+1} = 0, \ \ \forall j \in B \tag{B.2}$$

$$Y_{2j} - Y_{1j+1} = 0, \ \ \forall j \in B \tag{B.3}$$

2. Start at the origin.

$$X_{11} = 0 \tag{B.4}$$

$$Y_{11} = 0 \tag{B.5}$$

3. Maximum module length.

$$(X_{2j} - X_{1j})^2 + (Y_{2j} - Y_{1j})^2 \leq MaxL^2, \ \ \forall j \in J \tag{B.6}$$

4. Minimum module length.

$$(X_{2j} - X_{1j})^2 + (Y_{2j} - Y_{1j})^2 \geq MinL^2, \ \ \forall j \in J \tag{B.7}$$

5. Define behavior of binary DV C1 to be 1 when crossing Line1 and 0 if not.

$$(Line1[0] - X_{1j}) \cdot (Line1[0] - X_{2j}) \leq -\theta + M \cdot (1 - C1_j), \ \ \forall j \in J \tag{B.8}$$

$$(Line1[0] - X_{1j}) \cdot (Line1[0] - X_{2j}) \geq \theta - M \cdot C1_j, \ \ \forall j \in J \tag{B.9}$$

6. Prepare slope decision variable.

$$dX_j \cdot (X_{2j} - X_{1j}) = 1 - 2 \cdot u_j, \ \ \forall j \in J \tag{B.10}$$

7. Define slope of segments.

$$S1_j - 2 \cdot u_j \cdot S_j = (Y_{2j} - Y_{1j}) \cdot dX_j, \ \ \forall j \in J \tag{B.11}$$

8. Ensure that segments that cross the entrance of the cart do so above Line1 and below the top of the cart.

$$S1_j \cdot Line1[0] - S1_j \cdot X_{1j} + Y_{1j} + M \cdot (1 - C1_j) \geq Line1[1] + \delta, \ \ \forall j \in J \tag{B.12}$$

$$\begin{aligned} S1_j \cdot Line1[0] - S1_j \cdot X_{1j} + Y_{1j} + M \cdot (1 - C1_j) \leq -DoorH + WallH \\ -\delta + M \cdot (1 - C1_j), \ \ \forall j \in J \end{aligned} \tag{B.13}$$

9. Piece-wise linear (PWL) arc tangent function to define angles of segments w.r.t. horizontal.

$$A_j = PWL(arctan(S1_j)), \ \ \forall j \in J \tag{B.14}$$

10. Define maximum deflection of segments.

$$\frac{A_j - A_{j+1}}{\pi} \cdot 180 + 180 \cdot u_{j+1} \leq MaxD, \ \ \forall j \in B \tag{B.15}$$

$$\frac{A_j - A_{j+1}}{\pi} \cdot 180 + 180 \cdot u_{j+1} \geq -MaxD, \ \ \forall j \in B \tag{B.16}$$

11. Define behavior of binary DV u to take value 1 when segment j goes back in X-direction and 0 when not.

$$X_{2j} - X_{1j} \leq M \cdot (1 - u_j), \ \ \forall j \in J \tag{B.17}$$

$$X_{2j} - X_{1j} \geq -M \cdot u_j, \ \ \forall j \in J \tag{B.18}$$

12. The tip of the arm must end inside the cart. (Should be excluded when Belt end point is chosen.)

$$X_{2N} \geq CartDist + \theta \tag{B.19}$$

13. Binary constraints.

$$C1_j, u_j \in 0, 1, \ \ \forall j \in J \tag{B.20}$$

14. Angle bounds.

$$-\frac{1}{2}\pi \leq A_j \leq \frac{1}{2}\pi, \ \ \forall j \in J \tag{B.21}$$

B.1.5. All results 2D side model

All results of the 2D side model will be shown in this section. First, the different end points are computed for 3, 4, 5 and 6 segments. Later, both end points are run for 3, 4 and 5 segments with the parameter CartDist set to 5 and 10 meters to gain insights in the sensitivity of the results.

Example situation runs

3 segments - Shows no non-deflecting segments, unnecessary turns and does present an efficient trajectory.

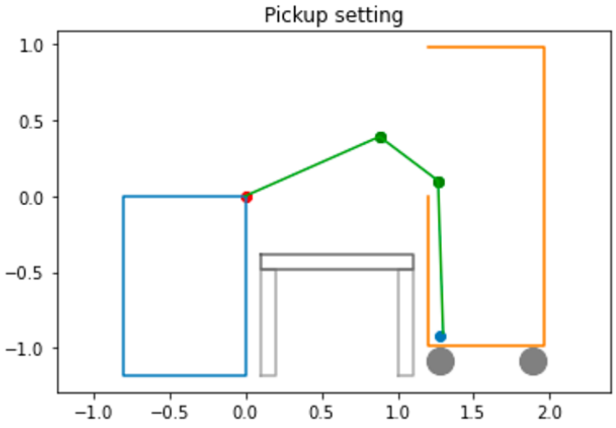

Figure B.2: *Left end point, 3 segments.*

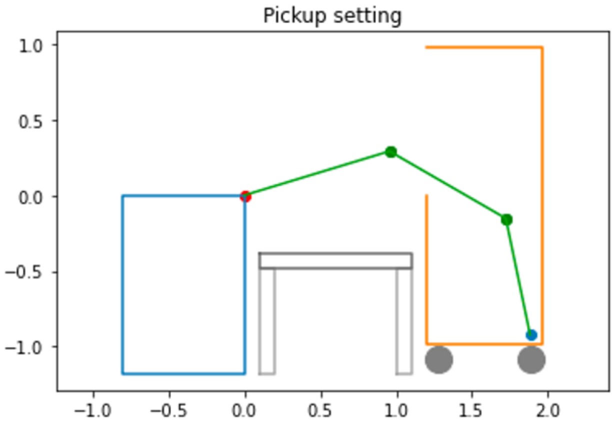

Figure B.3: *Right end point, 3 segments.*

Nr. of seg.	3
Seg. bounds	[0.2, 1.0] m
Seg. lengths	[0.96, 0.48, 1.0] m
Defl. (PWL)	[60.0, 53.4] deg
Run time	1800.02 s
CartDist	1.2 m
Package pos.	Lower left
Dist. to pack.	0.032 m

Nr. of seg.	3
Seg. bounds	[0.2, 1.0] m
Seg. lengths	[1.0, 0.89, 0.79] m
Defl. (PWL)	[46.8, 48.3] deg
Run time	4.05 s
CartDist	1.2 m
Package pos.	Lower right
Dist. to pack.	0.0 m

---

4 segments - These results do not necessarily show non-deflecting sections and pointless turns but do present over-complicated trajectories with respect to the 3 segment results.

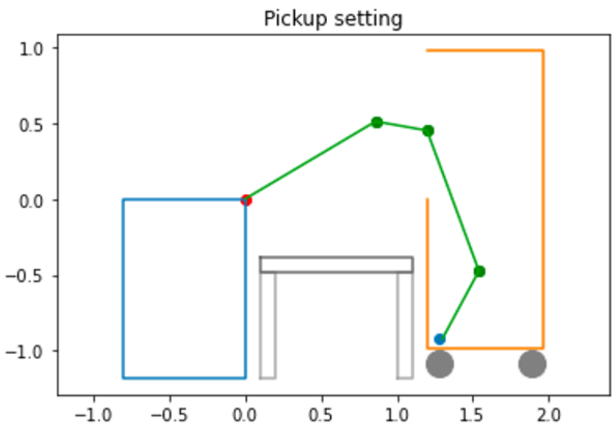

Figure B.4: *Left end point, 4 segments.*

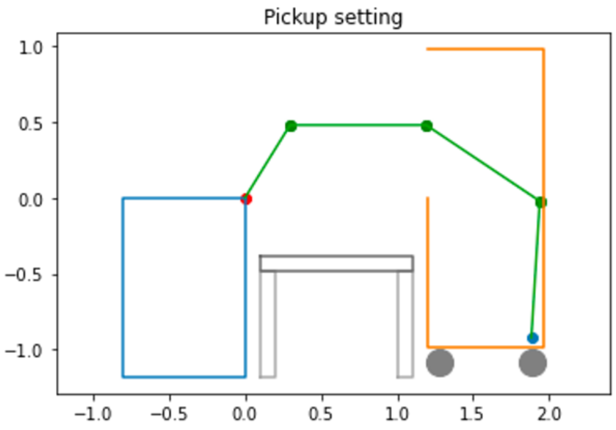

Figure B.5: *Right end point, 4 segments.*

Nr. of seg.	4
Seg. bounds	[0.2, 1.0] m
Seg. lengths	[1.0, 0.34, 0.99, 0.51] m
Defl. (PWL)	[40.5, 59.9, 48.7] deg
Run time	567.03 s
CartDist	1.2 m
Package pos.	Lower left
Dist. to pack.	0.024 m

Nr. of seg.	4
Seg. bounds	[0.2, 0.9] m
Seg. lengths	[0.56, 0.90, 0.90, 0.90] m
Defl. (PWL)	[58.1, 33.5, 60.0] deg
Run time	5.53 s
CartDist	1.2 m
Package pos.	Lower right
Dist. to pack.	0.0 m

---

5 segments - Many non-deflecting sections observed.

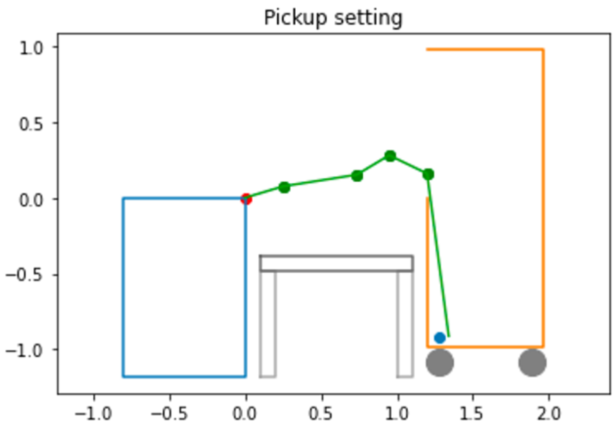

Figure B.6: *Left end point, 5 segments.*

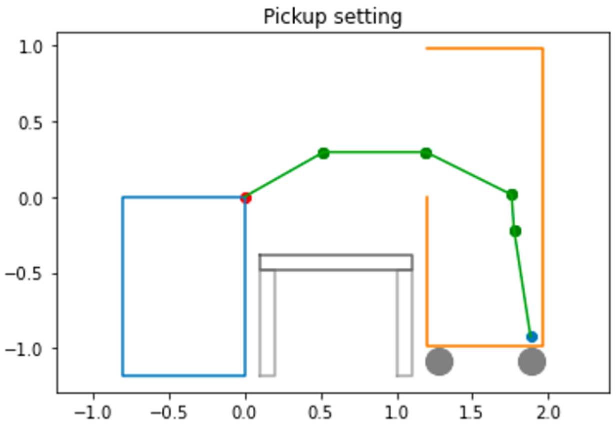

Figure B.7: *Right end point, 5 segments.*

Nr. of seg.	5
Seg. bounds	[0.2, 1.4] m
Seg. lengths	[0.26, 0.49, 0.25, 0.28, 1.08] m
Defl. (PWL)	[[7.9, -22.2, 56.3, 57.0] deg
Run time	600.04 s
CartDist	1.2 m
Package pos.	Lower left
Dist. to pack.	0.066 m

Nr. of seg.	5
Seg. bounds	[0.2, 0.9] m
Seg. lengths	[0.60, 0.68, 0.63, 0.23, 0.71] m
Defl. (PWL)	[29.4, 26.1, 60.0, -4.9] deg
Run time	6.29 s
CartDist	1.2 m
Package pos.	Lower right
Dist. to pack.	0.0 m

---

6 segments - Many non-deflecting segments and obvious unnecessary turns observed.

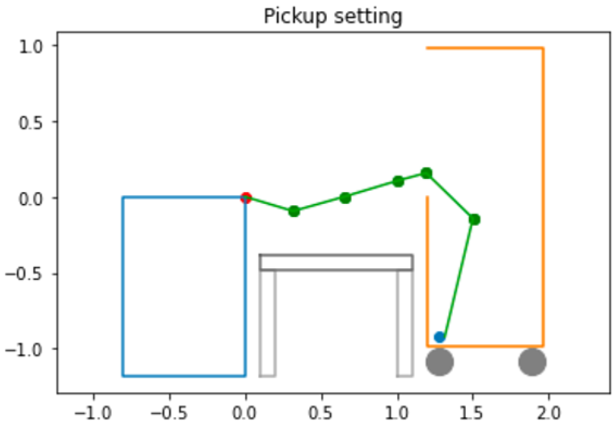

Figure B.8: *Left end point, 6 segments.*

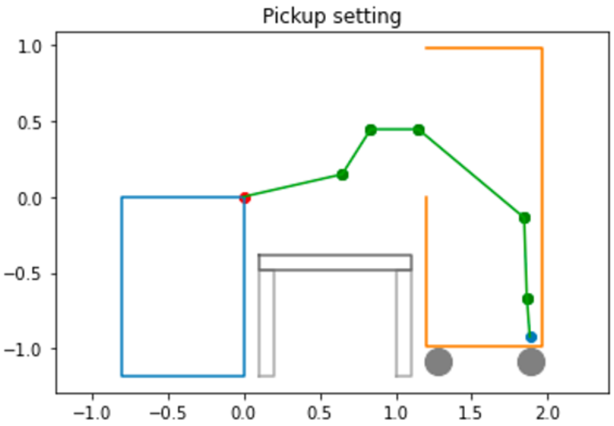

Figure B.9: *Right end point, 6 segments.*

Nr. of seg.	6
Seg. bounds	[0.2, 0.8] m
Seg. lengths	[0.33, 0.35, 0.36, 0.2, 0.43, 0.8] m
Defl. (PWL)	[-32.4, -1.0, 1.6, 59.0, 59.5] deg
Run time	300.02 s
CartDist	1.2 m
Package pos.	Lower left
Dist. to pack.	0.041 m

Nr. of seg.	6
Seg. bounds	[0.2, 1.0] m
Seg. lengths	[0.66, 0.35, 0.31, 0.91, 0.53, 0.26] m
Defl. (PWL)	[-44.8, 57.5, 39.6, 50.3, -4.3] deg
Run time	68.05 s
CartDist	1.2 m
Package pos.	Lower right
Dist. to pack.	0.0 m

Blowing up proportions

Now, the results will be shown for the situations with blown up proportions.

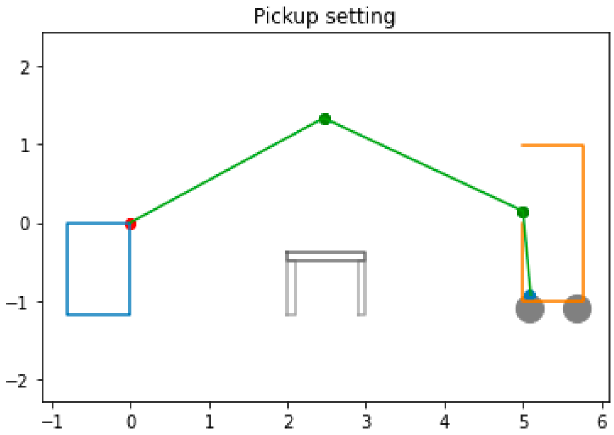

Figure B.10: *Left end point, 3 segments, 5 meter distance.*

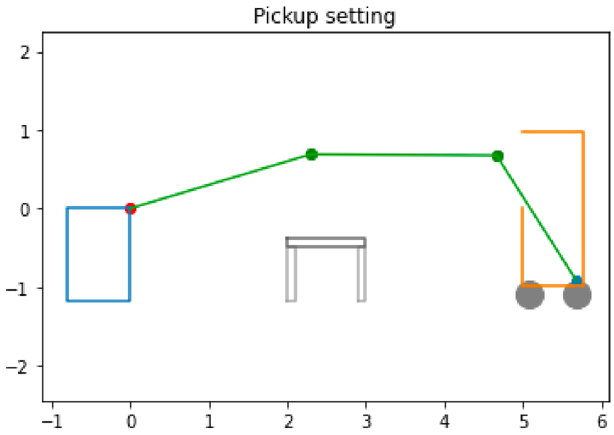

Figure B.11: *Right end point, 3 segments, 5 meter distance.*

Nr. of seg.	3
Seg. bounds	[0.2, 2.8] m
Seg. lengths	[2.8, 2.8, 1.07] m
Defl. (PWL)	[52.7, 60.0] deg
Run time	1044.61 s
CartDist	5 m
Package pos.	Lower left
Dist. to pack.	0.026 m

Nr. of seg.	3
Seg. bounds	[0.2, 2.4] m
Seg. lengths	[2.399, 2.367, 1.893] m
Defl. (PWL)	[17.0, 57.0] deg
Run time	1.89 s
CartDist	5 m
Package pos.	Lower right
Dist. to pack.	0.0 m

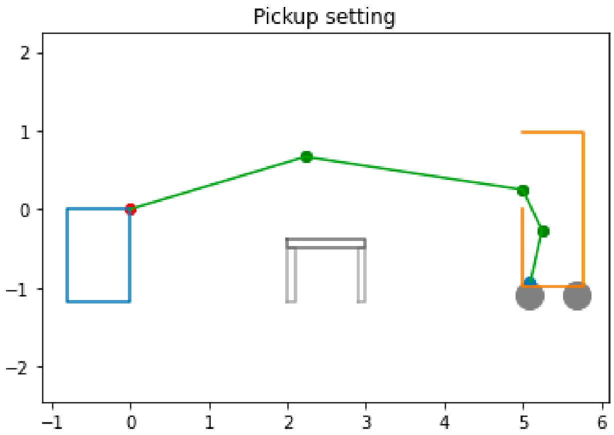

Figure B.12: *Left end point, 4 segments, 5 meter distance.*

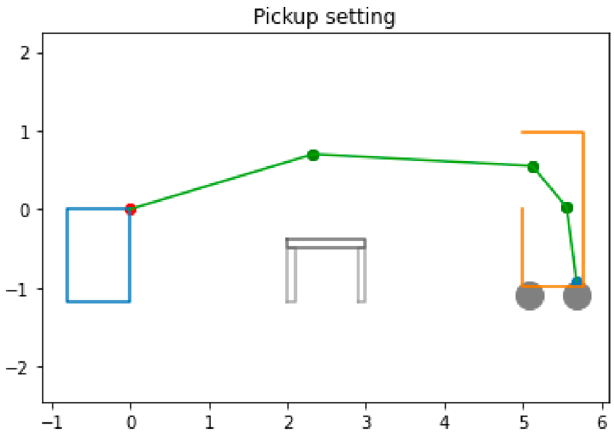

Figure B.13: *Right end point, 4 segments, 5 meter distance.*

Nr. of seg.	4
Seg. bounds	[0.2, 2.8] m
Seg. lengths	[2.33, 2.8, 0.57, 0.67] m
Defl. (PWL)	[25.1, 56.1, 37.8] deg
Run time	8.2 s
CartDist	5 m
Package pos.	Lower left
Dist. to pack.	0.024 m

Nr. of seg.	4
Seg. bounds	[0.2, 2.8] m
Seg. lengths	[2.43, 2.79, 0.68, 0.95] m
Defl. (PWL)	[19.7, 47.2, 32.2] deg
Run time	70.68 s
CartDist	5 m
Package pos.	Lower right
Dist. to pack.	0.0 m

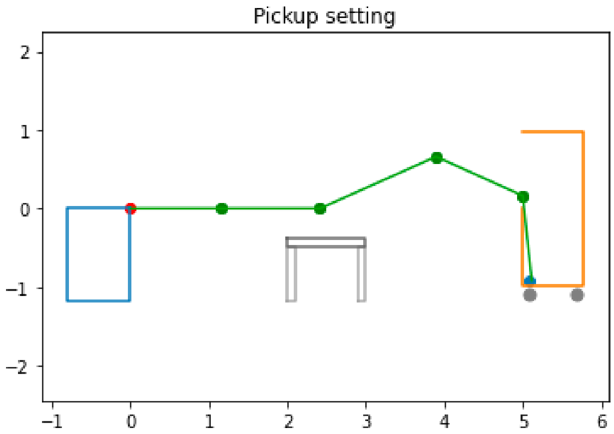

Figure B.14: *Left end point, 5 segments, 5 meter distance.*

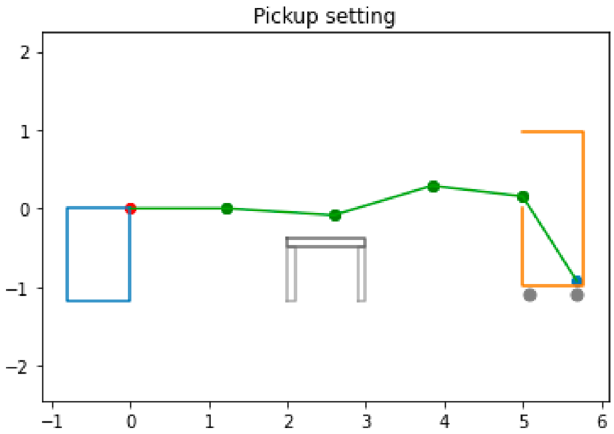

Figure B.15: *Right end point, 5 segments, 5 meter distance.*

Nr. of seg.	5
Seg. bounds	[0.2, 4.0] m
Seg. lengths	[1.16, 1.26, 1.62, 1.21, 1.08] m
Defl. (PWL)	[0.0, -23.6, 47.5, 60.0] deg
Run time	900.06 s
CartDist	5 m
Package pos.	Lower left
Dist. to pack.	0.039 m

Nr. of seg.	5
Seg. bounds	[0.2, 4.0] m
Seg. lengths	[1.23, 1.36, 1.31, 1.16, 1.28] m
Defl. (PWL)	[3.5, -20.2, 23.2, 50.7] deg
Run time	900.019 s
CartDist	5 m
Package pos.	Lower right
Dist. to pack.	0.002 m

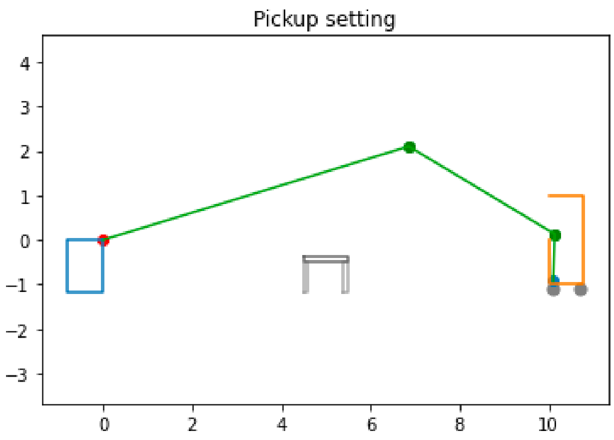

Figure B.16: *Left end point, 3 segments, 10 meter distance.*

Nr. of seg.	3
Seg. bounds	[0.2, 9] m
Seg. lengths	[7.17, 3.82, 1.05] m
Defl. (PWL)	[47.9, 59.3] deg
Run time	19.13 s
CartDist	10 m
Package pos.	Lower left
Dist. to pack.	0.024 m

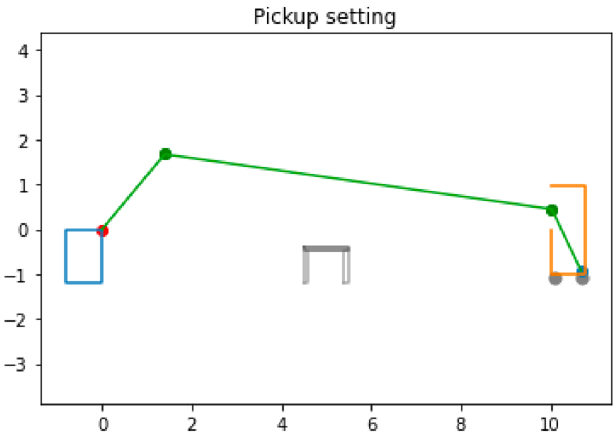

Figure B.17: *Right end point, 3 segments, 10 meter distance.*

Nr. of seg.	3
Seg. bounds	[0.2, 9] m
Seg. lengths	[2.18, 8.72, 1.52] m
Defl. (PWL)	[58.1, 56.6] deg
Run time	1.25 s
CartDist	10 m
Package pos.	Lower right
Dist. to pack.	0.0 m

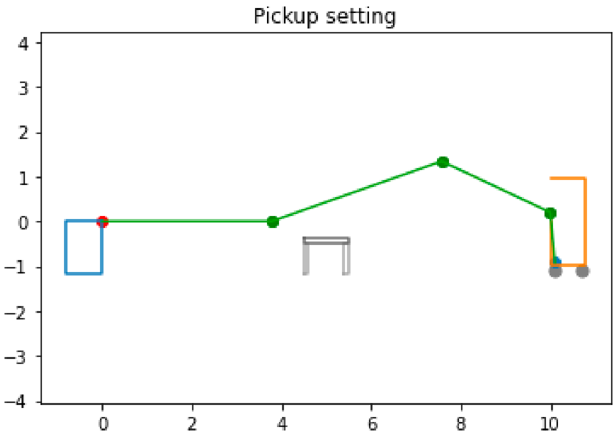

Figure B.18: *Left end point, 4 segments, 10 meter distance.*

Nr. of seg.	4
Seg. bounds	[0.2, 9] m
Seg. lengths	[3.79, 4.02, 2.68, 1.13] m
Defl. (PWL)	[-19.3, 44.1, 60.0] deg
Run time	600.01 s
CartDist	10 m
Package pos.	Lower left
Dist. to pack.	0.024 m

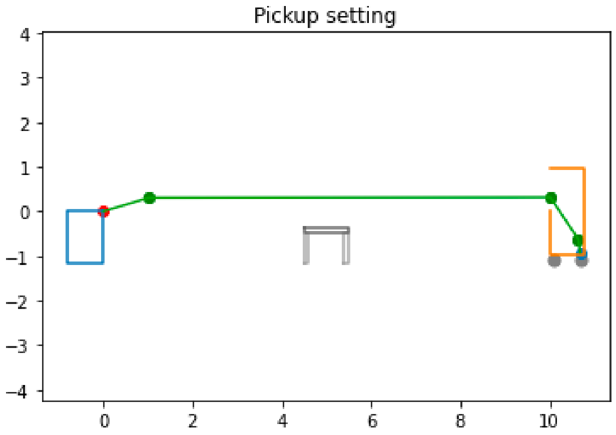

Figure B.19: *Right end point, 4 segments, 10 meter distance.*

Nr. of seg.	4
Seg. bounds	[0.2, 9] m
Seg. lengths	[1.06, 9.0, 1.13, 0.3] m
Defl. (PWL)	[16.6, 56.4, 26.1] deg
Run time	4.02 s
CartDist	10 m
Package pos.	Lower right
Dist. to pack.	0.0 m

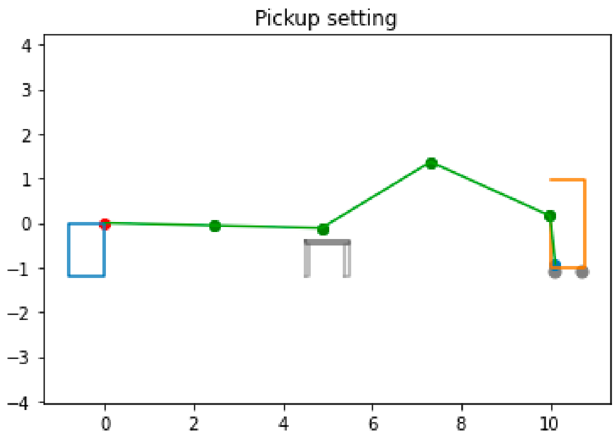

Figure B.20: *Left end point, 5 segments, 10 meter distance.*

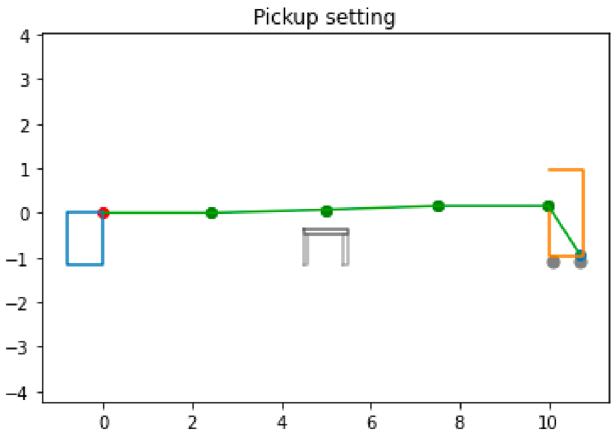

Figure B.21: *Right end point, 5 segments, 10 meter distance.*

Nr. of seg.	5
Seg. bounds	[0.2, 9] m
Seg. lengths	[2.45, 2.43, 2.86, 2.94, 1.08]m
Defl. (PWL)	[0.0, -32.6, 55.1, 60.0] deg
Run time	1800.02 s
CartDist	10 m
Package pos.	Lower left
Dist. to pack.	0.039 m

Nr. of seg.	5
Seg. bounds	[0.2, 9] m
Seg. lengths	[2.44, 2.56, 2.52, 2.48, 1.29] m
Defl. (PWL)	[-1.5, -0.5, 2.0, 56.9] deg
Run time	2481.55 s
CartDist	10 m
Package pos.	Lower right
Dist. to pack.	0.011 m

Belt runs

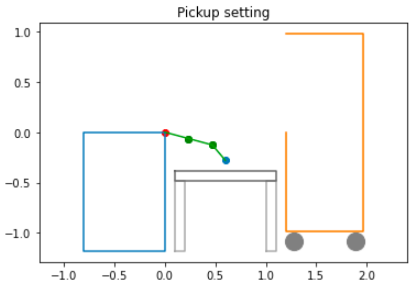

Figure B.22: *Belt end point 3 segments.*

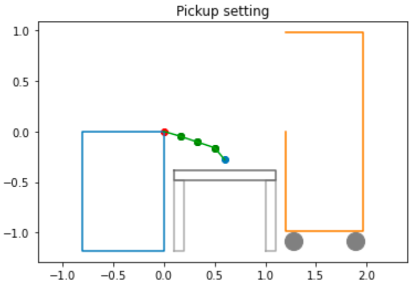

Figure B.24: *Belt end point 4 segments.*

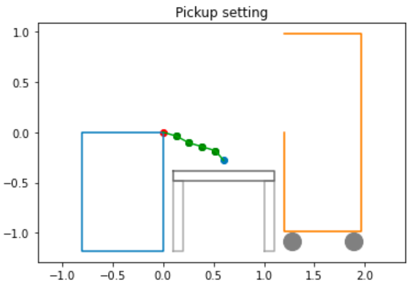

Figure B.26: *Belt end point 5 segments.*

Nr. of seg.	3
Seg. bounds	[0.1, 0.8] m
Seg. lengths	[0.24, 0.24, 0.20] m
Defl. (PWL)	[-0.0, 35.0] deg
Run time	5.0 s
CartDist	1.2 m
Package pos.	Belt
Dist. to pack.	0.0 m

Figure B.23: *3 segment belt run*

Nr. of seg.	4
Seg. bounds	[0.1, 0.8] m
Seg. lengths	[0.18, 0.17, 0.18, 0.15] m
Defl. (PWL)	[1.8, -0.2, 31.8] deg
Run time	300.02 s
CartDist	1.2 m
Package pos.	Belt
Dist. to pack.	0.0 m

Figure B.25: *4 segment belt run*

Nr. of seg.	5
Seg. bounds	[0.1, 0.8] m
Seg. lengths	[0.14, 0.14, 0.14, 0.14, 0.13] m
Defl. (PWL)	[11.0, -11.0, 0.0, 33.3] deg
Run time	300.01 s
CartDist	1.2 m
Package pos.	Belt
Dist. to pack.	0.0 m

Figure B.27: *5 segment belt run*

Figure B.28: *Side-by-side Images with Tables*

B.2. Top view mathematical model

The second model encompasses a simple 2D top view of the situation.

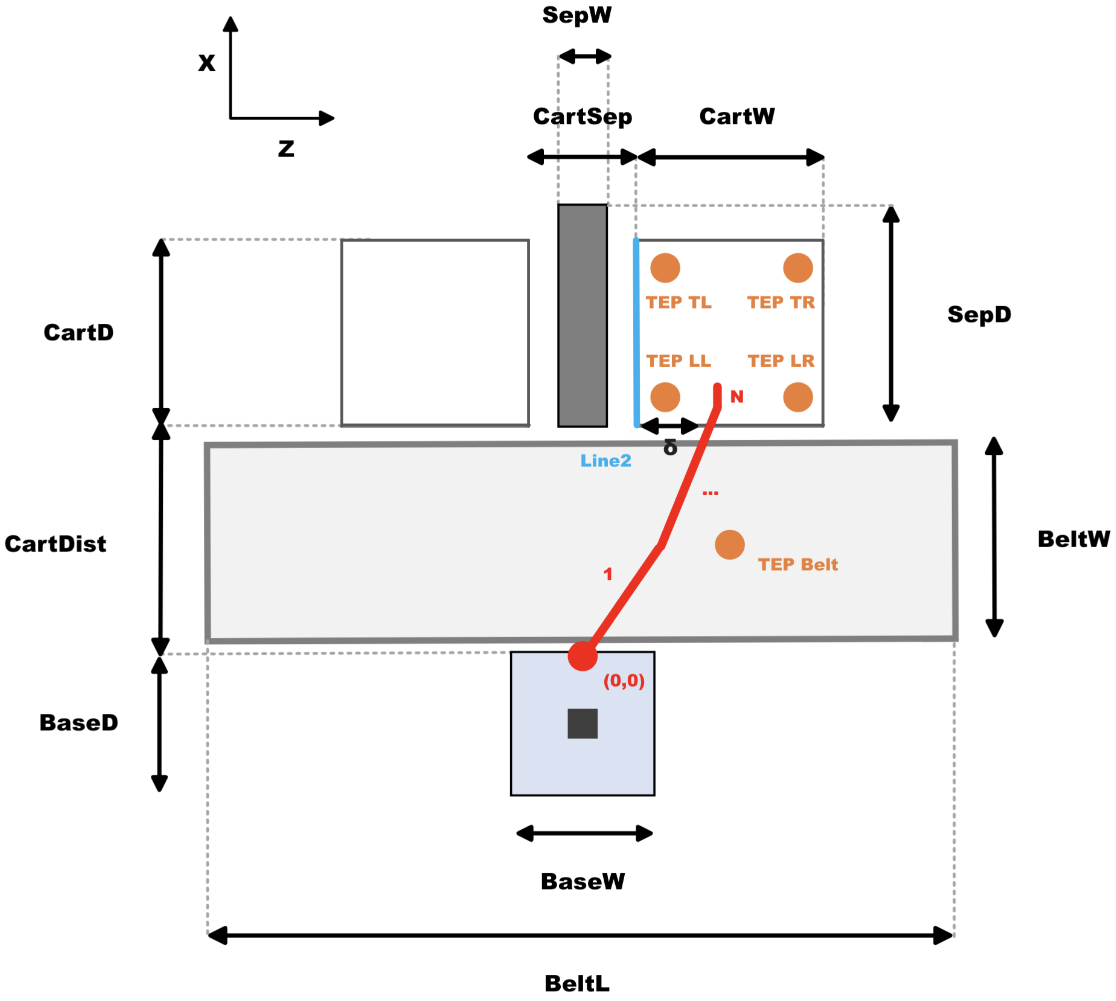

Figure B.29: *view model situational parameters explanation.*

B.2.1. Indices

Table B.8: *Indices*

Index	Description	
i	Point index of line segment	$i \in I$
j	Segment index	$j \in J$

Table B.9: *Sets*

Sets	Description	
I	Segment points	[1, 2]
J	Segments	[1, ..., N]

Table B.10: *Subsets*

Subset	Description		
B	Segments subset	[1, ..., N-1]	$B \in J$

B.2.2. Parameters

As with the side view, the parameters consist of fixed parameters, changeable parameters and 5 different end points, i.e. potential pick-up locations.

Table B.11: *Fixed parameters*

Parameter	Description	Value
BaseW	Width of the base of the robot	0.8
Base D	Depth of the base of the robot	0.8
CartD	Depth of cart	0.760
CartW	Width of the cart	0.760
BeltL	Length of belt conveyor	3
BeltW	Width of belt	1
SepW	Width of separation wall between carts	0.4
SepD	Depth of separation wall between carts	1
CartSep	Distance between carts	0.6
δ	Clearance the robot needs to pass the door	0.15
θ	Range parameter	0.0001
M	Big M	1000
EPM	End point margin w.r.t. cart	0.1

Table B.12: *Changeable parameters*

Parameter		
CartDist	Perpendicular distance between robot base and cart.	1.2
N	Number of robot segments.	2, 3, ..., N
MaxL	Maximum length of each module.	1.4
MinL	Minimum length of each module.	0.2
MaxD	Max deflection of each segment.	60
Line2 ([x1, y1, x2, y2])	[0.5 · CartSep, CartDist, 0.5 · CartSep, CartDist+CartD]	

Table B.13: *End points for arm model top view.*

TopEndPoint (TEP)	[X,Y]
TopLeft (TL)	[0.5 · CartSep+EPM, CartDist+CartD-EPM]
TopRight (TR)	[0.5 · CartSep+CartW-EPM, CartDist+CartD-EPM]
LowerRight (LR)	[0.5 · CartSep+CartW-EPM, CartDist+EPM]
LowerLeft (LL)	[0.5 4 CartSep+EPM, CartDist+EPM]
Belt	[0, 0.5 · CartDist]

B.2.3. Decision variables

This model does not incorporate a deflection constraint since the last segment of the arm will go down steeply. This could lead to very large deflections from a top view but this would not indicate a large deflection in the true situation. Therefore this model can comprise of only 5 decision variables.

Table B.14: *Decision variables*

DV	Description
Z_{ij}	Z-coordinate of point i of segment j. i takes value 1 for the starting point of segment j and 2 for the end point of segment j.
X_{ij}	X-coordinate of point i of segment j. i takes value 1 for the starting point of segment j and 2 for the end point of segment j.
$C2_j$	Binary decision variable indicating if segment j crosses Line2. Takes value 0 when it does not cross Line2 and value 1 when it does.
dZ_j	Inverse of difference between Z_{1j} and Z_{2j}. Auxiliary variable to achieve division.
$S2_j$	Slope of segment j.

B.2.4. Objective

As with the side view model, reaching the end point shall be considered the main objective, with minimizing the length of the arm as a sub objective. Again, appropriate weights are implemented.

$$Min\ \frac{999}{1000}((Z_{2N} - TEP[0])^2 + (X_{2N} - TEP[1])^2) + \frac{1}{1000}\sum_{j\in J}((Z_{2j} - Z_{1j})^2 + (X_{2j} - X_{1j})^2) \tag{B.22}$$

B.2.5. Constraints

1. Connect consecutive coordinates.

$$Z_{2j} - Z_{1j+1} = 0, \ \forall j \in B \tag{B.23}$$

$$X_{2j} - X_{1j+1} = 0, \ \forall j \in B \tag{B.24}$$

2. Start at the origin.

$$Z_{11} = 0 \tag{B.25}$$

$$X_{11} = 0 \tag{B.26}$$

3. Maximum module length.

$$(Z_{2j} - Z_{1j})^2 + (X_{2j} - X_{1j})^2 \leq MaxL^2, \ \forall j \in J \tag{B.27}$$

4. Minimum module length.

$$(Z_{2j} - Z_{1j})^2 + (X_{2j} - X_{1j})^2 \geq MinL^2, \ \forall j \in J \tag{B.28}$$

5. Define behavior of binary DV C2 to be 1 when crossing Line2 and 0 if not.

$$(Z_{1j} - Line2[0]) \cdot (Z_{2j} - Line2[0]) \leq -\theta + M \cdot (1 - C2_j), \ \forall j \in J \tag{B.29}$$

$$(Z_{1j} - Line2[0]) \cdot (Z_{2j} - Line2[0]) \geq \theta - M \cdot C2_j, \ \forall j \in J \tag{B.30}$$

6. Prepare slope decision variable.

$$dZ_j \cdot (Z_{2j} - Z_{1j}) = 1, \ \forall j \in J \tag{B.31}$$

7. Define slope of segment.

$$S2_j = (X_{2j} - X_{1j}) \cdot dZ_j, \ \forall j \in J \tag{B.32}$$

8. Ensure that segments that cross the entrance of the cart do so before Line2.

$$S2_j \cdot Line2[0] - S2_j \cdot Z_{1j} + X_{1j} \leq Line2[1] - \delta + M \cdot (1 - C2_j), \ \forall j \in J \tag{B.33}$$

9. The tip of the arm must end inside the cart. (Should be excluded when Belt end point is chosen.)

$$Z_{2N} \geq 0.5 \cdot CartSep + \theta \tag{B.34}$$

10. Binary constraints.

$$C1_j \in 0, 1, \ \forall j \in J \tag{B.35}$$

B.2.6. All results 2D top view model

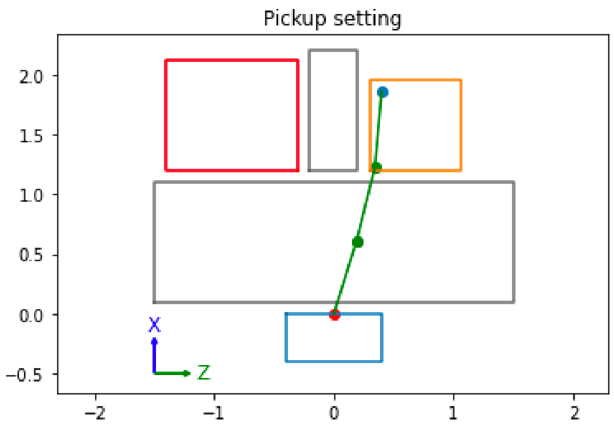

Figure B.30: *3 segment top view top left*

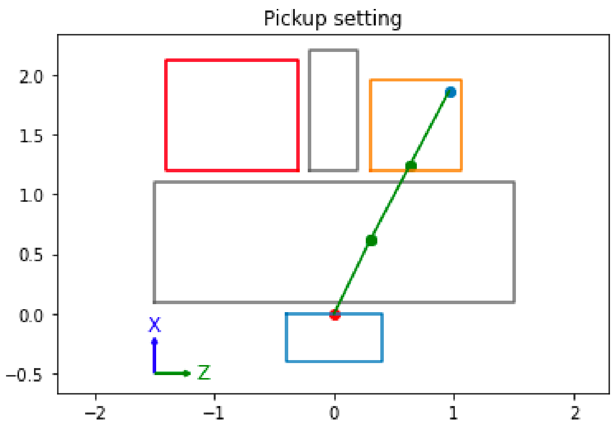

Figure B.31: *3 segment top view top right*

Nr. of seg.	3
Seg. lengths	[0.64, 0.63, 0.64] m
Run time	64.24 s
Package pos.	Top left
Dist. to pack.	0.001 m

Nr. of seg.	3
Seg. lengths	[0.69, 0.7, 0.7] m
Run time	0.40 s
Package pos.	Top right
Dist. to pack.	0.001 m

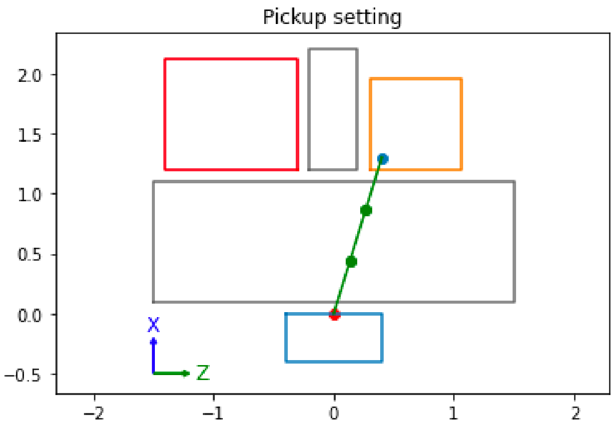

Figure B.32: *3 segment top view bottom left*

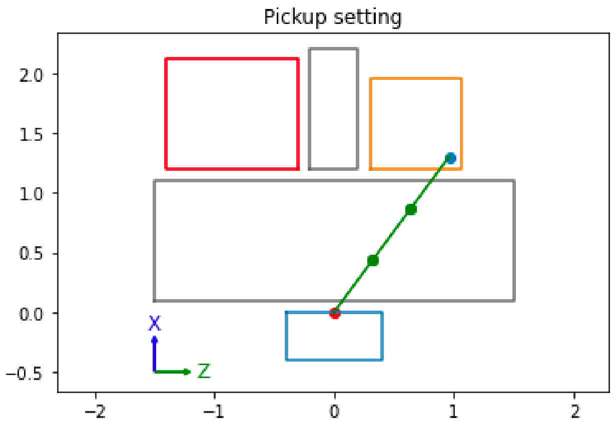

Figure B.33: *3 segment top view bottom right*

Nr. of seg.	3
Seg. lengths	[0.45, 0.45, 0.45] m
Run time	0.27 s
Package pos.	Lower left
Dist. to pack.	0.0 m

Nr. of seg.	3
Seg. lengths	[0.54, 0.54, 0.54] m
Run time	0.16 s
Package pos.	Lower right
Dist. to pack.	0.001 m

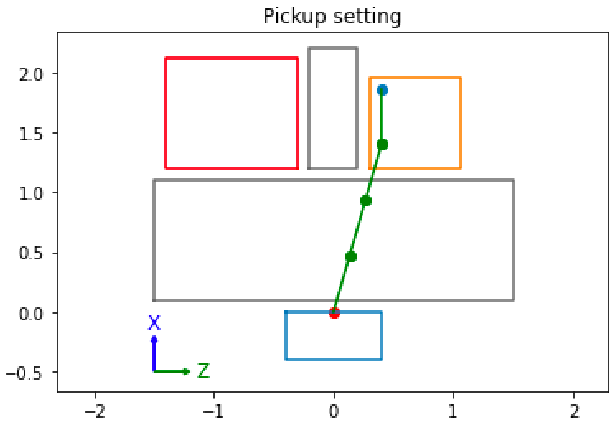

Figure B.34: *4 segment top view top left*

Nr. of seg.	4
Seg. lengths	[0.49, 0.49, 0.49, 0.46] m
Run time	120.01 s
Package pos.	Top left
Dist. to pack.	0.001 m

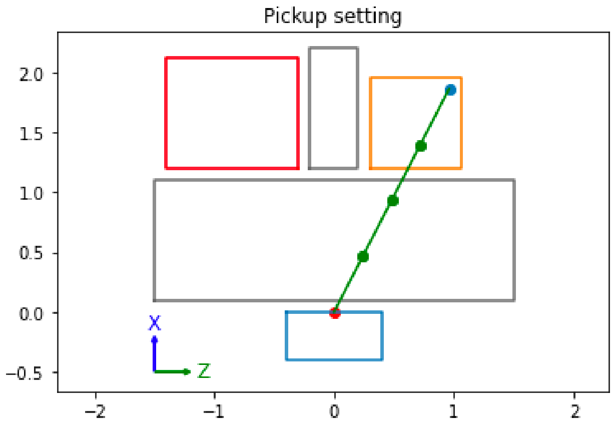

Figure B.35: *4 segment top view top right*

Nr. of seg.	4
Seg. lengths	[0.52, 0.52, 0.52, 0.52] m
Run time	0.78 s
Package pos.	Top right
Dist. to pack.	0.001 m

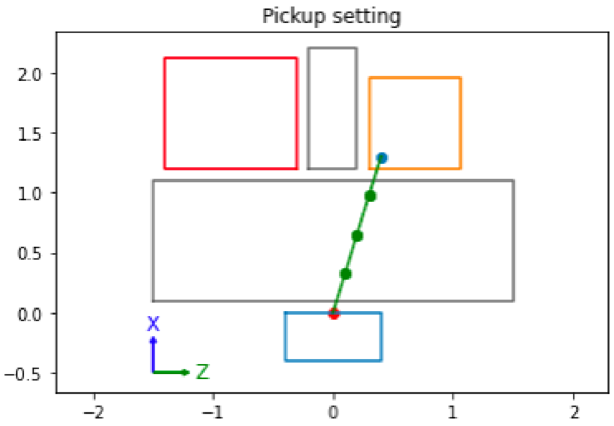

Figure B.36: *4 segment top view bottom left*

Nr. of seg.	4
Seg. lengths	[0.34, 0.34, 0.34, 0.34] m
Run time	0.90 s
Package pos.	Lower left
Dist. to pack.	0.001 m

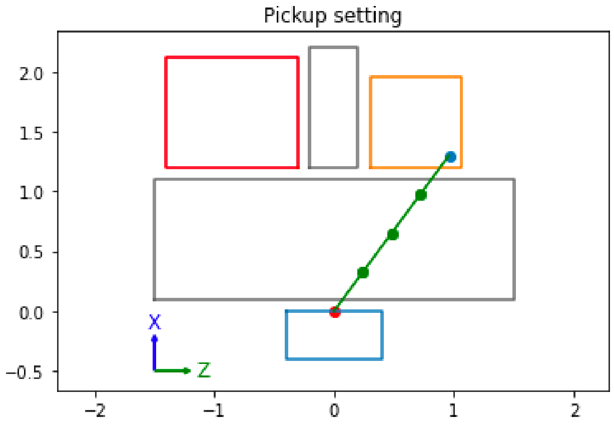

Figure B.37: *4 segment top view bottom right*

Nr. of seg.	4
Seg. lengths	[0.40, 0.40, 0.40, 0.40] m
Run time	0.75 s
Package pos.	Lower right
Dist. to pack.	0.0 m

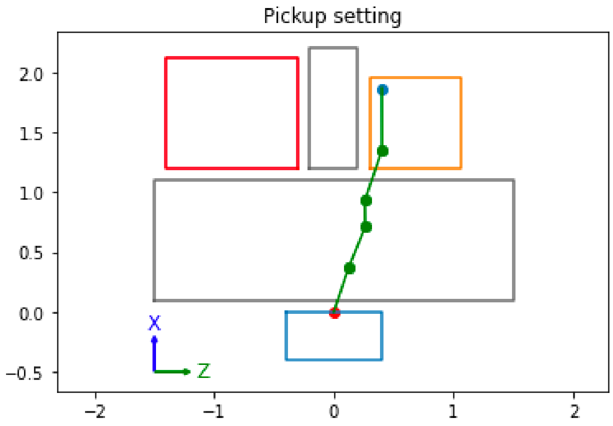

Figure B.38: *5 segment top view top left*

Nr. of seg.	5
Seg. lengths	[0.39, 0.37, 0.22, 0.44, 0.52] m
Run time	300.02 s
Package pos.	Top left
Dist. to pack.	0.009 m

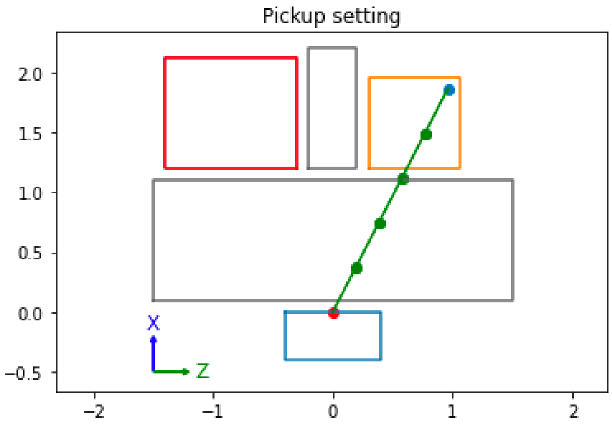

Figure B.39: *5 segment top view top right*

Nr. of seg.	5
Seg. lengths	[0.42, 0.42, 0.42, 0.42, 0.42] m
Run time	2.34 s
Package pos.	Top right
Dist. to pack.	0.0 m

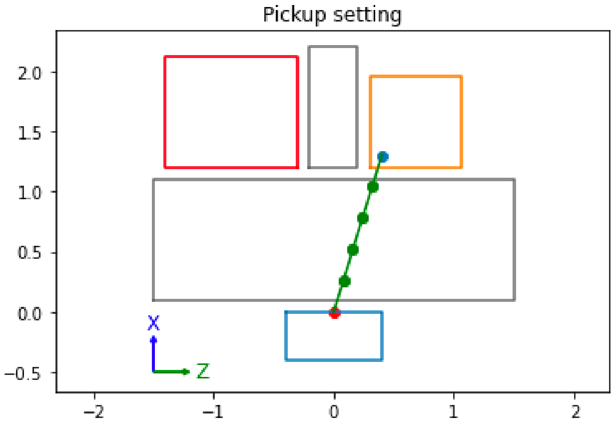

Figure B.40: *5 segment top view bottom left*

Nr. of seg.	5
Seg. lengths	[0.27, 0.27, 0.27, 0.27, 0.27] m
Run time	0.93 s
Package pos.	Lower left
Dist. to pack.	0.0 m

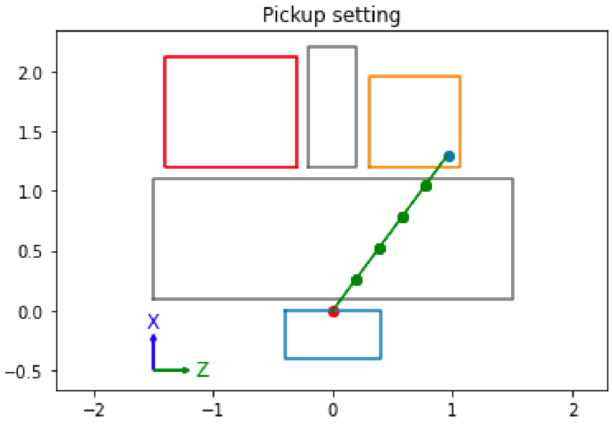

Figure B.41: *5 segment top view bottom right*

Nr. of seg.	5
Seg. lengths	[0.32, 0.32, 0.32, 0.32, 0.32] m
Run time	1.19 s
Package pos.	Lower right
Dist. to pack.	0.0 m

B.3. Sequential 3D mathematical model

The sequential 3D model is a merger of the models found in section B.1 and section B.2. First the side view model is run identically as found in section B.1. Secondly, the top view model is run, where the decision variable X_{ij} is replaced as a parameter, which uses the values of X found in the side view model.

B.3.1. Indices

Table B.15: *Indices*

Index	Description	
i	Point index of line segment	$i \in I$
j	Segment index	$j \in J$

Table B.16: *Sets*

Sets	Description	
I	Segment points	[1, 2]
J	Segments	[1, ..., N]

Table B.17: *Subsets*

Subset	Description		
B	Segments subset	[1, ..., N-1]	$B \in J$

B.3.2. Parameters

The parameters of this model uses a merger of the parameters from the side view model and the top view model. As with the top view model 5 end points are used.

Table B.18: *Fixed parameters*

Parameter	Description	Value
BaseH	Height of the base of the robot	1.18
BaseW	Width of the base of the robot	0.8
BaseD	Depth of the base of the robot	0.8
DoorH	Height of the lower door of the cart	0.99
LoadH	Loading height of the cart	0.185
CartD	Depth of the cart	0.760
CartW	Width of the cart	0.760
WallH	Height of cart walls excluding loading height	1.965
BeltH	Height of belt conveyor	0.8
BeltW	Width of belt	1
BeltL	Length of belt	3
EPM	End point margin w.r.t. the cart	0.1
CartSep	Distance between two carts	0.6
SepW	Width of cart separating wall	0.4
SepD	Depth of cart separating wall	1
δ	Clearance the robot needs to pass the door	0.15
θ	Less significant range parameter	0.0001
M	Big M	1000
lbz	PWL arctan lower bound	-15
ubz	PWL arctan upper bound	15

Table B.19: *Changeable parameters*

Parameter		
CartDist	Perpendicular distance between robot base and cart.	1.2
N	Number of robot segments.	2, 3, ..., N
MaxL	Maximum length of each module.	1.4
MinL	Minimum length of each module.	0.2
MaxD	Max deflection of each segment in XY-plane.	60
Line1 ([x1, y1, x2, y2])	[CartDist, 0, CartDist, -DoorH]	
Line2 ([x1, y1, x2, y2])	$[0.5 \cdot CartSep, CartDist, 0.5 \cdot CartSep, CartDist + CartD]$	

Table B.21: *Decision variables*

DV	Description
X_{ij}	X-coordinate of point i of segment j. i takes value 1 for the starting point of segment j and 2 for the end point of segment j.
Y_{ij}	Y-coordinate of point i of segment j. i takes value 1 for the starting point of segment j and 2 for the end point of segment j.
$C1_j$	Binary decision variable indicating if segment j crosses line 1. Takes value 0 when it does not cross line 1 and value 1 when it does.
dX_j	Inverse of difference between X_{1j} and X_{2j}. Auxiliary variable to achieve division.
$S1_j$	Slope of segment j.
A_j	Angle of segment j with respect to horizontal in radians.
u_j	Binary decision variable to indicate if segment j goes back in x-direction.

Table B.20: *End points for arm model.*

EndPoints		
Top left (TL)	EP	[CartDist+CartD-EPM, -BaseH+1.4·$LoadH$]
	TEP	[0.5·$CartSep + EPM, CartDist + CartD - EPM$]
Top right (TR)	EP	[CartDist+CartD-EPM, -BaseH+1.4·$LoadH$]
	TEP	[0.5·$CartSep + CartW - EPM, CartDist + CartD - EPM$]
Lower right (LR)	EP	[CartDist+EPM, -BaseH+1.4·$LoadH$]
	TEP	[0.5·$CartSep + CartW - EPM, CartDist + EPM$]
Lower left (LL)	EP	[CartDist+EPM, -BaseH+1.4·$LoadH$]
	TEP	[0.5·$CartSep + EPM, CartDist + EPM$]
Belt	EP	[CartDist-0.6, -BaseH+BeltH+0.1]
	TEP	[0.5·$CartSep + 0.5 \cdot CartW, CartDist - 0.6$]

B.3.3. Decision variables model 1

B.3.4. Objective function model 1

The objective function has been copied from the 2D side view model.

$$Min\ \frac{999}{1000}((X_{2N} - EP[0])^2 + (Y_{2N} - EP[1])^2) + \frac{1}{1000}\sum_{j \in J}((X_{2j} - X_{1j})^2 + (Y_{2j} - Y_{1j})^2) \tag{B.36}$$

B.3.5. Constraints model 1

1. Connect consecutive coordinates.

$$X_{2j} - X_{1j+1} = 0, \ \ \forall j \in B \tag{B.37}$$

$$Y_{2j} - Y_{1j+1} = 0, \ \ \forall j \in B \tag{B.38}$$

2. Start at the origin.

$$X_{11} = 0 \tag{B.39}$$

$$Y_{11} = 0 \tag{B.40}$$

3. Maximum module length.

$$(X_{2j} - X_{1j})^2 + (Y_{2j} - Y_{1j})^2 \leq MaxL^2, \ \ \forall j \in J \tag{B.41}$$

4. Minimum module length.

$$(X_{2j} - X_{1j})^2 + (Y_{2j} - Y_{1j})^2 \geq MinL^2, \ \ \forall j \in J \tag{B.42}$$

5. Define behavior of binary DV C1 to be 1 when crossing Line1 and 0 if not.

$$(Line1[0] - X_{1j}) \cdot (Line1[0] - X_{2j}) \leq -\theta + M \cdot (1 - C1_j), \ \ \forall j \in J \tag{B.43}$$

$$(Line1[0] - X_{1j}) \cdot (Line1[0] - X_{2j}) \geq \theta - M \cdot C1_j, \ \ \forall j \in J \tag{B.44}$$

6. Prepare slope decision variable.

$$dX_j \cdot (X_{2j} - X_{1j}) = 1 - 2 \cdot u_j, \ \ \forall j \in J \tag{B.45}$$

7. Define slope of segments.

$$S1_j - 2 \cdot u_j \cdot S_j = (Y_{2j} - Y_{1j}) \cdot dX_j, \ \ \forall j \in J \tag{B.46}$$

8. Ensure that segments that cross the entrance of the cart do so above Line1 and below the top of the cart.

$$S1_j \cdot Line1[0] - S1_j \cdot X_{1j} + Y_{1j} + M \cdot (1 - C1_j) \geq Line1[1] + \delta, \ \ \forall j \in J \tag{B.47}$$

$$S1_j \cdot Line1[0] - S1_j \cdot X_{1j} + Y_{1j} + M \cdot (1 - C1_j) \leq -DoorH + WallH \\ -\delta + M \cdot (1 - C1_j), \ \ \forall j \in J \tag{B.48}$$

9. Piece-wise linear (PWL) arc tangent function to define angles of segments w.r.t. horizontal.

$$A_j = PWL(arctan(S1_j)), \ \ \forall j \in J \tag{B.49}$$

10. Define maximum deflection of segments.

$$\frac{A_j - A_{j+1}}{\pi} \cdot 180 + 180 \cdot u_{j+1} \leq MaxD, \ \ \forall j \in B \tag{B.50}$$

$$\frac{A_j - A_{j+1}}{\pi} \cdot 180 + 180 \cdot u_{j+1} \geq -MaxD, \ \ \forall j \in B \tag{B.51}$$

11. Define behavior of binary DV u to take value 1 when segment j goes back in X-direction and 0 when not.

$$X_{2j} - X_{1j} \leq M \cdot (1 - u_j), \ \ \forall j \in J \tag{B.52}$$

$$X_{2j} - X_{1j} \geq -M \cdot u_j, \ \ \forall j \in J \tag{B.53}$$

12. The tip of the arm must end inside the cart. (Should be excluded when Belt end point is chosen.)

$$X_{2N} \geq CartDist + \theta \tag{B.54}$$

13. Binary constraints.

$$C1_j, u_j \in 0, 1, \ \ \forall j \in J \tag{B.55}$$

14. Angle bounds.

$$-\frac{1}{2}\pi \leq A_j \leq \frac{1}{2}\pi, \ \ \forall j \in J \tag{B.56}$$

B.3.6. Decision variables model 2

Table B.22: *Decision variables*

DV	Description
Z_{ij}	Z-coordinate of point i of segment j. i takes value 1 for the starting point of segment j and 2 for the end point of segment j.
$C2_j$	Binary decision variable indicating if segment j crosses Line2. Takes value 0 when it does not cross Line2 and value 1 when it does.
dZ_j	Inverse of difference between Z_{1j} and Z_{2j}. Auxiliary variable to achieve division.
$S2_j$	Slope of segment j.

B.3.7. Objective function model 2

Since X has become a (fixed) parameter for this model, some terms from the objective function of the top view model in section B.2 have become constants. Since they do not influence the objective function any more they are removed for simplicity. The objective function of the second model in the sequential optimization is found in Equation B.57.

$$Min \ \frac{999}{1000}((Z_{2N} - TEP[0])^2 + \frac{1}{1000}\sum_{j \in J}((Z_{2j} - Z_{1j})^2) \tag{B.57}$$

B.3.8. Constraints model 2

1. Connect consecutive coordinates.

$$Z_{2j} - Z_{1j+1} = 0, \ \ \forall j \in B \tag{B.58}$$

2. Start at the origin.

$$Z_{11} = 0 \tag{B.59}$$

3. Maximum module length.

$$(Z_{2j} - Z_{1j})^2 + (x_{2j} - x_{1j})^2 \leq MaxL^2, \ \ \forall j \in J \tag{B.60}$$

4. Minimum module length.

$$(Z_{2j} - Z_{1j})^2 + (x_{2j} - x_{1j})^2 \geq MinL^2, \ \ \forall j \in J \tag{B.61}$$

5. Define behavior of binary DV C2 to be 1 when crossing Line2 and 0 if not.

$$(Z_{1j} - Line2[0]) \cdot (Z_{2j} - Line2[0]) \leq -\theta + M \cdot (1 - C2_j), \ \ \forall j \in J \tag{B.62}$$

$$(Z_{1j} - Line2[0]) \cdot (Z_{2j} - Line2[0]) \geq \theta - M \cdot C2_j, \ \ \forall j \in J \tag{B.63}$$

6. Prepare slope decision variable.

$$dZ_j \cdot (Z_{2j} - Z_{1j}) = 1, \quad \forall j \in J \tag{B.64}$$

7. Define slope of segment.

$$S2_j = (x_{2j} - x_{1j}) \cdot dZ_j, \quad \forall j \in J \tag{B.65}$$

8. Ensure that segments that cross the entrance of the cart do so before Line2.

$$S2_j \cdot Line2[0] - S2_j \cdot Z_{1j} + x_{1j} \leq Line2[1] - \delta + M \cdot (1 - C2_j), \quad \forall j \in J \tag{B.66}$$

9. Ensure that arm stays within the perimeter of the cart in Z-direction.

$$Z_{ij} \leq 0.5 \cdot CartSep + CartW, \quad \forall i \in I, \forall j \in J \tag{B.67}$$

10. The tip of the arm must end inside the cart. (Should be excluded when Belt end point is chosen.)

$$Z_{2N} \geq 0.5 \cdot CartSep + \theta \tag{B.68}$$

B.3.9. All 3D model results

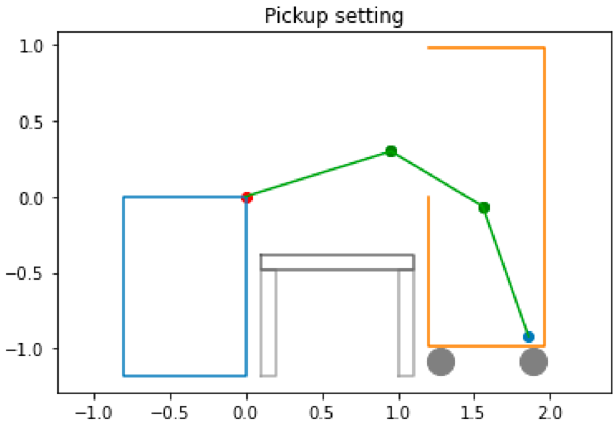

Figure B.42: *3 segment sequential side view top left*

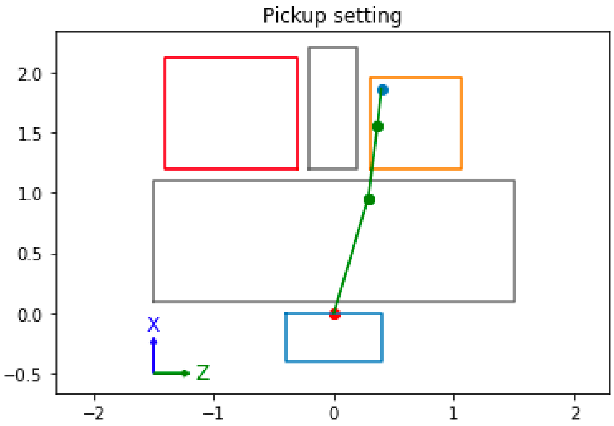

Figure B.43: *3 segment sequential top view top left*

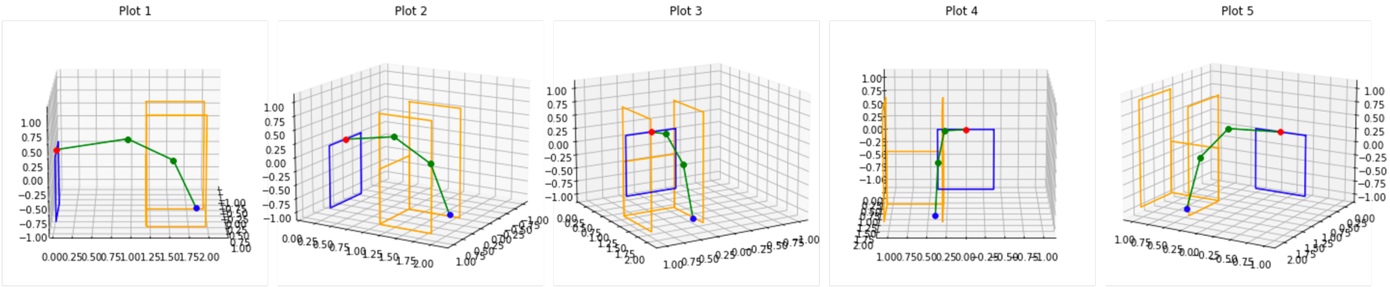

Figure B.44: *3 segment sequential 3D view top left*

Segments	3
Location	Top left
Run times	300.013/300.01 s
True 3D angles	[48.43 ; 40.14] deg
Segment lengths	[1.04, 0.71, 0.91] m
Total length	2.66 m

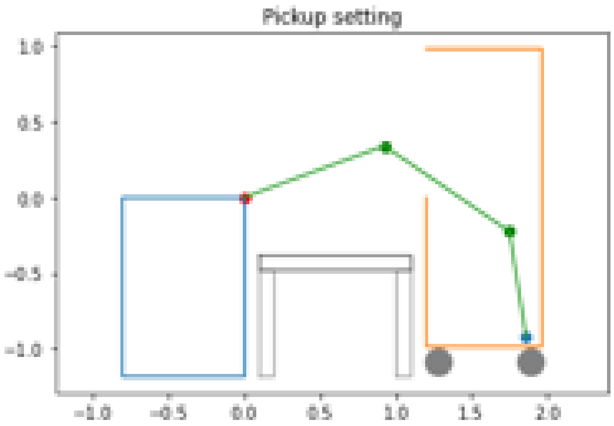

Figure B.45: *3 segment sequential side view top right*

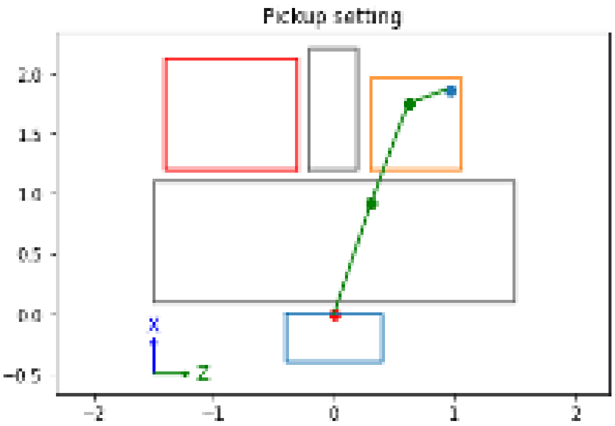

Figure B.46: *3 segment sequential top view top right*

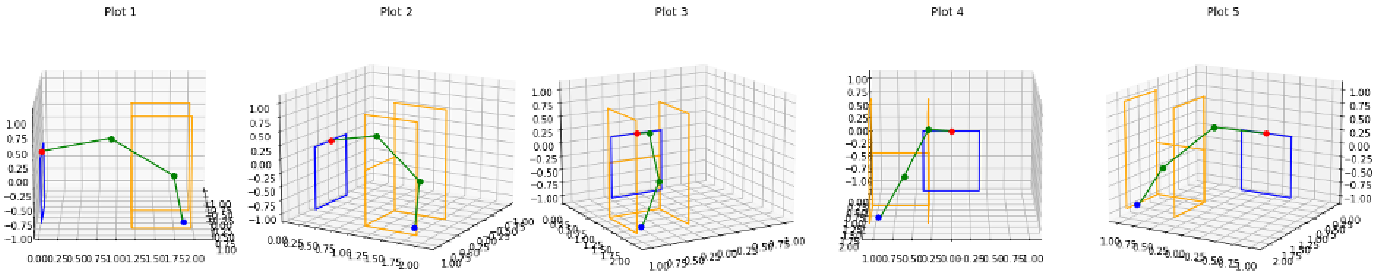

Figure B.47: *3 segment sequential 3D view top right*

Segments	3
Location	Top right
Run times	59.061/0.145 s
True 3D angles	[52.0; 43.31] deg
Segment lengths	[1.03, 1.05, 0.76] m
Total length	2.84 m

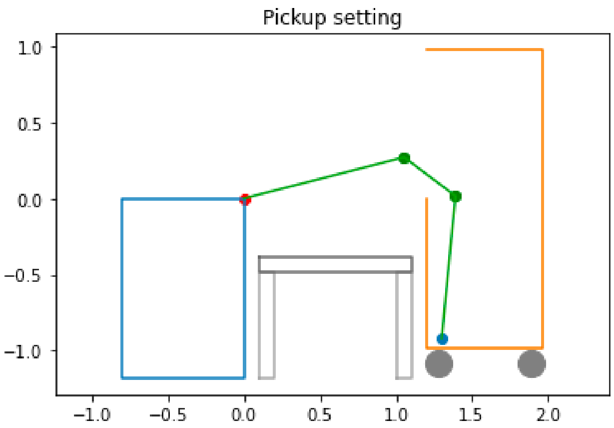

Figure B.48: *3 segment sequential side view bottom right*

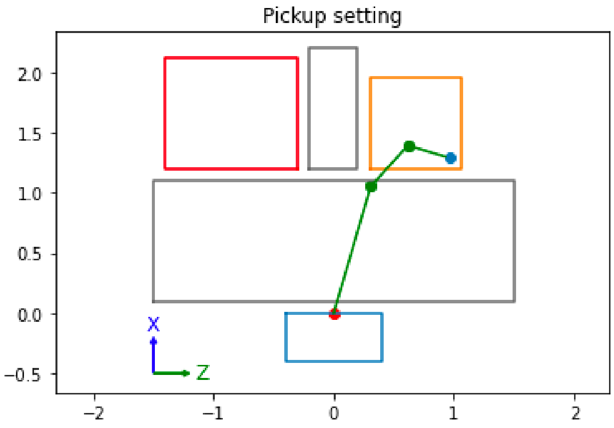

Figure B.49: *3 segment sequential top view bottom right*

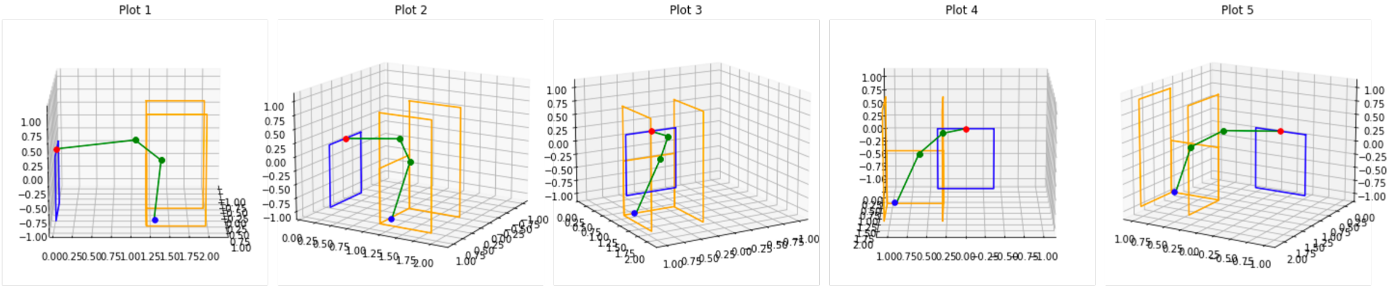

Figure B.50: *3 segment sequential 3D view bottom right*

Segments	3
Location	Lower right
Run times	1.492/0.167 s
True 3D angles	[48.99 ; 54.29] deg
Segment lengths	[1.13, 0.52, 0.99] m
Total length	2.64 m

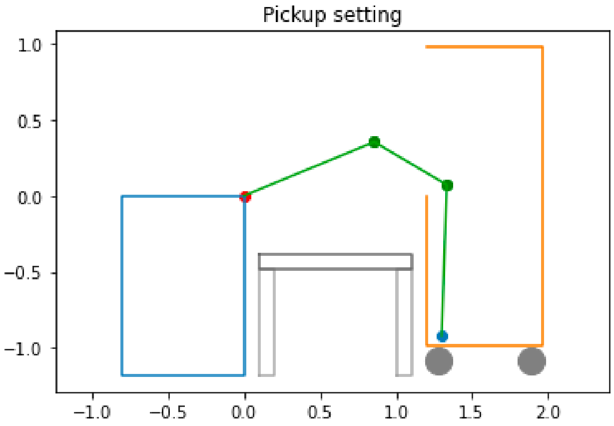

Figure B.51: *3 segment sequential side view bottom left*

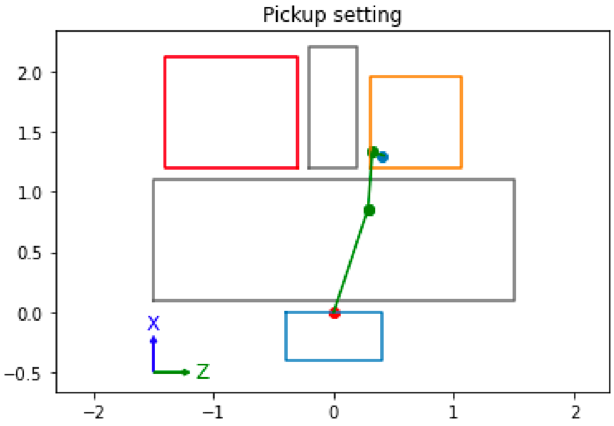

Figure B.52: *3 segment sequential top view bottom left*

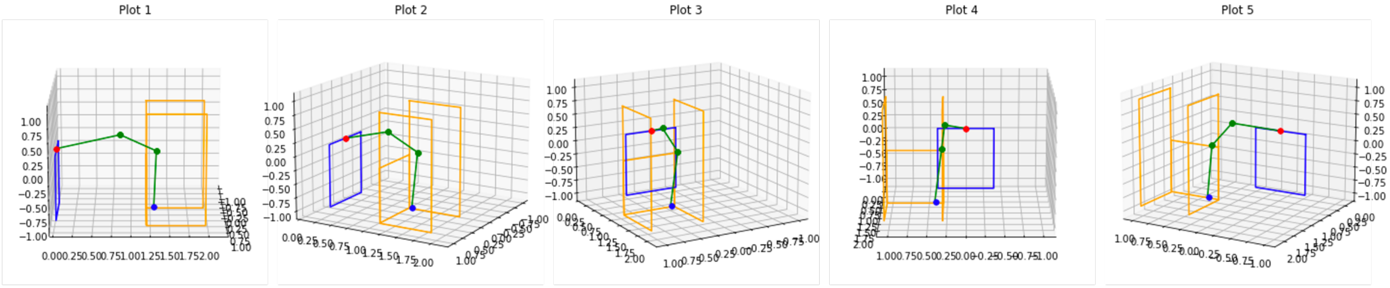

Figure B.53: *3 segment sequential 3D view bottom left*

Segments	3
Location	Lower left
Run times	300.016/2.509 s
True 3D angles	[53.57 ; 61.22] deg
Segment lengths	[0.97, 0.55, 0.99] m
Total length	2.52 m

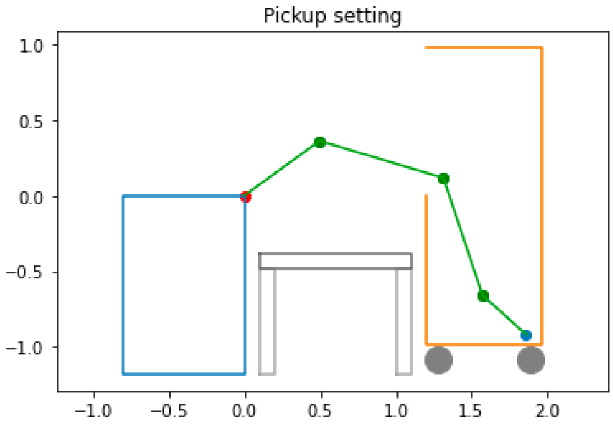

Figure B.54: *4 segment sequential side view top left*

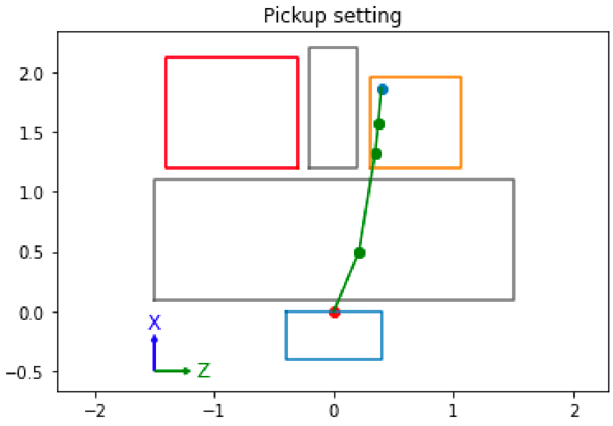

Figure B.55: *4 segment sequential top view top left*

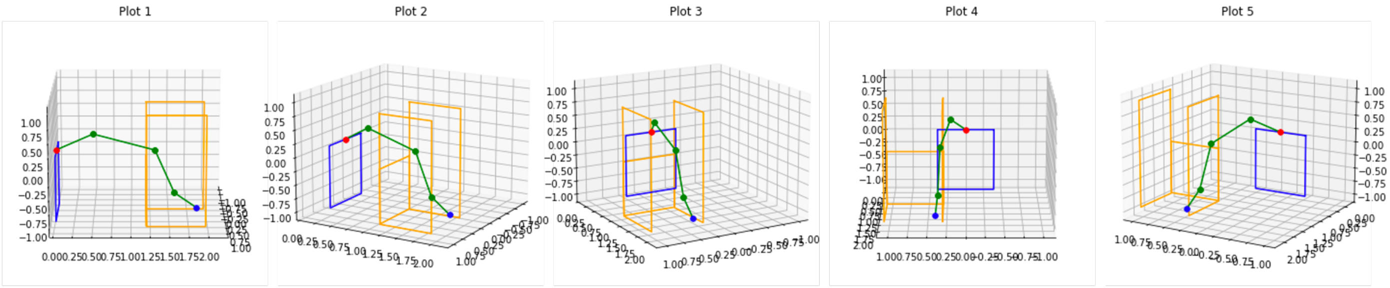

Figure B.56: *4 segment sequential 3D view top left*

Segments	4
Location	Top left
Run times	300.026/300.025 s
True 3D angles	[52.38 ; 55.38 ; 29.21] deg
Segment lengths	[0.65, 0.87, 0.82, 0.39] m
Total length	2.73 m

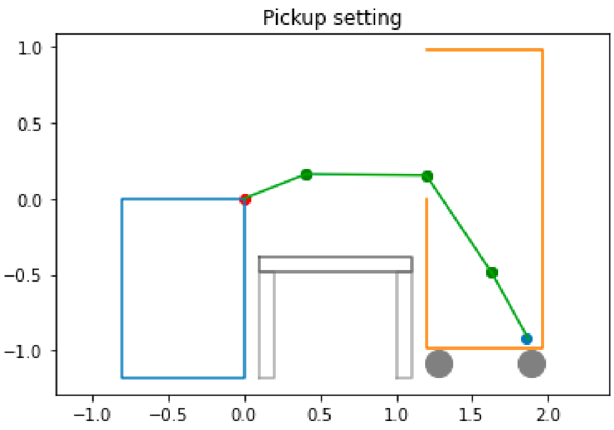

Figure B.57: *4 segment sequential side view top right*

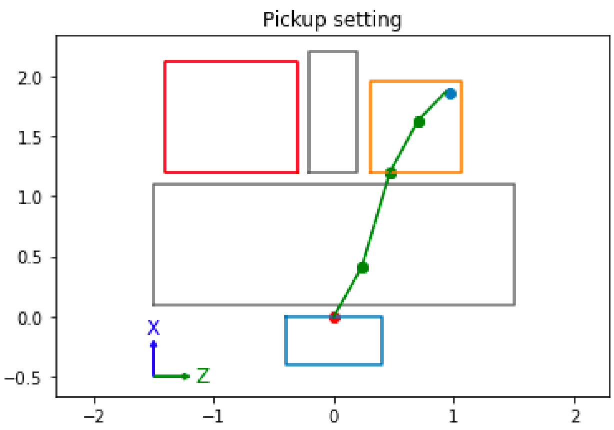

Figure B.58: *4 segment sequential top view top right*

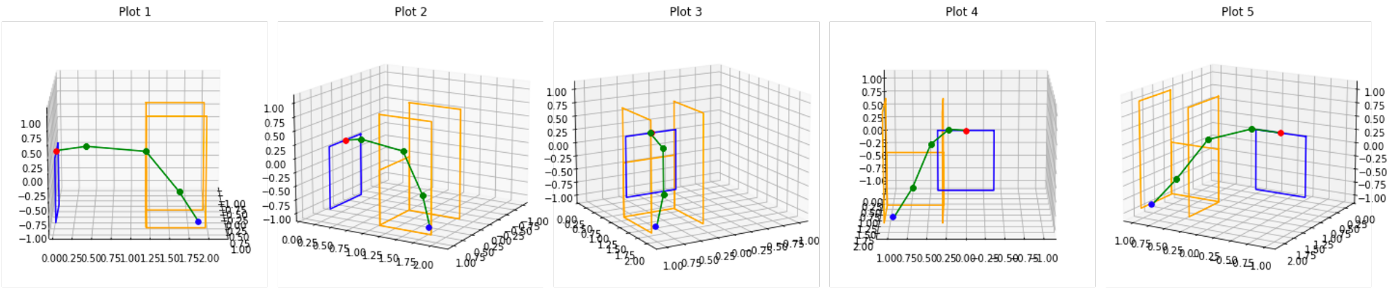

Figure B.59: *4 segment sequential 3D view top right*

Segments	4
Location	Top right
Run times	300.016/0.152 s
True 3D angles	[23.32 ; 52.92 ; 9.47] deg
Segment lengths	[0.50, 0.82, 0.80, 0.55] m
Total length	2.67

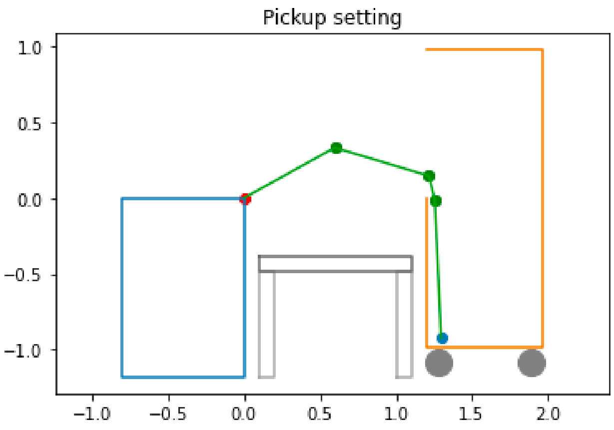

Figure B.60: *4 segment sequential side view bottom right*

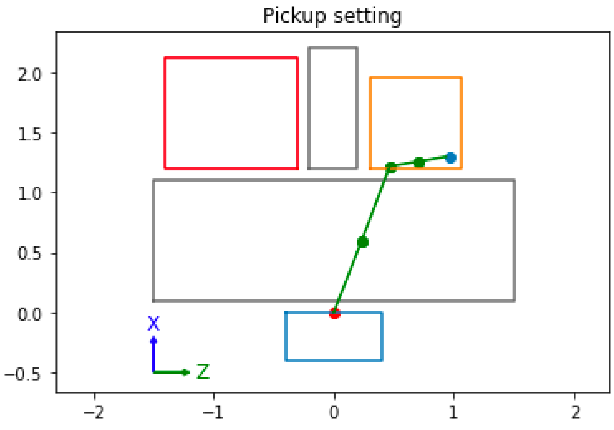

Figure B.61: *4 segment sequential top view bottom right*

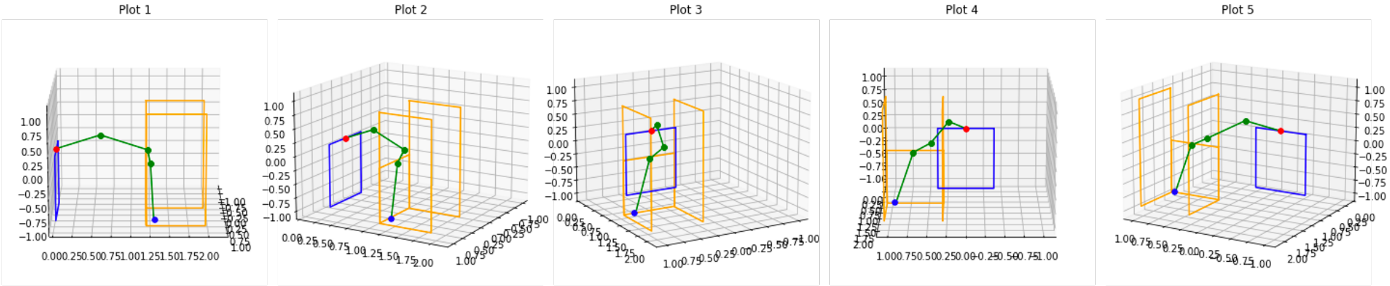

Figure B.62: *4 segment sequential 3D view bottom right*

Segments	4
Location	Lower right
Run times	600.017/0.079 s
True 3D angles	[43.01 ; 56.77 ; 41.24] deg
Segment lengths	[0.72, 0.69, 0.29, 0.94] m
Total length	2.63 m

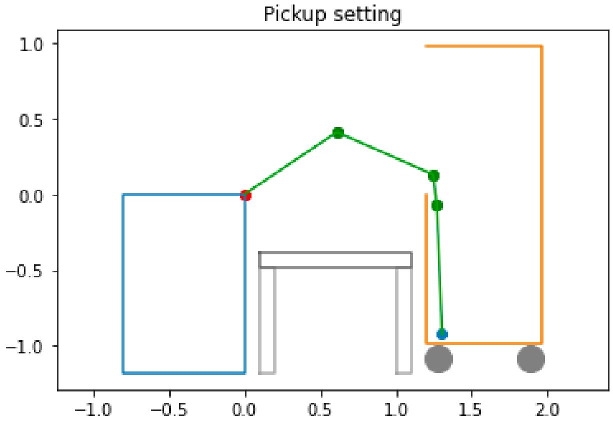

Figure B.63: *4 segment sequential side view bottom left*

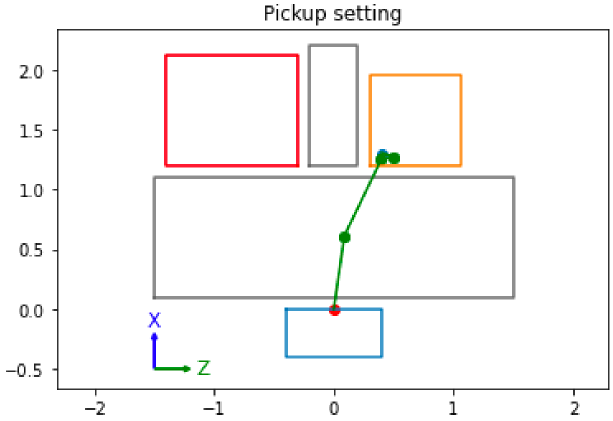

Figure B.64: *4 segment sequential top view bottom left*

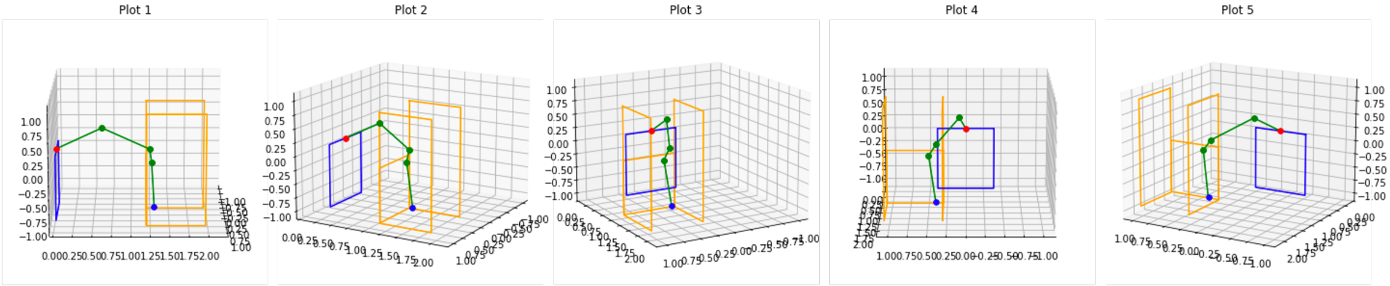

Figure B.65: *4 segment sequential 3D view bottom left*

Segments	4
Location	Lower left
Run times	300.018/300.023 s
True 3D angles	[57.81 ; 52.25 ; 31.33] deg
Segment lengths	[0.74, 0.76, 0.22, 0.86] m
Total length	2.58 m

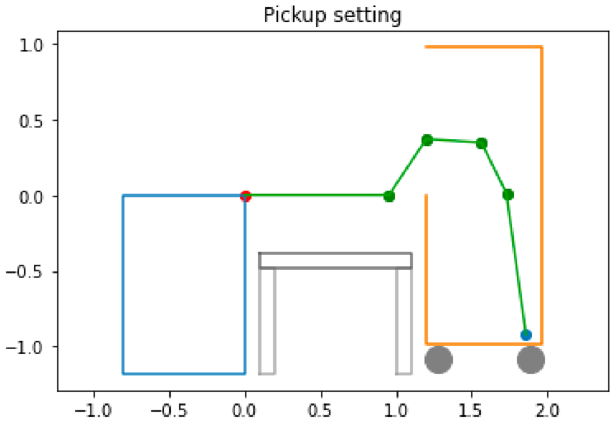

Figure B.66: *5 segment sequential side view top right*

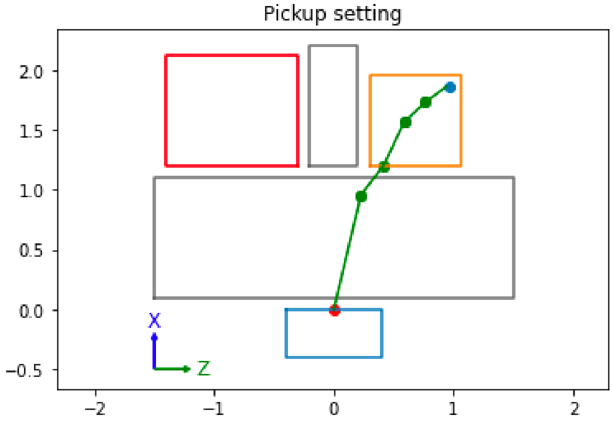

Figure B.67: *5 segment sequential top view top right*

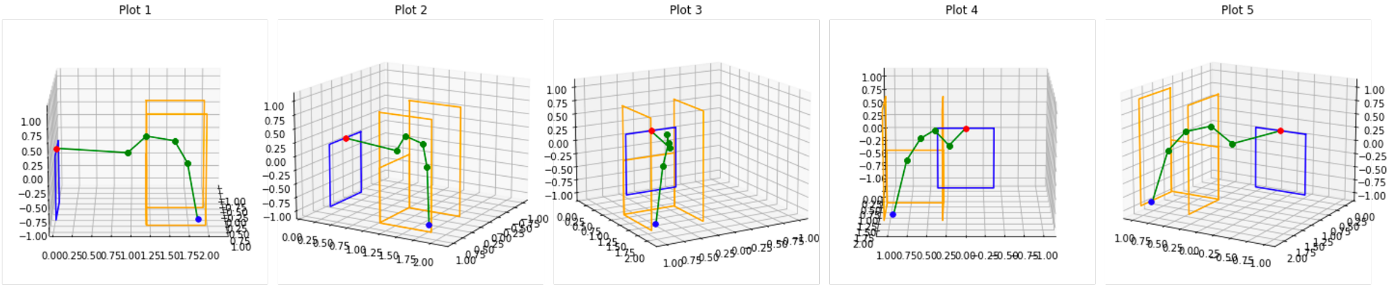

Figure B.68: *5 segment sequential 3D view top right*

Segments	5
Location	Top right
Run times	36.445/900.018 s
True 3D angles	[54.04 ; 54.4 ; 53.68 ; 22.98] deg
Segment lengths	[0.98, 0.48, 0.40, 0.41, 0.96] m
Total length	3.23 m

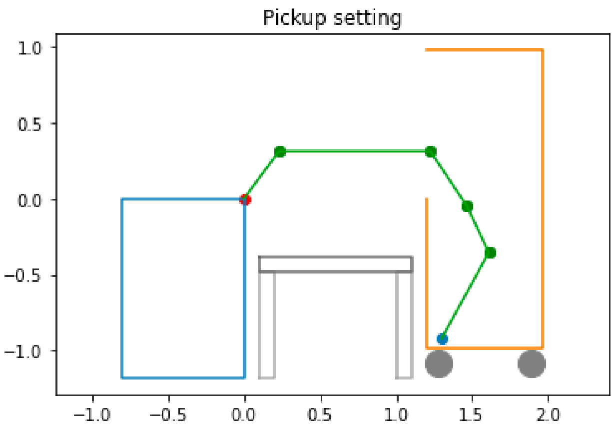

Figure B.69: *5 segment sequential side view bottom right*

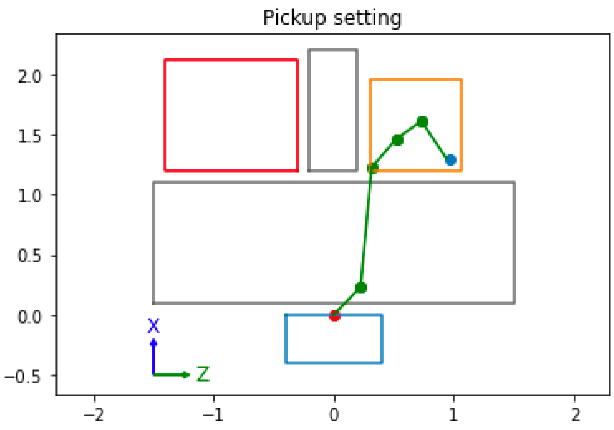

Figure B.70: *5 segment sequential top view bottom right*

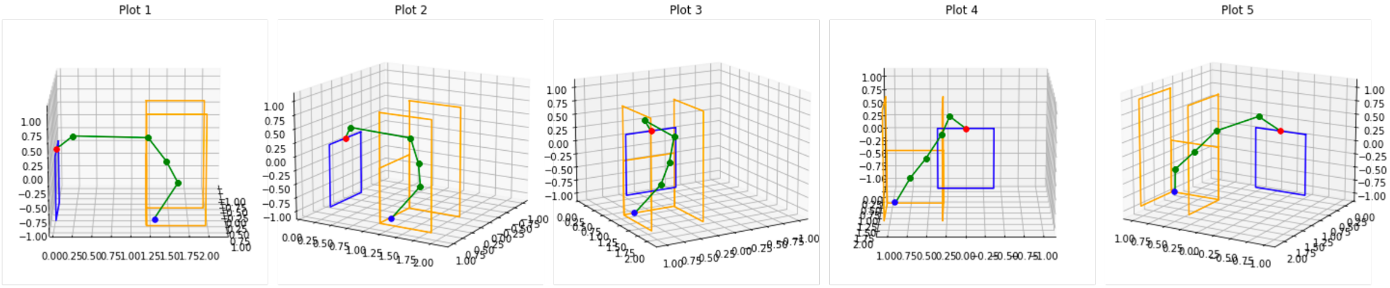

Figure B.71: *5 segment sequential 3D view bottom right*

Segments	5
Location	Lower right
Run times	646.199/9.303 s
True 3D angles	[56.04 ; 57.49 ; 9.06 ; 50.64] deg
Segment lengths	[0.45, 1.0, 0.48, 0.40, 0.68] m
Total length	3.00

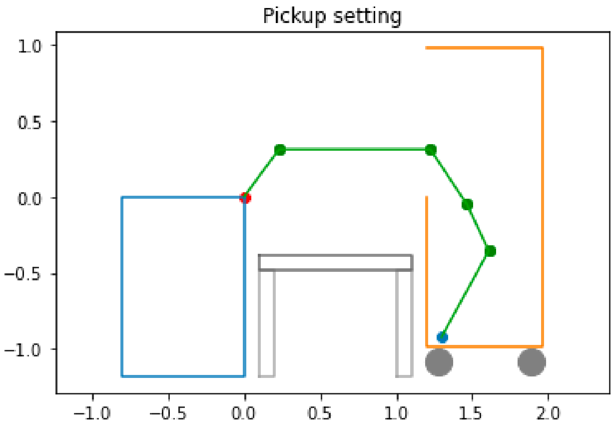

Figure B.72: *5 segment sequential side view bottom left*

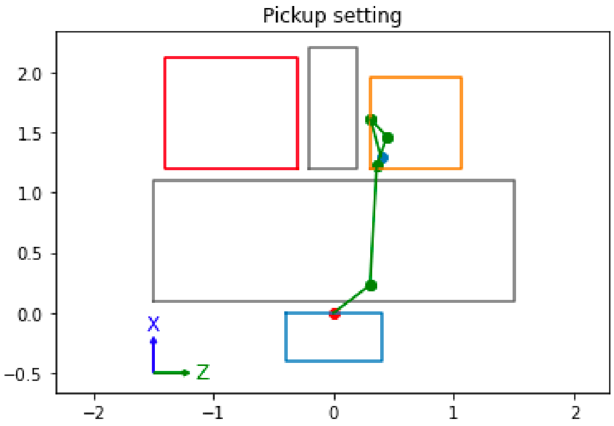

Figure B.73: *5 segment sequential top view bottom left*

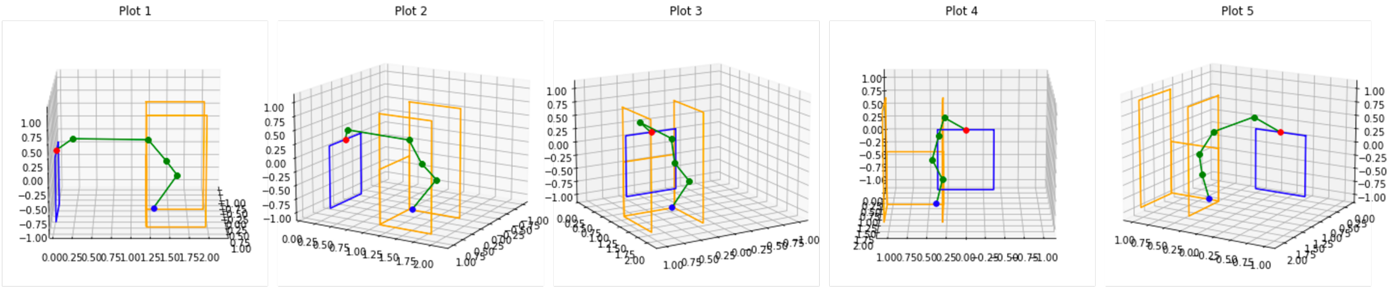

Figure B.74: *5 segment sequential 3D view bottom left*

Segments	5
Location	Lower left
Run times	648.953/900.028 s
True 3D angles	[59.79 ; 56.33 ; 33.73 ; 60.63] deg
Segment lengths	[0.49, 1.00, 0.44, 0.37, 0.65] m
Total length	2.94 m

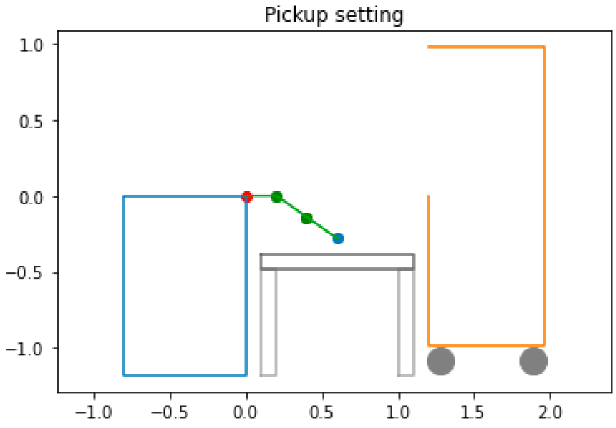

Figure B.75: *3 segment sequential side view belt*

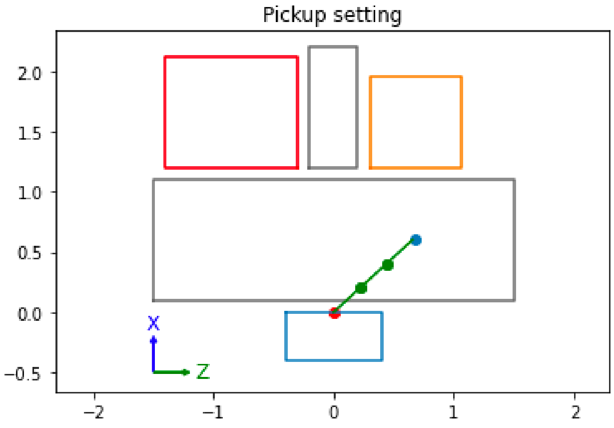

Figure B.76: *3 segment sequential top view belt*

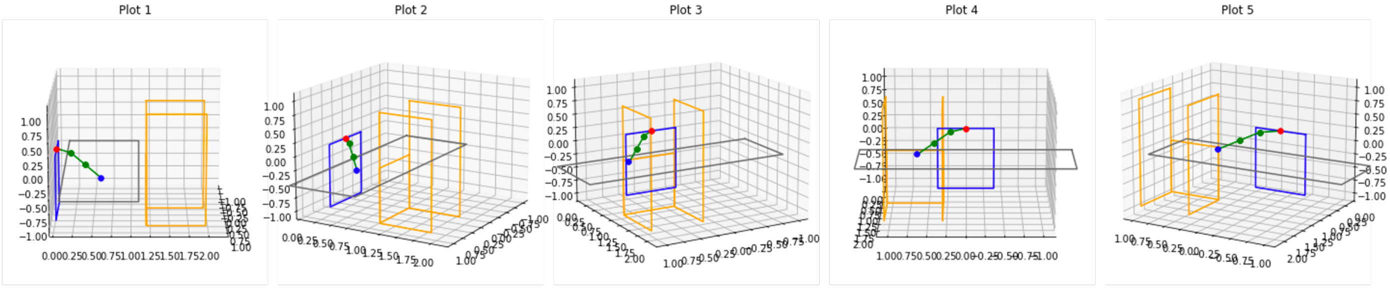

Figure B.77: *3 segment sequential 3D view belt*

Segments	3
Location	Belt
Run times	1.378/0.07 s
True 3D angles	[25.28 ; 0]
Segment lengths	[0.30, 0.33, 0.33] m
Total length	0.95

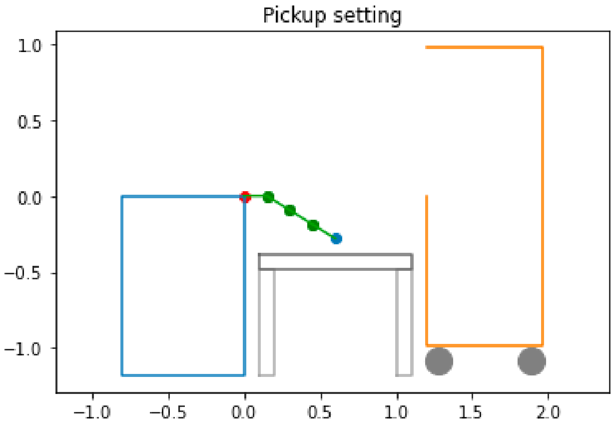

Figure B.78: *4 segment sequential side view belt*

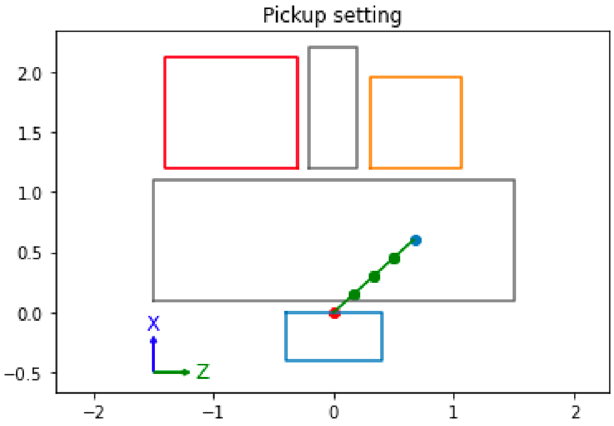

Figure B.79: *4 segment sequential top view belt*

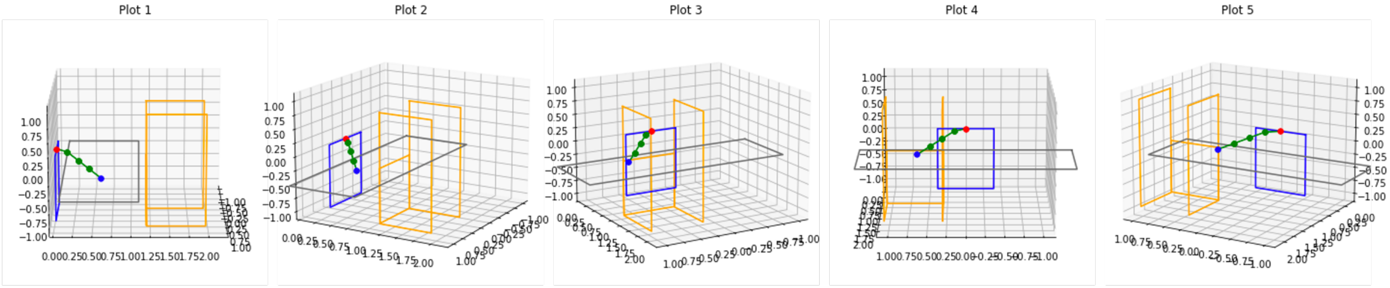

Figure B.80: *4 segment sequential 3D view belt*

Segments	4
Location	Belt
Run times	9.484/0.165 s
True 3D angles	[22.69 ; 1.06 ; 1.13] deg
Segment lengths	[0.22, 0.24, 0.24, 0.24] m
Total length	0.95

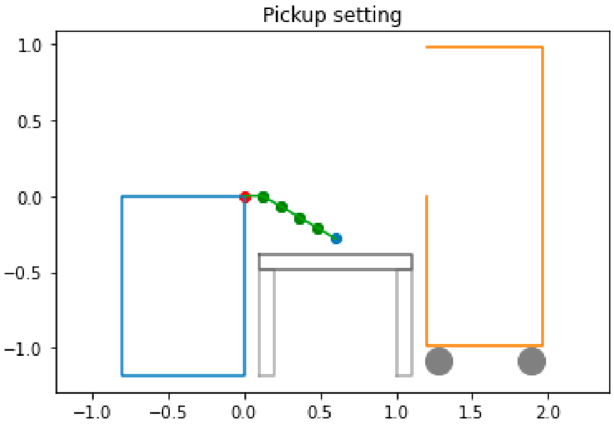

Figure B.81: *5 segment sequential side view belt*

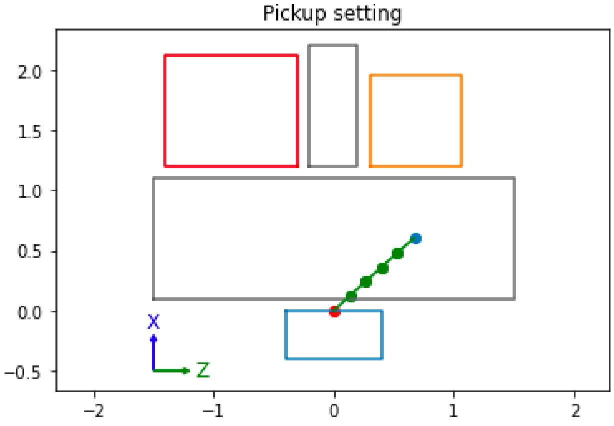

Figure B.82: *5 segment sequential top view belt*

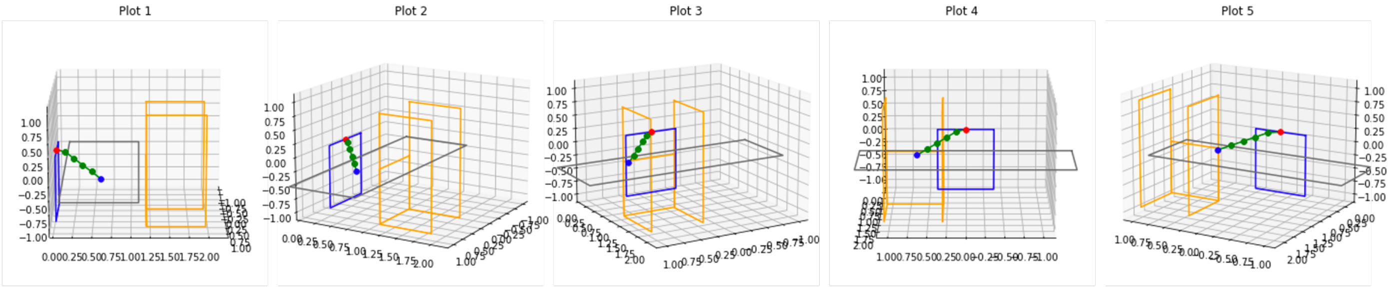

Figure B.83: *5 segment sequential 3D view belt*

Segments	5
Location	Belt
Run times	300.014/0.551 s
True 3D angles	[20.94 ; 1.6 ; 1.18 ; 1.21] deg
Segment lengths	[0.18, 0.19, 0.19, 0.19, 0.19] m
Total length	0.95

Appendix C

Actuator design

C.1. Silicon prototypes

Before the selection of the Kresling cylinder into the actuator, silicon bellows were explored. Before adopting the modeling approach, prototypes were constructed on a trial and error base to explore construction techniques. This appendix shall explain the process and convey its learnings.

Mk1

The bellow for the first prototype (Mk1) was casted from Smooth-On's Dragon Skin 30 with a bellow thickness of 2 mm. This tough type of silicon from Smooth-On was selected as the actuator required some stiffness and Dragon Skin is a tougher silicon type. Solenoid holders were constructed from various PLA components, 3D printed using a Prusa MK3s 3D printer, assembled using Pattex Crocodile super glue. Using coated D 0.3 mm copper wire (Velleman), coils were wrapped inside the solenoid holders until 50 turns were present per coil. This prototype contained a steel core, created from a rod with a diameter of 1 cm and a length of 1.5 cm and was contained in the centers of the coils using 3D printed PLA components, assembled with super glue.

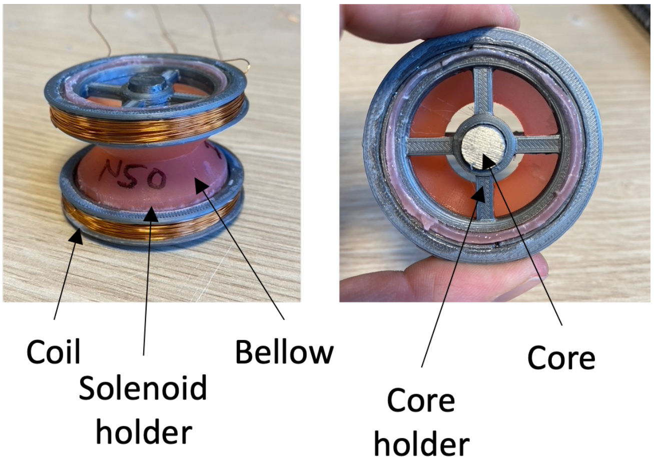

Figure C.1: *Prototype Mk1.*

After excitation with a current of 3A, no noticeable force was generated. However, the coils became relatively hot and started to soften the PLA solenoid holders, and smoke was created. Upon observing smoke generation the power supply was turned off immediately. Mk1 can be seen in Figure C.1. The bellow required substantial force to contract by hand and showed bi-stable behavior. It was concluded that with a similar number of turns, the bellow must pose less resistance in axial direction. The summary of Mk1 is presented in Table C.1.

Table C.1: *Mk1 summary*

Pros	**Cons**
Simple bellow casting	Negligible force generation
	Silicone too stiff
	Solenoid holders soften upon excitation
	Smoke generation

Mk2

To ensure less resistance in axial direction, the bellow for prototype 2 (Mk2) was fabricated from a more flexible Smooth-On product: Ecoflex 50. A new inner piece for the bellow casting was created using the Prusa PLA printer to achieve a bellow wall thickness of 1 mm. In an attempt to cope with the heat generation, a more heat resistant 3D print material was used. Mk2 contained solenoid holders comprising of resin printed components printed by a Formlabs resin printer using the Model V2 resin, which were assembled using super glue. As this material is printed using lithography technology and is cured afterwards, it cannot soften when heated which results in a more discrete life span as the material will start to burn at a higher temperature than when PLA starts to soften and melt. In the solenoid holders coils with 60 turns are wound using coated D 0.3 mm copper wire and identical core and core holders from Mk1.

Upon excitation (3A), Mk2 also showed no signs of force generation. However, the bellow was substantially softer than Mk1. Yet, Mk2 showed smoke generation, which is highly undesired. When experimenting with coil excitation and testing the magnetic attraction of the cores with iron items like pliers, still no promising force was observed. Mk2 is shown in Figure C.2. A summary of Mk2 is presented in Table C.2.

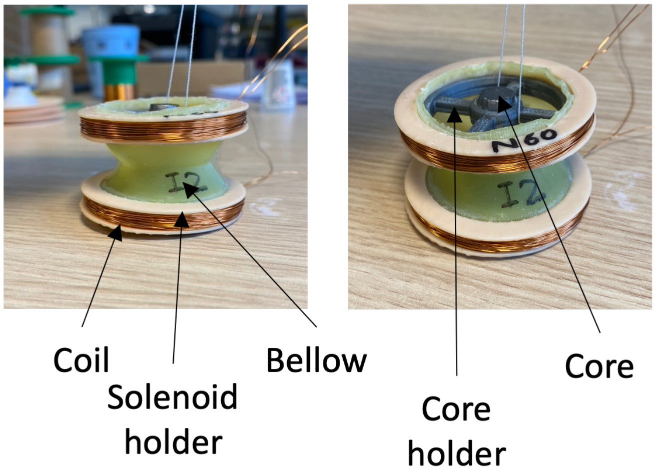

Figure C.2: *Prototype Mk2.*

Table C.2: *Mk2 summary*

Pros	Cons
Simple bellow casting	Negligible force generation
Flexible silicon in axial direction	Silicon too flexible in lateral direction
Solenoid holders maintains rigidity upon excitation	Smoke generation

Mk3

To account for more force generation, prototype 3 (Mk3) incorporated bigger coils (200 turns) and switched from a small rod-like core to a hollow disc core with a thickness of 4 mm. The cores are constructed from a double layer of 2 mm thick plate steel, formed using a CNC laser cutter. The silicone bellow was identical to that of Mk2, a wall thickness of 1 mm, made from Ecoflex 50. To accommodate these bigger coils, larger coil holders were printed using Model V2, printed by a Formlabs resin printer, and were assembled using super glue. Since the cores were large discs now, no core holder was required since the cores could directly be glued inside the bellow. Mk3 is shown in Figure C.3.

Upon excitation (3A), the coils showed a very noticeable attraction. With the top coil suspended on a line, the bottom coil would attract upwards. Again, smoke was observed and the resin printed coil holders started to make cracking sounds. After cooling, the coil holders showed signs of brittleness in the form of small cracks along the outer surfaces.

Table C.3: *Mk3 summary*

Pros	Cons
Significant force generation	Solenoid holders becoming brittle
Flexible silicon in axial direction	Silicon too flexible in lateral direction
Simple bellow casting	Smoke generation

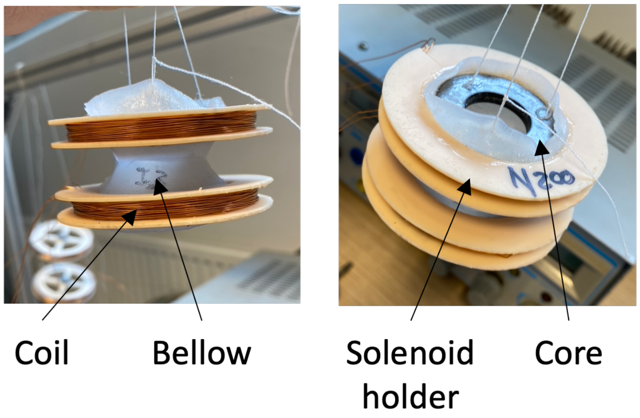

Figure C.3: *Prototype Mk3.*

Mk4

With substantial force generation shown in Mk3, prototype 4 (Mk4) included similarly sized coils (220 turns per coil). However, 3D printed solenoid holders did not possess the right capabilities to form durable prototypes for repeated testing. Therefore, aluminium solenoid holders were constructed using a lathe. Aluminium was chosen as it has a high melting temperature, is easy to work with, and from all metals is one of the lightest. The coils are hand-wound in the aluminium coil holders and the use of glue was avoided. The cores and bellow from Mk3 were adopted into the design of Mk4. Mk4 is shown in Figure C.4.

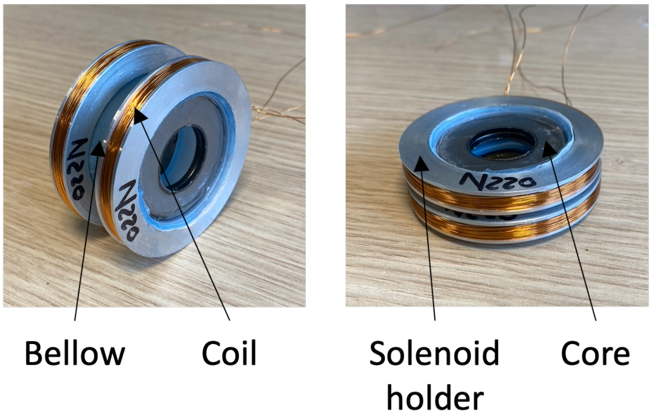

Figure C.4: *Prototype Mk4.*

Upon excitation (3A), the coils showed a slight improved attraction with respect to Mk3. The coil holders did rise in temperature but no smoke was observed. In a suspended setup, the bottom coil would attract upwards, but slowly with a lever effect, i.e. one side of the coil would first attract towards the top coil, followed by a slow completion of the attraction until both coils were pressed together. The attraction progression of Mk4 is shown in Figure C.5. Ideally, the two coils are faster and symmetrically attracted to one another to create a more reliable actuator.

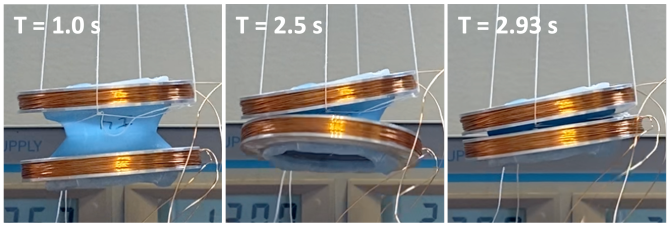

Figure C.5: *Actuation stroke of Mk4.*

Table C.4: *Mk4 summary*

Pros	**Cons**
Significant force generation	Attraction not reliable enough
Flexible silicon in axial direction	Silicon too flexible in lateral direction
Robust and rigid design	

Mk5

In an attempt to increase the magnetic attraction, disc cores without a large hole in the center and with an off set from the coil center along the central axis of the prototype has been tried in Mk5. A small hole was made in one of the cores to ensure that the inside of the bellow would not be air tight and maintained freedom to contract. Thinner cores with a thickness of 1 mm are used. The same number of turns as Mk4 are included but in a thinner packing. To enhance the stiffness in lateral direction, a bellow with a wall thickness of 2 mm, casted in Dragon Skin 30 is implemented.

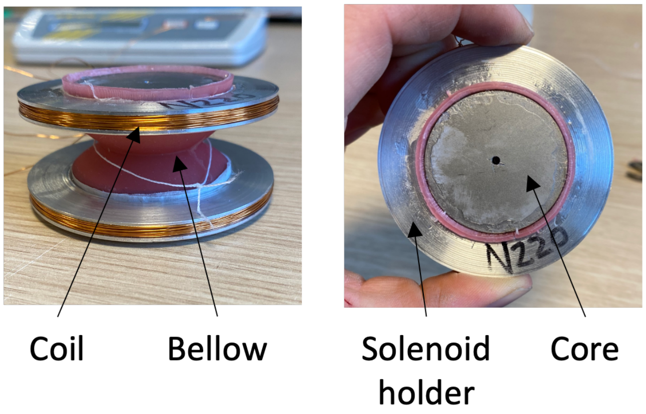

Figure C.6: *Prototype Mk5.*

Upon excitation (3A), the coils did not attract each other to initiate movement. Reasons for this could be that the core placement has a negative effect on the magnetic response or that the use of the different silicone posed to much resistance. As seen in Figure C.6, the top coil could be fully supported by the silicone bellow, indicating axial stiffness.

Table C.5: *Mk5 summary*

Pros	**Cons**
Robust and rigid design	Attraction not enough to contract silicone
Silicone stiffer in lateral direction	Silicon too stiff in axial direction

Mk6

In an attempt to overcome the silicone resistance, Mk6 used substantially larger coils with 300 turns, with a similar bellow as Mk5, and a bellow wall thickness of 1 mm. After acquiring qualitative data on the distribution of the magnetic field and modeling of forces it was concluded that a ferromagnetic core had most impact close to the coil windings (Figure C.8 A). Therefore, the cores for Mk6 are simplified to steel rings, consisting of 90% hole, with a thickness of 1 mm, placed in the center of the copper coils. From the modeling it was expected that this prototype would actuate.

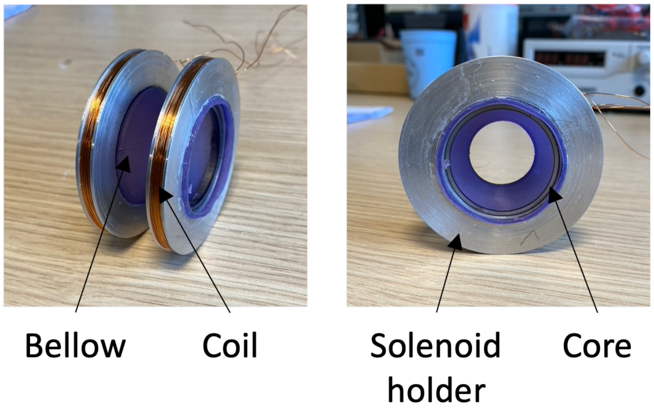

Figure C.7: *Prototype Mk6.*

Upon excitation (3A), no actuation was observed. In the model, the resistance of the Kresling cylinder was assumed to be negligible. Due to the contradictory result from the expectation, the resistance of the silicon would be considered in the next prototype. Despite the use of Dragon Skin 30, the silicon bellow still showed large deformation effects due to gravity in horizontal orientation which remained a challenge (Figure C.8 B). Combined with the large stiffness in axial direction alternatives were explored for an alternative Kresling cylinder. The new hollow core showed significant force generation, but not enough for actuation. The summary of Mk6 is found in Table C.6.

Table C.6: *Mk6 summary*

Pros	**Cons**
Robust and rigid design	Attraction not enough to contract silicone
Good magnetic response by new core	Silicon too stiff in axial direction
	Silicon too flexible in lateral direction

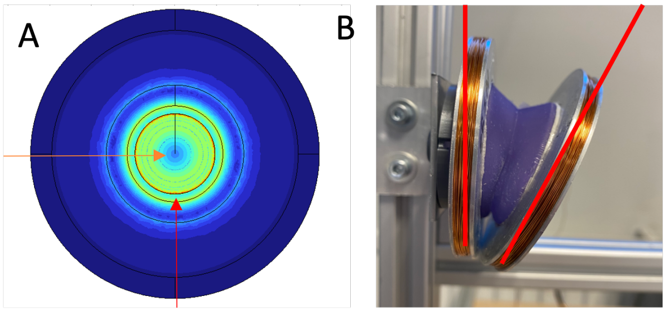

Figure C.8: *(A) Magnetic field intensity on color scale (intense to weak: red-green-blue). The red arrow indicates the peak of magnetic intensity on the outer border of the core disc and the orange arrow the minimum of the magnetic field in the center of the core disc. (B) Demonstration of flexibility of bellow in lateral direction from Dragon Skin 30 due to gravity of the solenoids.*

C.2. Silicone resistance

For post assessment of the prototypes found in Appendix A, the resistance of the silicone bellows is mapped. To measure the resistance, a load cell is slowly but consistently pressed upwards against the bottom of the silicon structure until the bottom is displaced about half of the resting length to ensure that no reaction forces are introduced from the top fixation. After 50% displacement is reached the load cell is released downwards until it is free from the bellow structure. This motion is repeated several times to calculate an average resistance. The procedure is depicted in Figure C.9. The resisting force due to the silicone bellow is refered to as F_{dis}.

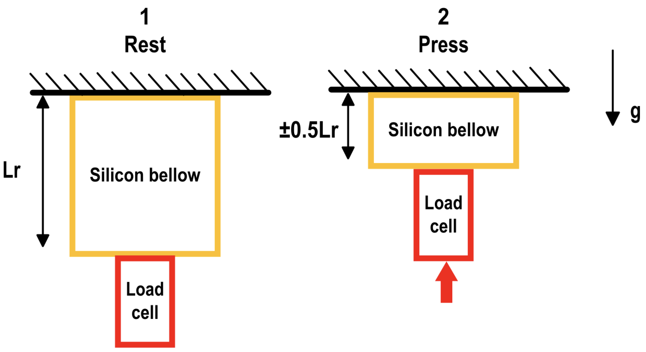

Figure C.9: *Method of measuring the resistance of the silicon Kresling cylinder. Lr indicates the resting length of the silicon structure when hanging free as depicted. Procedure: a load cell is slowly but consistently pressed upwards against the bottom of the silicon structure until the bottom is displaced about half of the resting length to ensure that no reaction forces are introduced from the top fixation. After 50% displacement is reached the load cell is released downwards until it is free from the bellow structure. This motion is repeated several times to calculate an average resistance.*

Table C.7 shows the details of forces in prototypes 1 to 6. Forces F_g imply gravitational forces of a single coil/core assembly, F_{dis} the resistance as determined in this appendix and F_m the force that each prototype should generate as obtained from the modeling and adjusted with the error between FEA model and real life. It shows that all prototypes lack magnetic force to overcome the gravitational force and the resisting force of the bellow.

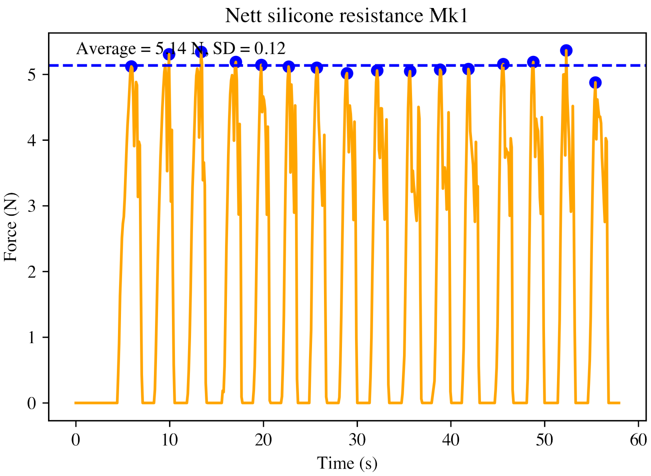

Figure C.10: *Nett silicon resistance of Mk1*

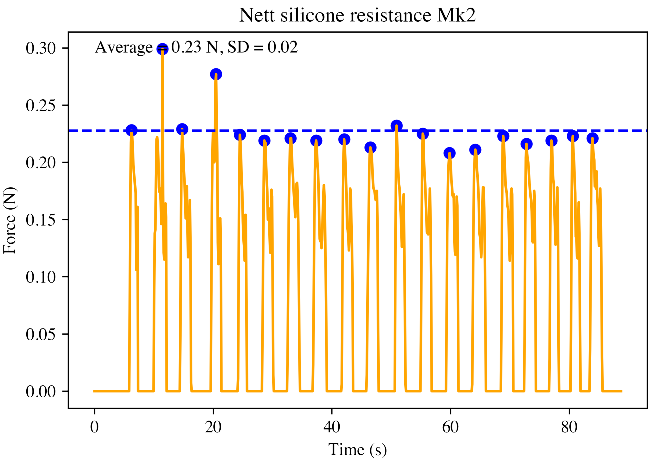

Figure C.11: *Nett silicon resistance of Mk2*

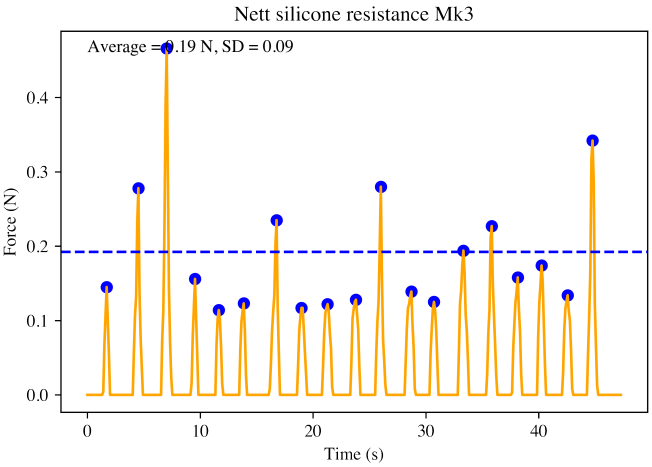

Figure C.12: *Nett silicon resistance of Mk3*

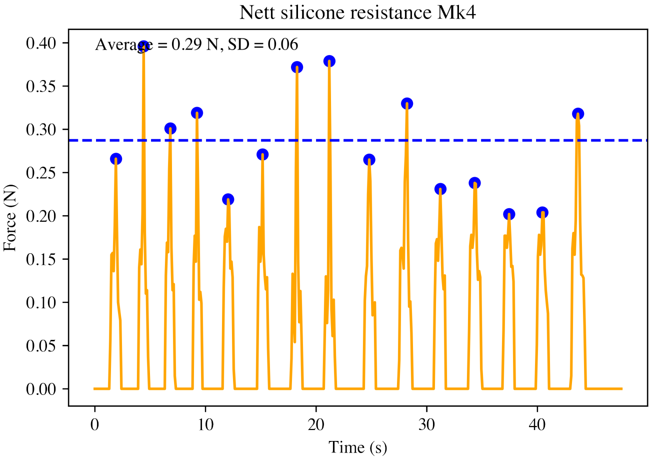

Figure C.13: *Nett silicon resistance of Mk4*

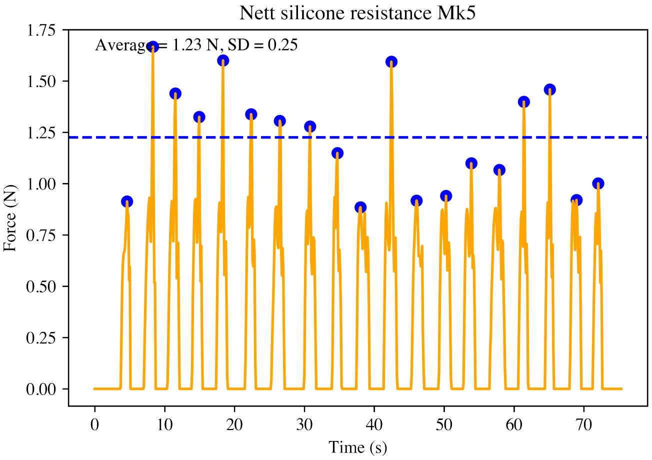

Figure C.14: *Nett silicon resistance of Mk5*

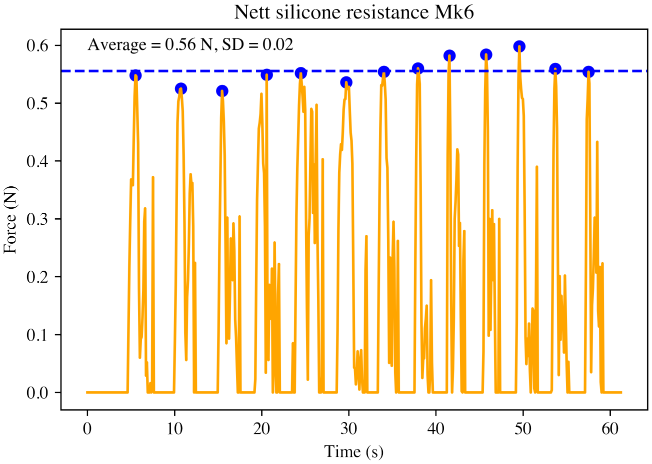

Figure C.15: *Nett silicon resistance of Mk6*

Table C.7: *Summary of forces in prototypes 1 to 6.*

	F_g	F_{dis}	F_m	
Mk1	0.190	5.137	0.020	N
Mk2	0.183	0.228	0.027	N
Mk3	0.585	0.192	0.353	N
Mk4	0.629	0.287	0.436	N
Mk5	0.598	1.226	0.403	N
Mk6	0.560	0.556	0.724	N

C.3. Additional material test setup

For reproduction of the experiments during prototyping, this section shall present some graphical information on the setup. The hanging test was conducted using a construction made from aluminium extrusion tubes as depicted in Figure C.16.

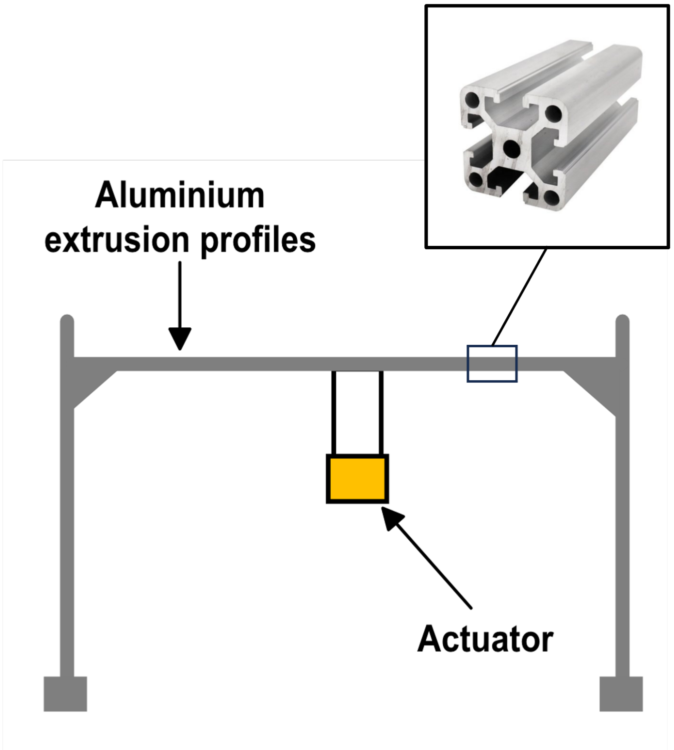

Figure C.16: *Global setup to execute the hanging test.*

The actuator was connected to the horizontal upper rod using threaded rods and nuts. The global attachment is shown in Figure C.17.

Using a precise spacing between the threaded rods, nuts were used to clamp the upper solenoid holder to hold the actuator in place as shown in Figure C.18. In case realising an exact spacing between the threaded rods is impossible, PLA holders can be printed to adhere to the exact sizes of the solenoid holders.

A photo of the overall setup used for this study has been shown in Figure C.19.

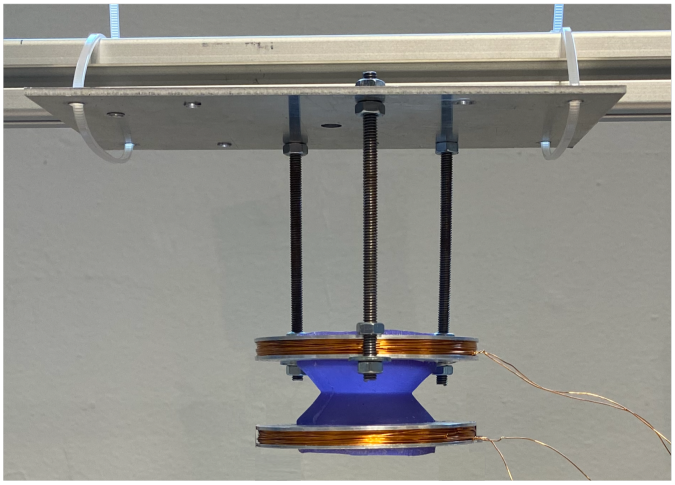

Figure C.17: *Global attachment of actuator in experimental setup, here one of the silicone prototypes, to the horizontal upper rod.*

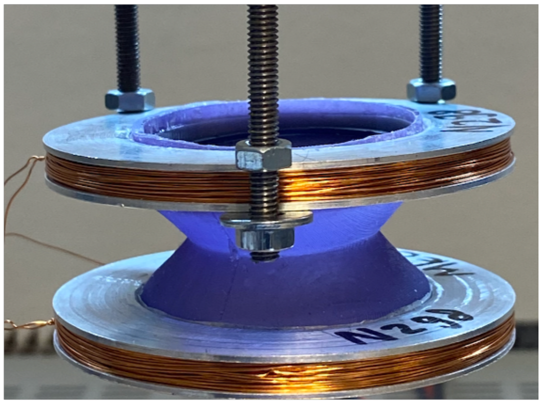

Figure C.18: *Close up of attachment of solenoid holder to threaded rods in experimental setup.*

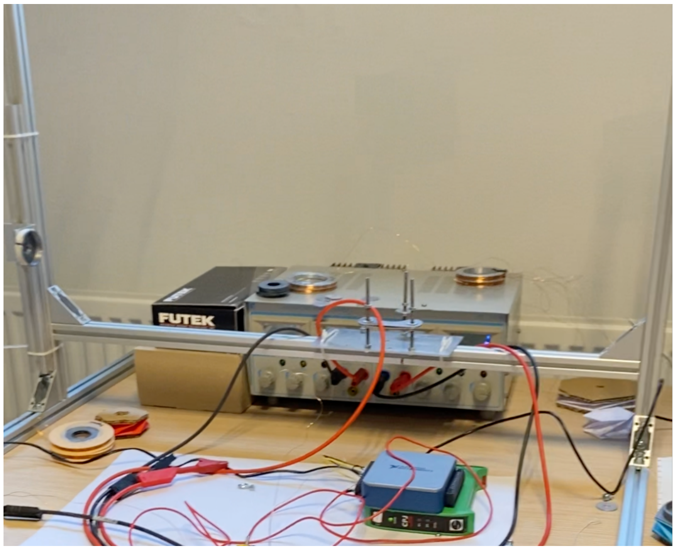

Figure C.19: *Overall setup for this study for experimental setup.*

C.4. Technical drawing solenoid holder

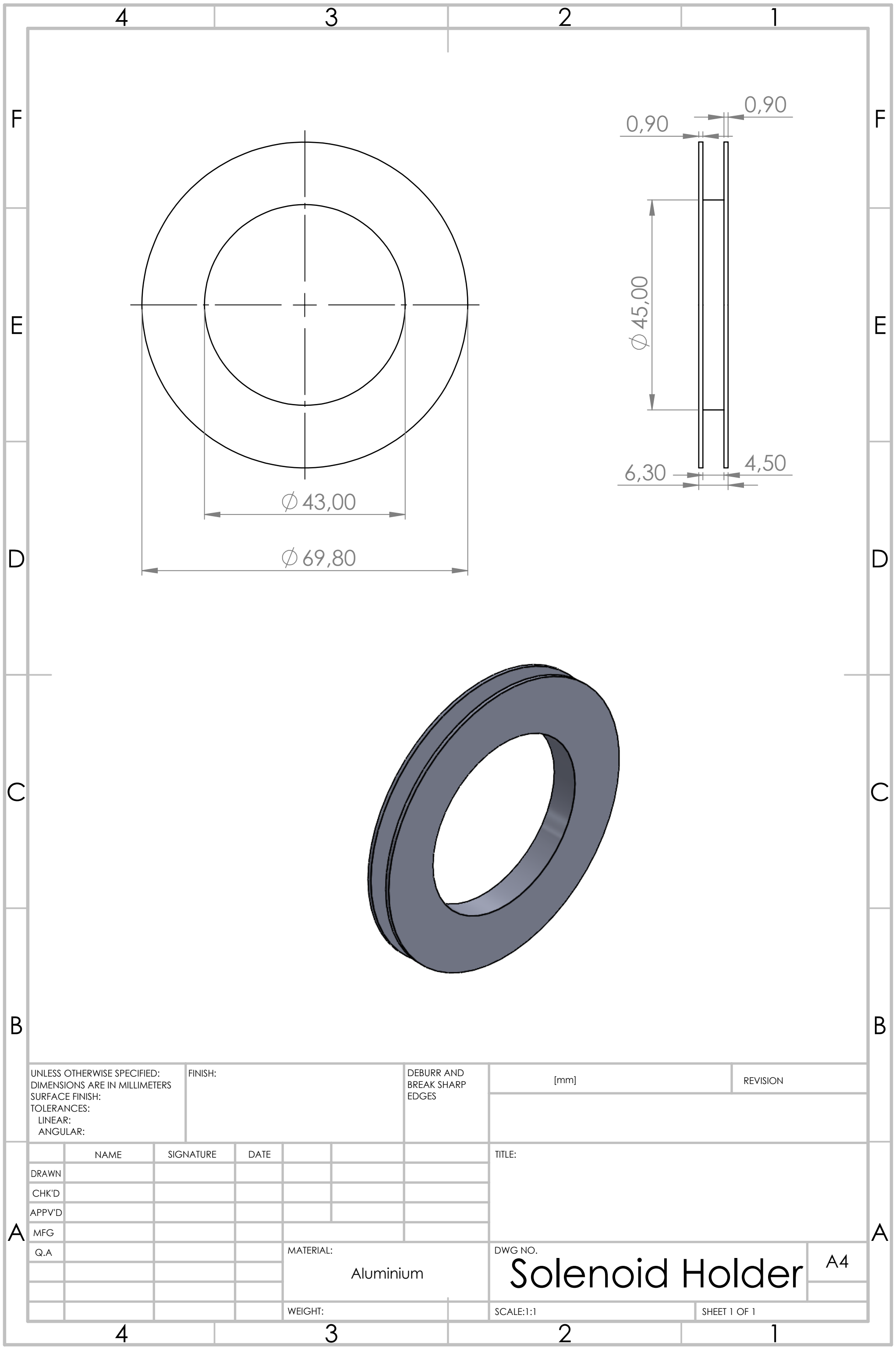

C.5. Technical drawing PLA link plate

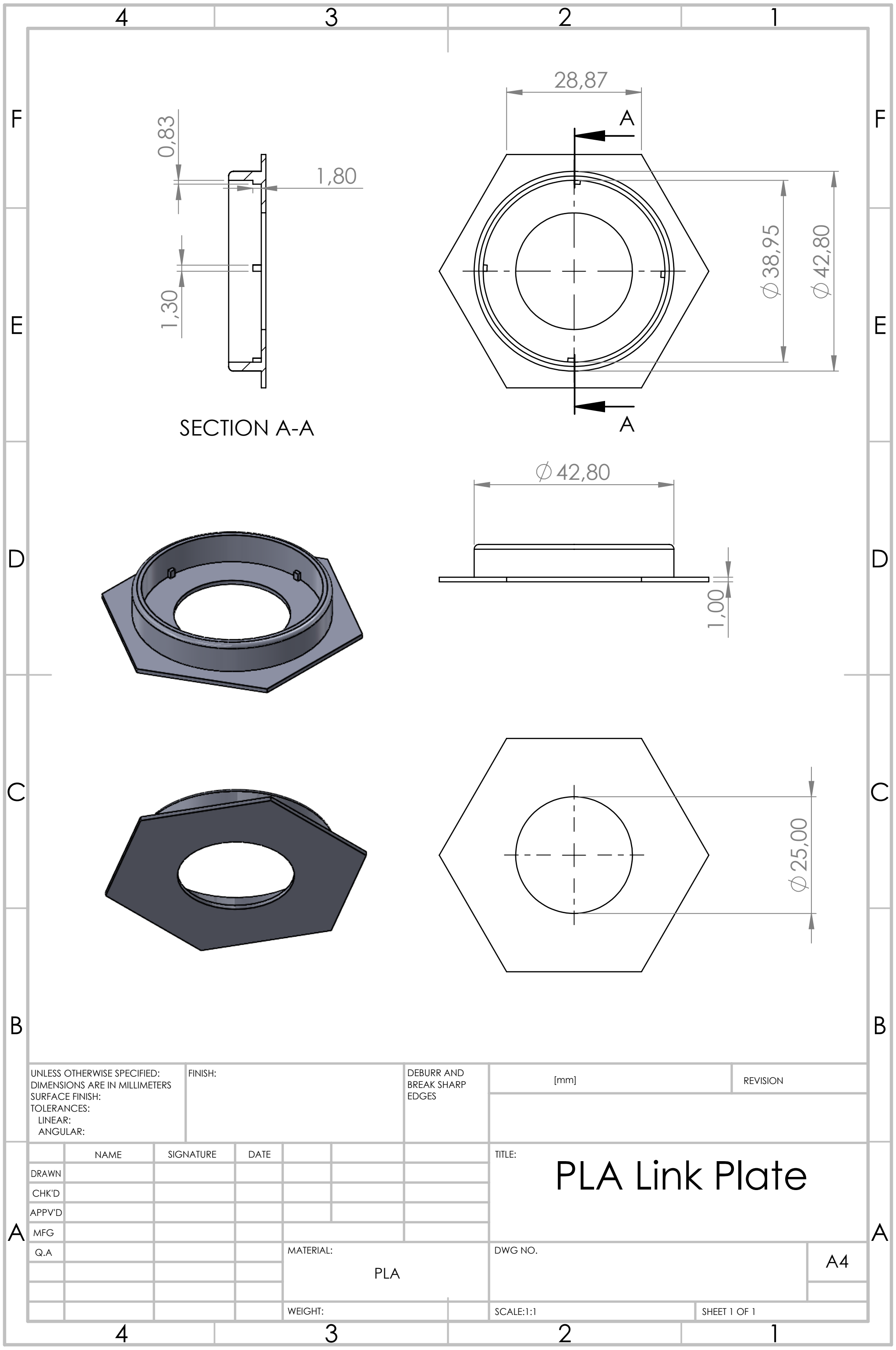

UNLESS OTHERWISE SPECIFIED:
DIMENSIONS ARE IN MILLIMETERS
SURFACE FINISH:
TOLERANCES:
LINEAR:
ANGULAR:

FINISH:

DEBURR AND
BREAK SHARP
EDGES

[mm]

REVISION

	NAME	SIGNATURE	DATE
DRAWN			
CHK'D			
APPV'D			
MFG			
Q.A			

TITLE: PLA Link Plate

MATERIAL: PLA

DWG NO.

A4

WEIGHT:

SCALE:1:1

SHEET 1 OF 1

C.6. Kresling pattern

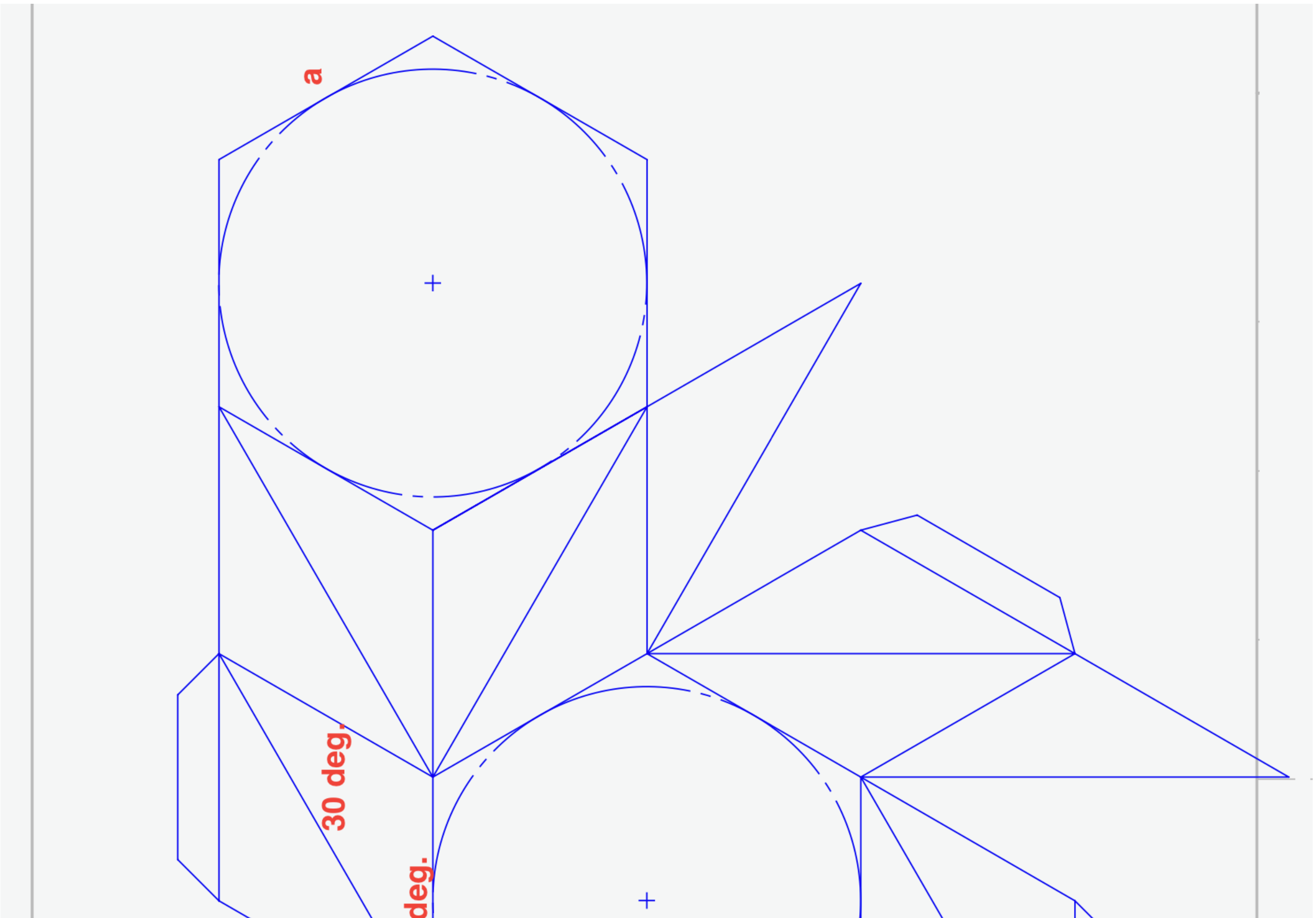

Figure C.20: *Folding pattern for Kresling cylinder as used for prototype. The angles α and β are set to the configuration used in this study but the length of a in this drawing is not to scale.*